



Analytical and Computational Approaches to Thrust, Torque, Steering Control for Tunnel Boring Machine and Automation in Rail.

Ahmad Samadi, Engineering Building & Infrastructure, contact@ebni.com.au
Dep. of Civil, Mechanical and Environmental Engineering, Western Sydney University, Hawkesbury, SYD, NSW, 2753. 21/08/2025

Abstract:

A multidisciplinary study provides a comprehensive investigation into the mechanical modelling, operational control, and manoeuvrability of Tunnel Boring Machines (TBMs), with particular emphasis on thrust and torque performance, steering precision, and the implications for rail alignment tolerances in curved tunnel sections. Traditional approaches to predicting cutterhead behaviour have relied heavily on empirical formulations and TBM diameter. In contrast, this research examines and compares four thrust and torque calculation models, including soil- and rock-based formulations, and evaluates their applicability under complex geological conditions. Field observations highlighted that eccentric TBM alignment during early curve steering generates high vertical stresses, segment distortion, and springline cracking, all of which can compromise tunnel lining integrity. Through mathematical modelling and simulation, yaw and pitch were identified as dominant drivers of horizontal and vertical deviations, while increased articulation angle was shown to reduce steering errors.

A key finding was that the degree of freedom progressively increases from the pinions to the disc cutters, amplifying the influence of cutterhead dynamics on overall steering behaviour. To address excavation efficiency in slurry TBMs, a coupled CFD-DEM two-phase model was developed to simulate slurry-rock interaction and assess the discharge performance of large-diameter screw conveyors. Complementary dynamic modelling of thrust systems was also carried out, integrating multi-cylinder hydraulics with a master-slave PID control mechanism to minimise displacement error and achieve synchronised motion. Importantly, the study extends beyond mechanical optimisation to assess TBM steering tolerance relative to railway curvature requirements, ensuring that tunnels constructed align within geometric limits that safeguard against train derailments.

The combined findings advance the mechanistic understanding of TBM performance and provide design guidance for steering control, segment protection, and discharge efficiency. Moreover, by linking excavation

tolerances to operational safety of subsequent rail systems, this research underscores the critical role of TBM modelling in delivering both construction efficiency and long-term transport reliability.

1. Introduction

Since Tunnel Boring Machines (TBMs) were introduced in the 1950s, engineers and contractors have been focused on accurately predicting their performance in specific project environments. Although significant progress has been made for simpler TBM applications, recent developments in using these machines in more complex geological conditions and the concept of a "Universal Machine" have added new layers of complexity and uncertainty. This has prompted the adoption of probabilistic methods for performance forecasting, where the TBM's advance rate (AR) is represented as a range rather than a fixed value. Similarly, project completion time is projected as a range, based on the probabilistic performance of the machine across different segments of the project. The factors influencing TBM performance include geological conditions, machine operations, and site management, each with a distribution of varying input parameters. This probabilistic approach was first implemented in the planning of Europe's Trans-Alpine tunnels in the 1990s (Einstein 2001). A tunnel boring machine (TBM) is a sophisticated and substantial piece of construction equipment extensively utilised in transportation, municipal, and water diversion projects, owing to its integrated functionalities, rapid tunnelling capabilities, and environmentally sustainable construction practices. (W. Sun et al. 2013)

1.1 Machine Types and Performances

Tunnel Boring Machines (TBMs) are engineered to excavate tunnels through various ground conditions, and their design and operation are influenced by the geological challenges encountered along the tunnel alignment. In cases where mixed ground conditions are present, clear-cut machine classifications are difficult to apply, leading to the development of hybrid TBMs, which combine features of both rock and soil machines, as well as shielded and gripper TBMs. Generally, TBMs are classified into two primary types: machines designed for soft ground and those for hard rock (Jamal Rostami 2016).

Soft Ground TBMs: These machines are shielded to protect the tunnel from wall and face collapses during excavation. Cutting in soft ground is typically performed using drag-type tools like scrapers, and the primary operational challenge lies in ensuring that the volume of material excavated matches the volume displaced by the TBM's forward movement. This balance is crucial to prevent ground subsidence or settlement due to over-excavation. The penetration rate of soft ground TBMs is usually maintained at a constant value during operation, and muck removal is carefully regulated to maintain face pressure. The machine's advance rate typically ranges from 100-120 mm/min for small-diameter machines (-3 m) to

30-40 mm/min for larger-diameter TBMs (~15 m). Even when encountering full-face rock, volume control ensures the stability of face pressure, with cutter load management being the primary focus in maintaining excavation efficiency.

Hard Rock TBMs: In contrast to soft ground machines, hard rock TBMs utilise disc cutters to fracture and break down rock at the tunnel face. These machines operate based on force control, where substantial thrust is applied to the cutters to penetrate the rock. Unlike soft ground TBMs, the volume of material generated is not a limiting factor, as broken rock can be efficiently transported away from the cutting face via buckets or conveyor systems. Cutter load and thrust capacity must be carefully monitored to avoid machine overload. In softer rock formations, excessive thrust can result in deeper penetration, necessitating higher torque and cutterhead power. In such cases, machine torque becomes the limiting factor, rather than thrust, and the rate of penetration (ROP) is governed by a balance between the forces acting at the face.

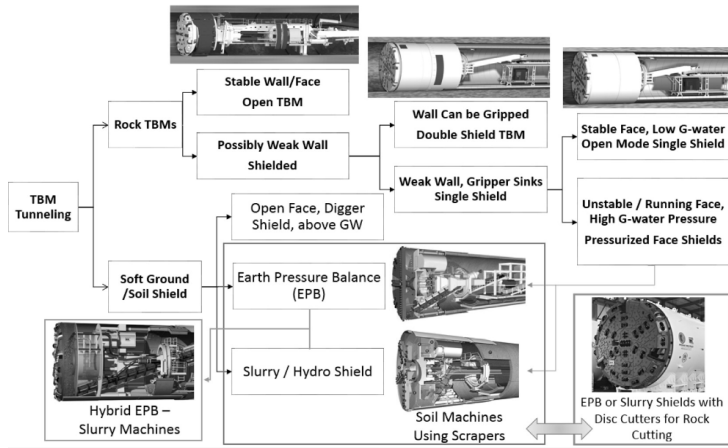


Figure 1: Various types and applications of boring machines based on the classification of the soil (Jamal Rostami 2016).

TBMs can also be broadly divided into open machines and shielded machines. Open TBMs are employed in stable hard rock conditions, where ground support is minimal or unnecessary, while shielded TBMs are used in less stable environments. Shielded machines are further classified into single shield (SS) and double shield (DS) types. DS machines are versatile and can operate in a range of geological conditions but are unsuitable for high groundwater pressure or squeezing ground conditions. SS TBMs, on the other hand, rely on the installed tunnel lining to advance and are divided into open-face and pressurised-face types. In pressurised environments, such as those with high groundwater pressure, pressurised-face TBMs are used to maintain stability at the tunnel face while preventing water ingress. These machines employ either Earth Pressure Balance (EPB) or slurry systems to ensure continuous excavation while managing face pressure. The operational principles for TBMs vary significantly between soft ground and hard rock. In soft ground, cutting is generally straightforward unless the presence of boulders or mixed face conditions complicates excavation. The focus is on maintaining

an equilibrium between the volume of material removed and the displaced ground to prevent settlement. In hard rock conditions, where substantial forces are required to break the rock, the key operational parameter is managing the cutter load and thrust to maximise penetration without overloading the machine. For harder rock types, the machine operates under thrust-limited conditions, with excess power being used to increase the cutterhead's rotational speed to optimise excavation efficiency.

The most straightforward and popular tunnelling analysis technique is the characteristic lines method. It is also used in relation to some of the problems with TBM digging in squeezed ground by (Kovářík and Anagnostou 1995). The convergence-confinement method was later used by (Vogelhuber 2007) to examine the crossing of a shear zone at deep depth using a double shielded TBM with a diameter of 10 m. As a result, he could distinguish between the ground's short-term and long-term behaviour. As demonstrated by (Billig et al. 2008) and (Schneider and Spiegl 2008), the characteristic lines method is still utilised today to analyse the ground-support interaction as well as the deformable segmental linings of shield-driven tunnels through squeezing rock.

(Lombardi 1981), who examined the impact of the advance rate on the lining loading for the simplified situation of a lining that begins to become laden 40 m behind the face, has already given the findings of spatial numerical studies. From a fundamental perspective, (Lombardi 1981) work addressed the subject of tunnelling in overstressed rocks. However, in the vast majority of examples documented in the literature, the numerical analyses were conducted within the context of particular TBM projects. For the Guadiaro–Majaceite Tunnel (Spain, D = 4.88 m), for instance, (Lombardi and Panciera 1997) and (Panciera and Piccolo 1997) examined the viability of a double shield TBM drive while accounting for the effects of advance rate and time-dependent ground behaviour.

(Matter et al. 2007) used axially symmetric numerical studies to examine the Wienerwald Tunnel's (Austria, single shielded TBM, D = 10.67 m) traversal of shear zones. (Graziani, Ribacchi, and Capata 2007) investigated the proposed Brenner Base Tunnel (Austria, double-shielded TBM, D = 11,000 m) as part of the TISROCK research project (for general information about TISROCK, (John and Schneider 2007)). (Cabreros et al. 2005) and (Simic 2005), who also take creep effects into account, used fully three-dimensional computational models for the Guadarrama Tunnel (Spain, double-shielded TBM, D = 9.51 m). (Wittke, Wittke-Gattermann, and Wittke-Schmitt 2007) conducted additional project-related investigations, including the evaluation of the stresses and deformations of the shield structure of the single shielded TBM in the Hallandsas Tunnel (Sweden, D = 10.70 m). They consider seepage flow and the structural detailing of the shield by simplifying the a priori assumption that the ground closes the steering gap at a distance of 4 m behind the working face.

1.2 TBM general operation

1.2.1. Cutting Head Mechanism

The cutting head is the core of the TBM, responsible for breaking through geological materials ranging from soft soil to hard rock. The size and design of the cutting head vary based on the tunnel diameter and geological challenges.

- **Cutting Head Diameter:** TBMs typically have cutting head diameters ranging from 10 m to 19 m, depending on the required tunnel size and project specifications. Larger diameters are used for transportation tunnels, while smaller heads are used in utilities.
- **Disc Cutters:** The cutting head is equipped with high-strength, replaceable disc cutters made of hardened steel. These cutters apply pressures of up to 20,000 kN to the rock or soil, effectively fracturing and removing material in small increments. The design of the disc cutters varies based on geological conditions, with some optimised for hard rock while others are suited for soft soils or mixed ground.
- **Rotation Mechanism:** The cutting head rotates at a controlled speed, powered by the main drive system, which consists of high-torque electric or hydraulic motors. This rotation allows continuous penetration into the geological material, with the rotation speed adjusted based on the specific ground conditions encountered.

Hard rock tunnelling has made extensive use of tunnel boring machines (TBMs) because of their great cost-effectiveness, efficiency, and safety (Q. Liu et al. 2016; Zheng, Zhang, and Zhao 2016). During tunnelling, the cutterhead revolves with the TBM spindle, shredding the rocks in front of the TBM into fragments using disc cutters affixed to the cutterhead. Adverse working circumstances frequently diminish the efficacy of disc cutters, leading to a deterioration in TBM tunnelling performance (J. Hassanpour et al. 2014). The TBM service life will be negatively impacted if the low-efficiency disc cutters are not replaced in a timely manner since there is a greater chance of cutter failures near the disabled disc cutters (Q. Liu et al. 2017). This could further harm seals, bearings, and potentially the entire cutterhead. Frequent disc cutter replacements and inspections are necessary during tunnelling in order to prevent this kind of situation (Lihui Wang et al. 2017), which has a significant impact on construction efficiency. To ensure tunnel safety and efficiency, it is crucial to detect the state of disc cutters without manual checks.

Disc cutter failure patterns can be broadly classified into six types: normal wear, fracture, flat wear, eccentric wear, local spalling, and secondary wear studied by (J. H. Yang et al. 2019; Khalid Elbaz et al. 2018; K. Elbaz et al. 2021). The failures of disc cutters are attributable to various factors, including rock characteristics, cutter structures, materials of construction, installation positions and arrangements, and TBM operating parameters. As a result, disc cutter failure prediction is a challenging multi-input task. A data-driven method, a sensor monitoring method, and an inspection method are the three

primary methods currently proposed for obtaining information on cutter failure.

In engineering projects, routine inspection is the most popular approach since it is the most straightforward and dependable. TBM cannot operate at peak efficiency prior to inspections, nevertheless, because the inspection procedure makes it hard to detect cutter faults in time. Additionally, in order to perform cutter inspections, TBM shutdowns are necessary, usually every few strokes or at specific times of the day. Typically, such downtime of TBMs accounts for about 15% of the tunnelling duration, significantly diminishing construction efficiency and escalating costs.

In contrast to the manual inspection method, the sensor monitoring technique facilitates the acquisition of real-time status information on the disc cutter. Nevertheless, the sensors affixed to the cutterhead must operate within a demanding environment characterised by elevated temperatures (70–90 °C), high humidity (80–90% Relative Humidity), and significant vibrations (10–20 times the acceleration of gravity), leading to suboptimal performance of detection methods reliant on light (Y. Liu et al. 2022), lubricant application (Gharahbagh et al. 2013), the magnetoresistive effect (Q. Gong et al. 2021), or the eddy-current effect (F. Wang et al. 2019; Lan et al. 2019). A further drawback of the sensor monitoring method is the challenging implementation of power supply, communication, and maintenance for the sensors. Consequently, the sensor-based approach renders real-time monitoring of cutter state nearly unattainable during tunnelling because to the limited dependability of the sensors. Additionally, sensors are costly, which is why the method is expensive. For example, a disc cutter ring wear monitoring equipment developed by German TBM manufacturer Herrenknecht costs more than \$100,000 USD, without considering the expense of maintaining worn disc cutter sensors.

Data-driven models have gained popularity as a result of the drawbacks of both manual inspection and sensor monitoring techniques. Before tunnelling begins, the data-driven approach can plan maintenance and forecast disc cutter consumption.

Three types of data-driven approaches can be broadly distinguished: tunneling-parameters-based methods (K. Elbaz et al. 2021; H. Yu et al. 2021; Acaroglu, Ozdemir, and Asbury 2008), mechanism-based methods (Jafar Hassanpour 2018; Zhenchuan Sun et al. 2019; Lihui Wang et al. 2012; Park et al. 2021; Zhao et al. 2019), and empirical methods (Karami, Zare, and Rostami 2021; Jafar Hassanpour et al. 2015).

Using historical data, empirical approaches examine the regression of geological parameters and cutter health metrics. Mechanism-based approaches model the rock breaking process using mechanical analysis or energy theory. Then, the wear of the disc cutter is mapped using pertinent parameters, including the cutterhead topological structure (Park et al. 2021), standard force of a single disc cutter (Lihui Wang et al. 2012), uniaxial compressive strength (UCS) (Jafar Hassanpour 2018), Cerchar abrasivity index (CAI) (Mucha 2023), cutterhead rotation speed (Zhenchuan Sun et al. 2019), penetration rate (Lihui Wang et al. 2017), and so forth. It is easy to tell when a

disc cutter will break down because of wear. Relying heavily on relatively stable geological parameters is a significant drawback of both empirical and mechanism-based methods. In real time, though, these models can make severe errors because the structure of tunnels changes over time.

1.2.2. Main Drive and Power Systems

The main drive is the powerhouse of the TBM, delivering the necessary torque to rotate the cutting head.

- **Drive Type:** Modern TBMs use electric motors or hydraulic motors to power the cutting head. These motors provide the torque required to break through varying ground types.
- **Power Output:** The torque delivered by these motors is proportional to the size and speed of the TBM. It is crucial for overcoming resistance in challenging materials such as hard rock or mixed geology.

The power system also regulates auxiliary systems, including ventilation, spoil removal, and hydraulic jacks that propel the machine forward. A tunnel boring machine (TBM) is a substantial and advanced construction apparatus operated by the rotation and extrusion of cutters affixed to the cutter head for excavation and propulsion. The apparatus has functions like tunnelling, slag discharge, and alignment, which can significantly diminish labour intensity (K. Zhang et al. 2010). Tunnel Boring Machines (TBM) are extensively utilised in many tunnel engineering projects, including subways, railways, and highways. Recent advancements in TBM technology have led scholars to achieve significant progress in its propulsion systems. (Sugimoto and Sramoon 2002) constructed and validated a dynamic model of a shield body in a study on a mechanical system that incorporates friction and dynamic balancing. The response in the cutter head that is reduced by external load was discovered by (Komiya et al. 1999) in a finite element model. (S. Zhou, Wang, and Huang 2009) investigated the impact of the torque and force generated by the propulsion system. Nonetheless, TBM may also induce an imbalance in the distribution of driving torque. Meanwhile, because of intricate and diverse geological circumstances, TBM is simultaneously subject to axial force, radial force, and overturning moment. During tunnelling, the slew bearing withstands the external load of the cutter head, resulting in elastic deformation. Deformation of the driving gear and the ring gear in the slew bearing results in displacement disturbances due to multi-point meshing. Complex geological conditions make it easy for a blocking accident to happen during tunnelling, and fracture phenomena in small gear shafts and gear teeth will occur (Ding, Tu, and Wang 2010; Ramoni and Anagnostou 2011). Due to the compatibility of deformation, a cutter head system is a complex, time-varying, and strong coupling system; nonlinear elements including periodic time-varying stiffness and backlash, as well as multiple pinion drives, minimise this deformation (Kahraman 1993; Theodossiades and Natsiavas 2000; Cheng and Lim 2000). In multi-mesh gear systems, periodic mesh stiffness can result

in server vibrations and parametric instabilities (K.-Z. Zhang et al. 2011; G. Liu 2007).

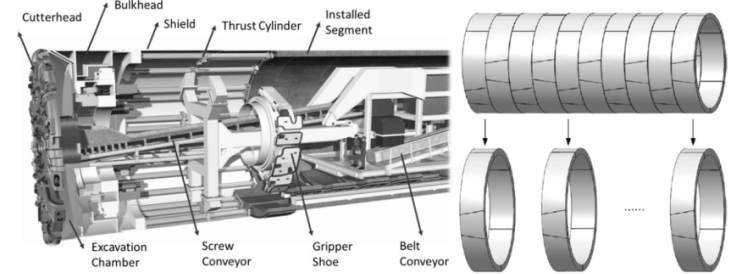


Figure 2: Components of TBM and precast tunnel rings. (Nagrecha et al. 2020)

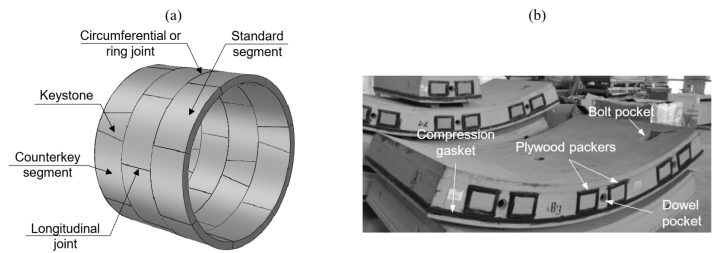


Figure 3: The configuration of the concrete tbm ring lining: (a) general arrangement and (b) lining accessories in standard segments.

Each TBM has an overall length of 148 metres, which includes 11 backup gantries. The length of the TBM shield components, which include the cutter head, front, middle, and tail shields, is 11.1 metres. Segmental lining rings made of precast fibre-reinforced concrete that are placed inside the TBM tail skin provide the tunnel's continuous support. Grout is used to fill the annulus that exists between the segment extrados and the excavated face. The purpose of tunnel backup gantries was to provide auxiliary systems for TBM mining operations. Each TBM in the WWDT has eleven backup gantries; the supporting information is shown below (Salepciler et al. 2023).

For tunnel boring, rock tunnel boring machines (TBMs) are powerful engineering devices. The 1919 patent for a tunnel boring machine is where the ground-breaking idea for these machines originated (Soil, Association, and Others 1998), (Bruland 2000). The device's main idea is to use a spinning cutter head to hammer out concentric circular tracks in the tunnel face while chipping the rock in between the tracks. A significant advancement in TBMs transpired in the 1950s when Robbins invented the disc cutter (Rutschmann 1979), (Hansen 1998). The basic machine design and rock-breaking procedure haven't changed since then.

Previous researchers investigated the rock-breaking mechanism of disc cutters through experimental and numerical approaches. Full-scale Linear Cutting Machines (LCM) and Rotary Cutting Machines (RCM) have demonstrated reliability and precision, as they can handle a comprehensive spectrum of loads and penetrations, eliminate scale effects, and

yield results that are directly applicable to the performance evaluation of Tunnel Boring Machines (TBMs) (Cho et al. 2013), (Cho et al. 2010). Because of these factors, a large number of research have been conducted using the LCM or RCM test results (N. Bilgin et al. 2006), (H. Y. Liu et al. 2002), (Q. M. Gong, Jiao, and Zhao 2006), (Q.-M. Gong, Zhao, and Jiao 2005). A notable accomplishment was the development of rock-cutting force prediction models by the Colorado School of Mines (CSM) (Jamal Rostami 2008), (Nilson and Ozdemir 1993). These large-scale tests have a lot of benefits, but they are expensive and take a long time because the rock samples have to be brought from the site to a lab to be made and put into a testing box. These problems were fixed by running a number of computer simulations on the rock-breaking process of disc cutters (N. Bilgin et al. 2000), (Z. Yu 2012).

Only a small number of publicly published investigations have focused solely on the aforementioned technologies. Three groups of hydraulic systems are used in a patent (Heitkamp and Stoltz 1978) to control the advance of a tunnel drive shield; the first two groups use throttle valves, while the third group uses pressure relief valves. Three groups of another patented hydraulic control system are also used to regulate tunnelling operations (Weirich and Heitkamp 1983), and each group uses the same control technique. It solely comprises pressure control valves, yet incorporates an energy recycling concept. Unfortunately, the ability to precisely adjust pressure and velocity is lacking in all of these devices.

The possibility is made possible as a result of the development of electro-hydraulic proportional control. This work introduces a thrust hydraulic system featuring compound control of pressure and flow. The system is regulated in six groups, each generally consisting of a flow control proportional valve and a pressure relief proportional valve. Pressure and velocity control are handled by proportional integral derivative (PID) controllers. The analysis also takes into account the synchronous motions of the thrust cylinders for straight line tunnelling, which arise from the cutter's unequal load under the challenging and complex digging conditions. The master-slave synchronous motion control utilising a PID controller ensures minimal synchronous error between the cylinder movements.

This project by (Huayong et al. 2009) involves conducting experiments using an EPB simulation test rig, which comprises a shield machine, an earth box filled with pressurised earth of varying characteristics for testing, and a PLC control system. In synchronous motion control, an unequal force is exerted on the hydraulic cylinders positioned symmetrically.

1.2.3. Tunnel Lining and Structural Support

To prevent tunnel collapse, TBMs simultaneously install tunnel linings during the excavation process.

- **Precast Concrete Segments:** Tunnel linings are typically composed of precast concrete segments with 15 degrees of curvature, which are installed in a circular fashion to form a complete ring around the tunnel. Each ring is made up of six segments, with

tongue-and-groove interlocking systems for precise alignment and structural integrity.

- **Segment Installation:** Hydraulic jacks temporarily hold each segment in place during installation. Once all segments are positioned and bolted together, the system becomes self-supporting. Mortar is injected into the gaps between the segments and surrounding rock or soil to ensure a water-tight seal.
- **Mortar Injection:** The gaps between the installed segments and surrounding ground are filled with grout or mortar, depending on the geological conditions. This grout helps secure the tunnel lining, preventing groundwater intrusion and further stabilising the structure.

When digging tunnels in soft terrain, a shield tunnelling machine is frequently utilised (Yukinori Koyama 2003). Segment assembling and shield tunnelling are the two primary processes that occur sequentially during tunnel construction. It is beyond question that the former is the fundamental process, while the latter is also indispensable for the construction's safety, efficiency, and quality. Fundamental configurations of a tunnel and a shield tunnelling apparatus. To create a permanent support for the tunnel, the prefabricated concrete pieces are fitted onto the excavated surface after the cutter head rotates to dig the tunnel. A actual "segment erector," a robotic manipulator used in the segment assembly process, operating in a functional shield tunnelling machine. Depending on the tunnel's diameter, heavy segments can weigh several tonnes, so the segment erector must handle them with extreme precision. It provides comprehensive manipulation of the segment with six degrees of freedom (6 DOFs), encompassing radial lifting, axial sliding, and rotation along the central axis of the shield tunnel machine, together with three degrees of freedom for rolling, pitching, and yawing in the clamping head (Lintao Wang et al. 2013). Currently, nearly all segment erectors utilised in construction are operated by humans; however, automation has emerged as a significant trend aimed at enhancing efficiency and safety in tunnel building. Both the segment assembly (L. Wang et al. 2017), (Y. Zhou et al. 2018) and (Y. Zhou, Luo, and Yang 2017) stated the automation of the full shield tunnelling machine also (Sebbeh-Newton et al. 2021), (W. Sun et al. 2018), (X. Gao et al. 2019) have received a lot of attention lately. All segment erectors are, to our knowledge, powered by hydraulic systems due to their superior power-to-weight ratio by (Yin et al. 2018), (T. Lin et al. 2021), (T. Lin et al. 2020) and (W. Shen and Wang 2022). One of the essential technologies for automation is closed-loop motion control of the segment erector.

In TBM tunnelling with passively articulated shield tails, concrete segmental rings in curved tunnel sections are prone to ring deformation and structural degradation (Yukinori Koyama 2003); (Y. Yang et al. 2018); (Gruebl 2006). For example, according to the statistical analysis of field records from 50 Japanese sites, (Sugimoto 2006) identified longitudinal concrete cracking as the predominant type of segment damage, constituting roughly 40% of the total recorded damage incidents. A further 70% of the longitudinal cracks occurred in tunnel sections

with curved alignments, typically at springline segments, and 72% of the cracks developed during the TBM advance, either prior to or during tail seal passage. (Gruebl 2006) revealed that longitudinal cracks are frequently observed in the early phases of tunnelling in segments situated on the exterior of tight curves. In contrast to the straight sections of the tunnel, the curved sections showed characteristic squatting ring forms, according to field monitoring data on ring convergence from a tunnel driven in uniform ground that (Y. Koyama 2003) provided. (Y. Koyama 2003) asserted that, in acute curves, the transient lining pressures during the TBM transit could induce segment cracking, spalling, and water infiltration. The majority of the concrete cracks detected in various sites were attributed by (J. S. Chen and Mo 2009) to the skewed orientation between the TBM and lining and the application of uneven ram loads, both of which are characteristic of TBM steering around curves (Maidl et al. 2013), (D. Festa 2015), (Alsahly, Marwan, and Meschke 2019), (Saleta Gil Lorenzo 2022). With passive articulation, the shield tail follows the shield body during steering (Biggart 2010; Brundan and Danno 2020). The propulsion mechanism of the articulated TBM comprises uniformly distributed hydraulic cylinders (Tunnel Engineering Committee 2007; Xie et al. 2012) linked to the front bulkhead and equipped with ram shoes at the back (Figure below). Discrete jack forces are dispersed along the touching segments' circumferential face with the aid of the ram pads. The cylinders' alignment is maintained at standstill by detachable fasteners. The floating shoes follow the relative changes in position of the touching segments, and the cylinders can freely pivot within a permitted angular range during advance (Engineering Committee 2007), (Saleta Gil Lorenzo 2022). The lining's transverse bracing is necessary to achieve stable balance because the hinged cylinders can only support axial loads.

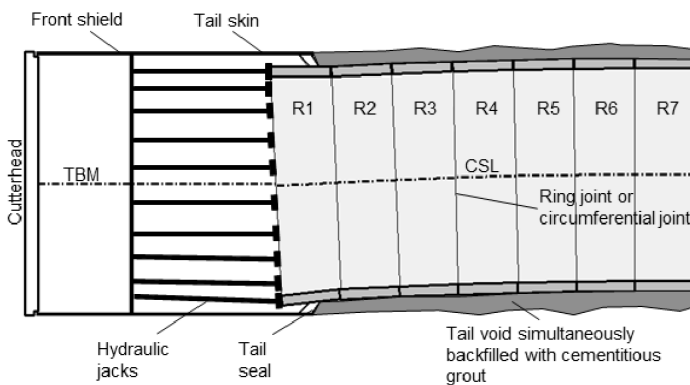


Figure 4: Schematic representation of the interfaces of tunnel construction in contemporary mechanised shield tunnelling.

If the cylinders assume an inclined position, the contacting segments may be subjected to transverse jack forces at the interfacial plane. The thrust cylinders are often organised in clusters and function in pressure regulation mode, allowing the TBM operator to modify the thrust pressures in each control group to rectify deviations of the TBM's position from the

intended alignment (D. Festa 2015). Uneven thrust forces result in active changes in machine orientation (Harding, n.d.). During the steering of the TBM around a curve, the cylinder groups on the outer side generate greater thrust forces than those on the interior side. The jacking system's maximum thrust force can be reached by the outer jack forces (S. Gil Lorenzo 2018).

TBMs and traditional tunnelling by drilling are the two primary methods of tunnel excavation. TBMs are frequently utilised in urban tunnels where strict safety standards and quick excavation are necessary. Due to the presence of several subterranean structures in urban areas, including utility tunnels and building foundations, newly constructed tunnels frequently feature a blend of linear and curved alignments. For tunnel curves to be produced successfully, TBM steering systems are therefore essential.

In their theoretical model for TBM excavation, (Sugimoto and Sramoon 2002) simulated TBM operation, assessed shield behaviour, and conducted sensitivity analysis of the model parameters used for shield behaviour in both straight and curved line excavations. The model was based on the dynamic loading concept. The simulation confirmed that ground features could influence shield movement, with a more pronounced effect on shield behaviour in curved excavations compared to straight-line excavations.

By using mathematical and geometrical models, (Xuesong Shen, Lu, and Chen 2011) were able to ascertain the three-dimensional orientations of a TBM as it advanced, and they deduced a transformation matrix to determine the attitude of the TBM's position with respect to yaw, pitch, and roll, using the coordinates of a single tracking point.

Curved excavation requires three operational factors, which (Chanchaya and Suwansawat 2014) outlined: the articulation angle, the difference in shield jack length, and the copy cutter stroke. They also deduced methods for calculating these factors and for forming curved alignments, such as circular and spiral curves, in two-dimensional space. A comparison was also made between three operational factors that were derived from theoretical calculations and those that were measured in a true guidance system. By incorporating the horizontal and vertical tendencies of the TBM, which are calculated from the deviations of two reference points caused by the yaw and pitch of the shield. On the basis of these trends, they compared the relative positioning of the TBM with its intended tunnel alignments.

(S. O. Kang et al. 2017) conducted a numerical simulation to assess the structural stability of the TBM shield during a sharply curved excavation, elucidating the load transfer mechanism from articulation and shield jacks to the shield skin, as well as the impact of this load transfer on the structural integrity of the shield skin.

To explain the behaviour of thrust pressure based on various shield jacking force systems and articulation angles for curved excavation, (S. H. Kang et al. 2017) created a model experiment at a size of 1:17.7. In light of the inconsistent pressure, they

suggested a protocol for the allocation of thrust force based on the articulation angle.

The entire TBM steering system and the associated process needed for extremely tight curved excavation were recently detailed by (Brundan and Danno 2020). They also provided field case histories of TBM design and operational technology that have been proven effective in extremely tight curved excavation.

In the design of the steering system for the TBM simulator, these previous studies have underscored the limitations. A number of aspects pertaining to shield behaviour were described by (Sugimoto and Sramoon 2002), operational considerations for TBM curved excavation were introduced by Chanchaya and Suwansawat (Sugimoto and Sramoon 2002), and both works included some discussion of the TBM navigation system, which is an essential component of the steering system. In contrast to a navigation system in three dimensions, which requires at least three reference points, (Xuesong Shen, Lu, and Chen 2011) proposed calculating the TBM location and its variation due to pitch, yaw, and roll, but they just took into account one reference point. The horizontal and vertical tendencies were calculated by (Daniele Festa, Broere, and Bosch 2013), (D. Festa, Broere, and Bosch 2015) using two reference locations (front and rear). Nonetheless, two-dimensional space was taken into consideration when designing the navigation system. Additional investigations have also contributed to the comprehension of the whole TBM steering system (S. O. Kang et al. 2017; S. H. Kang et al. 2017; Brundan and Danno 2020). (Daniele Festa, Broere, and Bosch 2013) and (D. Festa, Broere, and Bosch 2015) defined the position and orientation of the TBM shield using two reference points and explained the kinematic behaviour of a TBM in soft ground.

1.2.4. Slurry TBM (Hydroshield Mode)

When tunnelling in waterlogged environments, TBMs can switch to hydroshield mode, which is specifically designed to handle the challenges posed by high groundwater pressure and loose soils.

Bentonite Slurry Operations: In hydroshield mode, bentonite slurry is injected into the excavation chamber to stabilise the tunnel face and counteract groundwater pressure. The slurry fills the excavation chamber, forming a pressurised shield that prevents uncontrolled inflows of water and ground material.

Pressurisation System: The pressurisation of the slurry system is carefully controlled. Compressed air is introduced into the rear chamber of the TBM to act as a spring, regulating the support pressure applied by the slurry. This system ensures that the slurry penetrates the surrounding ground to a depth sufficient to balance the groundwater pressure.

Separation Plant: The slurry is continuously pumped out of the TBM, along with the excavated material, and sent to a separation plant. Here, the solid particles are removed, and the bentonite is replenished and recycled for further use. This closed-loop system maintains excavation efficiency and minimises environmental impact.

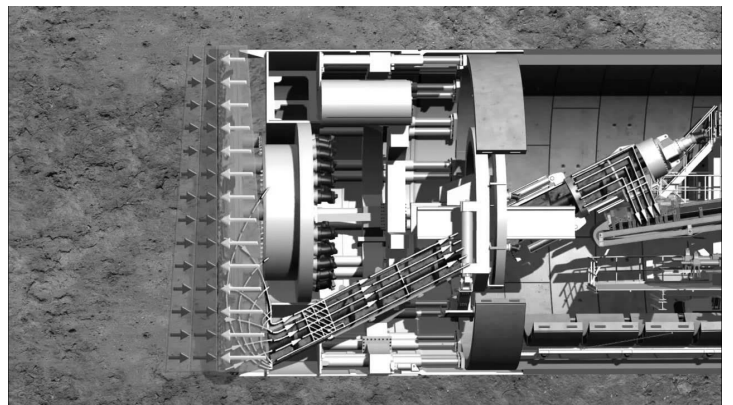


Figure 5: Operation of TBM Under water table and soil pressure

Accelerating urbanisation and fostering sustainable economic development require extensive subterranean space exploration (Yan et al. 2022; Debrick, Van Acker, and Admiraal 2023; Z. Wang et al. 2023; Ma and Peng 2023). According to (X. Li et al. 2018; M. et al. 2022; P. Lu et al. 2022; X. Shen et al. 2023; Guo, Jin, et al. 2023), there have been a lot of underground projects going on all over the world in recent years. The slurry tunnel boring machine (TBM), a fully mechanised tunnelling method, combines soil cutting, soil discharge, lining, and deviation correction (W. Li et al. 2022; X. Wang et al. 2022). It is widely employed in the construction of subway tunnels (Huang et al. 2022; Jin et al. 2023), highway tunnels (Guo, Li, Sun, et al. 2023; Z. Geng, Jin, and Yuan 2023), and railway tunnels (N. Zhang et al. 2018) due to its high efficiency and safety, particularly in cross-river and submarine. In slurry TBM tunnelling, fresh bentonite slurry is introduced into the excavation chamber in several stages through the feeding pipeline to equilibrate the soil and water pressure at the tunnel face. The bentonite slurry can be recycled since the discharging pipeline pumps the enormous amounts of muck to the ground to screen and filter presses in several stages.

However, if the disc cutter's rock-breaking capacity is inadequate, the rock may not split adequately when a slurry TBM is tunnelling in challenging terrain, including hard rock, producing larger-sized rock chips (Haeri, Shahriar, and Marji 2013; Marji 2015; Abdollahi et al. 2019). When the slurry circulate system's discharging capacity is insufficient, the excavated rocks are then easily deposited at the bottom of the excavation chamber. Over time, the excavation chamber gets clogged, which causes the discharging system to become stagnant and blocked (Zhonghai, Hengyu, and Buhai 2019; Guo, Jin, et al. 2023). This could put construction security at risk and decrease tunnelling efficiency by raising the slurry pressure inside the excavation chamber, which could destabilise the excavation face and cause an unusual shutdown of the slurry TBM (W. Liu et al. 2023). To give just two examples, the Shiziyang Tunnel Project in Guangzhou, China, and the Tuan-Jiu Part of the South-to-North Water Transfer Project in Beijing, China, both experienced frequent clogging issues with their excavation chambers, which reduced the efficiency of their respective processes. The safe and effective tunnelling of

ultra-large-diameter slurry TBM thus depends on the slurry circulate system operating continuously.

The transport and flow behaviour of pipeline systems are currently the main focus of study on the muck discharging of slurry TBM (Kaushal and Tomita 2002; Vlasak, Kysela, and Chara 2014; Edelin et al. 2015). Indoor experiments are a prevalent methodology employed by researchers. (Souza Pinto et al. 2014) examined the particle trajectories within the pipe at various fluid flow rates and identified the key velocity distinguishing deposition from suspension across varied flow patterns. Advancements in computational technology and mathematical methodologies have led to the extensive application of various numerical methods in the investigation of muck particle transport and discharge (Kaushal et al. 2012; Januário and Maia 2020; Ma and Peng 2023), including computational fluid dynamics (CFD) and the coupling of computational fluid dynamics with the discrete element method (CFD-DEM). (Guo, Li, Jin, et al. 2023) assessed the reverse circulation efficacy of slurry shield pipelines utilising the CFD-DEM coupling methodology, discovering that the slurry inflow velocity V and reverse circulation duration substantially influence reverse circulation performance. This led to the recommendation and implementation of a sensible reverse circulation strategy in real engineering.

The main way to reduce excavation chamber clogging in practical engineering is to optimise the structural lectotype of slurry TBM from the standpoint of slurry TBM design.

Therefore, it is fundamental and important to implement a targeted and innovative design to enhance the discharging performance of slurry TBMs in order to alleviate the issue of excavation chamber clogging. Subsequently, the effectiveness of the targeted design in resolving the slurry chamber clogging and the discharging performance of the slurry TBMs under various conditions should be investigated. To date, there have been a few reports of screw conveyors being connected in series with slurry shield's slurry circulation system to reduce clogging and blockages in the excavation chamber. (W. Liu et al. 2023) reported that the screw conveyor was utilised in the Guangzhou Metro Line 12 Project, with a flight diameter of 840 mm, a screw shaft diameter of 245 mm, and a screw pitch of 680 mm. But the majority of the examples that are currently available are for the design of screw conveyors in slurry shields with small to medium diameters, and the screw conveyor itself has a short pitch and flight diameter. Instances of screw conveyors utilised in large-diameter slurry shields (exceeding 14 m in diameter) are scarce, and there is a lack of assessments on the discharge efficacy of screw conveyors in slurry shield tunnelling.

To reduce slurry chamber clogging in the Qingdao Jiaozhou Bay Second Undersea Tunnel, a large-diameter short screw conveyor that actively discharges rocks was used. Based on the CFD-DEM coupling approach, a full-scale two-phase model of a short screw conveyor actively discharging pebbles was developed in order to assess the discharging performance of large-diameter short screw conveyors in various scenarios. In the fluid domain of the coupling model, sliding mesh technology was employed to represent the rotations of the

atmospheric composite cutterhead and short screw conveyor. Dynamic particle factories were developed in the coupling model's particle domain to generate rock particles in response to the cutterhead's rotation. Additionally, by contrasting the simulated results with field-monitored data, the correctness and dependability of the CFD-DEM simulation findings were confirmed.

A thorough parameter analysis was conducted to investigate the impact of TBM advancing rate, cutterhead rotational speed, screw conveyor rotational speed, rock size, and screw conveyor geometric design on the discharging performance of a large-diameter short screw conveyor. In light of these findings, an appropriate rotating speed for the screw conveyor was proposed and implemented in the Qingdao Jiaozhou Bay Second Undersea Tunnel project by (Guo, Li, Jin, et al. 2023), resulting in favourable outcomes. The results of this study may serve as a reference for mitigating slurry chamber obstruction during ultra-large-diameter slurry TBM tunnelling in hard rock for analogous future projects.

1.2.5. Control and Monitoring Systems

Modern TBMs are equipped with advanced control systems that allow operators to monitor and adjust machine performance in real-time.

- **Control Cabin:** Located at the rear of the TBM, the control cabin houses the equipment used by engineers and operators to manage all aspects of the TBM's operation. The control systems allow for the real-time adjustment of key parameters such as cutting head speed, hydraulic pressure, and slurry flow rates.
- **Geotechnical Monitoring:** In urban tunnelling projects, nearby structures are continuously monitored for movement or vibration. Sensors placed above the tunnel track changes in surface conditions, ensuring that excavation does not cause damage to nearby buildings or infrastructure.

1.2.6. Challenges in Different Geological Conditions

TBMs must adapt to various geological conditions, including soft soils, hard rock, and mixed ground, each presenting unique challenges.

- **Earth Pressure Balance (EPB):** In urban environments with soft ground, TBMs employ Earth Pressure Balance (EPB) technology to balance the pressure at the tunnel face, preventing ground collapse and minimising surface subsidence.
- **Retrofitting for Different Conditions:** TBMs can be retrofitted to switch between dry excavation in rock and slurry mode for soft or waterlogged soils. This adaptability allows for smooth transitions when tunnelling through varying ground layers.

2. TBM Launch

The underground space is in high demand due to the societal necessity to enhance the urban landscape in conjunction with the ongoing accelerated urbanisation (Choi and Lee 2010; Kong, Jung, and Lee 2017; Rezaei, Shirzehhagh, and Golpasand 2019). The construction of urban tunnels using a tunnel boring machine (TBM) is frequently preferred over the drilling-and-blasting-based excavation method, which can result in noise- and vibration-related issues and complaints from adjacent residents through (Q. Liu et al. 2016; D. Festa, Broere, and Bosch 2012) research. The high cost of a TBM is a contributing factor to its frequent re-use. Subsequently, the TBM is tailored to the desired ground conditions and transported to the construction site.

From a performance standpoint, this type of re-used TBMs may be inferior to a TBM that has been newly designed and constructed specifically for a specific site. This is due to the fact that the re-used TBMs were originally constructed for various ground conditions in the past by (Phadke and Titirmare 2017). However, if some parts have been replaced, the performance and specifications of a repurposed TBM may differ from what was originally produced in the factory and may even deteriorate with time. The use of a re-used TBM without a thorough examination of its specifications and performance can result in a variety of unforeseen excavation issues, as well as an unintended increase in the cost of tunnel construction. Consequently, it is of the utmost importance to evaluate and confirm the current status of the repurposed TBM before it is installed on a construction site. The most common issues are typically related to the maximum working cutter head rotation speed, the maximum applicable cutterhead torque, or the maximum applicable thrust, which are significantly lower than the actual specifications.

Massive resources are needed to examine these parameters, though. For instance, in order to create the maximum cutterhead torque, an enormous counter-force must hold the entire TBM cutterhead. The ambiguities and uncertainties surrounding the current state of re-used TBMs impede their recycled or refurbished application, notwithstanding the associated economic advantages. The performance of a TBM is often defined by its ability to excavate the subsurface ground of interest. The performance of TBM excavation is influenced by both ground conditions and machine specifications (Ebrahim Farrokh 2020). (Q. M. Gong, Jiao, and Zhao 2006; Yagiz 2008) have implemented numerous investigations regarding the impact of ground conditions on the efficiency of TBM excavation. There have been recent attempts to use machine learning techniques to forecast the performance of TBM excavations beyond the practical and financial constraints by taking into account important ground characteristics and machine parameters (Khalid Elbaz et al. 2019, 2020; M.-Y. Gao et al. 2020). However, to create reliable models using machine learning or statistical techniques, a basic understanding of the roles that TBM specifications and ground conditions play in TBM excavation mechanism is needed. The cutter and cutterhead are regarded as the most critical components

(Acaroglu, Ozdemir, and Asbury 2008). Common assessments comprise the cutter wear test (Bruland 1998), the linear cutting machine (LCM) test (Balci 2009; Tumac and Balci 2015; Entacher and Schuller 2018), and the rotary cutting machine (RCM) test (G. Qi, Zhengying, and Hao 2016; Pan et al. 2018; Peng et al. 2018). One example is a recently designed testing device that can inspect a real full-scale cutterhead (Q. Geng et al. 2016). While the method of checking each individual machine component is legitimate, the assembling of these multiple parts may nevertheless pose a risk of defects in the entire intact machine. Segment damage from imbalanced thrust, thrust loss due to lodged mud in the TBM chamber, and friction between the TBM body surface and ground are specific risks that might occur during the excavation operation (Ramoni and Anagnostou 2010a; Jung et al. 2011). According to (Pan et al. 2019), there is a discrepancy between the cutting performance of cutters calculated by the LCM test and that of cutters used in full-scale TBM excavation.

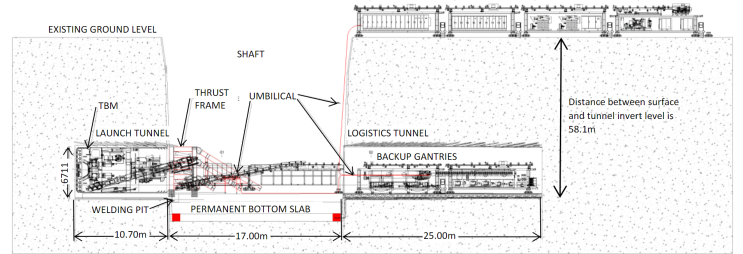


Figure 6: TBM launch sketch: Cross-sectional view (Salepciler et al. 2023).

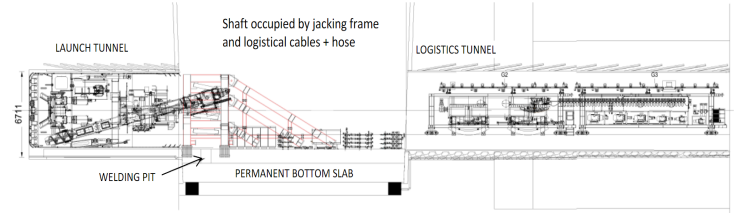


Figure 7: Logistic Tunnel cross-section (Salepciler et al. 2023).

3. Mathematical Models:

3.1 Thrust and torque TBM launch

TBM considers the thrust and torque of the equipment, the number of disc cutters, the arrangement, spacing, and opening ratio of the cutters, as well as how these factors affect the TBM's excavation performance. There have been recent reports of instances in which the TBM design errors resulted in insufficient thrust and torque during construction (Ates, Bilgin, and Copur 2014; Nuh Bilgin and Algan 2012). As a result, the design of the total thrust force F_{th} and total torque T_q , which are necessary for the shield TBM to be excavated steadily, is based on empirical elements such as ground conditions, as seen in Figure 8.) and TBM diameter (D), which have only been

calculated (Anastasopoulos, Gerolymos, and Drosos, n.d.). A shield TBM with a diameter of 6.3 m has a wide range of thrust values, from 20 to 43 MN, making it challenging to design the ideal thrust hydraulic system and select acceptable hydraulic components. The thrust and torque should be found by taking into account the ground conditions (such as excavation depth, groundwater level, uniaxial compressive strength, lateral earth pressure coefficient, etc.), the equipment factors (such as TBM diameter, TBM shield frame length, opening ratio, etc.), and the operating factors that affect the force that is applied to the equipment when a shield TBM is used to dig. Research in Korea has focused on enhancing and forecasting the excavation efficacy of shield tunnel boring machines (TBMs) by employing the Colorado School of Mines (CSM) model, which is appropriate for rocky substrates, alongside the NTNU model devised by the Norwegian University of Science and Technology (NTNU) (Chang et al. 2011, 2013). Furthermore, utilising the Japanese thrust calculation formula, which accounts for stress relaxation in soil ground as a result of excavation, the structural stability of shield TBMs during construction on steep curves was investigated (S. H. Kang et al. 2017). This work delineates and categorises four formulas for thrust and torque calculations utilised in TBM design: the Japanese and modified Japanese models for soil, and the CSM and NTNU models for rock. The values derived from each method were compared and analysed.

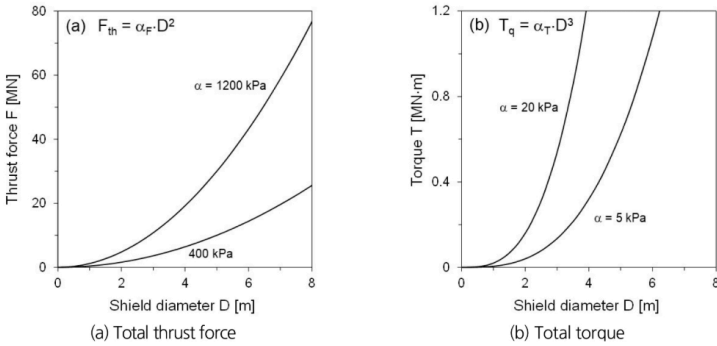


Figure 8: Earth pressure balance diameter characteristics.

To assess the stresses around a shield TBM, it is essential to first compute the vertical stress along the tunnel, considering the stress relaxation in the soil from the tunnel crown to the ground surface resulting from excavation. Figure below shows the equilibrium of the forces operating around the tunnel by creating small elements between the ground surface and the tunnel top.

(1) $\sum F_y = 0 \rightarrow \sigma'_v \cdot 2B_o - (\sigma'_v - d\sigma'_v) \cdot 2B_o + \gamma \cdot 2B_o \cdot dh - 2(\sigma'_v \cdot ka \cdot u)dh = 0$
 since $h = \text{distance of the top of tunnel (m)}$, $u = \tan\phi$ coefficient of friction of soil, $c = \text{cohesion of soil (kPa)}$,
 $\gamma = \text{unit weight of the soil (kN/m}^3\text{)}$,
 $ka = \text{active soil pressure means coefficient}$.

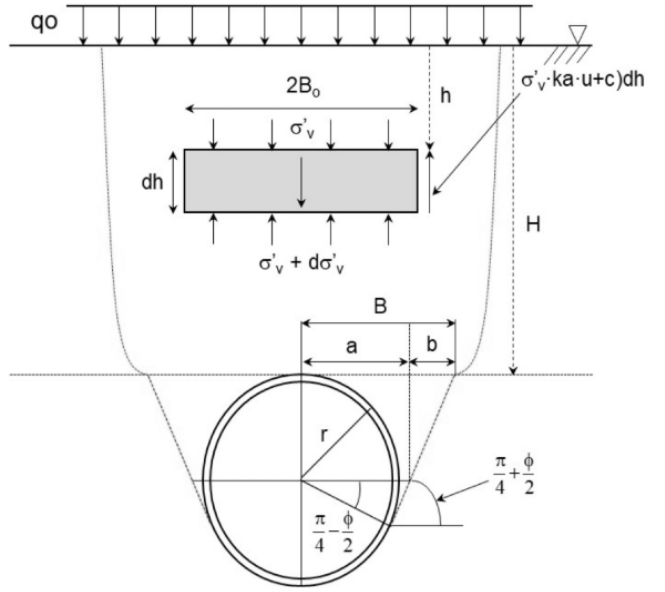


Figure 9: Underground excavation induces a free body diagram of tension relaxation and failure line (Afshani et al. 2014).

In particular, the soil moves towards the tunnel due to the tension relaxation of the soil near the tunnel side and the arching effect that occurs around the tunnel during excavation, resulting in active failure $2B_o \cdot dh$. The following first-order linear nonhomogeneous differential equation is obtained by splitting and rearranging equation above (1).

$$(2) \frac{d\sigma'_v}{dh} + \frac{ka \cdot u}{B_o} (\sigma'_v) = \gamma - \frac{c}{B_o},$$

(3) $\sigma'_v = e^{-\frac{ka \cdot u}{B_o} h} \left[\frac{B_o}{ka \cdot u} \cdot e^{\frac{ka \cdot u}{B_o} h} \cdot (\gamma - \frac{c}{B_o}) + A \right]$ Equation (3) is subjected to boundary conditions that apply a surcharge load to the ground surface ($h = 0 \rightarrow \sigma'_v = qo$), and the integration constant is determined. The equation can be expressed as follows if it is

discovered. (4) $\sigma'_v = \frac{B_o}{ka \cdot u} \left(\gamma - \frac{c}{B_o} \right) \cdot \left(1 - e^{-\frac{ka \cdot u}{B_o} h} \right) + qo \cdot e^{-\frac{ka \cdot u}{B_o} h}$,

The vertical effective stress operating on the top of the TBM can be found using equation (4) ($B_o \rightarrow B$, $h \rightarrow H$, $qo = 0$).

$$(5) \sigma'_v = \frac{B}{ka \cdot u} \left(\gamma - \frac{c}{B} \right) \left(1 - e^{-\frac{ka \cdot u}{B} (H)} \right),$$

$$(6) B = a + b = r \left[\frac{1}{\sin\left(\frac{\pi}{4} + \frac{\phi}{2}\right)} + \frac{1}{\tan\left(\frac{\pi}{4} + \frac{\phi}{2}\right)} \right] = r \cdot \cot\left(\frac{\pi/4 + \phi/2}{2}\right)$$

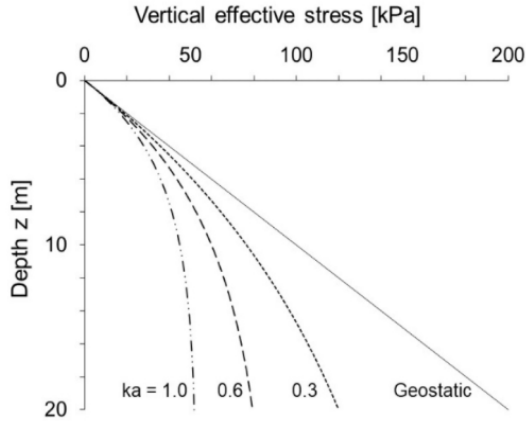


Figure 10: Vertical effective stress variation using various active earth pressure coefficients.

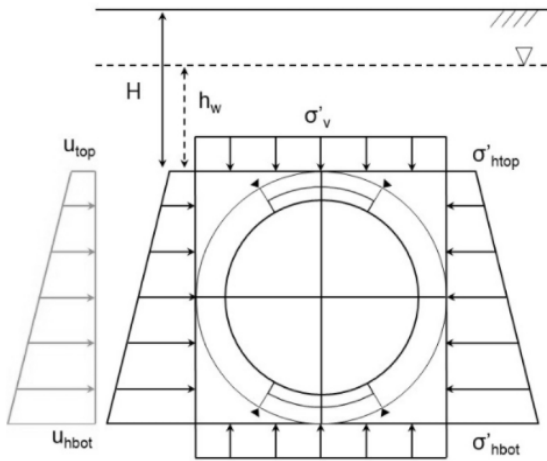


Figure 11: Pore water pressure and effective stress distribution around the TBM tunnel(Chong et al. 2020).

Direction	Symbol	Equation
Top Vertical	σ_v (effective stress)	(5)
	u_{top} (pore pressure)	$\gamma_w \times h_w$
	σ_v (total stress)	$\sigma_v + u_{top}$
Top Horizontal	σ_{htop} (effective stress)	$\sigma_v \times Ka$
	u_{top} (pore pressure)	$\gamma_w \times h_w$
	σ_{htop} (Total stress)	$\sigma_{htop} + u_{top}$
Bottom Horizontal	σ_{hbot} (effective stress)	$\sigma_{hbot} \times D \cdot \gamma_w \cdot ka$
	u_{bot} (pore pressure)	$\sigma_{hbot} \times D \cdot \gamma_w$
	σ_{htop} (Total stress)	$\sigma_{hbot} + u_{top}$

$$(7) F_1 = \sigma_{h-avg} (A_1) = \frac{\pi D^2}{4} \left[\left(\frac{\sigma_{htop} + \sigma_{hbot}}{2} \right) \cdot (1 - \rho) + p_c \cdot \rho \right],$$

p_c = chamber pressure,

ρ = opening ration,

F_2 = friction resistance shield/outer seurface,

σ_m = stress on the outer diameter of the shield.

$$(8) F_2 = \sigma_m (A_2) (\mu_1) = \left[\frac{2\sigma_v + \sigma_{htop} + \sigma_{hbot}}{4} \right] \cdot \pi \cdot D \cdot L \cdot \mu_1, \quad L = \text{frame length},$$

μ_1 = friction coeff between shield and surouounding ground ,

Specifically, the influence of hydrostatic pressure was removed when computing the transverse stress in the shield surface earth pressure case, in contrast to the frontal friction resistance. When excavating rock ground, further rock crushing is necessary due to the properties of residential ground; therefore, the rock's uniaxial compressive strength and disc cutter resources (net penetration area A_{bit-p})

N_c = total number of cutters. F_4 is the segment and shield frame resistance and F_5 is the backup car transport resistance. do not

constitute thrust components because they were either not included in the original design due to their small proportion—less than about 2%—or because their inclusion was contingent upon the operation of the equipment on-site. The percentage of certain thrust components must be composed in order to determine the overall design thrust when excavating along a steep curve or at the soil-rock border (S. H. Kang et al. 2017). Five components are used to compute the design torque needed for a sealed shield TBM. The cutting torque T_1 , determined by the load on the disc cutters affixed to the face plate, should theoretically be calculated as the aggregate of the moment loads of each disc cutter, which is the sum of the products of the rotational load of each cutter and the distance from the centre of the face plate to the respective cutter. But because it was hard to find the disc cutters' rotational stress and moment distance, the following rough calculation was applied. (9) $T_1 \approx F_r \cdot N_c \cdot \frac{r}{2} = [\sigma_c \cdot \omega_{cutter} \cdot p \cdot f] \cdot N_c \cdot \frac{r}{2}$,

$$(10) T_2 = \frac{\pi D^3 (1-p)}{12} \left(\frac{\sigma_{htop} + \sigma_{hbot}}{2} \right) \mu_1. \quad (11) T_3 = \frac{\pi D^2 B_g}{2} \left(\frac{2\sigma_v + \sigma_{htop} + \sigma_{hbot}}{2} \right) \mu_1$$

Here, the thickness of the cutter head B_g (m) is being discussed. Furthermore, the torque components were not included in the torque components due to the low proportion of the stirring resistance T_4 generated within the chamber installed to facilitate the transfer of excavated soil to the screw conveyor and the bearing friction resistance T_5 installed in the drive unit, which is insignificant in comparison to the uncertainty of numerous input variables required for the calculation and the design torque (X.-P. Zhou and Zhai 2018).

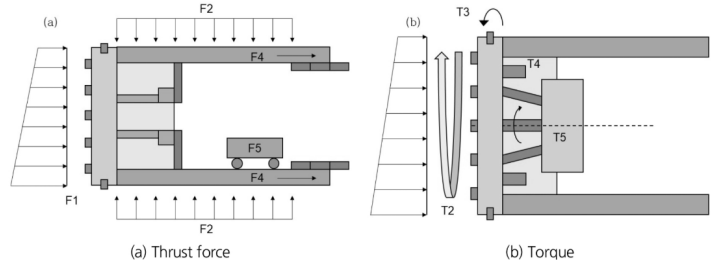


Figure 12: Factors influencing the front and area of the TBM shield(Chong et al. 2020)

Methods for thrust and torque calculation previously proposed by the Japanese did not account for the fact that the effective stress operating on the top and sides of a TBM varies with the TBM diameter. This modification is reflected mathematically in the thrust and torque calculation methods provided in this section (Shi et al. 2011; Lintao Wang et al. 2012). Using the polar coordinate system, the resistance force F_1 that changes with the TBM front tunnel's diameter was determined. The hydrostatic pressure F_{11} and the transverse effective stress F_{12} were then determined as follows.

$$(12a) F_{11} = \int_0^{2\pi} \int_0^{\frac{D}{2}} \gamma_{\omega} [h_w + r(1 - \sin\phi)] r dr d\phi = \frac{\pi D^2}{4} \gamma_{\omega} (h_w + \frac{D}{3})$$

$$(12b) F_{12} = \int_0^{2\pi} \int_0^{\frac{D}{2}} ka \cdot \gamma [h_w + r(1 - \sin\phi)] r dr d\phi = \frac{\pi D^2}{4} \gamma \cdot ka (h_w + \frac{D}{3})$$

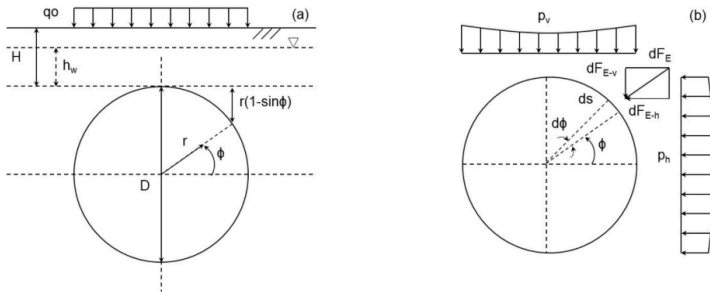


Figure 13: Illustration of soil pressure and pore water pressure on the surface of a shield tunnel boring machine (TBM)

Additional weight applied to the ground surface q_0 extra frontal load F_{13} , face plate opening ratio, and chamber pressure resulting from In light of this, the formula is articulated as follows.

(14a) $p_v = \gamma [H + \frac{D}{2} (1 - \sin\phi)]$, (14b) $p_h = \gamma [H + \frac{D}{2} (1 - \sin\phi)]$, using the previous equations the forces acting at the upper side of the tunnel are the obtained as following:

$$(15a) F_{E-v} = \int_0^{\frac{\pi}{2}} dF_E \sin\phi = \int_0^{\frac{\pi}{2}} p_v \frac{D}{2} d\phi \sin\phi \sin\phi = \gamma \cdot D \cdot (-\frac{\pi H}{8} + \frac{\pi D}{16} - \frac{D}{6})$$

$$(15b) F_{E-h} = \int_0^{\frac{\pi}{2}} dF_E \cos\phi = \int_0^{\frac{\pi}{2}} p_h \frac{D}{2} d\phi \cos\phi \cos\phi = \gamma ka D \cdot (-\frac{\pi H}{8} + \frac{\pi D}{16} - \frac{D}{6})$$

The following is the expression for the circumferential frictional resistance F_2 of the shield, which is induced by the ground pressure acting along its diameter and frame:

$$(17) T_2 = \int_0^{2\pi} \int_0^{\frac{D}{2}} ka \cdot \mu_1 \cdot \gamma \cdot [H + r(1 - \sin\phi)] \cdot r^2 dr d\phi = \left[\frac{\pi D^3}{4} \cdot ka \cdot \mu_1 \cdot \gamma \cdot (\frac{H}{3} + \frac{D}{8}) \right] \cdot (1 - \rho)$$

Equation (14a) and the horizontal effective stress are the two components of the torque T_3 , which is the outer diameter of the shield. Equation (14b) can be used to determine the torque acting on the top and sides of the tunnel in relation to the thickness of the cutter

$$\text{head.} (18a) T_v = \int_0^{2\pi} p_v \frac{D}{2} d\phi \cdot \sin\phi \cdot \sin\phi \cdot \frac{D}{2} = \frac{\pi D^2}{4} \gamma (H + \frac{D}{2})$$

$$(18b) T_v = \int_0^{2\pi} p_v \frac{D}{2} d\phi \cdot \cos\phi \cdot \cos\phi \cdot \frac{D}{2} = \frac{\pi D^2}{4} \gamma \cdot ka \cdot (H + \frac{D}{2}),$$

(18c) $T_3 = (T_v + T_h) B_g \mu_1 = \frac{\pi D^2}{4} \gamma B_g [H(1 + ka) + (1 + ka)] \mu_1$. By analysing the rock cutting force, the CSM model can forecast TBM excavation performance. This model is based on large amounts of data collected from long-term field data and full-scale LCM trials (J. Rostami and Ozdemir 1993).

$$(19) \phi = \cos^{-1}(\frac{R-p}{R})$$

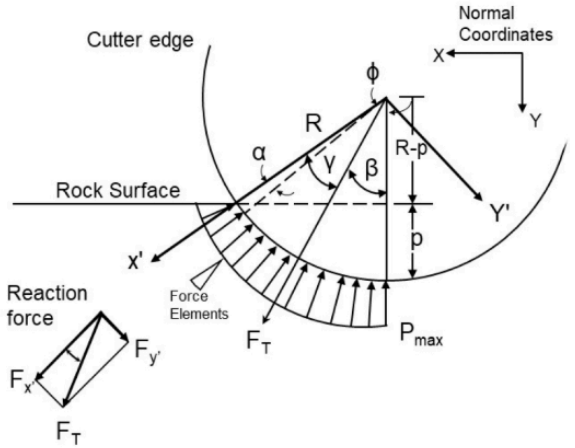


Figure 14: Pressure distribution and geometric conditions of rock surface cutting with disc cutter (J. Rostami and Ozdemir 1993).

(20) $P = P_{max} (\frac{\alpha}{\phi})^{\lambda}$ where, $P_{max} = C \cdot \sqrt[3]{\frac{\sigma_c^2 \sigma_t S}{\phi \sqrt{RT}}}$ since α is the angle from ϕ which is the incidence changes to S which is the gap between the cutters. T is the cutter tip width, σ_t is the tensile strength of the rock. C refer to the dimensionless coefficient ≈ 2.12 . The pressure shape coefficient influences the distribution of cutting pressure. It varies by cutter type, ranging from -0.2 (wider tip cutter) to 0.2 (V-shaped cutter). The distribution of cutting rock can be uniform ($\lambda=0$), straight line ($\lambda=1$), or nonlinear distribution ($0 < \lambda < 1$). Furthermore, another function can be used to represent the cutting pressure distribution (Labra, Rojek, and Oñate 2017). The following equation uses Taylor series to calculate the direction of the actions reaction forces through the integration system.

$$(21a) F_x = \int_0^{\phi} dF \cos\alpha = \int_0^{\phi} TR p_{max} (\frac{\alpha}{\phi})^{\lambda} d\alpha \cos\alpha = \sum_{i=0}^n (-1)^{i-1} \frac{\phi^{2i+\lambda+1}}{(2i+\lambda+1)(2i)}$$

$$(21b) F_y = \int_0^{\phi} dF \sin\alpha = \int_0^{\phi} TR p_{max} (\frac{\alpha}{\phi})^{\lambda} d\alpha \sin\alpha = \sum_{i=0}^n (-1)^{i-1} \frac{\phi^{2i+\lambda+2}}{(2i+\lambda+2)(2i+1)}$$

(22) $\gamma = \tan^{-1}(\frac{F_y}{F_x})$, Thrust and torque calculations use the Cartesian coordinate F_T system to determine the total resultant force.

The cutting coefficient's (CC) site of action needs to be estimated. The cutting coefficient is the ratio of rotational force

to vertical force. Each is expressed as follows.(23) $CC = \tan\beta$ where, $\beta = \tan^{-1}[\tan(\phi - \gamma)]$

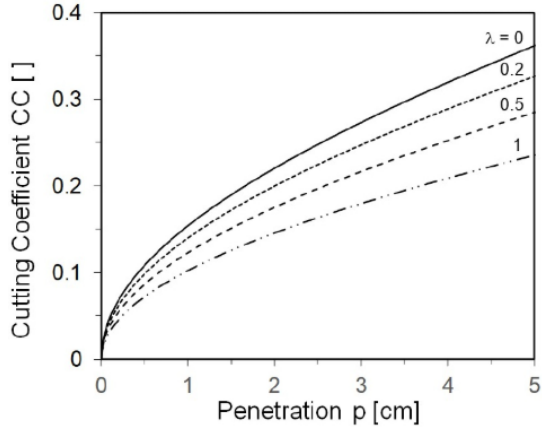


Figure 15: effect of pressure shape coefficient on the cutting coefficient

$$(24) F_T = \int_0^\phi dF = \int_0^\phi T \cdot R \cdot P_{max} \cdot \left(\frac{\alpha}{\phi}\right)^\lambda \cdot d\alpha = \frac{T \cdot R \cdot \phi}{1+\lambda} \cdot P_{max} = \frac{T \cdot R \cdot \phi}{1+\lambda} \cdot C \cdot \sqrt[3]{\frac{\sigma_e^2 \cdot \alpha \cdot t \cdot s}{\phi \cdot \sqrt{RT}}}$$

. Overall cutting force resulting from the action F_T . The force derived from F_N vertical motion and rotational dynamics. The thrust is as follows, assuming that the cutting pressure ($\beta = \phi/2$) is distributed uniformly (the centre of the contact area is where the whole force is applied): and thrust formulas for calculations can be expressed by:

$$(25 a) F_{th} = N_c F_T \cos\left(\frac{\phi}{2}\right), (25 b) T_q = 0.3 \cdot N_c \cdot D \cdot F_T \cdot \sin\left(\frac{\phi}{2}\right)$$

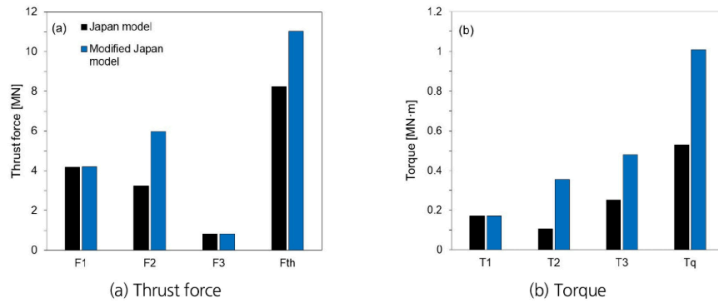


Figure 16: Comparison between Japanese model and modified model for thrust and torque

The Japan model estimates thrust force and torque by deriving vertical stress relaxation induced by TBM excavation, with pore water pressure and overburden soil stress considered linearly around the TBM. While it can be applied to rock TBM excavation, it requires many input parameters. The Modified Japan model improves upon this by calculating pore water pressure and soil pressure more accurately along the TBM, while still requiring numerous inputs and incorporating the Japan model framework. In contrast, the CSM model determines thrust force and torque based on cutter reaction forces and cutting geometries. However, it does not account for pore water pressure or overburden soil stress, limiting its use to

rock TBM excavation, and faces challenges in measuring and quantifying pressure distribution along the cutting surface.

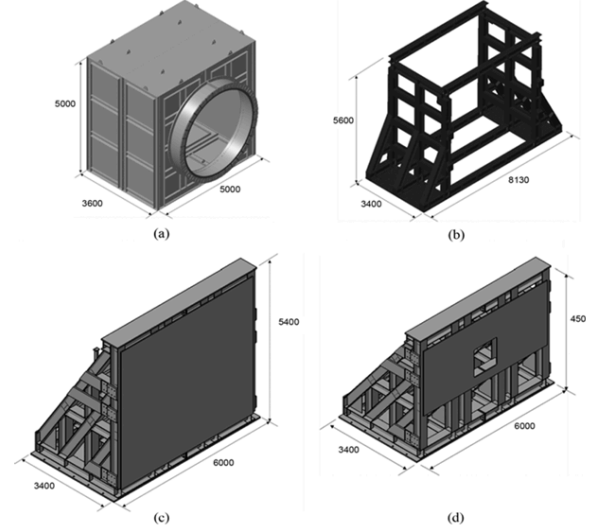


Figure 17: The dimensions can vary of the sample mould and support walls are in millimetres (mm). (a) The sample mould, (b) Lateral Support, (c) Front-Side Abutment Wall, and (d) Back-Side Abutment Wall.)

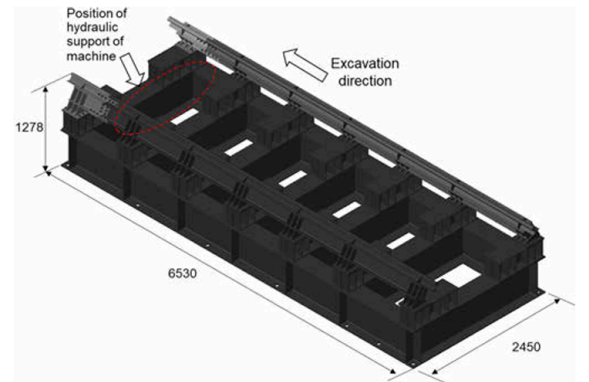


Figure 18: Machine support system dimensions can vary(G.-I. Lee et al. 2021)

Such small cross-sectional TBMs are typically seen in tunnel segments that are between 1.2 and 1.5 meters long. The sample mold's height and breadth are set at 5 m and 3.54 m, respectively, in accordance with the TBM diameter. The ability to deconstruct the sample mould into its component parts and reassemble it is helpful when removing a tested sample from the mould once the test is over. The geologic sample's volume change within the mould can be limited by the lid of the mould. The thrust forces exerted during TBM excavation are substantial, reaching several thousand kN. Thus, four support walls are erected in total to endure such thrust and reaction forces: One front-side abutment wall, one back-side abutment wall, and two lateral supports on either side of the mould. The lateral supports, the front-side abutment wall, The walls and

mould are engineered to sustain a force of 8,000 kN. The front and rear abutment walls are anchored to the floor and interconnected by H-beams on both sides.

3.1.1 Technical Review

The technical sections of TBM are listed as below:

Section	Technical chambers of TBM(Salepciler et al. 2023).
1	Foam generator, control cabinet, and operator cabinet.
2	Grouting system and Quick unloading device.
3	Transfer pump, polymer tank, foam solution tank, foam tank, and hydraulic pump station.
4	Grease barrel transfer hoist and grease system.
5	Frequency converter cabinet and water tank.
6	Transformer, Bentonite tank, HV switch cabinet, and metal detector.
7	Air compressor, generator, wastewater tank, and cooling water tank (internal circulating water tank).
8	Chiller unit and emergency shelter for refugees.
9	Emergency refuge chamber.
10	Crew room, pipe storage space, and pipe extension hoist.
11	Workspace, conference room, and backup generator.

Tunnel Boring Machines (TBM) are mechanised tunnelling systems widely used in civil infrastructure projects, especially for the construction of transport and utility tunnels. TBMs offer a mechanised alternative to traditional methods, ensuring efficient excavation while minimising surface disruption. Figure 4 and 5 seeks to demystify the core components of TBMs, analyse their operational principles, and provide insight into the challenges of tunnel excavation under varied geological conditions. Since the introduction of Tunnel Boring Machines (TBMs) in the 1950s, design engineers and contractors have been preoccupied with the issue of accurately estimating the performance of TBMs in a specific project context (Jamal Rostami 2016). This method was initially employed in the planning of the Trans-Alpine tunnels in Europe during the 1990s. In general, the estimation of specific parameters for a TBM is referred to as performance estimation(Einstein 2001).

These parameters include:

- The rate of penetration (ROP), also known as the penetration rate (PR), is the linear footage of excavation per unit time when the machine is engaged with the ground and producing work. It is often given in metres per hour.
- Representing the ratio of boring time to the overall time, utilisation rate (U) is stated in percent (%).
- The concept of total time may encompass the quantity of hours worked during workdays, uneventful days, or calendar days. The advance rate (AR), which represents the daily progress measured in metres per day, is determined by the following calculation:

$$AR = ROP \cdot U \cdot Ns \cdot Sh,$$

where Ns represents the daily shift count and Sh denotes the duration of each shift in hours.

3.2. Estimate of ROP or PR under rock

Evidence suggests that TBM ROP can be predicted with reasonable accuracy in most projects using these models. However, the precision of these models is somewhat constrained by the accuracy of input parameters, primarily the variability of the ground in relation to the index parameters utilised in the models to compute ROP(Sharp and Ozdemir 1991). The formulae demonstrate good accuracy in uniform rock formations with fewer joints or discontinuities. Conversely, the models' accuracy diminishes when machines operate in jointed rocks, particularly where joint frequency and orientation fluctuate, as well as in blocky grounds, shear zones, and mixed face conditions. Consequently, one of the most intricate issues requiring further investigation is how to account for the impact of joints on machine performance, considering the nature of rock joints and the degree of spatial variability in terms of spacing or frequency, and orientation relative to the tunnel axis(E. Farrokh 2012).

$$FPI = \text{Exp}(1.97 + 0.0063 \cdot RQD + 0.103 \cdot CAI + 0.00685 \cdot UCS)$$

$$PR = (0.06RPM \cdot Fn) / FPI \quad \text{since}$$

$$PR = ROP = \text{Rate of penetration in m/h}$$

$$CAI = \text{Cerchar Abrasivity Index}$$

$$RPM = \text{Cutter head rotation speed rev/min}$$

$$RQD = \text{Rock quality designation}$$

$$UCS = \text{uniaxial compressive strength in MPa}$$

$$Fn = \text{Disc cutter normal force in kN}$$

Recall that models based on FPI should ensure that machine torque is not exceeded for low FPI values by reducing Fn and checking for cutterhead torque limitations in rocks below 100 MPa.

Machine utilisation rate is crucial for assessing Tunnel Boring Machine (TBM) performance, reflecting the percentage of time the machine is actively excavating. Typically, TBM utilisation ranges from 20-30%, with ideal conditions allowing up to 55%. The rest of the time is consumed by downtimes, such as maintenance, repairs, ground support, and other logistical issues, which account for 70-80% of total time.

Ground conditions significantly affect TBM utilisation, especially for open-type machines in unstable areas, where support installation or shield entrapment can cause delays. Groundwater inflow and gas presence also disrupt operations. Human and logistical factors, like contractor experience and site management, further influence machine performance. Predicting utilisation remains difficult due to these complex and variable factors, making estimates often based on local practices and past experiences (Ozdemir 1977).

An alternative method of approximating machine utilisation involves assessing delay times by means of downtimes attributed to distinct activity types. This idea is applied to both CSM and NTNU models, where the whole time is divided into smaller tasks like surveying, machine repair, back-up repair, boring, regripping, cutter inspection/change, haulage delays, and so on. The machine utilisation is the ratio of the total time components to the time spent boring, and these components are represented by the related time spent during the shift. A thesis work represents some of the recent advances in estimating such downtime components(E. Farrokh 2012).

Table 2: General guidelines for estimation of TBM utilisation.

Machine Type	Ground Conditions	Muck Haulage	Suggested utilisation rate (%)
Open	Simple/consistent or uniform	Train	Continuous/conveyor 35-40
	Complex/faults	Train	40-45
Single Shield	Simple/consistent or uniform	Train	20-25
	Complex/faults	Contentious/conveyor	25-30
Double Shield	Simple/consistent or uniform	Train	15-20
	Complex/faults	Continuous/conveyor	20-25
Double Shield	Simple/consistent or uniform	Train	25-30
	Complex/faults	Contentious/conveyor	30-35
Double Shield	Simple/consistent or uniform	Train	20-25
	Complex/faults	Continuous/conveyor	25-30

$$Tb = 1000/PR (h/Km)$$

$$U = (Tb) / (Tb + Tt_{bm} + Tbu + Tc + Ty + Tsp + Tw + Tg + Ttr + Tr + \dots)$$

Table 3: List of components of downtime for rock TBMs:

Category Name	Definition	Suggested formulas
<i>TBM, T_{tbm}</i>	TBM breakdowns time	See figure 19
<i>BU, T_{bu}</i>	Backup breakdown times	See figure 19
<i>Cutter, T_c</i>	Cutter check/change time	See figure 19
<i>Support, T_{sp}</i>	Support installation time	See figure 19
<i>Regrip, T_r</i>	Resetting times of TBM after each excavation stroke	$Tr = \frac{1000 \cdot tr}{60 \cdot Ls} + \frac{409,000}{R^2}$ Ls is stroke length (m), tr is regripping time (min) per stroke And R is radius of curves (m)
<i>Maintenance, T_m</i>	Routine maintenance of cutter head, TBM, and backup	Based on ground conditions: Good, Massive, 50–100 h/km soft to medium rock 100–200 h/km for normal, massive hard rock weak: expansive clay, significant water ingress and clogging rates in weak cementations, and extremely high rock strength for TBM (300 h/km).
<i>Ground, T_g, T_w</i>	Downtimes related to unfavourable ground condition, which needs additional or support or dewatering	See figure 20
<i>Probe, T_p</i>	Probing times for ground exploration	Estimated based on the field conditions
<i>Utility, T_u</i>	Line Extension times	$Tu = 1.3 \times \theta (h/km)$ where θ tunnel slope degree
<i>Survey, T_y</i>	Time for surveying tunnel direction	$Ty = 192,000/R^2 (h/Km)$ R = tunnel turning radius (m)
<i>Other, T_o</i>	Unclassified times	Up to 200 h/km for crew with low experience
<i>Transport, T_{tr}</i>	Times related to muck transportation and unloading	

Condition	T _{tr} (h/Km)	Comment
Very Good	<50	Tunnel conveyor belt prone to no or very low breakdowns

Good	50	Belat or Train, low breakdown
Normal	150	Belt or Train, normal breakdowns
Poor	350	High breakdowns (especially in long tunnels)
Very Poor	>500	Trains, very high breakdowns

3.2.1 TBM performance estimates under challenging conditions

The ITA work group WG-14 on mechanised tunnelling outlines criteria for challenging projects using TBMs, particularly in rock tunnelling. Difficult conditions include rock strength above 300 MPa, low RQD (<25%), water inflow exceeding 30 l/s, highly abrasive rocks, fault zones covering over 20% of the tunnel alignment, and squeezing ground with over 10% convergence. Additional complexities include mixed face conditions, gases like methane and H₂S, and weak, unstable rock leading to ground collapses or cutterhead jamming (Jamal Rostami 2016). High in-situ stresses, combined with weak rock, can cause shield entrapment, requiring hand mining to release the machine. Squeezing ground and blocky terrain lead to difficulties in gripping and steering, impacting machine performance. Abrasive rocks accelerate cutter wear, requiring frequent replacements, while stronger rocks can jam the head and cause cutter failures. Faults with weak materials or water inflow cause operational interruptions, with issues like flooding and equipment damage. Hydrocarbon gases such as methane pose explosion risks, while toxic gases like H₂S require immediate halts in operations. Managing these difficult conditions depends on the machine's capabilities, crew expertise, and site management, with no model available to predict outcomes accurately in such challenging environments (Hauge and Støvneng 1989).

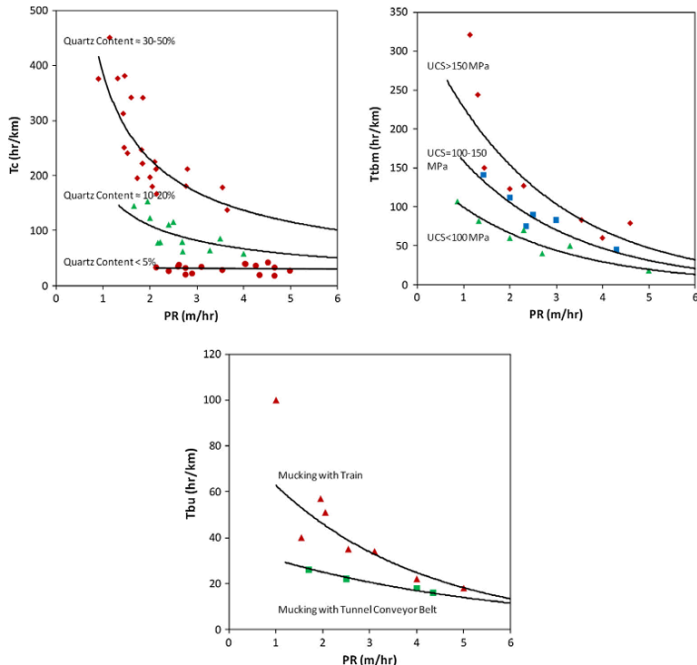


Figure 19: Hard rock TBM downtime components (Left to right Tc, Tbm and Tbu)

Water condition code:

- 1: Almost dry
- 2: Water inflow at tunnel affect the tunnel excavation me (or water inflow/tunnel diameter $\approx 1-3$)
- 3: High water inflow at face (or water inflow/tunnel diameter $\approx 3-4$)
- 4: Water inflow at tunnel face may stop the tunnel excavation (Extreme Mining Area, or water inflow/Tunnel $\gg 4$, or Diam > 10) Note: water inflow in litre/sec and tunnel diameter in m

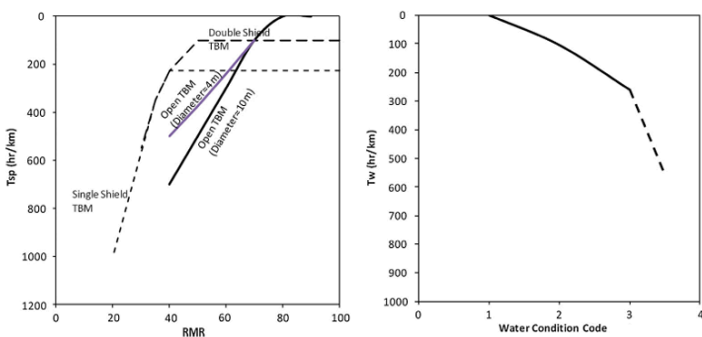


Figure 20: Hard rock TBM downtime components (Left, Tsp, right Tw)

3.1.2. Analysis of TBM Bearing Fatigue

To model the interaction between the roller and raceway, a nonlinear spring component was incorporated. The transient dynamic approach was then employed to examine the vibration

response of the Tunnel Boring Machine (TBM) following damage to its main bearing. This research investigates the mechanistic aspects of vibration responses resulting from bearing faults, potentially informing intelligent shield tunnelling techniques that utilise machine learning and data-driven methodologies.

As fatigue damage progresses, the mechanical properties of the material gradually deteriorate, resulting in alterations to the vibration response of the bearing. Consequently, monitoring the response changes induced by bearing damage can effectively facilitate fault warning and diagnosis. In response, researchers have proposed numerous fault diagnosis and life cycle performance prediction models (H. Zhang and Qu 2023). Numerous investigations have demonstrated that cyclic shear stress is the primary factor contributing to bearing fatigue damage, whilst the mean shear stress value has minimal impact on such damage. GCr15 steel is typically employed in the construction of TBM main bearing rollers, and its torsional S-N equation (Abdullah and Khan 2022).

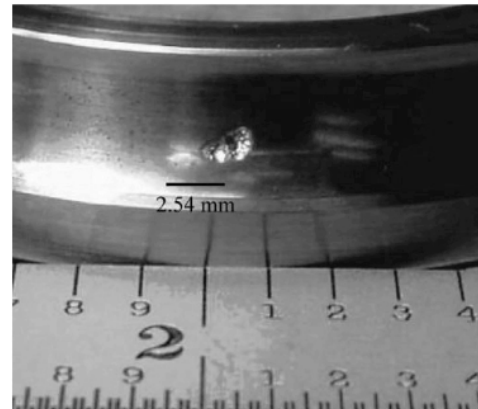


Figure 21: Formation of fatigue spall endurance life experiments (F. Li et al. 2018)

$$(26) \tau_{max} = \frac{\Delta\tau}{2} = 2.636N^{-0.12}$$

For high-cycle fatigue, the damage evolution equation can often be set as (Abdullah and Khan 2022)

$$(27) \frac{dD}{dN} = \left[\frac{\Delta\sigma}{\sigma_r(1-D)} \right]^m$$

Here, N is the number of cycles, and $\Delta\sigma$ is the difference between the highest and lowest stresses. The material parameter associated with the average stress is denoted by σ_r ; m is a read of temperature-related material parameters.

Since shear stress is the primary driving force behind contact fatigue of the primary bearing, $\Delta\sigma$ is substituted for $\Delta\tau$ in the formula above, resulting in the following transformation:

$$(28) \int_0^N dN = \int_0^1 \left[\frac{\sigma_r(1-D)}{\Delta\tau} \right]^m dD \rightarrow \Delta\tau = \frac{\sigma_r}{[(m-1)N]^{1/m}}$$

Formulas (1) and (3) can be compared to determine that: $m = 9.7874$, $\sigma_r = 6722$ MPa. Thus, for GCr15 steel, the damage evolution equation is:

$$(29) \frac{dD}{dN} = \left[\frac{\Delta\tau}{6722(1-D)} \right]^{9.7874}$$

The primary bearing ring is typically composed of 42CrMo steel, however in this study, the comparable 18CrNiMo7-6 steel is used instead. The damage evolution equation for 18CrNiMo7-6 steel can be expressed as follows(Z. Liu, Zhang, and Qu 2023):

$$(30) \frac{dD}{dN} = \left[\frac{\Delta\tau}{3521.2(1-D)} \right]^{10.3}$$

For all three rows of rollers in the TBM's main bearing, cylindrical rollers were employed. To simplify the computational process, the contact interaction between rollers and rings was reduced to a plane strain problem. Figure 8 illustrates the finite element model, with the raceway of the ring depicted in blue and the roller shown in grey. Table 4 presents the material characteristics of both the raceway and roller (Jiang 2013).Because the model was symmetric, only one-fourth of it was required for the calculations. The mesh in the contact region between the roller and the raceway had elements measuring 0.05 mm on each side. In Abaqus, CPE4R elements were used in the finite element model, totaling 16,000 elements. Normal contact was defined as "hard contact," while the tangential friction coefficient was set to 0.05(F. Li et al. 2018).

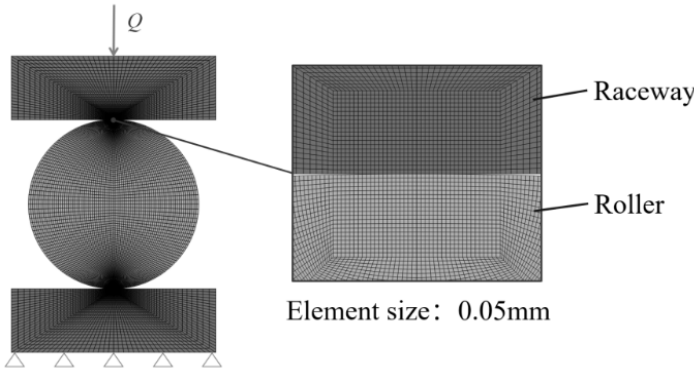


Figure 22: Finite element model of interaction between rollers and raceways

Table 4: Material properties of bearing steel

	Density	Young's Modulus	Poisson's Ratio	Yield Strength	Tensile strength
Raceway	7850 Kg/m^3	210 GPa	0.3	1047 MPa	1134 MPa
Roller	7850 Kg/m^3	209 GPa	0.28	1617 MPa	2310 MPa

Two steps were implemented in Abaqus. In the first step, a slight pressure was applied to the upper area of the raceway to help the model form a stable contact relationship. The second step involved applying a cyclic load Q to the upper section of the raceway, with its time-dependent changes shown in Figure 9. Assuming a main bearing speed of 6 r/min, the relationship between time and cycle count can be determined from geometric relationships, as described in Table 5.

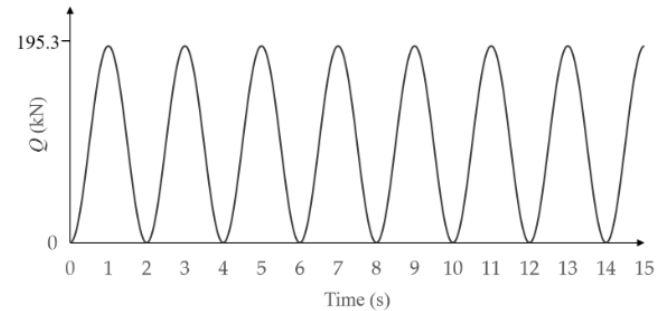


Figure 23: Cyclic road Q (kN) frequency with respect with time

Table 5: Investigation between the relation between the number of load cycles of roller raceway and the working time.

t (h)	Mail Roller	Main Raceway	Reserve Roller	Reserve Raceway	Radial Roller	Radial Raceway
1000	2.68×10^7	3.38×10^7	5.46×10^7	2.56×10^7	5.6×10^7	5.76×10^7

In the Abaqus Property module, a field was active, and this field was D. As a result, the elastic modulus E was linearly connected with this field. Using a roller as an example, we set D = 0 and D = 1 equal to the maximum value of E of 209,000 MPa and the minimum value of 0. E would thus be linearly dependent on D in this manner. After that, the USDFLD subroutine was built using formulas (29) and (30) and interfaced with Abaqus. Consequently, every time the shear stress reaches a peak, the damage and stiffness of the raceway and roller might be updated. The maximum shear stress for plane problems can be written as follows:

$$(31) \Delta\tau = \sqrt{\left(\frac{\sigma_x - \sigma_y}{2}\right)^2 + \tau_{xy}^2}$$

Based on the operational parameters found in the literature (Jiang 2013), the cutterhead experienced an overturning moment (M) of 8000 kNm, a weight (G) of 800 kN, and a thrust (F) of 5000 kN. Under these conditions, the maximum loads recorded for the main rollers were 195.3 kN, for the reverse rollers were 30 kN, and for the radial rollers were 20.2 kN. It is important to note that the load distribution among the rollers is not uniform. For instance, the maximum load on the reverse rollers, which reached 30 kN, was situated at the upper end of the main bearing, specifically at the π rad position, as illustrated in Figure 10. Given that the loads on each roller vary, we assume that the roller completes one full rotation around the ring and experiences load only in the area of maximum stress, specifically between $3/4\pi$ and $5/4\pi$, where it consistently bears 30 kN. This assumption also extends to the main rollers and radial rollers. The simulation of fatigue damage for the main bearing was conducted using the methodology described in the previous section. The resulting damage (D) for each component of the main bearing under varying operational hours is presented in Table 6.

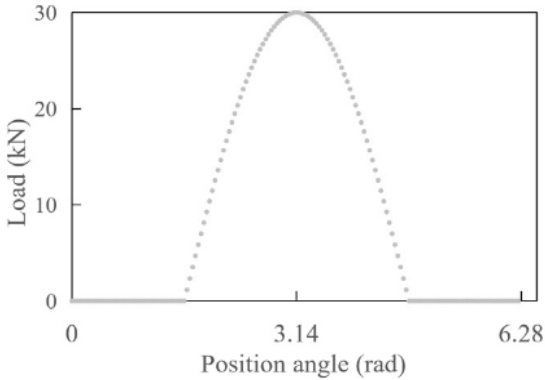


Figure 23: Applied load on each reserve roller with respect to angle positioning

Table 6: At different times, the damage D of each part of the main bearing recorded.

t(h)	Main Raceway	Reverse Raceway	Radial Raceway	Main Roller	Reverse Roller	Radial Roller
10,000	0.11	0.015	9.0×10^{-3}	6.0×10^{-3}	1.1×10^{-3}	5.0×10^{-3}
20,000	0.99	0.03	2.1×10^{-3}	1.1×10^{-3}	2.3×10^{-3}	1.2×10^{-3}

After 20,000 hours of main bearing operation, the racetrack fails, although the damage to the roller is minimal compared to the damage to the raceway. Figure 7 depicts the damage nephogram of the main roller and raceway. Damage to the rollers and raceway in the reversing and radial rows.

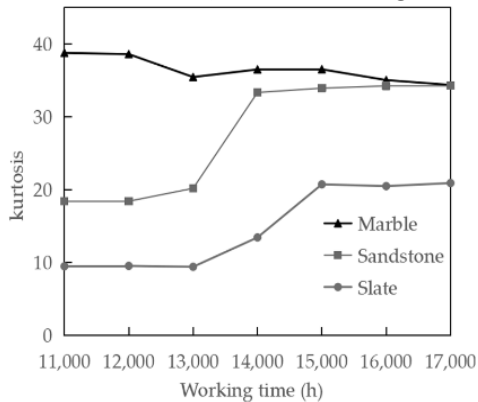


Figure 24: Curve of Kurtosis with time

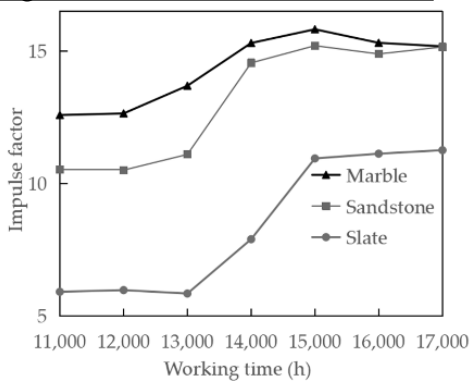


Figure 25: Curve of impulse factor with time

As dimensionless metrics, kurtosis, impulse factor, and margin factor are frequently used as bearing defect detection indicators since they are independent of the operating circumstances and sensitive to the health state of the bearings, representing the vibration signal's departure degree from the formal distribution, which is better suited for early fault identification. Figure 6 shows that the vibration signal's kurtosis grows with time under slate and sandstone geologies. The vibration signal's kurtosis is constant and consistently high in marble geology. Marble has a high UCS value, which explains this. The cutterhead load variation is more pronounced at the same penetration degree, and the vibration signal's fault features are muffled by loud background noise.

The vibration signal's margin factor rises with time before stabilising, as seen in Figure 24. In summary, upon damage to the main bearing, the vibration signal's kurtosis, pulse factor, and margin will all vary noticeably, the vibration signal's impact component will rise, and the main bearing will depart from its typical operating state.

The ratio of the peak value to the arithmetic mean value, or impulse factor, is what determines whether shock components are present in the signal. The vibration signal's impulse factor curves with time under three different genealogies are displayed in Figure 25.

Numerical analysis of the rock fragmentation process in tunnel boring machines standard disc cutters

(Rojek et al. 2011) examined how cutter spacing affects rock breaking using 2D DEM and particle discrete algorithms. The advantage of this model is that Newton's second law can readily describe the movements of small hard balls, eliminating the need for the constitutive model of rock. Visualise crack start and propagation. The study (Baek and Moon 2003) examined how restricting pressure and cutter spacing affect chipping using 2D FDM and Fast lagrangian analysis of continua. These approaches have limitations because to their 2D nature, as they cannot account for rolling force, despite their advantages. Disc cutters' rock-breaking efficacy is typically assessed by calculating the specific energy, which is significantly influenced by the rolling force.

Specifically representative papers are based on AUTODYN-3D and ABAQUS platforms to estimate the optimal spacing of disc cutters (Cho et al. 2010). This limitation does not exist for 3D finite element modelling (FEM), which provides a solution to the problem. However, the simulation accuracy needs improving due to rock constitutive models. The Drucker-Prager (D-P) and Mohr-Coulomb (M-C) models are the two most used constitutive models of rocks (Geng Qi et al. 2016), (Chunyu, Zhengjun, and Mingxiang 2019). The M-C model can differentiate between tensile and compressive rock strengths and account for hydrostatic pressure. As the yield surface in the major stress space is a hexagonal pyramid with six singular points, numerical simulations may not converge due to this model. A simplified method called the D-P model was proposed to get around this restriction.

A computational error frequently occurs because tensile and compressive strengths cannot be differentiated. The main drawback of the D-P model is: However, the stress-strain

condition in various regions of a rock being cut is varied and cannot be well described by a single stress-strain equation. Instead, the relationship between equivalent stress and equivalent plastic strain characterises the plasticity of rock. Using the D-P model for rock-breaking simulations may result in excessive rock cutting beneath the disc cutters, while rocks between the cutters remain (F. Lu et al. 2016).

3.2 Numerical model for disc cutters and rock

To rotate the rock specimen, the two disc cutters spin around both the global z-axis and the local x-axes related to the centre of each cutter (Points p1 and p2). Cutter 1 rotates 5 degrees before cutter 2, representing the next cutting phase. S represents cutter spacing, H represents cut depth, 1w and 2w represent cutter angular velocities, and lz represents rock specimen thickness.

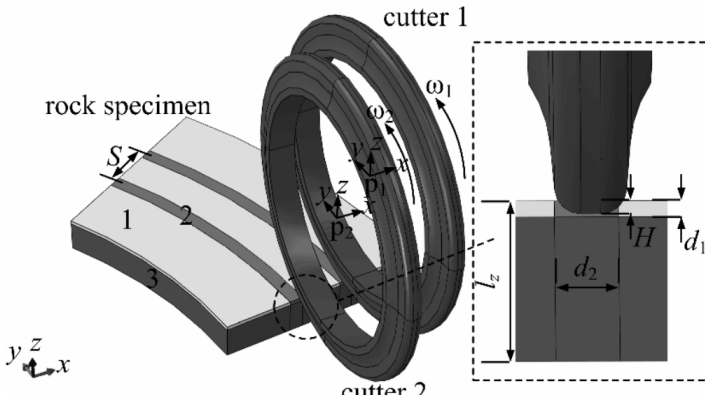


Figure 26: The rock-breaking simulation included three numerical models: Part 1 (compressive-tensile hardening), Part 2 (compressive hardening), and Part 3.

In the numerical model, two disc cutters with a CCS profile by (Cigla, Yagiz, and Ozdemir 2001) and a 432 mm diameter were used, along with a fixed fan-shaped rock specimen (Figure 26). To rotate the rock specimen, the two disc cutters spin around both the global z-axis and the local x-axes related to the centre of each cutter (Points p1 and p2). The successive cutting procedure is represented by cutter 1, which rotates 5 degrees in advance of cutter 2. S represents cutter spacing, H represents cut depth, 1w and 2w represent cutter angular velocities, and lz represents rock specimen thickness.

According to the CSM model (Ozdemir 2003), compressive strength describes rock breaking beneath the cutter tip, while tensile strength describes chip production between cuts (Figure 26). Under the cutter tip, rocks were crushed into powder, while chips formed beside the cut.

To determine the hardening and failure rules of each section, the rock specimen was separated into three parts. (Figure 26) depicts the division method and hardening type of each rock specimen part. Only parts 1 and 2 had a failure rule to imitate rock debris cleanup by deleting elements. Parts 1 and 2 had a

thickness d_1 significantly more than the cut depth H . It was defined component 2 d_2 width as the cutting tip width.

Dividing the rock specimen based on our rock-breaking tests, which showed that the debris thickness in the penetration direction is typically less than the cut depth. The statistical analysis of rock debris thickness from three tests $H = 30 \text{ mm}$. P represents the penetration feed, which represents the cut depth per cutter head revolution. Previous research on flat intender-penetrated rock holes support the result (Xiaohe and Jing 1984).

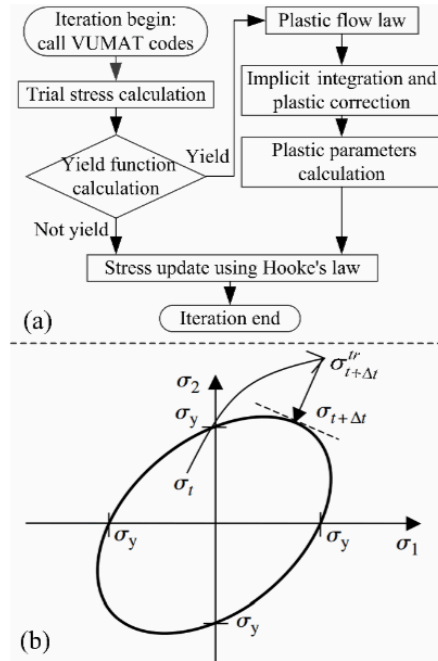


Figure 27: Examples of implicit integration of constitutive equations: (a) flowchart and (b) von Mises plasticity diagram (Dunne and Petrinic 2005).

In the figure above, an implicit integration scheme is used to calculate the stress-strain status of each element during the rock-breaking process. The trial stress increment is calculated using generalised Hooke's law, causing the updated stresses $\sigma_{t+\Delta t}^{\text{tr}}$ to move away from the yield surface. The stress is updated with a plastic correction to return to the yield surface at time $t + \Delta t$, based on the consistency condition. Finally, all variables are retrieved at the conclusion of a time step $t + \Delta t$. The stress at $t + \Delta t$ is only σ , while at the start of the time step is σ_t .

The model's initial constitutive equation is as follows:

(32) $f = \sqrt{3J_2} + AI_1$, Hooke's law can be expressed in a multiaxial format utilising stress and strain tensors as follows:

(33) $\sigma = 2G\varepsilon^e + \lambda \text{Tr}(\varepsilon^e)I = 2G(\varepsilon_t^e + \Delta\varepsilon - \Delta\varepsilon^p) + \lambda \text{Tr}(\varepsilon_t^e + \Delta\varepsilon - \Delta\varepsilon^p)I = \sigma^{\text{tr}} - 2G\Delta\varepsilon^p - \lambda \text{Tr}(\Delta\varepsilon^p)I$ the derivative form of stress can be written as: (34) $\dot{\sigma} = \sigma + \text{Tr}(\dot{\sigma})I/3$, Trial stress:

$$(35) \sigma^{tr} - Tr(\sigma)I/3 = 2G(\varepsilon_t^e + \Delta\varepsilon) + \lambda Tr(\varepsilon_t^e + \Delta\varepsilon)I\sigma' - KTr(\varepsilon_t^e)I$$

$= \sigma^{tr} + KTr(\Delta\varepsilon^p)I$ To characterise the related flow property of the rock, the yield function and the plastic potential function are defined identically. The increase in plastic strain can be computed using the orthogonal flow rule as:

$$(36) \Delta\varepsilon^p = \Delta p \frac{\partial f}{\partial \sigma} = \Delta p \left(\frac{3\sigma'}{2\sigma_e} + AI \right), \text{ from equations (33) and (34)}$$

the following equation can be written as:

$$(38) \sigma_e = \sqrt{3J_2} = \sigma_e^{tr} - 3G\Delta p, \text{ stress can be derived as}$$

$$(39) \sigma_m = \frac{I_1}{3} = 3K\varepsilon_m^e = 3K(\varepsilon_t^e + \Delta\varepsilon - \Delta\varepsilon^p)_m = \frac{I_1^{tr}}{3} - 3KA\Delta p,$$

$$(40) f = \sqrt{3J_2} + AI_1 - r - \sigma_y = f + \frac{\partial f}{\partial \Delta p} d\Delta p + \dots \text{ equation (9) can be obtained by substituting the above two equations}$$

$$(41) d\Delta p = \frac{\sigma_e^{tr} + AI_1^{tr} - 3(G+3KA^2)\Delta p - \sigma_y}{3(G+3KA^2)\Delta p + h}, \text{ the integration can be written as}$$

as (42) $r^{(i)} = r_t + h\Delta p^{(i)}$, $\Delta p^{(i+1)} = \Delta p^{(i)} + d\Delta p$, The increase of the plastic strain tensor, referred to as the plastic corrector of strain, can be ascertained as (43) $\Delta\varepsilon^p = \frac{3}{2}\Delta p \frac{\sigma}{\sigma_e} \equiv \frac{3}{2}\Delta p \frac{\sigma^{tr}}{\sigma_e^{tr}}$ since

the stress increment can be given by:

(44) $\Delta\sigma = 2G(\Delta\varepsilon - \Delta\varepsilon^p) + \lambda I Tr(\Delta\varepsilon - \Delta\varepsilon^p)$ when the following parameters can be desibed as the following:

J_2 = stress deviator tensor in the second variant,

I_1 = first invariant of the stress tensor,

A = stress influencer parameter in bulk

$A = \tan\beta/3$

β = internal friction angle of rock, $\lambda = \frac{E\mu}{(1+\mu)(1-2\mu)}$ is the lame constant. $G = \frac{E}{2(1+\mu)}$ shear modulus. $K = \frac{E}{3(1-2\mu)}$ is the bulk modulus, E = young's modulus, μ = Poisson's ratio,

ε^e = Elastic strain, $\Delta\varepsilon^p$ = Plastic strain increment,

Δp = Effective plastic strain,

$d\Delta p$ = increment in effective plastic strain, σ_y = yeild stress,

r = isotropic hardening function, h = hardening constant. From

the experiments detailed, the isotropic hardening curve is a representation of the effective plastic strain Δp and the effective stresses. The effective yield stress after isotropic hardening and kinematic can be calculated using the following equations, assuming that the effective plastic strain $\Delta p^{(i+1)}$ falls within the interval between Δp_n and Δp_{n+1} , which are the n^{th} and $(n+1)^{th}$

strain values of the experimental data, in the i^{th} integration step. (45) $\sigma^{-(i+1)} = \sigma_n^- + \frac{\sigma_{n+1}^- - \sigma_n^-}{\Delta p_{n+1} - \Delta p_n} (\Delta p^{(i+1)} - \Delta p_n)$, σ_y^-

$= \sigma_1^- + (\sigma^{-(i+1)} - \sigma_1^-)B$, since $0 \leq B \leq 1$, if $B = 0$, kinematic

hardening applies, $B = 1$ isotropic hardening applies σ_1^-, σ_n^- ,

σ_{n+1}^- are the first n^{th} and $(n+1)^{th}$ of the effective stress. The

data obtained of the hardening is expressed as:

$$(46) \sigma_n^- = k(1 - A)\sigma_{1c} + (1 - k)(1 + A)\sigma_{1t},$$

$\Delta p_n = \frac{2}{3} [k\varepsilon_{1c}^p + (1 - k)\varepsilon_{1t}^p]$. Where k is a parameter that

determines the percentage of compression and tension, ε_{1c}^p , and σ_{1c} denote the stress and plastic strain in the axial direction of the uniaxial compression tests, respectively; σ_{1t} and ε_{1t}^p denote the stress and plastic strain in the axial direction of the uniaxial tensile tests, respectively (The Brazilian split test is used as an alternative in the present paper). $k = 1$ indicates that the material is entirely compressive, while $k = 0$ indicates that the material is completely tensile. For portions 2 and 3, k was presumed to be 1, while for part 1, it ranges from 0 to 1.

$$(47) E = E_0(1 - D),$$

as

$$D = \frac{D_c}{\varepsilon_R - \varepsilon_D} \left[\frac{2}{3} (1 + \mu) + 3(1 - 2\mu) \left(\frac{\sigma_m}{\sigma_e} \right)^2 \right] \left(\frac{y}{Y} \right)^2 d\Delta p$$

Table 5: Values of k , ε_R and ε_D

k	ε_R	ε_D
0.1	$6.08(10^{-5})$	$7.6(10^{-5})$
0.3	$1.18(10^{-4})$	$1.48(10^{-5})$
0.5	$1.76(10^{-4})$	$2.2(10^{-5})$
0.7	$2.34(10^{-4})$	$2.92(10^{-5})$
0.9	$2.91(10^{-4})$	$3.64(10^{-5})$
1	$3.2(10^{-4})$	$4(10^{-5})$

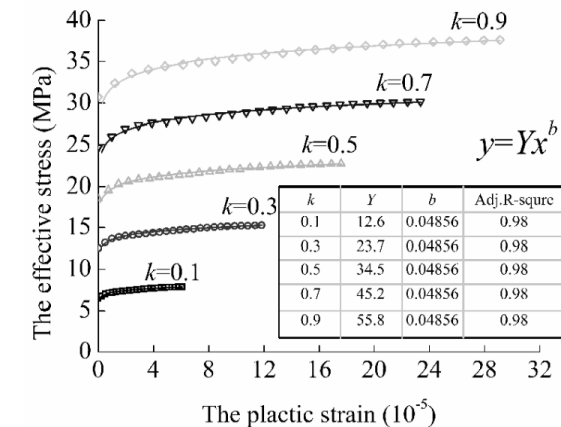


Figure 28: Fitting the flow stress curves for various k values

In this context, E_0 represents the initial Young's modulus. The variable D signifies the damage factor. The three damage constants, ε_D , ε_R and D_c , are associated with the plastic strain at the damage threshold, the plastic strain at rupture, and the critical damage value at rupture, respectively. The variable y indicates the flow stress curve, which has been fitted using the data from $\sigma_n^- \sim \Delta p_n$. Lastly, Y denotes the strength coefficient. (Figure 28) above displays the fitted curves for various k values. The fitting procedure was carried out using the data from the second-half elastic and plastic phases shown in (Figure 29). The experimental results documented in the literature by Lemaitre (Lemaitre 1985) indicate that the value of D_c is of the same order of magnitude as the value of $(\varepsilon_R - \varepsilon_D)$. The potential

value of D_{c1} for parts 2 and 3 was assigned a range between $1(10^{-4})$ and $9(10^{-4})$. The value of D_{c2} is equivalent to kD_{c1} and was assigned for part 1. The values of D_e and R_e corresponding to various k values were obtained from the standard rock-breaking test data.

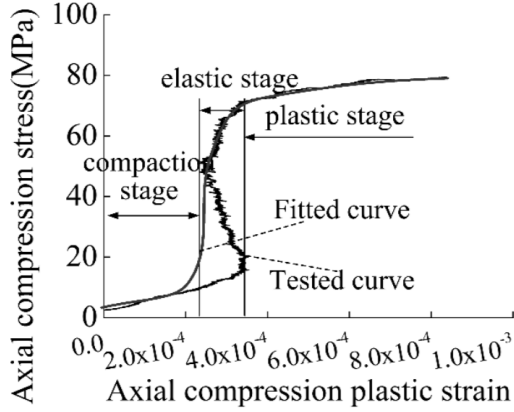


Figure 29: Stress-plastic strain curve of the uniaxial compression test (K-Z. Zhang et al. 2011)

The process of deleting rock elements was governed by the damage factor D . Upon reaching a value of 1 for D , the associated rock elements will be removed to replicate the process of cutting off rock debris.

As seen in the figure 30 below, the rock-breaking forces may be categorised into three directions: the normal force, which acts in the direction of penetration; the rolling force, which is tangent to the cutting path; and the side force, which aligns with the cutter shaft. In the rotating rock-breaking simulations presented in this study, the forces in the axial directions of the global coordinate system (F_x, F_y, F_z) may be directly obtained by establishing contacts between the rock specimen and the disc cutter. The 3D forces can be obtained through the following equations: $F_n = F_z$; $F_r = F_x \sin\theta - F_y \cos\theta$; $F_s = -F_x \cos\theta - F_y \sin\theta$. where θ represents the angle between the x-axis and the connecting line between the cutting point and the original point.

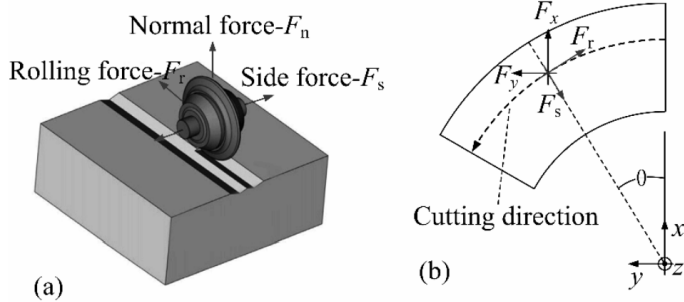


Figure 30: Process of the forces: (a) Idealised geometry of rock fragmentation via linear cutting and three-dimensional forces

(Cho et al. 2010); (b) Schematic depiction of the forces involved in rotary cutting.

The specific energy (SE), which is used to assess the rock-breaking efficiency, was calculated by averaging the peak values and comparing the experimental and numerical findings. $SE = \frac{F_{r1}l_1 + F_{r2}l_2}{m/\rho}$, F_{r1}, F_{r2} = mean rolling forces of cutters l_1, l_2 = cutting distances, m = weight and ρ = density of rocks

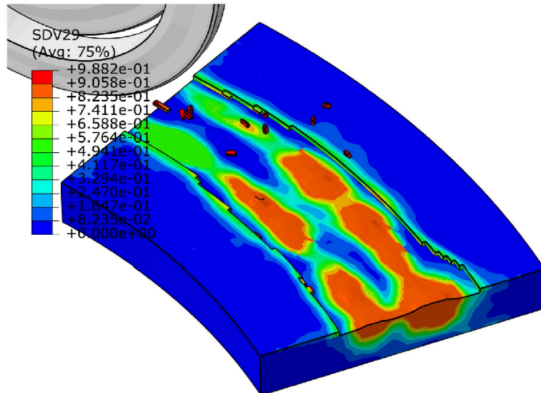


Figure 31: fine element analysis of disc cutters spacing S=64mm

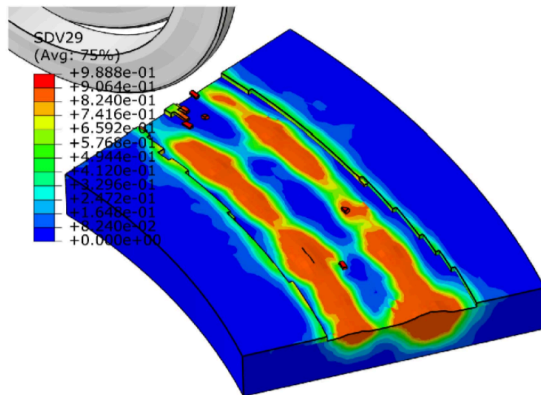


Figure 32: fine element analysis of disc cutters spacing S=72mm

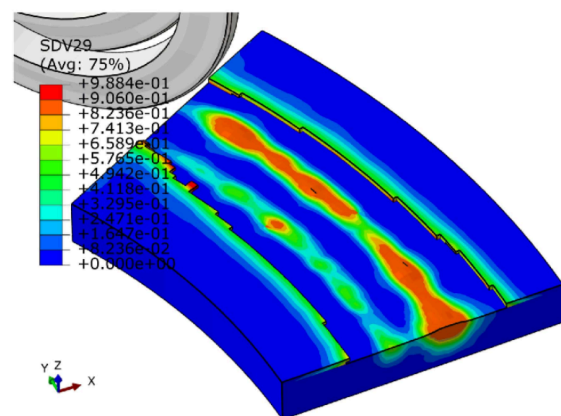


Figure 33: fine element analysis of disc cutters spacing S=72mm

3.3 Computational fluid dynamics for sludge

A rear-mounted jaw crusher is employed to pulverise large-size rocks, and certain slurry TBMs employ a large-diameter short screw conveyor to actively discharge rocks. Two slurry communicating conduits connect the excavation chamber and the air cushion. The excavation chamber and air cushion have lengths of 1720 mm and 2290 mm, respectively. The pebbles are actively discharged by connecting the inlet of the short screw conveyor to the bottom of the excavation chamber via the submerged wall. The crushing box, which has a volume of 15 m³, is connected to the outflow of the short screw conveyor. The middle maintenance window is welded to the main slurry discharging pipeline DN500, and the upper sideline and wear-resistant elbow of the connection portion are employed. The DN500 main slurry feeding pipeline is divided into numerous smaller pipelines to communicate with the lower side, which is equipped with a slurry TBM for reverse circulation. Furthermore, a groove design is implemented at the intersection of the lower portion of the submerged wall and the inlet of the short screw conveyor to guard against the obstruction of the inlet. The short screw conveyor has a shaft diameter of 457 mm, a flight diameter of 1600 mm, a screw pitch of 1000 mm, an installation angle of 36, an operating power of 800 kW, and a maximum rotational speed of 22 rpm. Its total length is 10.4 m. Additionally, in order to mitigate the wear and damage of the screw conveyor flights and extend the service life of the screw conveyor machine, the outer edges of the screw conveyor flight are enclosed by welded wear-resistant steel plates with a thickness of 3 to 5 mm.

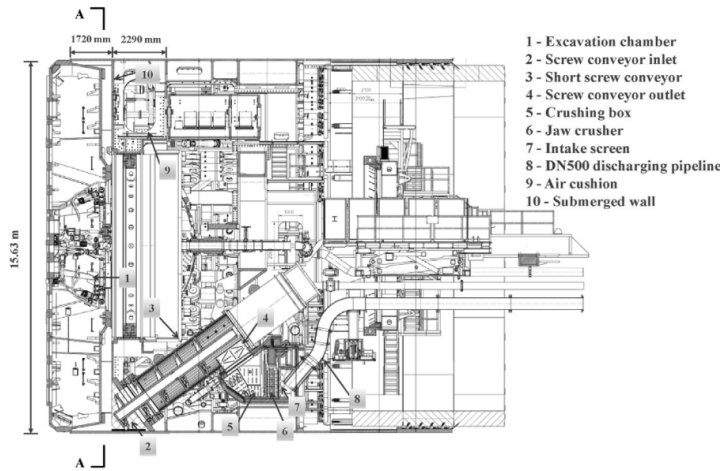


Figure 34: Side view of the "Deep Blue" slurry TBM schematic

During the simulation of the flow state in Computational fluid dynamics (CFD), the sediment is represented as the homogeneous fluid phase. Consequently, the slurry flow process adheres to the momentum conservation law and the mass conservation law (Versteeg 2007). The Herschel-Bulkley (H-B) model is typically more appropriate for the rheological characterisation of bentonite slurry (Kök, Batmaz, and Güçüyener 2000) than the Bingham model (Min, Song, and Zhang 2018). The bentonite slurry's rheological characteristics

were described in this work using the H-B rheological model. The following are the rheological equations:

$$(48) \tau = \tau_0 + k\gamma^n \quad (\lvert \tau \rvert > \tau_0) \quad , \quad \gamma = 0 \quad (\lvert \tau \rvert \leq \tau_0) \quad \text{when}$$

τ = shear stress, γ = shear rate, τ_0 = yield stress,

k = viscosity coefficient, n = power law index. The RST-SST Rheometer, manufactured by Brookfield, can be employed to ascertain the correlation between shear stress and shear rate. Furthermore, the bentonite slurry was mixed at 200 rpm for 1 minute prior to conducting the rheological experiments to prevent the slurry sample from settling. 0.886 Pa.sⁿ, 4.598 Pa, and 0.654 are the H-B viscosity coefficient, yield stress, and power law index for the bentonite slurry sample, respectively. These values can be readily entered into the CFD software.

The particle phase, which is represented by the large rocks in the excavation chamber, will be propelled through the slurry, excavation chamber wall, short screw conveyor, and other large rocks during ultra-large-diameter slurry TBM tunnelling in the hard rock strata.

The discrete element method can be employed to solve the transport and collisions of the rock particles in accordance with Newton's second law of motion (Cundall and Strack 1979).

The transport and flow characterisation of rock particles in the slurry chamber are significantly influenced by their size. In accordance with the cutter spacing arrangement of the disc cutter, (Dajun 2008) found that the breadth of the rock chips following cutting typically does not surpass the cutter spacing. The cutter spacing in the actual undertaking ranges from 80 to 130 mm. Therefore, in order to as closely as possible understand the transport and flow characterisation of the rock particles in the dynamic-discrete element modelling (DEM), rock particles with diameters of 80 mm, 100 mm (control group), and 120 mm were established, as illustrated in (Figure 35a). These rock particles were subsequently named SPH80, SPH100, and SPH120, respectively. Additionally, (Mindlin and Deresiewicz 1953) described the contact behaviours between the rock particles and the TBM wall and other rock particles using the Hertz-Mindlin no-slip contact model. The screw pitch PS of 500 mm, 1000 mm (used in the actual project), 1500 mm, and 2000 mm were established to investigate the impact of geometric design (including the screw pitch-to-flight diameter ratio and the installation angle) on the discharging performance of the short screw conveyor, as illustrated in (Figure 35b). And the flight diameters are also 1600 mm. (Figure 35c) depicts the installation angles of short screw conveyors with 16, 26, 36 degrees (used in the project), and 46. (49) $F_b = -\frac{\rho_f}{\rho_p} g$,

$$(50) F_d = \frac{18\mu}{\rho_p d_v^2} \frac{C_p R_{ep}}{24} (U_f - U_p), \quad (51) F_p = -\frac{1}{\rho_p} \Delta p_f, \quad \text{since}$$

ρ_f = density of fluid phase, U_f = velocity of vector fluid phase,

U_p = velocity of vector particle, ρ_p = particle density,

d_v = diameter of the volume sphere, μ = fluid viscosity,

p_f = pressure fluid phase, R_{ep} = Reynolds number of particle,

g = acceleration of gravity, C_D = drag coeff,

(52) $C_D = a_1 + \frac{a_2}{Re} + \frac{a_3}{Re^2}$ $a_1, a_2, a_3 = \text{contacts indicated in the following table:}$

Table 6: Values of a_1 , a_2 , and a_3 within a variety of Re ranges.

Range of Re	a_1	a_2	a_3
$0 < Re \leq 0.1$	0	24	0
$0.1 < Re \leq 1$	3.69	22	0.0903
$1 < Re \leq 10$	1.222	29.1667	-3.8889
$10 < Re \leq 100$	0.6167	46.5	-116.67
$100 < Re \leq 1000$	0.3644	98.33	-2778
$1000 < Re \leq 5000$	0.357	148.62	-47500
$5000 < Re \leq 10000$	0.46	-490.546	578700
$Re \geq 100000$	0.5191	-1662.5	5416700

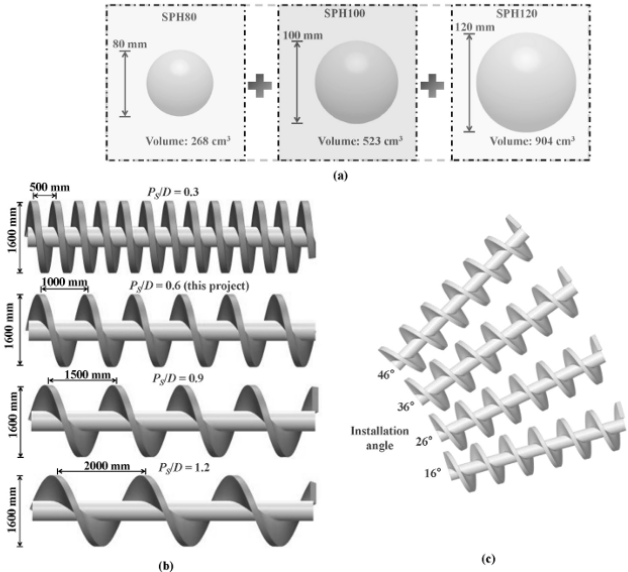


Figure 35: The DEM model includes a particle model, screw pitch-to-flight diameter ratios (PS/D) of 0.3, 0.6 (real project), 0.9, and 1.2, and installation angles of short screw conveyors of 16, 26, 36, and 46.

In the CFD model, fluid zones included the excavation chamber, short screw conveyor, and feeding pipelines. The feeding pipelines consisted of six small branch pipelines at various locations, determined by the actual slurry TBM structure and set to slurry velocity inlet 1×10^6 . Consider rotations of A fixed mesh zone and two fluid zones were created in the CFD mesh for the cutterhead and short screw conveyor flight.

Two interfaces were created between the rotational mesh zone and the fixed mesh zone. To match the DEM model, the rotational mesh zones were made to rotate at a constant speed, and the sliding mesh approach was employed to represent the rotation. Additionally, the fluid mesh has 534807 nodes and 158989 elements. The 1600 mm diameter short screw conveyor exit was installed as a pressure outlet. Reference project values were used to set the velocity inlet and pressure outlet values. The wall boundary was considered non-slip (Guo, Li, Sun, et al. 2023).

The slurry TBM geometric model was created in the DEM model using rigid wall parts based on the geometry provided. Shortscrew conveyor flight and cutterhead rotating speed were set to a constant value using a displacement control approach. Six dynamic particle factories were formed at the cutterhead opening sites (Figure 34), rotating at the same speed. To imitate the process of rock chips entering the excavation chamber from the cutterhead, six particle factories were used to manufacture rock particles at a consistent speed and mass flow rate (depending on TBM advancing rate). The CFD and DEM zones were integrated to create a short screw conveyor for ultra-large-diameter slurry TBMs, actively conveying rock particles.

A significant impact on CFD DEM coupling simulation accuracy and computing effort is the time step used (Washino et al. 2016; M. Wang et al. 2022). (Tsuji, Kawaguchi, and Tanaka 1993) found that fluid phase time steps can be 10e100 times that of particle phases. The study used a fluid time step of 0.001 s and a particle time step of 1×10^{-5} s. (52) $\eta = \frac{Q_t}{Q_t}$,

$$(53) Q_t = rlt(\pi(D^2 - d^2)/4)$$

Q_t = flow rate of rock particles (kg/s) and

Q_t = theoretical mass flow rate of short screw (kg/s)

r = rotational speed of short screw conveyor (rpm),

l = screw pitch (m),

D = flight diameter,

d = screw shaft diameter

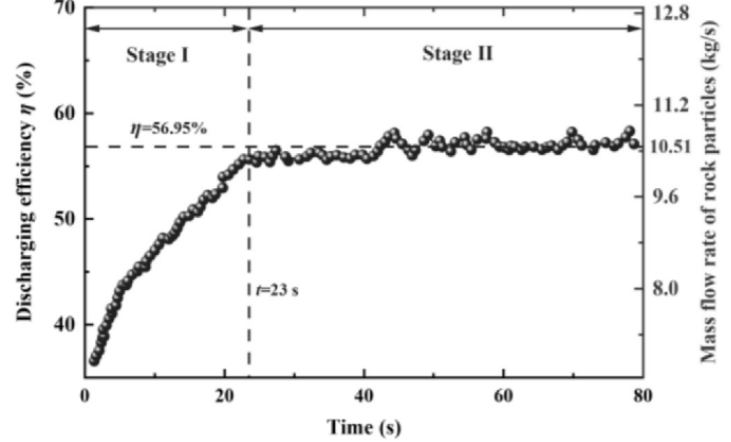


Figure 36: The evolution of the mass flow rate and discharging efficiency η of rock particles.

The discharging efficiency η and mass flow rate of rock particles can be divided into two phases as they vary over time. The discharging efficiency η and mass flow rate of rock particles increase progressively in the first stage until they reach a stable value of approximately 56.95% and 10.51 kg/s at $t = 23$ s. This discharging efficiency is ideal and contributes to the enhancement of construction efficiency. In the second stage, the discharging efficiency η and mass flow rate of rock particles are maintained at stable values over time. It is observed that there is no significant sudden decrease in discharging efficiency after the discharging efficiency is

stabilised, thereby eliminating the possibility of the excavation chamber becoming clogged.

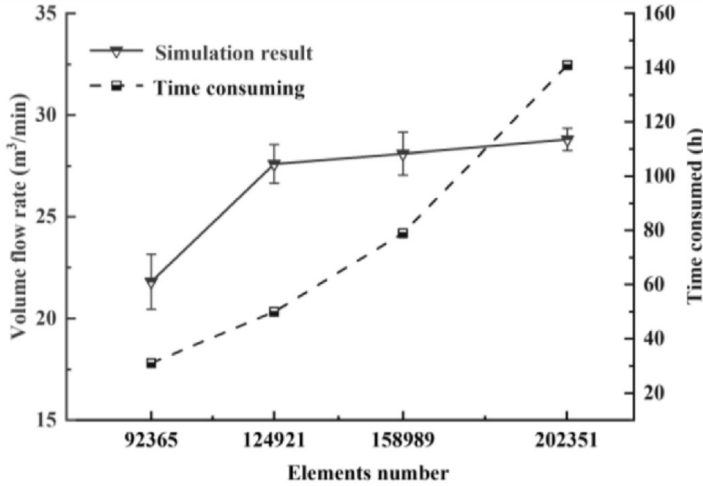


Figure 37: Computational time and simulation results comparisons with varying mesh sizes.

(Figure 38) shows that rock particle velocities are asymmetrically distributed on both sides of the excavation chamber under cutterhead rotation. The left side of the chamber has slightly higher flow characteristics than the right side. High flowability is seen in rock particles at the short screw conveyor input. An area of high fluidity was also seen near the short screw conveyor's inlet as the simulation time increased. This area is brought on by the short screw conveyor's muck discharge.

While rotating the cutterhead, the rock particles tend to ascend from left to right, forming inclined surfaces that slope downward from right to left. This is due to cutterhead rotation. As the cutterhead spun rock particles to a specific height, gravity caused them to fall down to the excavation chamber, creating a high-fluidity zone (red) in (Figure 40) at the short screw conveyor input. Additionally, rock particles near the A12.1, A12.2, and A17.1 slurry pipelines exhibit improved mobility during bentonite slurry flushing.

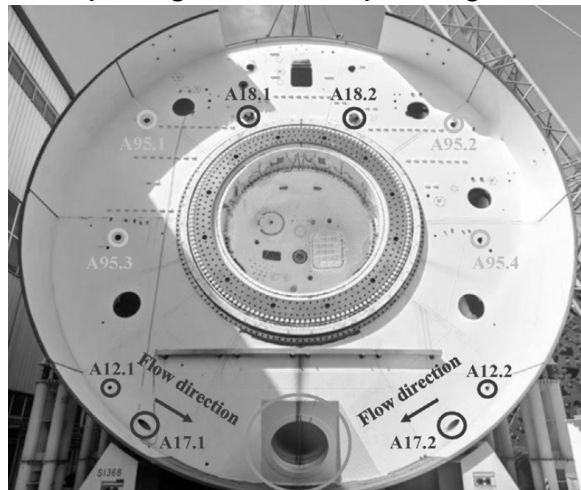


Figure 38: cross section of flow direction to short crew conveyor

Figure 10 shows the velocity distribution of bentonite slurry in the excavation chamber at three instants. Fig. 10 shows similar velocity distribution patterns at three time instants, indicating the impact of the rotating cutterhead on slurry velocity. Research indicates that the slurry feeding pipeline significantly affects slurry velocity distribution, creating an acceleration zone near pipelines A17.1 and A17.2. This is due to their unique inlet orientation, which increases fluidity near the short screw conveyor inlet, facilitating smooth rock transportation. Consider orienting the intake direction of slurry feeding pipelines A17.1 and A17.2 towards the short screw conveyor inlet to enhance flushing flow rate.

Figure 11 shows slurry pressure distribution in the excavation chamber at three instants. According to (Figure 42), the pressure distribution in the excavation chamber is nearly symmetric on both sides. High pressure zones are only seen near the excavation chamber edge due to the revolving cutterhead. The peripheral portion of the excavation chamber showed an increase in total pressure. Total pressure in the excavation chamber remains stable throughout time, indicating that the excavation face is stabilised while the short screw conveyor discharges rock particles.

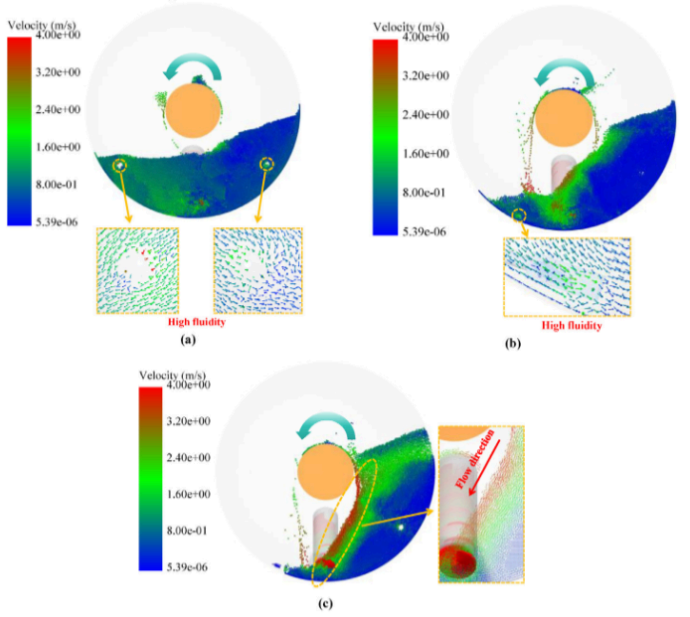


Figure 40: Analysis of rock particle flow in the excavation chamber at three time instants: (a) 15 s, (b) 30 s, and (c) 60 s.

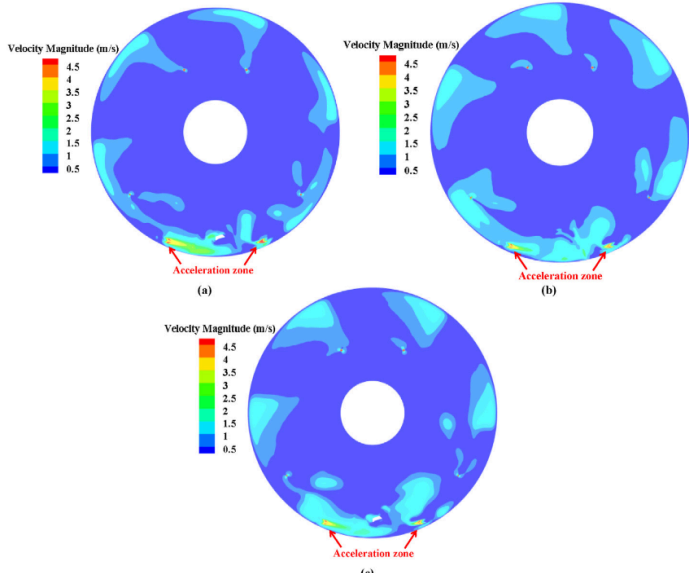


Figure 41: Slurry velocity distribution in the excavation chamber at three time instants: (a) 15 s, (b) 30 s, and (c) 60 s.

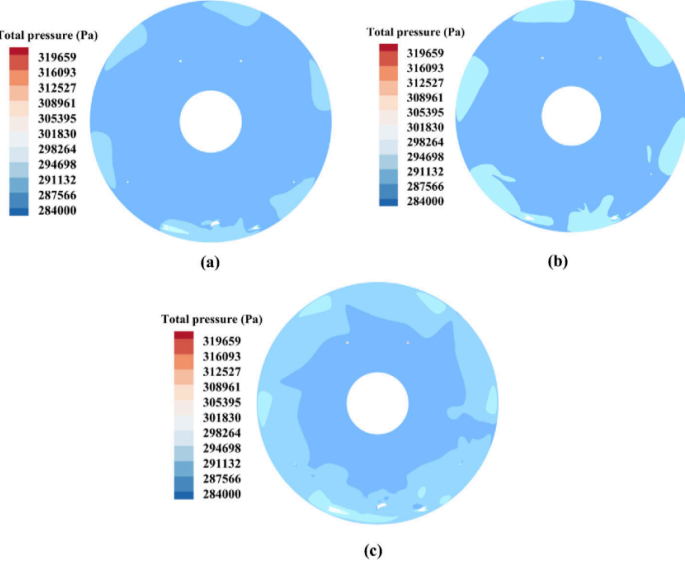


Figure 42: Slurry pressure distribution in the excavation chamber in three time instants: (a) 15 s, (b) 30 s, and (c) 60 s.

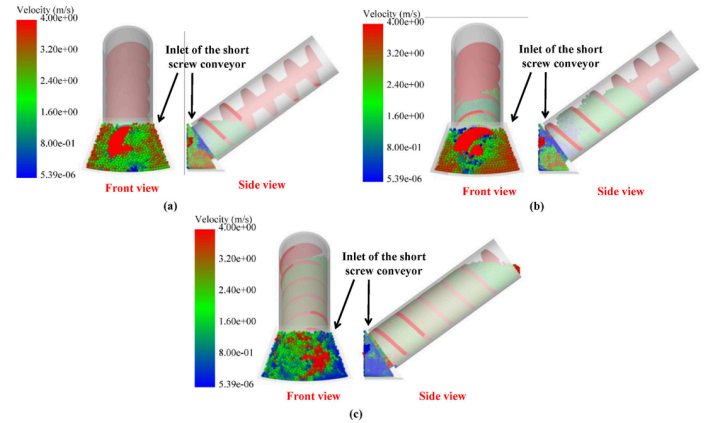


Figure 43: The flow characteristics of rock particles in the large-diameter short screw conveyor were examined at three time instants: (a) 15 s, (b) 30 s, and (c) 60 s

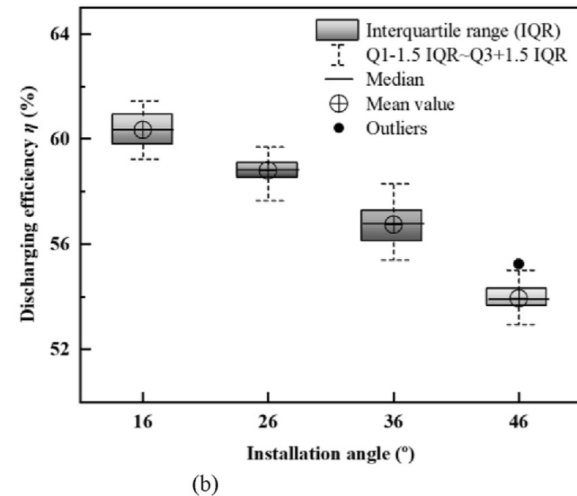
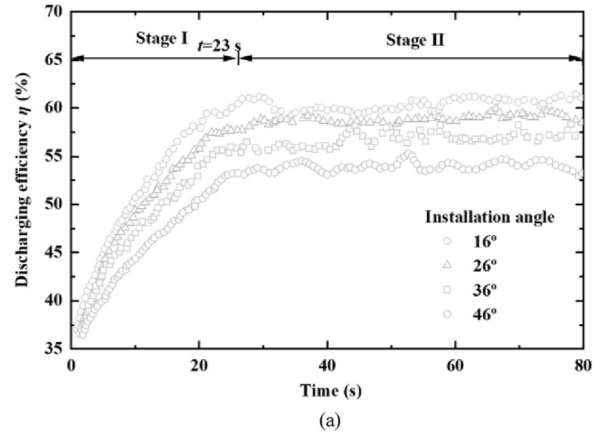


Figure 44: The screw conveyor's discharge efficiency at different installation angles is shown in (a) time histories for four installation angles and (b) a boxplot of the discharge efficiency following stabilisation for four installation angles.

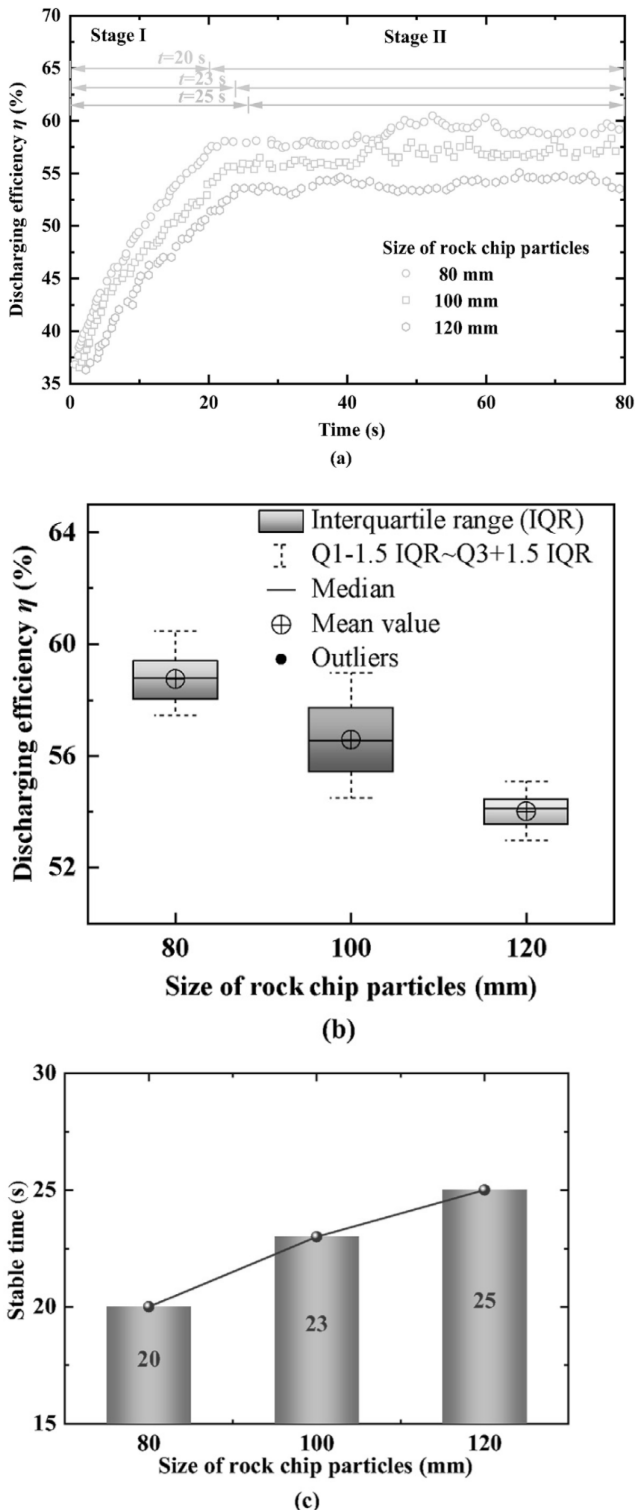


Figure 45: Various rock particle sizes' discharge efficiency is shown in (a) time histories for three sizes, (b) a boxplot of the discharge efficiency following stabilisation for three sizes, and (c) the stable time of the discharge efficiency.

When the TBM travels over high angle shear zones, for example, larger particles have the ability to slip out of the face and perhaps reach the excavation chamber. This is one of the situations in which greater particle sizes may occur. The discharge performance of a short screw conveyor in the aforementioned exceptional instances is worthy of further investigation, and the purpose of this study is to investigate the discharging performance of a short screw conveyor for the purpose of reducing the occurrence of excavation chamber clogging failure during conventional slurry TBM tunnelling.

3.4 Numerous Degrees of Freedom in the Coupling Cutterhead System.

The cutterhead, a critical component of the full-face rock tunnel boring machine (TBM), is responsible for the crushing of rock, the stabilisation of the excavated opening, and other functions. These functions have an impact on the whole machine's efficacy and performance (H. L. Li 2010). In numerous projects, such as the Qinling tunnel, Dahuofang tunnel, and Zhongtianshan tunnel (Zhu, Wang, and Chen 2020) (M. X. Qi, Wang, and Li 2009), cutterheads are subjected to multipoint random impact loads as a result of complex geological conditions and variable tunnelling parameters. As a consequence, certain engineering faults may manifest, including severe vibration, anomalous wear of cutting tools, cracking of the cutterhead panel, and the failure of the main bearing's seal. These faults establish stringent design requirements for the structural strength, reliability, and fatigue life of the cutterhead.

Consequently, the research on the coupled nonlinearity and dynamical characteristics of TBM cutterhead systems with random impact loads is of significant theoretical value and practical significance, as it aims to achieve absorbance of dynamic impact loads, high reliability, a long fatigue life, and superior static and dynamic characteristics.

Numerous studies regarding the design of the TBM cutterhead system have been conducted for an extended period. (Samuel and Seow 1984) investigated the fluctuations in cutter forces during field testing, and they compared the instantaneous forces to the global machine performance. The testing methods were proposed by (Z. X. Zhang, Kou, and Lindqvist 2003) based on the results of the measured cutter forces on a boring machine during fieldboring in a hard rock laboratory. The distribution of cutters is essential for the performance of the cutterhead to be balanced, as per (Jamal Rostami 2008). The hard rock TBM's cutterhead system design methodologies were investigated in accordance with various performance factors. The tunnel machine's energy consumption was evaluated using a specialised energy model (Lihui Wang et al. 2012), (Q. Zhang et al. 2012). Then, the model was implemented by employing the testing data from a metro project to determine the optimal ranges of cutterhead performance under a variety of geological conditions and cutter spaces. The results were then compared to those of a cutting test. The following are examples of comparable works. Additionally, the discrete element method was employed by (Xia et al. 2012), (Tan et al.

2012) to investigate the impact of the results were compared to those of a cutting test, and the influence of cutterhead performance under various geological conditions and cutter spaces was investigated using the discrete element method. The following are examples of comparable works. The dynamic characteristics of a split-cutterhead system with multidegree-of-freedom coupling are comprehensively examined, taking into account the time-varying external excitations, time-varying meshing stiffness, gearbox errors, clearance, and bearing stiffness. The proposed research by (W. Sun et al. 2013) is more effective in resolving complex project problems than conventional design methods and models. This provides a solid foundation for the assessment of the life of fatigue fracture propagation and dynamic performance optimisation of the cutterhead structure.

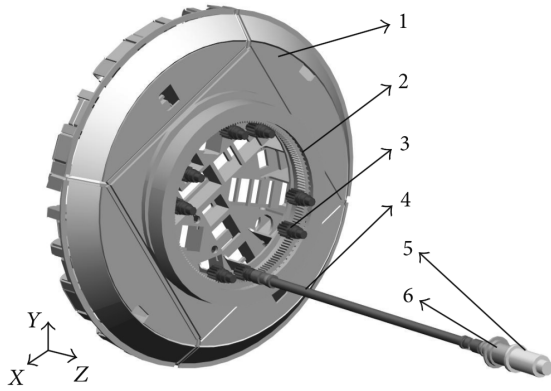


Figure 46: illustrates the components of the TBM cutterhead system. Piece 1: Cutterhead. 2. Primary bearing ring. 3. Pinion. 4. Coupling. 5: Engine. 6. Reducer.

Planetary gear reducers and couplings allow variable-frequency motors to drive the various pinions in the TBM cutterhead system. The cutterhead is driven by the pinions, which spin an inner ring gear clockwise under redundant control. The gear and flange are fastened together with bolts. We only illustrate one motor driving system here, however Figure above shows the whole TBM cutterhead system with all of its components. On the other hand, Figure below shows the TBM split-cutterhead structure.

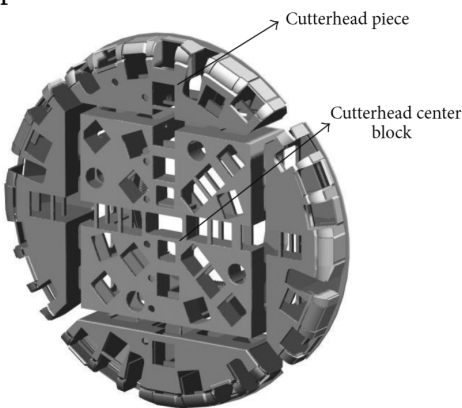
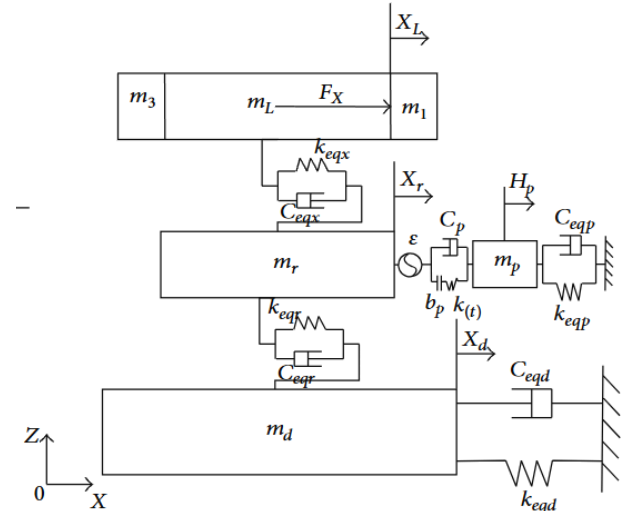


Figure 47: The divided cutterhead structure of a TBM.

In this research, a dynamic mathematical model of the TBM cutterhead system has been established utilising the lumped-parameter method, as detailed herein. The parameters k_{mpQ} and k_{rLQ} represent the torsional stiffness of the gear shaft connections and the cutterhead shaft connection, respectively. The parameters $k_{eqy}, k_{eqL}, k_{eqr}, k_{eqz}, k_{eqd}, k_{eqdz}$ denote the equivalent radial stiffness and axial stiffness of the cutterhead, inner ring gear, and support shield body, respectively. Additionally, k_{eqp} and $k_{(t)}$ correspond to the support equivalent stiffness of the pinions and the time-varying meshing stiffness between the inner ring gear and the pinions, respectively. Lastly, $k_{L\eta i}, k_{L\eta p}$, and k_{Li} signify the equivalent tangential stiffness, radial stiffness, and axial stiffness of each cutterhead piece, respectively. The damping coefficient, denoted as c_{xxx} (where xxx represents the subscript), corresponds to the stiffness in question. The variables $T_{p1}, T_L, F_x, F_y, F_L, M_x$, and F_{Lz} correspond to the input torque, load torque, lateral force, longitudinal force, axial force, as well as the transverse overturning moment of the cutterhead centre block, together with the axial force associated with each cutterhead piece, respectively. b_p represents the blowback between each pinion and the inner ring gear, whereas ε represents the meshing faults. Also, r_{br} and r_{bp} show the inner ring gear and pinions' base circle radii, respectively.



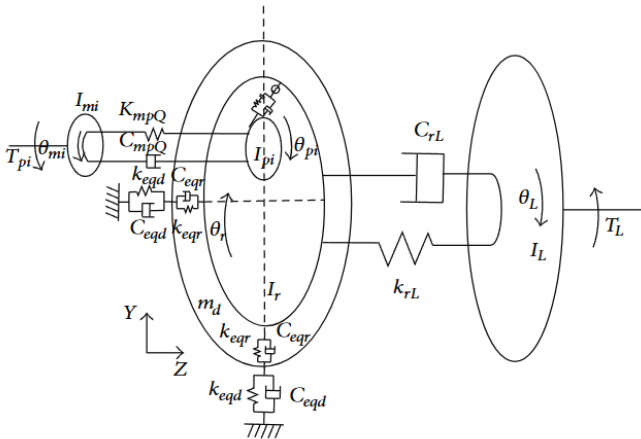


Figure 48 (a): dynamic model coupled with bending torsion of cutterhead system.

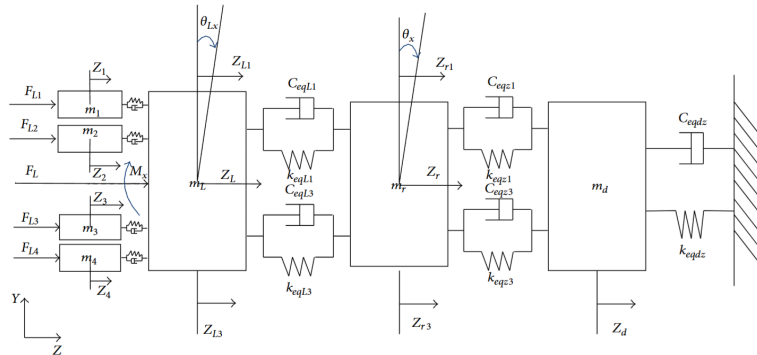


Figure 49 (b): Dynamic model of cutter head system coupled with torsion-axial model

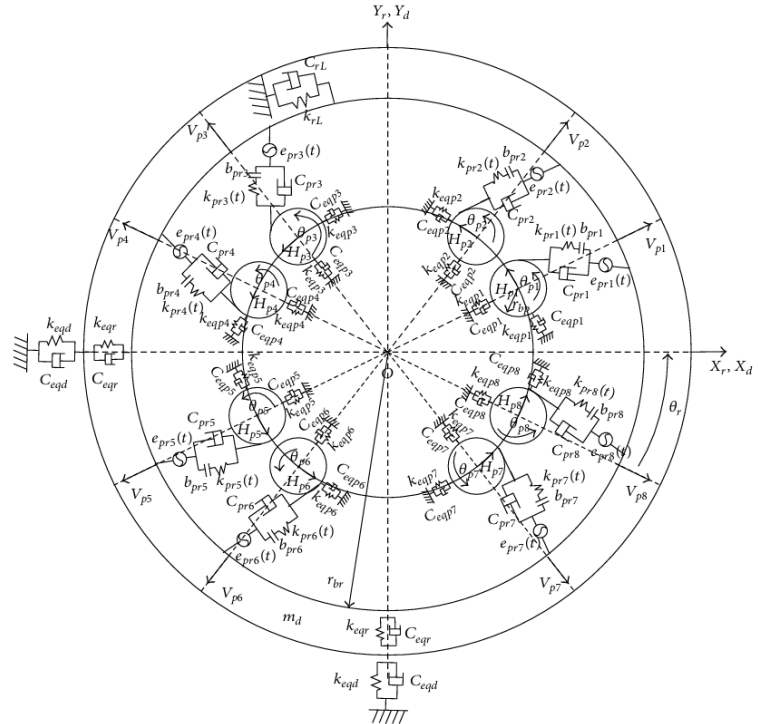


Figure 50: Dynamic model of the TBM cutterhead system with multidegrees of freedom coupling.

In the dynamic model of the cutterhead system previously mentioned, moving coordinate systems are employed for convenient modelling. (Figure 50) illustrates the coordinates, where X , Y , and Z represent the horizontal direction, vertical direction, and tunnelling direction, respectively. The cutterhead, inner ring gear, and support shield body are positioned within this coordinate system.

ζ = radial directions of cutterheads,

η = tangential directions of cutterheads,

H_p = radial directions of pinions, V_p = tangential directions of pinions

. The use of various subscripts serves the purpose of convenient distinction. The subscript i designates the cutterhead components, and the pinions and motors are denoted by p and m , respectively. The cutterhead centre block, inner ring gear, and support shield body are denoted by L , r , and d .

The configuration illustrated in (Figure 50) possesses a total of $(27 + 4N)$ degrees of freedom, with N representing the quantity of pinions involved. The generalised vibration displacement is represented as

$X = (\zeta_i, \eta_i, Z_i, X_L, Y_L, Z_L, \theta_{Lx}, \theta_{Ly}, \theta_{Lz}, X_r, Y_r, Z_r, \theta_{rx}, \theta_{ry}, \theta_r, X_d, Y_d, Z_d)^T$. In this representation, ζ_i , η_i , and Z_i are the vibration displacement of each cutter head. X_L , Y_L , and Z_L represent the translational vibration displacements. The parameters θ_{Lx} and θ_{Ly} denote the bending vibration displacements in the X and Y directions, respectively, while θ_L indicates the torsional vibration displacement in the centre block. X_r , Y_r , Z_r , θ_{rx} , θ_{ry} , and θ_r represent the respective vibration displacements of the inner ring gear. X_d , Y_d , and Z_d represent

the translational vibration displacements of the support shield body. H_{pj} and V_{pj} are the transverse and longitudinal vibration displacements of the mass centre of each pinion, respectively. θ_{pj} = torsional vibration displacements of each pinion, while θ_{mj} = displacements caused by torsional vibrations in every motor. The Coriolis forces accelerometer's low cutterhead speeds. In published models, both rotations and centripetal accelerations are disregarded. The differential equations for each component are presented below, derived from Lagrange's equation.

For

$$(54) I_{mj} \ddot{\theta}_{mj} + C_{mpQ}(\theta_{mj} - \theta_{pj}) + k_{mpQ}(\theta_{mj} - \theta_{pj}) = T_{pj}, \quad \text{Pinions:}$$

$$(55) I_{pj} \ddot{\theta}_{pj} + (F_{prj} + D_{prj})r_{bp} +$$

$$C_{mpQ}(\theta_{pj} - \theta_{mj}) + k_{mpQ}(\theta_{pj} - \theta_{mj}) = 0,$$

$$m_{pj} \ddot{H}_{pj} + (F_{prj} + D_{prj})\cos\alpha + C_{eqpj}H_{pj} + k_{eqpj}H_{pj} = 0,$$

$$m_{pj} \ddot{V}_{pj} + (F_{prj} + D_{prj})\sin\alpha + C_{eqpj}V_{pj} + k_{eqpj}V_{pj} = 0, \quad x_{prj} = \text{displacement between each pinnion and dynamic inner gear ring}$$

expressed as:

$$(56) x_{prj} = r_{bp} \theta_{pj} - r_{br} \theta_r + V_{pj} \sin\alpha + H_{pj} \cos\alpha + X_r \sin(\alpha + \varphi_j)$$

$- Y_r \cos(\alpha + \varphi_j) - \varepsilon_{prj}(t)$, $\varepsilon_{prj}(t)$ ($j = 1 -$) known fo the system errr excitations, α for meshing angle, φ_j for azimuth angle for each pinnion. (57) $F_{prj} = k_{prj}(t) \cdot f(x_{prj}, b_{prj})$, the nonlinear function of $f(x, b)$ can be expressed as:

$$(58) f(x, b) = \begin{cases} x - b & x > b \\ 0 & -b \leq x \leq b \\ x + b & x < -b \end{cases}$$

(59) $D_{prj} = C_{prj} \cdot \dot{x}_{prj}$ since D_{prj} = damping force , for inner ring

$$(60) m_r \ddot{X}_r + \sum_{j=1}^N (F_{prj} + D_{prj}) \sin(\varphi_j + \alpha) + C_{eqr}(X_r - X_d) + C_{eqx}(X_r - X_L) + k_{eqr}(X_r - X_d) + k_{eqx}(X_r - X_L) = 0$$

$$m_r \ddot{Y}_r + \sum_{j=1}^N (F_{prj} + D_{prj}) \cos(\varphi_j + \alpha) + C_{eqr}(Y_r - Y_d) + C_{eqy}(Y_r - Y_L) + k_{eqr}(Y_r - Y_d) + k_{eqx}(Y_r - Y_L) = 0$$

$$m_r \ddot{Z}_r + \sum_{i=1}^4 [C_{eqLi}(Z_{ri} - Z_{li}) + C_{eqzi}(Z_{ri} - Z_d)] + k_{eqLi}(Z_{ri} - Z_{li}) + k_{eqzi}(Z_{ri} - Z_d) = 0$$

$$+ k_{eqLi}(Z_{ri} - Z_{li}) + k_{eqzi}(Z_{ri} - Z_d) = 0$$

$$I_{rx} \ddot{\theta}_x + r_r [C_{eqL1}(Z_{r1} - Z_{L1}) - C_{eqL3}(Z_{r3} - Z_{L3}) + C_{eqz1}(Z_{r1} - Z_d) - C_{eqz3}(Z_{r3} - Z_d)] +$$

$$r_r [K_{eqL1}(Z_{r1} - Z_{L1}) - k_{eqL3}(Z_{r3} - Z_{L3}) + k_{eqz1}(Z_{r1} - Z_d) - k_{eqz3}(Z_{r3} - Z_d)] = 0,$$

$$I_{ry} \ddot{\theta}_y + r_r [C_{eqL2}(Z_{r2} - Z_{L3}) - C_{eqL4}(Z_{r4} - Z_{L4}) + C_{eqz2}(Z_{r2} - Z_d) - C_{eqz4}(Z_{r3} - Z_d)] +$$

$$+ C_{eqz2}(Z_{r2} - Z_d) - C_{eqz4}(Z_{r3} - Z_d) +$$

$$r_r [k_{eqL2}(Z_{r2} - Z_{L2}) - k_{eqL4}(Z_{r4} - Z_{L3}) + k_{eqz2}(Z_{r2} - Z_d) - k_{eqz4}(Z_{r4} - Z_d)] = 0$$

$$I_r \ddot{\theta}_r - \sum_{j=1}^N (F_{prj} + D_{prj})r_{br} + C_{rLQ}(\theta_r - \theta_L) + k_{rLQ}(\theta_r - \theta_L) = 0,$$

Regarding cutter head centre block:

$$(61) m_L \ddot{X}_L - \sum_{i=1}^4 [(k_{L\zeta i} \delta_{1\zeta i} + C_{L\zeta i} \delta_{L\zeta i}) \sin(\omega t + \varphi_i) + (k_{L\eta i} \delta_{L\eta i} + C_{L\eta i} \delta_{L\eta i}) \cos(\omega t + \varphi_i) + K_{eqx}(X_L - X_r) = F_x, \quad m_L \ddot{Y}_L - \sum_{i=1}^4 [(k_{L\zeta i} \delta_{1\zeta i} + C_{L\zeta i} \delta_{L\zeta i}) \cos(\omega t + \varphi_i) + (k_{L\eta i} \delta_{L\eta i} + C_{L\eta i} \delta_{L\eta i}) \sin(\omega t + \varphi_i) + K_{eqy}(Y_L - Y_r) = F_y, \quad m_L \ddot{Z}_L + \sum_{i=1}^4 [(C_{Li}(Z_{Li} - Z_i) + k_{Li}(Z_{Li} - Z_i) + C_{eqLi}(Z_{Li} - Z_i) + K_{eqLi}(Z_{Li} - Z_{ri}) = F_{L_i}, \quad I_{Lx} \ddot{\theta}_{Lx} + a_L [C_{L1}(Z_{L1} - Z_1) - C_{L3}(Z_{L3} - Z_3) + k_{L1}(Z_{L1} - Z_1) - k_{L3}(Z_{L3} - Z_3)] + r_r [C_{eqL1}(Z_{L1} - Z_{r1}) - C_{eqL3}(Z_{L3} - Z_{r3}) + k_{eqL1}(Z_{L1} - Z_{r1}) - k_{eqL3}(Z_{L3} - Z_{r3})] = M_x, \quad I_{Ly} \ddot{\theta}_{Ly} + a_L [C_{L2}(Z_{L2} - Z_2) - C_{L4}(Z_{L4} - Z_4) + k_{L2}(Z_{L2} - Z_2) - k_{L4}(Z_{L4} - Z_4)] + r_r [C_{eqL2}(Z_{L2} - Z_{r2}) - C_{eqL4}(Z_{L4} - Z_{r4}) + k_{eqL2}(Z_{L2} - Z_{r2}) - k_{eqL4}(Z_{L4} - Z_{r4})] = M_y, \quad I_L \ddot{\theta}_L + C_{rLQ}(\theta_L - \theta_r) + k_{rLQ}(\theta_L - \theta_r) = -T_L]$$

For support shield body:

$$(62) m_d \ddot{X}_d + C_{eqr}(X_d - X_r) + C_{eqd}X_d + k_{eqr}(X_d - X_r) + k_{eqd}X_d = 0, \quad m_d \ddot{Y}_d + C_{eqr}(Y_d - Y_r) + C_{eqd}Y_d + k_{eqr}(Y_d - Y_r) + k_{eqd}Y_d = 0, \quad m_d \ddot{Z}_d + C_{eqz1}(Z_d - Z_{r1}) + C_{eqz2}(Z_d - Z_{r1}) + C_{eqz3}(Z_d - Z_{r3}) + C_{eqz4}(Z_d - Z_{r4}) + k_{eqz1}(Z_d - Z_{r1}) + k_{eqz2}(Z_d - Z_{r2}) + k_{eqz3}(Z_d - Z_{r3}) + k_{eqz4}(Z_d - Z_{r4}) + k_{eqdz}Z_d = 0.$$

Model for cutter head pieces:

$$(63) m_i \ddot{\zeta}_i + k_{L\zeta i} \delta_{L\zeta i} + C_{L\zeta i} \delta_{L\zeta i} = F_{\zeta i}, \quad m_i \ddot{\eta}_i + k_{L\eta i} \delta_{L\eta i} + C_{L\eta i} \delta_{L\eta i} = F_{\eta i}, \quad m_i \ddot{Z}_i + k_{Li} (Z_i - Z_{li}) + C_{Li} (Z_i - Z_{li}) = F_{Li} \quad \text{since}$$

F_{Li} = axial force of cutter head, $F_{\eta i}$ = normal force,

$F_{\zeta i}$ = tangential force,

$\delta_{L\zeta i}$ = tangential deformations between cutter head

and central block.,

$\delta_{L\eta i}$ = radial deformations between cutter head and central block.

(64) $\delta_{L\zeta i} = \zeta_i - X_L \sin\varphi_i + Y_L \cos\varphi_i$, $\delta_{L\eta i} = \eta_i - X_L \sin\varphi_i + Y_L \cos\varphi_i$

since φ_i = azimuth angle for each cutter head and four pieces are evenly distributed, $\varphi_i = \pi(i-1)/2$ ($i = 1 - 4$). Based on the

above discussions, it is important to note that the assembly of the system equations in matrix form of yields (65) $MX^+ + CX^+ + KX = F$

Dynamic excitation for cutter head system in TBM consist of two types:

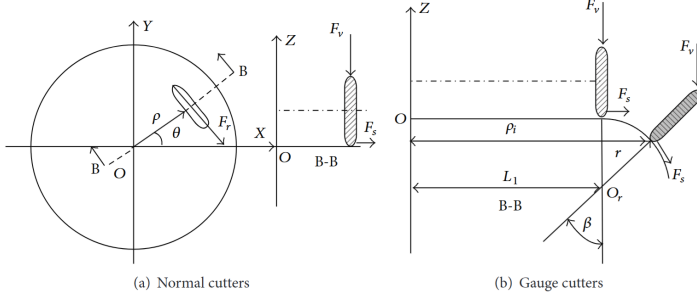


Figure 51: Forces acting on a gauge cutter and a standard cutter (W. Sun et al. 2011)

External Excitation are contingent upon the time variability of the parameters of the disc cutters' layout, geological conditions, tunnelling parameters, and so forth. Based on the field data, the dynamic loads between disc cutters and the neighbouring rock are determined and adjusted (Samuel and Seow 1984)

As a result, the TBM cutterhead system's total loads are determined by aggregating the individual force contributions of each cutter, which can be supplied to the dynamic model's external excitations. The mean normal force, which is 0.15 times the mean tangential force and 0.1 times the mean side force, is equivalent to the nominal load of the disc cutter when taking into account the complexity of actual rock breaking loads (Z. X. Zhang, Kou, and Lindqvist 2003).

Disregarding the losses in the transfer process, the total loads on the cutterhead correspond to the resultant force exerted by each disc cutter. It is shown in Figure above that when the cutterhead turns, the disc cutters experience normal forces F_v , tangential forces F_r , and side forces F_y . Here, ρ is the radius from the centre of the cutterhead, θ is the position angle of the cutter, and β is the tilt angle of the gauge cutter. To facilitate load calculations, the assumptions are articulated as follows regarding Axial force and radial forces.

Axial Forces: (66) $F_L = \sum_{i=1}^n F_{vi} + \sum_{j=1}^m F_{vj} + \sum_{k=1}^p (F_{vk} \cos \beta_k + F_{sk} \sin \beta_k)$, F_{vi} ($i = i, j, k$) representing the normal forces of the center cutter, normal cutters and gauge cutters respectively. F_{sk} = side force of k^{th} gauge cutter, n = number of center cutter, m = normal cutter, p = gauge cutter respectively. β_k = tilt angle of k^{th} F_{Li} can be calculated by (67) however different number of discs apply.

Radial Forces compromising lateral force and longitudinal force expressed as follow respectively: (67) $F_X = F_{vx\Sigma} + F_{rx\Sigma} + F_{sx\Sigma}$ since

$$F_y = F_{vy\Sigma} + F_{ry\Sigma} + F_{sy\Sigma}$$

$F_{vx\Sigma}$ = resultant force of normal forces and

$F_{rx\Sigma}$ = tangential forces, $F_{sx\Sigma}$ = side forces in X direction same for the Y direction. $F_{\zeta i}$, $F_{\eta i}$ are calculated by (68) with similar approach. Due to the load of the central block the overturning moment can be established as bellow:

$$(68) M_X = \sum_{i=1}^n F_{vi} l_{ix} + \sum_{j=1}^m F_{vj} l_{jx}, M_Y = \sum_{i=1}^n F_{vi} l_{iy} + \sum_{j=1}^m F_{vj} l_{jy} \text{ since } l_x, l_y$$

represents the distance to X, Y axis of the t^{th} cutter when $t = i, j$. The torque load is produced by the tangential forces, which correspond to the resultant torque of each tangential force about the Z axis through the following:

$$(69) T_L = \sum_{i=1}^n F_{ri} \rho_i + \sum_{j=1}^m F_{rj} \rho_j + \sum_{k=1}^p F_{rk} \rho_k \text{ as } T_{pi} = 1/N(\text{load torque})$$

without considering the power loss.

Temporal Fluctuation Stiffness of Gear Pair Engagement The meshing stiffness of spur gears has a clear step periodicity that changes abruptly when the degree of coincidence is non-integer, leading to the generation of dynamic excitation forces (J. Liu et al. 2014). GB3480-1997 offers a method to determine both the maximum and mean meshing stiffness. The variation in meshing stiffness can be depicted by a series of square wave functions. Ultimately, it is represented in a Fourier series without higher-order terms as follows:

$$(70) k(t) = k_m + \sum_{i=1}^n [k_{pi} \sin(iwt) + k_{ci} \cos(iwt)],$$

ω = meshing frequency

n = harmonic number of meshing stiffness,

k_m = mean of meshing stiffness,

k_{pi} = sinusoidal amplitude of the i^{th} order, k_{ci} = cosine amplitude.

Harmonic functions can be used to model the error excitations (J.-X. Zhou, Liu, and Ma 2011). These are the primary errors taken into account in this study: the eccentric error E_{pj} , the manufacturing error E_r , the installation error A_r , the tooth thickness deviation ε_{pj} , and the profile error δ_{pj} in the inner ring gear, with the corresponding parameters in the pinions A_{pj} , ε_{pj} and δ_{pj} . Consequently, the internal meshing line and the equivalent accumulated error caused by the aforementioned defects are expressed as (71) $\varepsilon_{pj}(t) = E_r \sin(\omega_r t + \alpha + \varphi_j - \beta_r) + A_r \sin(\alpha + \varphi_j - \gamma_r) + E_{pj} \sin(\omega_p t + \alpha - \beta_{pi}) + A_{pj} \sin(\alpha - \gamma_{pj}) + \varepsilon_r + \varepsilon_{pj} + \sigma_r + \sigma_{pj}$, ($j = 1 - 8$), α = meshing angle, β and γ = phase angle of errors,

ω_p = angular velocity of pinion, ω_r = ring gear. The radial load is supported by each pinion, and the equivalent stiffness of the support is determined using the following empirical formula (Chao et al. 2017): (72) $K_r = 0.34 \times 10^4 F_r^{0.1} Z^{0.9} l^{0.8} (\cos \beta)^{1.9}$ since F_r = radial load, Z = number of rollers,

l = effective contact length of rollers

β = contact angle of rollers. The torsional stiffness of shaft couplings can be articulated as per the Mechanics of Materials.

(73) $k_Q = \frac{G I_p}{L}$ Since I_p = moment inertia, G = shear modulus, L = length of shaft connections. The axial stiffness is defined for radial-thrust bearings, which include positive and negative thrust rollers (Luo and Luo 2009). (74) $F_a = K_n Z(\sin\Psi)^{n+1} \delta_a^n$,

$K_a = \frac{dF_a}{d\delta_a} = n K_n Z(\sin\Psi)^{n+1} \delta_a^{n-1}$, $K_n = 2.89 \times 10^4 l_e^{0.82} D_\omega^{0.11}$, where F_a is the axial load of the bearing, n is equal to 1.11 about the roller bearing, K_n is the stiffness coefficient, Z is the number of rollers, Ψ is the contact angle of rollers, δ_a is the axial displacement of the bearing, l_e is the effective contact length of rollers, and D_ω is the effective diameter of rollers. The empirical formula that follows is used to calculate the meshing damping

coefficient (Xiao et al. 2024): (75) $C_{pr} = 2\zeta \sqrt{\frac{k(t)m_1 m_2}{(m_1 + m_2)}}$, $\zeta = 0.03 - 0.17$ representing the damping ratio in the following study it is considered to be 0.03. The torsional

damping of the shaft is represented as: (76) $C_Q = 2\xi_Q \sqrt{\frac{k_Q I_m I_p}{(I_m + I_p)}}$

when ξ_Q = torsional damping ratio = 0.005 – 0.007. The stiffness of additional components, including the cutterhead and support shield body, is determined through the application of the finite element method (FEM). The damping coefficient is determined using the following formula (Huo et al. 2015): (77) $c = 2\xi \sqrt{m k}$. In this context, ξ represents the damping ratio, which ranges from 0.02 to 0.05 during the elastic stage of the steel, with this study utilising a value of 0.02. Additionally, m_e and k_e denote the equivalent mass and equivalent stiffness, respectively.

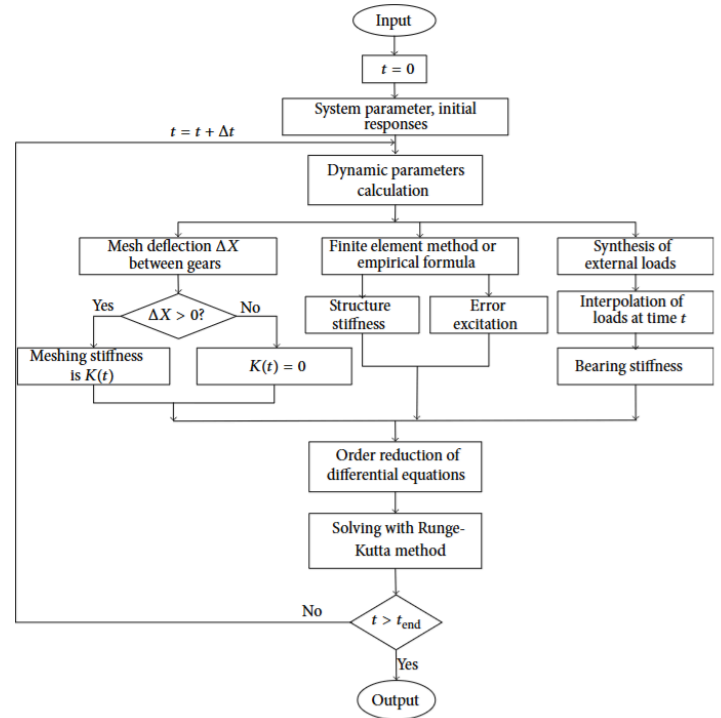


Figure 52: Flowchart illustrating the solution of the dynamic model.

The TBM cutterhead system's multidegree-of-freedom coupling dynamic model is introduced. The structural modal characteristics and dynamic responses are examined in light of the cutters' forces and the actual project's parameters. The following is a summary of the key findings:

(1) The cutterhead system's lowest fifteen natural vibration modes are divided into three categories: rigid mode, pinion and motor rotational vibration modes, and translational and overturning coupled cutterhead and inner ring gear vibration modes. The corresponding natural frequencies are 57 Hz and 61 Hz, respectively, and are higher than the pinion rotation frequency and the internal excitation meshing frequency. However, because natural frequencies and external excitations coincide, the cutterhead system's resonance can be unavoidable.

(2) With the same magnitude of amplitude in each translational direction, the cutterhead's vibration responses resemble the variation of external excitations. The axial amplitude is approximately 0.55 mm, the radial amplitude is nearly 0.25 mm, the angular amplitude around the X and Y axes is approximately 0.016 mrad, and the torsional amplitude is nearly 0.065 mrad.

(3) The findings could serve as a guide for the cutterhead drive system design and the support rib weld strength check. Dynamic response frequencies are primarily focused in the following ranges: 100–120 Hz, 224 Hz, 236 Hz, 390 Hz, and 693 Hz. Additionally, it is advised that when performing the cutterhead's structural design and matching the boring

parameters, the two frequencies of 112 Hz and 120 Hz be avoided.

(4) It is demonstrated that the cutterhead joint surface loads vary quickly with significant amplitudes and complicated nonlinear features when taking into account the influence of internal and external excitations. As evidenced by the rain flow results, the standard deviation in each direction increases by 12–15 times. Cutterhead structural design should primarily take the amplifying effect of dynamic loads into account in order to set the stage for dynamic optimisation and fatigue life assessment.

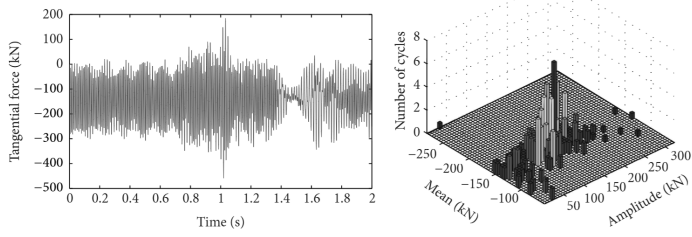


Figure 53: Graph illustrating time history of tangential force and rain flow counting statistics of the force.

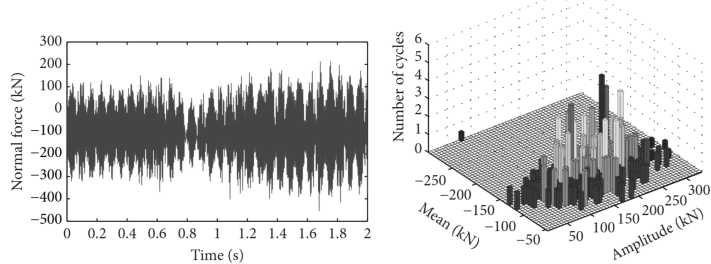


Figure 54: Time history of the normal force and rain flow counting of the statistics of the force.

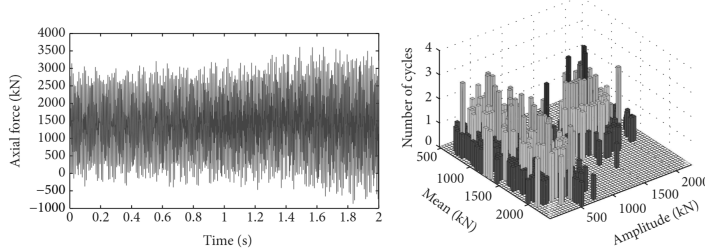


Figure 55: Time histories varying and statistics results of the cutterhead joint surface loads.

Table 7: Statistical distribution of loads on the cutterhead joint surface.

Joint Surface loads	External excitations	
	Mean/kN	Standard deviation/kN
Tangential	-139.69	93.25
Normal	-106.27	130.03
Axial	1410.55	915.48
	139.66	7.40
	106.32	11.04
	1410.55	60.00

Load sharing and dynamic analysis of pinnions and gears in TBM

In order to conduct excavation, the TBM employs numerous pinion actuators. Nevertheless, TBM can also result in an imbalance in the distribution of driving torque. Concurrently, the TBM is subjected to radial force, axial force, and overturning moment as a result of the intricate and diverse geological conditions. The slew bearing experiences elastic deformation as a result of the external load applied by the cutter head during tunnelling. Due to multi-point meshing, deformation induces displacement perturbation in the driven gear and ring gear of a slew bearing. The complex geological conditions of tunnelling can easily lead to a blocking accident, which can also result in fracture phenomena in tiny gear shafts and gear teeth (Ramoni and Anagnostou 2011) (Ding, Tu, and Wang 2010). Due to the compatibility of deformation, a cutter head system is a complex, time-varying, and robust coupling system. This movement is alleviated by multi-pinion actuators and nonlinear elements, such as periodic time-varying stiffness and backlash (Kahraman 1993) (Cheng and Lim 2003). In multi-mesh gear systems, parametric instabilities and server vibrations can be caused by periodic mesh stiffness (K.-Z. Zhang et al. 2011) (G. Liu 2007).

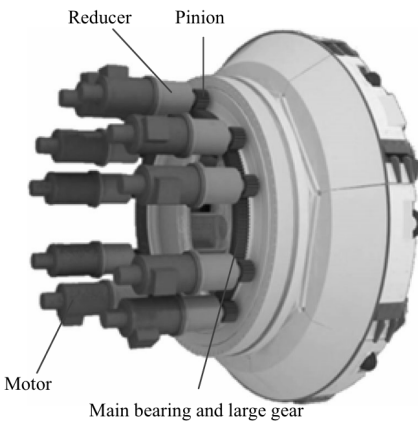


Figure 56: Cutter head of a TBM mechanical driving components (W. Sun, Wang, et al. 2016).

In addition to frequency conversion (Wei et al. 2013) have determined that adjusting the speed in response to the external load fluctuations using a variable-frequency motor, the cutter head drive torque endures a dynamic process in the wave tunnelling torque load of the composite strata. The torque from the cutter head drive induces asynchronous movement in the drive motors, resulting in the breakdown of critical components. The utilisation of a motor-planetary speed reducer results in an increase in the device's inertia. The inertia of the motor-planetary speed reducer causes the load-sharing behavior of multiple pinion drives in shield tunneling to differ from that of traditional wheel and pinion systems used in low-speed transmissions. When performing dynamic modeling and analysis of the multi-gear drive, it is essential to consider the inertia of both the motor-planetary speed reducer and the cutter head rotation for systems with multiple pinions (Wei et al. 2013).

3.5 Multi pinion drivers model

The analysis incorporates the nonlinear coupling effects between the ring gear and the multiple pinions to examine the dynamic load-sharing characteristics. Insights gained from this analysis support gear design improvements and enhance the synchronized control of multi-pinion systems. Four primary drive motors use a planetary system to power the multiple pinion drive system. The pinions propel the inner ring gear, which then drives the cutter head. The multiple pinion drive system satisfies grade 6 precision standards. Gear backlash has an average value of 250 μm . The ring gear has a pitch circle diameter of 1164 mm, while the pinion has a diameter of 180 mm. The rotating mechanism is powered by many pinions that rotate the ring gear in a clockwise direction. When the input power at each pinion is $iP(i = 1 - N)$, the power accumulated in the ring gear is ΣP_i . When the input speed of each pinion is n_p , the input torque for each pinion is $T_{ini} = T_{pi}$, and the load torque on the ring gear is $T_{out} = T_r$.

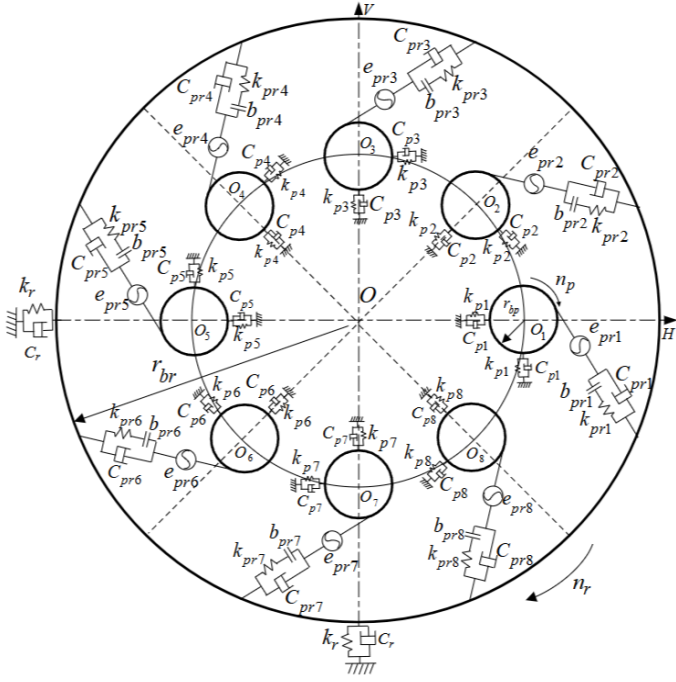


Figure 57: Dynamic model equivalent for the sheer torsion of multiple pinion drives (Wei et al. 2013).

The ring gear and pinions are considered floating elements, while each component of the main drive rotation system is considered a rigid body (Figure 57). The equivalent spring stiffness is used to depict the elastic deformation of support shafts, gears, and bearings. The $k_{pri}(t)$ variable represents the time-varying stiffness that exists between the pinions and the ring gear. For pinions and ring gear, k_{pi} and k_r denote the equivalent spring stiffness support, respectively. The suspension coefficient between the ring gear and pinions is denoted by C_{pri} . The suspension coefficient of the pinions and

the ring gear are represented by C_{pi} and C_r , respectively. The internal meshing line generates equivalent time-varying and accumulated meshing errors, which are denoted by $e_{pri}(t)$. b_{pri} is the expression of the backlash in the ring gear and pinions. The ring gear and pinions' base circle radius are denoted by r_{br} and r_{bp} , respectively. On the basis of the equivalent dynamic model, an equivalent dynamic model of pure torsion for multiple pinion drives evaluates the impact of inertia on the drive and cutter head. The input torque in each pinion is denoted as T_{in} , while the load torque in the cutter head is denoted as T_{out} . Where N is the number of pinions, the system depicted in Figure above has a degree of freedom of $(4N + 4)$.

(78) $x_{pri} = r_{bp}\theta_{pi} - r_{br}\theta_r + \xi_i \sin \alpha + n_i \cos \alpha + H_r \sin(\alpha + \varphi_i) - e_{pri}(t)$ since $\alpha = \text{angle of pressure at pitch of cylinder}$, $\varphi_i = \text{phase angle at each pinion}$, when

$2b_{pri} = \text{gear backlash of each pinion and ring gear}$,

(79) $F_{pri} = k_{pri}(t) \cdot f(x_{pri}, b_{pri})$, the nonlinear function of $f(x, b)$ can be expressed as (58) discussed in section 3.4 regarding the numerous degree of freedom for the coupling head system in TBM.

(80) $D_{pri} = C_{pri} \cdot \dot{x}_{pri}$ since $D_{pri} = \text{damping force}$,

(81) $k_{pri}(t) = k_m + \sum_{n=1}^N (a_n \cos n\omega_0 t + b_n \sin n\omega_0 t)$, as

$\omega_0 = \text{meshing fundamental gear frequency}$,

$k_m = \text{average gear meshing stiffness}$ can be found within gear standards as AGMAISO 1328-1 and DIN3990.

$a_n = \text{expansion coeff of fourier series}$,

$b_n = \text{subscript } n \text{ of } a_n \text{ and } b_n \text{ when } n = 1, 2, 3..N$,

(82) $c_{pri} = 2\xi_g \sqrt{\frac{k_m m_p m_r}{m_p + m_r}}$, $c_{pri} = \text{meshing of gear damping}$,

$\xi_g = 0.03 - 0.17$, the differential equation comes as the following:

$$\begin{aligned}
 & I_{mi} \ddot{\theta}_{mi} + C_{mpQ}(\dot{\theta}_{mi} - \dot{\theta}_{pi}) + k_{mpQ}(\theta_{mi} - \theta_{pi}) = T_{pi} \\
 & I_{mi} \ddot{\theta}_{mi} + (F_{pri} + D_{pri})r_{bp} + C_{mpQ}(\dot{\theta}_{pi} - \dot{\theta}_{mi}) + k_{mpQ}(\theta_{pi} - \theta_{mi}) = 0 \\
 & m_{pi} \ddot{\xi}_i + (F_{pri} + D_{pri}) \sin \alpha + C_{pi} \ddot{\xi}_i + k_{pi} \xi_i = 0 \\
 & I_L \ddot{\theta}_L + C_{rLQ}(\dot{\theta}_L - \dot{\theta}_r) + k_{rLQ}(\theta_L - \theta_r) = -T_r \\
 & I_r \ddot{\theta}_r - \sum_{i=1}^N (F_{pri} + D_{pri})r_{br} + C_{rLQ}(\dot{\theta}_r - \dot{\theta}_L) + k_{rLQ}(\theta_r - \theta_L) = 0 \\
 & m_r H_r \ddot{r} + \sum_{i=1}^N (F_{pri} + D_{pri}) \sin(\varphi_i + \alpha) + C_r H_r + k_r H_r = 0 \\
 & m_r V_r \ddot{r} - \sum_{i=1}^N (F_{pri} + D_{pri}) \cos(\varphi_i + \alpha) + C_r V_r + k_r V_r = 0
 \end{aligned}$$

Since I_m, I_p, I_r, I_L = moment of inertia regarding motor-planetary speed reducer, pinion, ring gear, cutter head. And $\theta_m, \theta_p, \theta_r, \theta_L$ = torsional vibration displacement,

k_{mpQ} = torsional displacement of the input gear shaft,

k_{rLQ} = stiffness of the output gear shaft,

C_{mpQ} = torsional damping coefficient input gear,

C_{rLQ} = output ring gear, so (84) $mx'' + cx' + kx = F$,

x = vector of vibration displacement, m = mass matrix,

k = stiffness matrix, c = damping matrix,

F = incentive force vector

The eccentric error of pinions E_{pi} , manufacturing error of ring gear E_r , installation error of pinions A_{pi} and ring gear A_r , tooth thickness deviation of pinions ε_{pi} and ring gear ε_r , and profile error of pinions σ_{pi} and ring gear σ_r are the errors that affect the load distributions between pinions and the ring gear. Expression of the equivalent accumulated meshing error caused by the aforementioned defects along the internal meshing line:

$$(85) e_{pri}(t) = E_r \sin(\omega_r t + \alpha + \varphi_i - \beta_r) + A_r \sin(\alpha + \varphi_i - \gamma_r) + E_{pi} \sin(\omega_g t + \alpha - \beta_{pi}) + A_{pi} \sin(\alpha - \gamma_{pi}) + \varepsilon_r + \varepsilon_{pi} + \sigma_r + \sigma_{pi} (i = 1 \sim N)$$

α = meshing angle, φ_i = azimuth angle of a pinion, if four pinions are not distributed evenly then $\varphi_i = 2\pi(i-1)/8 (i = 1 \sim 8)$. β and γ = phase angles of errors, ω = angular velocity

There is a significant overturning moment that the cutter head of the TBM experiences. The overturning angular displacement is disturbed by this overturning moment, and it is impossible to disregard it. The four effects of perturbation in gear radial displacement and overturning moment are as follows:

3.5.1. Modification of the centre distance

The actual centre distance is L_{12} , while the original centre distance is L_{12}^* when the change value of the centre distance is ΔL . Figure illustrates the geometric relationship between the actual centre distance and the original one. This figure illustrates that the meshing force between the pinion and the ring gear is indicated by F_{12} . The actual centre distance and the change value of the centre distance can be expressed as follows:

$$(86) o_1 o_2 = L_{12} = [(L_{12} + x^{(2)} - x^{(1)})^2 + (y^{(2)} - y^{(1)})^2]^{1/2},$$

$$(87) \Delta L = L_{12} - L_{12}^* \approx x^{(2)} - x^{(1)}$$

since $x^{(2)}, x^{(1)}$ = coordinates value of in x direction of gears

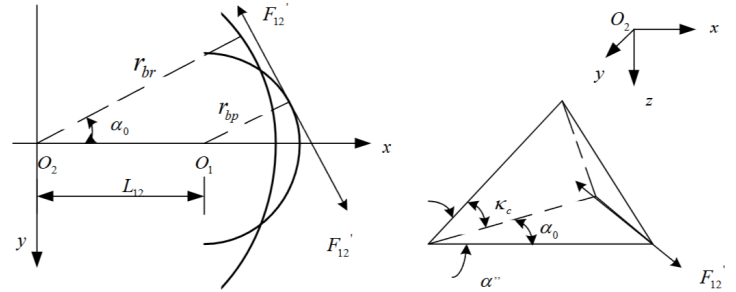


Figure 58: Geometric formulas that account for the overturning angular disturbance of central distance variation and meshing angle

The internal meshing gears' centre distance and meshing angle have the following relationship:

$$(88) \cos \alpha_0 = \frac{r_{br} - r_{bp}}{L_{12}}, \quad (89) \Delta \alpha \approx \frac{-(r_{br} - r_{bp})(x^{(2)} - x^{(1)})}{L_{12}^2 \cos \alpha_0} = \frac{x^{(1)} - x^{(2)}}{L_{12}^2 \tan \alpha_0},$$

$\Delta \alpha$ = angle increment of $\Delta \alpha_0$ = original meshing angle

(90) $k_c = k_{x,i} \sin \alpha_0 + k_{y,i} \cos \alpha_0$ as k_c = overtuning angle in plane, yo_2z = centered at o_2 since $k_{x,i}$ and $k_{y,i}$ are components of pinion in x and y directions. In plane yo_2z , the original meshing angle α_0 is likewise centred at o_2 . The disturbance in overturning angular displacement affects the real meshing angle α , and k_c, α_0 satisfy the space law of cosines. The relationship between α , k_c , and α_0 can be represented as follows, according to the space law of cosines:

$$(91) \cos \alpha'' = \cos k_c \cos \alpha_0, \quad (92) \Delta \alpha'' = \arccos(\cos k_c \cos \alpha_0) - \alpha_0,$$

(93) $\Delta \alpha = \Delta \alpha + \Delta \alpha''$, $\Delta \alpha$ = meshing angle change, as

$$(94) \alpha = \alpha_0 + \Delta \alpha = \frac{(x^{(1)} - x^{(2)})}{L_{12} \tan \alpha_0} + \arccos(\cos k_c \cos \alpha_0),$$
 the deflection angle between the actual and theoretical centre line:

$\beta_{12} \approx \tan \beta_{12} \approx \frac{(y^{(1)} - y^{(2)})}{L_{12}}$. The displacement disturbance and the original centre distance L_{12} immediately express the deflection angle β_{12} between the theoretical centre line $o_1 x$ and the actual centre line $o_1 o_2$. The variation of the meshing line and $o_2 x$ can be expressed as the following: (95) $\Delta \alpha''' = \Delta \alpha - \beta_{12}$

Table 8: geometric Parameters of ring gear and pinnion

	Pinnion	Ring Gear
Module m (mm)	12	12
Tooth Number z	15	97
Rated power p (kw)	27.487	109.948
Rated speed n (rpm)	5.82	0.9
Norm. Modification coef.	0.5	0.5
Pressure angle in pitch α	20	20
Center distance a(mm)	492	492
Addendum coefficient h_a	1	1
Dedendum coefficient c^*	0.25	0.25
Manufacturing Error E μm	71	100

Installation Error A μm	31.5	31.5
Tooth thickness error ε (μm)	-180	-400
Profile error σ (μm)	16	22

3.5.2. Dynamic load for load sharing coefficient

Numerical equation solutions induce dynamic load F_{pri} at a specific moment. System load-sharing coefficient is solved. At a particular point in time, the load-sharing coefficient is the measurement index that is used to determine the load that is distributed unevenly over each pinion. For each tooth frequency cycle, the loadsharing coefficient must be calculated without considering transient dynamic load. The load-sharing coefficient for each tooth frequency cycle is computed as

$$\text{follows: (96)} d_{prij} = \frac{N(F_{prij})}{\sum_{i=1}^N(F_{prij})_{max}}, \text{ since } i = 1 - N, j = 1 - n,$$

$$n = \text{number of tooth frequency}, \quad (97) D_{pri} = |d_{prij} - 1|_{max} + 1, \quad \text{where}$$

$i = 1 \sim N, j = 1 \sim n$

d_{prij} = load sharing coef. in each tooth,

D_{pri} = load sharing coef. in system period

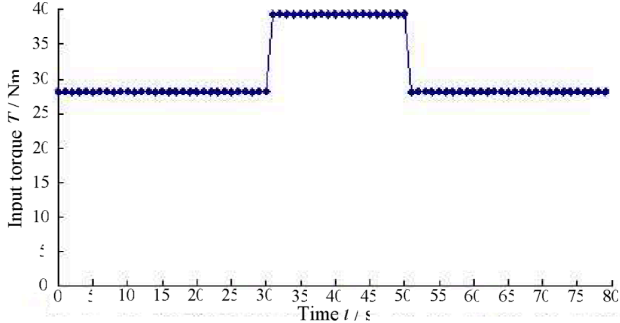


Figure 59: Simulated cutter head load torque

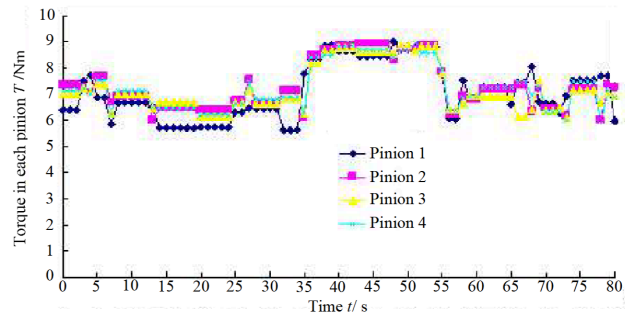


Figure 60: Actual torque in each pinion as measured

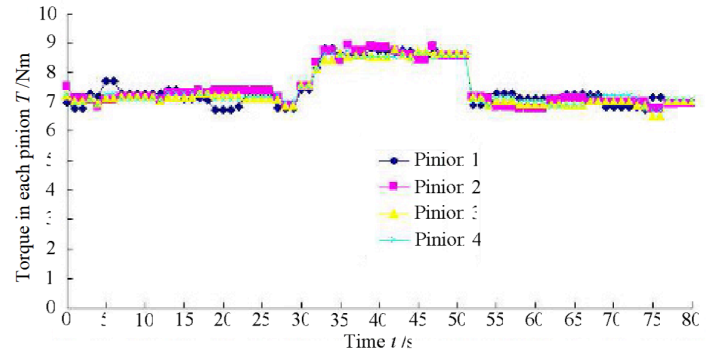


Figure 61: The coupling control method and the actual measured torque

(Figure 58) illustrates the simulated load torque curve, which incorporates the cutter head's load catastrophe characteristic. (Figure 60) illustrates the torque curve that was actually measured in the simulated experiment platform. Even though the burden in the cutter head remains constant, the load-sharing coefficients in each pinion can reach 1.262, as illustrated in this figure.

This outcome is in accordance with the numerical simulation. Random vibration properties are shown by the torque in the pinion, as indicated by the foregoing analysis. In the present control strategy, each motor is distinct from the other motors, and there is no synchronisation error compensation among the strategy. Torque load fluctuation is considered system noise that can be directly incorporated into the control system in the control strategy. The torque distribution imbalance for multiple pinion drives is considerably reduced by the reduction of the load-sharing coefficients to 1.051 under the loop coupling control strategy. In (Figure 61), the torque that was actually measured with the coupling control strategy is illustrated. the motors in multiple pinion drives. This study illustrates a novel control strategy that employs loop coupling control.

Table 9: Coefficients of load sharing at various rotational speeds

Cutter head rotational speed (r/min)	Load-sharing coefficients
0.5	1.189
0.7	1.213
0.9	1.181
1.1	1.206
1.3	1.247
1.5	1.199

In table 9 there are different rotational speeds and load-sharing coefficients. Multiple pinion drives do not have a constant load-sharing coefficient. It displays a non-linear pattern in relation to the rated power of the driving motor and the cutter head's spinning speed. At a cutter head rotational speed of 0.9 r/min, the load-sharing coefficient is 1.181 at its minimum and 1.247 at its maximum. When the cutter head rotational speed is between half a revolution per minute and one and a half revolutions per minute, the load-sharing coefficient of several

pinion drives is approximately 1.2. Thus, even though the cutter head rotates at a modest speed, the dynamic torque and dynamic meshing force of each pinion oscillate around the static torque of each pinion; the torque's amplitude is approximately 1.2 times that of the static torque.

3.5.3. Effect of Inertia

The effects of inertia on the propulsion mechanism and cutter head are taken into account in a dynamic model of multi-gear drive. The findings of this investigation are as follows:

(1) The maximal dynamic load and load-sharing coefficient are higher when bending-torsional coupling is present than when it is absent. A high load-sharing coefficient and maximal dynamic load are the result of bending-torsional coupling.

(2) The combined impact of the nonlinear coupling factors between the ring gear and multiple pinions, as well as the moments of inertia of the drive mechanism and cutter head, causes the load-sharing coefficients to exceed 1.2–1.3. Gear design and synchronisation control should take into account the impact of load-sharing characteristics.

(3) The control system can be directly coupled to the torque in the pinion, which exhibits unpredictable vibration properties. The torque can significantly mitigate the imbalance in torque distribution for multiple pinion drives by employing a loop coupling control strategy.

3.6. Cutter head driving system shock vibration in TBM

Tunnel boring machine (TBM) cutterhead drive system (CDS) failure frequently happens in shock and vibration situations. An electromechanical coupling model of CDS is created to examine the dynamic characteristics and further minimise system vibration. This model comprises the purely torsional dynamic model of a multistage gear transmission system and the model of a direct torque control (DTC) system for a three-phase asynchronous motor.

Load sharing and vibration reduction of CDS in TBM have been the subjects of much research in the past few years. Numerous studies have concentrated on the dynamic analysis of CDS. A dynamic model of a multigear driving system was created by Wei et al., who also investigated how inertia affected the loadsharing feature (Wei et al. 2013). (W. Sun, Ding, et al. 2016) developed a dynamic model of the cutterhead drive system with a hierarchical modelling approach and acquired the dynamic response in mixedface settings through an examination of the dynamic characteristics of TBM by (K. Zhang et al. 2010). In order to lessen vibration, developed a multiobjective optimisation model based on dynamic analysis and gear gearbox system parameters (Qin 2012). More and more people are also interested in the multimotor synchronisation control method of CDS. (R. Liu et al. 2014) investigated the load-sharing characteristics of several motors and presented a flexible control strategy to enhance the compliance capability of CDS (R. Liu et al. 2011) (J. Sun et al. 2009). All of these studies

have successfully optimised the multimotor control technique and conducted dynamic analysis in order to design CDS. On the other hand, the inverter motor's external excitation was simply a constant value substituted for the real driving torque in these investigations. The dynamic performance of the gearbox mechanism may be influenced by the torque disturbance that is an inevitable factor caused by the variable frequency speed control system, as per numerous studies (Kanaan, Al-Haddad, and Roy 2003). Neglecting the effects of actual driving torque may lead to erroneous dynamic analysis of gear gearbox. Consequently, it is essential to consider the operational characteristics of the inverter motor while constructing the electromechanical coupling model and analysing the dynamic characteristics of the multistage gear transmission system in CDS.

In the context of the DTC driving system, the static coordinate system of the α - β phase is selected as the reference frame for the mathematical model of the three-phase asynchronous motor:

$$(98) \quad \begin{vmatrix} \mu_{s\alpha} \\ \mu_{s\beta} \\ 0 \\ 0 \end{vmatrix} = \begin{vmatrix} R_s + 0 & pL_m & 0 \\ 0 & R_s + p & 0 \\ pL_m & L_s \omega & R_r + L_r \omega \\ -\omega L & pL_m & -\omega L & R_r + \end{vmatrix} \begin{vmatrix} i_{s\alpha} \\ i_{s\beta} \\ i_{r\alpha} \\ i_{r\beta} \end{vmatrix}$$

Flux equation:

$$(99) \quad \begin{vmatrix} \Psi_{s\alpha} \\ \Psi_{s\beta} \\ \Psi_{r\alpha} \\ \Psi_{r\beta} \end{vmatrix} = \begin{vmatrix} L_s & 0 & p & 0 \\ 0 & L_s & 0 & L_m \\ L_m & 0 & L_r & 0 \\ 0 & L_m & 0 & L_r \end{vmatrix} \begin{vmatrix} i_{s\alpha} \\ i_{s\beta} \\ i_{r\alpha} \\ i_{r\beta} \end{vmatrix}$$

Torque equation:

$$(100) \quad T_e = n_p L_m (i_{s\beta} i_{r\alpha} - i_{r\beta} i_{s\alpha}) = n_p (i_{s\beta} \Psi_{s\alpha} - i_{s\alpha} \Psi_{s\beta}) = n_p (\Psi_s \otimes i_s) \text{ since } u_{s\alpha}, u_{s\beta} = \text{stator voltages.}$$

$i_{s\alpha}, i_{s\beta}, i_{r\alpha}, i_{r\beta} = \text{stator/rotor currents,}$

$\Psi_{s\alpha}, \Psi_{s\beta}, \Psi_{r\alpha}, \Psi_{r\beta} = \text{stator/rotor fluxes,}$

$R_s, R_r = \text{stator/rotor resistances,}$

$L_s, L_r, L_m = \text{Inductance of stator/rotor/mutual,}$

$T_e = \text{electro magnetic torque, } \omega = \text{electrical angular speed of rotor}$

$, n_p = \text{pole numbers in pairs, } p = \text{differential operator}$

Based on the aforementioned equations, the DTC system of CDS has been established using the Simulink module within

the Matlab software, as illustrated in Figure .The model selected as the stator flux observer can be expressed as follows:

$$(101) \Psi_{s\alpha} = \int (u_{s\alpha} - R_s i_{s\alpha}) dt, \Psi_{s\beta} = \int (u_{s\beta} - R_s i_{s\beta}) dt$$

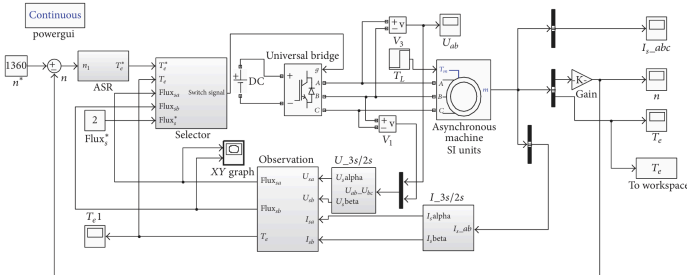


Figure 62: Three-phase asynchronous motor with direct torque control system

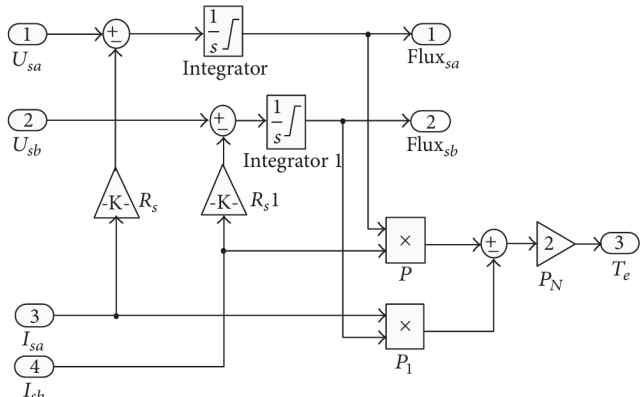


Figure 63: Torque flex model of a stator

Figure 64 shows the torque and stator flux observer model based on (100)-(4=101). Figure 4 illustrates how the DTC system regulates electromagnet torque by maintaining the amplitude and angle of the stator flux ψ_r with inverter voltage space vector switch state controls asynchronous motor.

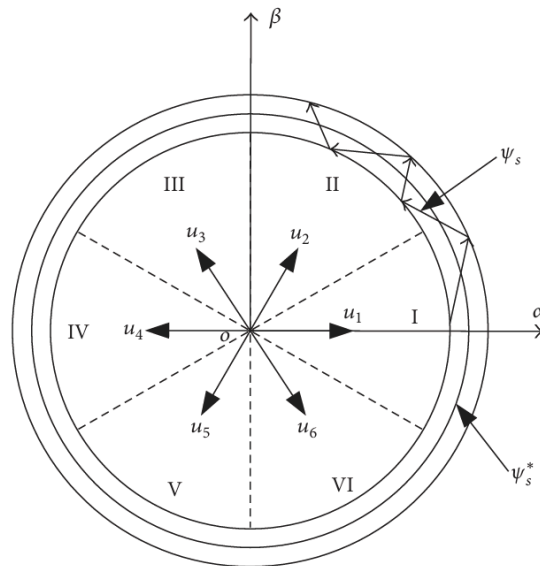


Figure 64: The control principle of the DTC system.

After directly calculating stator flux and torque, the optimal switching table selects driving signals. Calculate the stator flux location in the α - β phase static coordinate system by comparing observed and provided values of ψ_s^* and T_e^* . Inverter motor frequency regulation can be simulated and electric torque calculated using the DTC drive system model. An example of a multi-gear transmission system is a three-stage planetary reducer and a one-stage pinion-ring gear. $s^{(i)}, r^{(i)}, c^{(i)}$ and $p_j^{(i)}$. In the i^{th} stage, the sungear, ringgear, and planet are symbolised by j (1,2,3,4). carrier and the planetary reducer's i^{th} stage, j^{th} planet gear. Opinion-ring gears are denoted by g_1 and g_2 . The lumped mass approach creates a torsional dynamic model of a multistage gear gearbox system. Each part is stiff. Pressure on the tooth surface should cause positive meshing line displacement. The equivalent math paradigm uses Newton's Second Law.

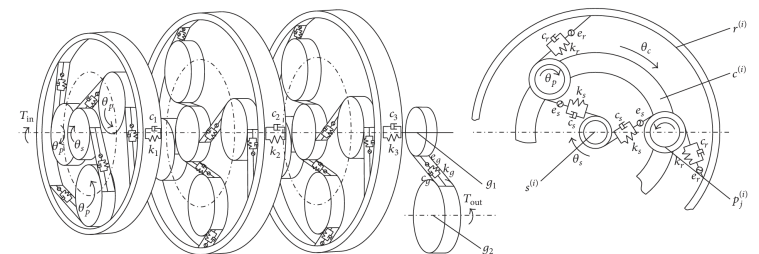


Figure 65: Fundamentally torsional dynamic model of a multistage gear gear transmission system.

$$\begin{aligned}
(102) \quad & I_s^{(1)} \theta_s^{(1)} = T_{in} - \sum_{j=1}^3 k_{sj}^{(1)} x_{sj}^{(1)} r_s^{(1)} - \sum_{j=1}^3 c_{cj}^{(1)} x_{sj}^{(1)} r_s^{(1)}; \\
I_{p1}^{(1)} \theta_{p1}^{(1)} &= k_{s1}^{(1)} x_{s1}^{(1)} r_{p1}^{(1)} - k_{r1}^{(1)} x_{r1}^{(1)} r_{p1}^{(1)} + c_{s1}^{(1)} x_{s1}^{(1)} r_{p1}^{(1)} - c_{r1}^{(1)} x_{r1}^{(1)} r_{p1}^{(1)}; \\
I_{p2}^{(1)} \theta_{p2}^{(1)} &= k_{s2}^{(1)} x_{s2}^{(1)} r_{p2}^{(1)} - k_{r2}^{(1)} x_{r2}^{(1)} r_{p2}^{(1)} + c_{s2}^{(1)} x_{s2}^{(1)} r_{p2}^{(1)} - c_{r2}^{(1)} x_{r2}^{(1)} r_{p2}^{(1)}; \\
I_{p3}^{(1)} \theta_{p3}^{(1)} &= k_{s3}^{(1)} x_{s3}^{(1)} r_{p3}^{(1)} - k_{r3}^{(1)} x_{r3}^{(1)} r_{p3}^{(1)} + c_{s3}^{(1)} x_{s3}^{(1)} r_{p3}^{(1)} - c_{r3}^{(1)} x_{r3}^{(1)} r_{p3}^{(1)}; \\
I_c^{(1)} \theta_c^{(1)} &= \sum_{j=1}^3 [(k_{sj}^{(1)} x_{sj}^{(1)} + k_{rj}^{(1)} x_{rj}^{(1)}) r_c^{(1)} \cos \alpha] \\
&+ \sum_{j=1}^3 [(c_{sj}^{(1)} x_{sj}^{(1)} + c_{rj}^{(1)} x_{rj}^{(1)}) r_c^{(1)} \cos \alpha] - k_c^{(1)} \theta_c^{(1)} - c_c^{(1)} \theta_c^{(1)} \\
&- k_1 (\theta_c^{(1)} - \theta_s^{(2)}) - c_1 (\theta_c^{(1)} - \theta_s^{(2)}) \\
I_s^{(2)} \theta_s^{(2)} &= k_1 (\theta_c^{(1)} - \theta_s^{(2)}) - c_1 (\theta_c^{(1)} - \theta_s^{(2)}) \\
&- \sum_{j=1}^4 k_{sj}^{(2)} x_{sj}^{(2)} r_s^{(2)} - \sum_{j=1}^4 c_{cj}^{(2)} x_{sj}^{(2)} r_s^{(2)}; \\
I_{p1}^{(2)} \theta_{p1}^{(2)} &= k_{s1}^{(2)} x_{s1}^{(2)} r_{p1}^{(2)} - k_{r1}^{(2)} x_{r1}^{(2)} r_{p1}^{(2)} + c_{s1}^{(2)} x_{s1}^{(2)} r_{p1}^{(2)} - c_{r1}^{(2)} x_{r1}^{(2)} r_{p1}^{(2)}; \\
I_{p2}^{(2)} \theta_{p2}^{(2)} &= k_{s2}^{(2)} x_{s2}^{(2)} r_{p2}^{(2)} - k_{r2}^{(2)} x_{r2}^{(2)} r_{p2}^{(2)} + c_{s2}^{(2)} x_{s2}^{(2)} r_{p2}^{(2)} - c_{r2}^{(2)} x_{r2}^{(2)} r_{p2}^{(2)}; \\
I_{p3}^{(2)} \theta_{p3}^{(2)} &= k_{s3}^{(2)} x_{s3}^{(2)} r_{p3}^{(2)} - k_{r3}^{(2)} x_{r3}^{(2)} r_{p3}^{(2)} + c_{s3}^{(2)} x_{s3}^{(2)} r_{p3}^{(2)} - c_{r3}^{(2)} x_{r3}^{(2)} r_{p3}^{(2)}; \\
I_{p4}^{(2)} \theta_{p4}^{(2)} &= k_{s4}^{(2)} x_{s4}^{(2)} r_{p4}^{(2)} - k_{r4}^{(2)} x_{r4}^{(2)} r_{p4}^{(2)} + c_{s4}^{(2)} x_{s4}^{(2)} r_{p4}^{(2)} - c_{r4}^{(2)} x_{r4}^{(2)} r_{p4}^{(2)}; \\
I_c^{(2)} \theta_c^{(2)} &= \sum_{j=1}^4 [(k_{sj}^{(2)} x_{sj}^{(2)} + k_{rj}^{(2)} x_{rj}^{(2)}) r_c^{(2)} \cos \alpha] \\
&+ \sum_{j=1}^4 [(c_{sj}^{(2)} x_{sj}^{(2)} + c_{rj}^{(2)} x_{rj}^{(2)}) r_c^{(2)} \cos \alpha] - k_c^{(2)} \theta_c^{(2)} - c_c^{(2)} \theta_c^{(2)} \\
&- k_2 (\theta_c^{(2)} - \theta_s^{(3)}) - c_2 (\theta_c^{(2)} - \theta_s^{(3)}) \\
I_s^{(3)} \theta_s^{(3)} &= k_2 (\theta_c^{(2)} - \theta_s^{(3)}) + c_2 (\theta_c^{(2)} - \theta_s^{(3)}) \\
&- \sum_{j=1}^4 k_{sj}^{(3)} x_{sj}^{(3)} r_s^{(3)} - \sum_{j=1}^4 c_{cj}^{(3)} x_{sj}^{(3)} r_s^{(3)}; \\
I_{p1}^{(3)} \theta_{p1}^{(3)} &= k_{s1}^{(3)} x_{s1}^{(3)} r_{p1}^{(3)} - k_{r1}^{(3)} x_{r1}^{(3)} r_{p1}^{(3)} + c_{s1}^{(3)} x_{s1}^{(3)} r_{p1}^{(3)} - c_{r1}^{(3)} x_{r1}^{(3)} r_{p1}^{(3)}; \\
I_{p2}^{(3)} \theta_{p2}^{(3)} &= k_{s2}^{(3)} x_{s2}^{(3)} r_{p2}^{(3)} - k_{r2}^{(3)} x_{r2}^{(3)} r_{p2}^{(3)} + c_{s2}^{(3)} x_{s2}^{(3)} r_{p2}^{(3)} - c_{r2}^{(3)} x_{r2}^{(3)} r_{p2}^{(3)}; \\
I_{p3}^{(3)} \theta_{p3}^{(3)} &= k_{s3}^{(3)} x_{s3}^{(3)} r_{p3}^{(3)} - k_{r3}^{(3)} x_{r3}^{(3)} r_{p3}^{(3)} + c_{s3}^{(3)} x_{s3}^{(3)} r_{p3}^{(3)} - c_{r3}^{(3)} x_{r3}^{(3)} r_{p3}^{(3)}; \\
I_c^{(3)} \theta_c^{(3)} &= \sum_{j=1}^4 [(k_{sj}^{(3)} x_{sj}^{(3)} + k_{rj}^{(3)} x_{rj}^{(3)}) r_c^{(3)} \cos \alpha] \\
&+ \sum_{j=1}^4 [(c_{sj}^{(3)} x_{sj}^{(3)} + c_{rj}^{(3)} x_{rj}^{(3)}) r_c^{(3)} \cos \alpha] - k_c^{(3)} \theta_c^{(3)} - c_c^{(3)} \theta_c^{(3)} \\
&- k_3 (\theta_c^{(3)} - \theta_{g1}^{(1)}) - c_3 (\theta_c^{(3)} - \theta_{g1}^{(1)}) \\
I_{g1} \theta_{g1}^{(1)} &= k_3 (\theta_c^{(3)} - \theta_{g1}^{(1)}) + c_3 (\theta_c^{(3)} - \theta_{g1}^{(1)}) \\
&- k_g (r_{g1} \theta_{g1} - r_{g2} \theta_{g2} + e_g) - c_g (r_{g1} \theta_{g1} - r_{g2} \theta_{g2} + e_g); \\
I_{g1} \theta_{g1}^{(1)} &= n [k_g (r_{g1} \theta_{g1} - r_{g2} \theta_{g2} + e_g) + c_g (r_{g1} \theta_{g1} - r_{g2} \theta_{g2} + e_g)] - T_{out} \\
I_{s'} I_{p'} I_{c'} I_{g1} I_{g2} &= \text{mass moment of inertia of sun, planet gears, carrier in reducer, pinnion ring gears} \\
r_s' r_{p'} r_{c'} r_{g1} r_{g2} &= \text{base radius sun, planet gears, carrier in reducer, pinnion ring gears, } T_{in} = \text{driver torque of}
\end{aligned}$$

inverter motor = T_e in DTC, T_{out} = enlarged driving torque by gear transmission system, k_c = totional stiffness of planet carrier, k_1, k_2, k_3 = totional stiffness of each stage connecting stage, c_c = totional damping of planet carrier; c_1, c_2, c_3 = totional damping of each stage connecting stage; α = pressure angle of pitch cyclinder, n = number of pinnions, x_s = sun and each plannet gear displacement line, x_r = displacement along the ring line between the ring gear and each planet gear. There for, x_s, x_r can be expressed as the following:

$$\begin{aligned}
(103) \quad & x_{sj}^{(i)} = r_s^{(i)} \theta_s^{(i)} - r_{pj}^{(i)} \theta_{pj}^{(i)} - r_c^{(i)} \theta_c^{(i)} \cos \alpha + e_{sj}^{(i)}; \\
x_{rj}^{(i)} &= r_{pj}^{(i)} \theta_{pj}^{(i)} - r_c^{(i)} \theta_c^{(i)} \cos \alpha + e_{rj}^{(i)} \text{ since } e_s = \text{transmission error between planet and sun gear and } e_r = \text{transmission error between ring and each planet gear.}
\end{aligned}$$

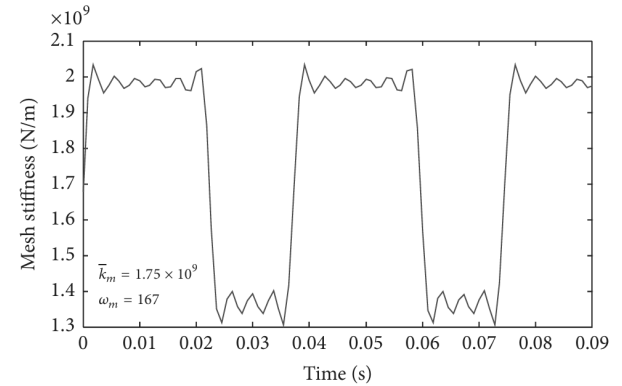


Figure 66: Mesh stiffness time varying

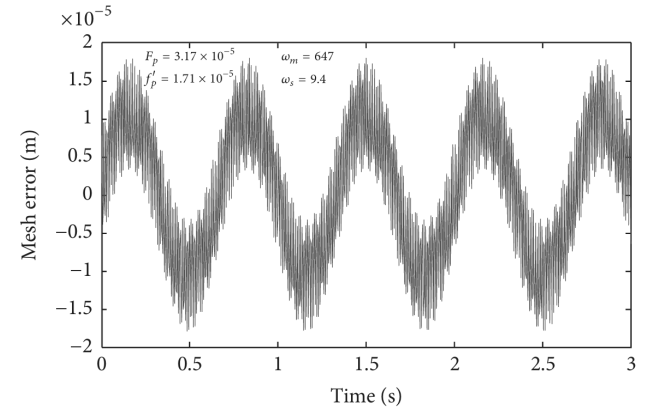


Figure 67: mesh error transmissions

k_s, k_r, k_g = tiffnes time variant mesh mesh can be expressed by means of fourrier series.

$$(104) \quad k_m(t) = k_m^- + \sum_{n=1}^N B_n \cos i \omega_m (t + \varphi), \quad m = s, r, g \quad k_m^- = \text{average mesh stiffness which can be obtained based on gear standards such as AGMA ISO 1328-1 and DIN 3390 and } B_n = \text{harmonic amplitude in Fourrier series. } c_s, c_r \text{ and } c_g = \text{demping of mesh}$$

$$c_m = 2\zeta\sqrt{\frac{k_m m_n}{m_m + m_n}} ; \quad m \text{ or } n = s, r, p, g, \quad \zeta = 0.03 - 0.17 \text{ for damping ratio, } m_n, m_m \text{ are mass of two meshing gear.}$$

$$(105) e_n = 0.5F_p \sin(2\pi\omega_s t + \varphi_s) + 0.5f_p \sin(2\pi\omega_m t + \varphi_m), \quad n = s, r, g,$$

where F_p denotes the total cumulative pitch error; f_p represents the tangential tolerance of an individual tooth; ω_s and ω_m indicate the rotational frequency and mesh frequency, respectively; and φ_s and φ_m refer to the initial phase of the shaft and mesh phase.

Table 10: TBM cutter heads driving mechanism parameters

Driving motor	Rated Power Speed Range	160 kW 0-1480 rpm
Transmission system	Reducer Ring-pinion	Gear ratio, $i_1 = 51.2$ Gear ratio, $i_{II} = 12.6$
Cutterhead	Rated power Speed range Rated torque	1600 kW (10*160 kW) 0-2.1 rpm-4.7 rpm 7230 KNm @ 2.1 rpm

Table 11: three phase asynchronous motor parameters

Parameters	Value
Rational inertia J	2.9 kg. m ²
Mutual inductance L_m	7.69 mH
Rotor inductance L_r	0.152 mH
Stator inductance L_s	0.152 mH
Rotor resistance R_r	0.007728 Ω
Stator resistance R_s	0.01379 Ω
Rated frequency f_N	50 Hz
Rated voltage U_N	400 V
Rated power P_N	160 kW

The numerous inverter motors are intended to be synchronous, and the TMB cutter head is selected to operate at a rotating speed of $n_c = 2.1$ rpm. Consequently, the load torque of the motor may be computed based on the mean value of the load. Electromechanical Dynamic Analysis of CDS

$$(106) T_L = 9549 \frac{P_N}{i_1 i_{II} n_c}, \quad \text{since} \quad P_N = \text{rated power},$$

$$i_1 = \text{gear ration of reducer}, \quad i_{II} = \text{gear ratio of pinnion},$$

$$n_c = \text{rated speed of cutter head}, \quad n = \text{number of pinnion},$$

As geological conditions change, the load torque T_L in the actual tunnelling process is unstable and rapidly varies. The rated torque T_L is 1120 N·m at the rated rotational speed $n_c = 2.1$ rpm, as indicated in (106), which corresponds to the actual T_L at approximately 310 seconds in (Figure 66). In the time interval of 314.2 seconds to 315.2 seconds, the torque level is stable near the rated torque for the first 0.2 seconds, subsequently rising sharply to 1700 Nm at 314.4 seconds. After 314.5 seconds, T_L stabilises at approximately 1700 Nm with minimal

fluctuations. The operational characteristics of an inverter motor under shock loading are examined with a duration of T_L set to 1 second. The interval from 314.2 seconds to 315.2 seconds is chosen for simulation as a piecewise function. In the DTC driving system, the load torque T_L is a critical parameter. Simulation duration: 2 seconds T_L is 1100 Nm for the duration of 1.35 s, and it increases to 1700 Nm from 1.35 s to 2 s. The actual driving torque of the DTC system is obtained and illustrated in (Figure 67). In the startup phase, the inverter motor functions at maximum torque to swiftly reach the rated speed. After 1 second of operation, the electromagnetic torque T_e aligns with the actual load torque at the rated speed. The fitting result demonstrates that the DTC drive system exhibits a rapid response to changes in load torque T_L . Electromagnetic torque T_e demonstrates considerable torque ripple.

$$(107) T_e^{(k+1)} = T_e^{(k)} + \Delta T_{e1}^{(k)} + \Delta T_{e2}^{(k)} ; \quad \Delta T_{e1}^{(k)} = -T_{e1}^{(k)} \left(\frac{R_s}{L_s} + \frac{R_r}{L_r} \right) \frac{T_s}{\sigma};$$

$$\Delta T_{e2}^{(k)} = \frac{3}{2} n_p \frac{L_m}{\sigma L_s L_r} [(u_s^{(k)} - j\omega_r^{(k)} \psi_s^{(k)}) \cdot j\psi_r^{(k)}] T_s$$

Table 12: Parameters of 3-stage planetary reducer in TBM

Parameter	Sun			Planet			Ring			Carrier		
	1st	2nd	3rd	1st	2nd	3rd	1st	2nd	3rd	1st	2nd	3rd
Mass m (kg)	3.69	9.55	14.06	2.37	5.78	14.06	17.76	30.06	42.98	18.32	32.1	47.35
I (kg·m ²)	0.004	0.019	0.032	0.002	0.007	0.032	0.132	0.39	0.88	0.145	0.56	1.86
Tooth number z	25	27	24	20	21	24	65	69	72	—	—	—
Module m_n							$m_{n1} = 4, m_{n2} = 5, m_{n3} = 6$					
Tooth width b (m)							$b_1 = 0.06, b_2 = 0.085, b_3 = 0.11$					
Pressure angle α							$\alpha_1^{(1)} = \alpha_2^{(2)} = \alpha_3^{(3)} = 20^\circ, \alpha_1^{(1)} = \alpha_2^{(2)} = \alpha_3^{(3)} = 20^\circ$					
Mesh stiffness \bar{k}_m (N/m)				$\begin{cases} \bar{k}_1^{(1)} = 9.872 \times 10^8 \\ \bar{k}_2^{(1)} = 1.179 \times 10^9 \end{cases}$		$\begin{cases} \bar{k}_3^{(2)} = 1.3225 \times 10^9 \\ \bar{k}_4^{(2)} = 1.4366 \times 10^9 \end{cases}$		$\begin{cases} \bar{k}_5^{(3)} = 1.7362 \times 10^9 \\ \bar{k}_6^{(3)} = 1.7543 \times 10^9 \end{cases}$				

Where $T_e^{(k+1)}$ and $T_e^{(k)}$ represent the electromagnetic torques at moments K+1 and k , respectively; $\Delta T_{e1}^{(k)}$ = torque attenuation due to stator and rotor resistance; $\Delta T_{e2}^{(k)}$ = torque variation caused by voltage space vector; T_s = sampling time; σ = constant related to L_m and L_s and L_r ; ω_r signifies the speed of the rotor.

torque ripple is unavoidable and is influenced by sampling time, motor speed, flux, and voltage vector, all of which are closely associated with the computational capacity of the digital controller and switching frequency. Consequently, the external excitation of the gear gearbox system, specifically the torque ripple of electromagnetic torque T_e , may be elevated during the actual motor driving process, thereby affecting the dynamic characteristics of the gear gearbox system.

3.6.1. Modal Property of Multistage Gear Transmission System.

In a multistage gear transmission system, a one-stage pinion ring gear comprises several pinions g_1 and a ring gear g_2 . The size of ring gear g_2 is significantly larger than that of other gears, and the inherent properties of the planetary reducer cannot be clearly presented under the influence of ring gear g_2 . Consequently, the modal properties of the planetary reducer are

selected for analysis in this paper. Based on the matrix calculated above in equation 5 the planetary reducer model can be expressed in the form of matrix:

$$(108) M\ddot{q}(t) + C\dot{q}(t) + Kq(t) = F(t)$$

Table 13 : reducer of natural frequency planetary

Motion modes	Natural frequency (Hz)
Rigid motion mode	$f_1 = 0$
Rotational vibration modes	$f_2 = 308, f_3 = 529,$ $f_4 = 2806, f_8 = 3772,$ $f_9 = 4644, f_{13} = 5919,$ $f_{16} = 5919, f_{17} = 8338$
Planet vibration modes	$f_5 = f_6 = f_7 = 3598;$ $f_{14} = f_{14} = 6655$ $f_{10} = f_{11} = f_{12} = 4965$

(109) $\omega_i^2 M\varphi_i = K^- \varphi_i$, since $\omega_i = i$, order natural frequency, K^- = average stiffness matrix, $\varphi_i = i$, order vibration mode vector as:

$$(110) \varphi_i = [\phi_{is}^{(1)}, \phi_{ip1}^{(1)}, \phi_{ip2}^{(1)}, \phi_{ip3}^{(1)}, \phi_{ic}^{(1)}, \phi_{is}^{(2)}, \phi_{ip1}^{(2)}, \phi_{ip2}^{(2)}, \phi_{ip3}^{(2)}, \phi_{ip4}^{(2)}, \phi_{ic}^{(2)}, \phi_{is}^{(3)}, \phi_{ip1}^{(3)}, \phi_{ip2}^{(3)}, \phi_{ip3}^{(3)}, \phi_{ip4}^{(3)}, \phi_{ic}^{(3)}]$$

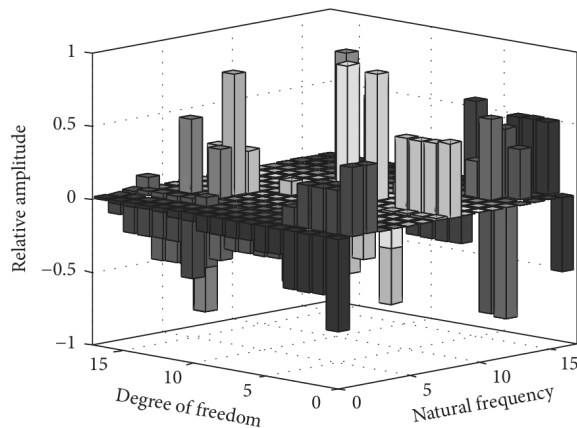


Figure 68: vibration modes of planetary reducer results

The electromechanical coupling model can be solved to determine the vibration displacement. The dynamic response of the gear gearbox system may be influenced by the torque fluctuation of the inverter motor, as demonstrated and discussed above. Consequently, vibration displacements under electromagnetic torque T_e with ripple and ideally calculated separately. The driving torque, θ_{se} , is defined as the vibration displacement of the sun gear under electromagnetic torque T_e , while θ_{sm} is defined as the vibration displacement of the sun gear under idealised piecewise torque. For 0.35s and 1s, the mean values of θ_{se} and θ_{sm} are identical and equal to 0.0286, indicating that the equilibrium position is not influenced by the actual driving torque of the inverter motor. Nevertheless,

the standard deviation of θ_{se} is 0.0092 and that of θ_{sm} is 0.0045. This suggests that the vibration amplitude under electromagnetic torque T_e is greater than that under idealised piecewise torque. Therefore, it is enticing to infer that the torque ripple caused by the actual driving torque of the inverter motor may exacerbate the vibration of the gear gearbox system.

3.6.2. Dynamic Meshing Force:

The failure of a gear transmission system, such as the attrition or pitting of gear teeth, is directly influenced by the dynamic meshing force.

$$(110) F_{sj}^{(i)} = k_{sj}^{(i)} x_{sj}^{(i)} + k c_{sj}^{(i)} x_{sj}^{(i)}; F_{rj}^{(i)} = k_{rj}^{(i)} x_{rj}^{(i)} + c_{rj}^{(i)} x_{rj}^{(i)} \quad \text{since}$$

F_s, F_r = external/internal meshing forces, k_s, k_r = time-variant mesh stiffnesses, x_s = displacement between sun and planet gear each, x_r = displacement between ring gear and each planet gear. The dynamic meshing forces in each stage are calculated under the external excitation of electromagnetic torque T_e , and a portion of them are illustrated in Figures 13 and 14. At 0.35s, electromagnetic torque T_e changes, and external meshing forces rise quickly. Mesh forces also rise by a natural frequency stage based on gear ratio. The meshing forces of the first-stage planet gears fluctuate more dramatically than those of the other two stages at the changing point. This phenomenon is likely due to the fact that the first-stage solar gear is directly affected by external excitation. The meshing forces of planet gears are also distinct during the same stage. The highest load-sharing level is that of the third stage, while the lowest load-sharing level is that of the first stage. This discrepancy may be attributed to the phase difference of mesh rigidity and gearbox error.

The (figure 70) below illustrate the spectral analysis of the external meshing force in the Achstage. In this context, the i-order natural frequency is denoted by f_{ni} ($i = 2,3$), while the j-stage mesh frequency is denoted by f_{mj} ($j = 1,2,3$). As illustrated in (Figure 68), the meshing forces in each stage vibrate in the low frequency domain, which is in close proximity to f_{mj} and its multiple frequencies. In addition, the internal excitations contain low-order natural frequencies ($f_{n2} = 308$ and $f_{n3} = 529$), with f_{n2} having the highest amplitude.

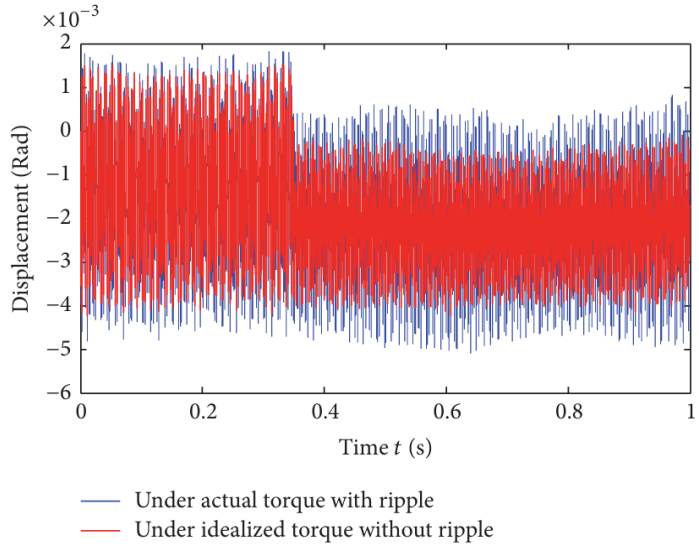
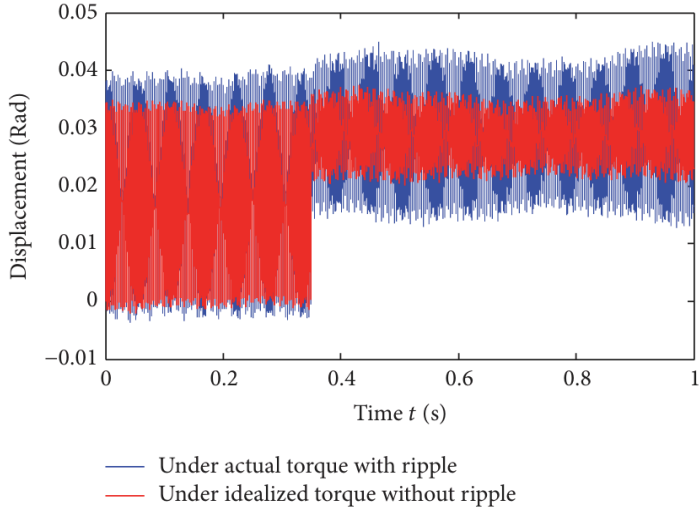


Figure 70: Response of dynamics of TBM of first and second stage of sun gear

3.6.3. Vibration of gear transmissions

The vibration of the gear transmission system is increased under electromagnetic torque T_e in comparison to the idealised drive torque. The electromagnetic torque T_e and its torque ripple may be the cause of the vibration increases in each component. To assess the impact of electromagnetic torque T_e on the vibration of each component, it is suggested that an influence index δ of torque ripple be calculated using the vibration displacements, as expressed:

(111) $\delta = \frac{A_e - A_m}{A_{m \max}}$ Where A_e , A_m = deviations from equilibrium under electromagnetic torque T_e and idealised torque, respectively. A_m = max vibration degree, while A_{ei} and A_{mi} can be

stated as: (17) $A_s = |\theta_s - \bar{\theta}_s|$ ($s = e, m$) since
 θ_s = displacement vibration, $\bar{\theta}_s$ = mean value of θ_s at equilibrium

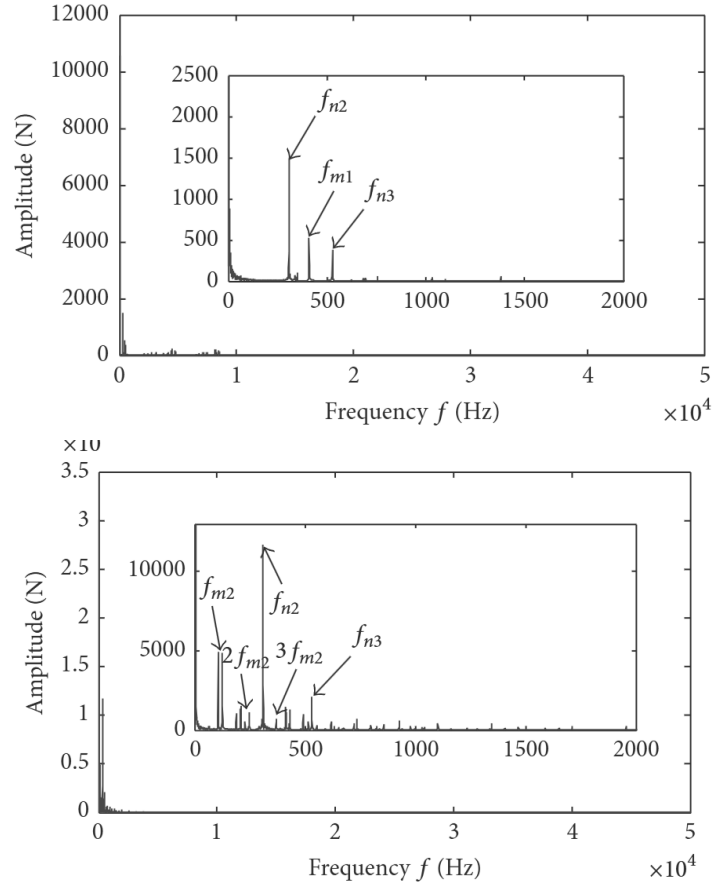


Figure 71: shock and vibration frequency at first and second stage

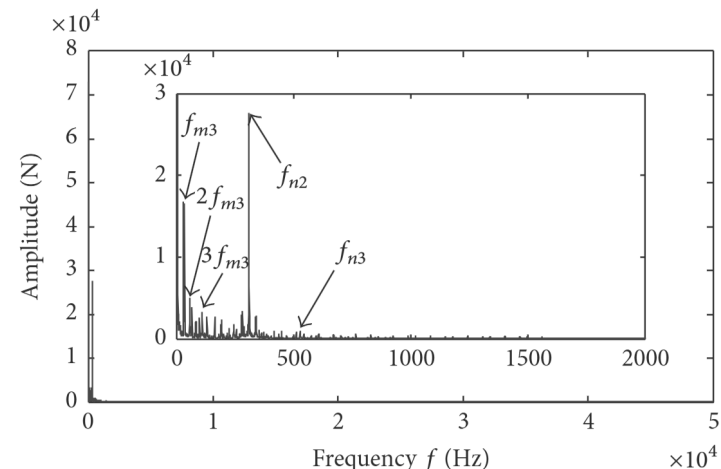


Figure 72: Shock and vibration frequency at third stage

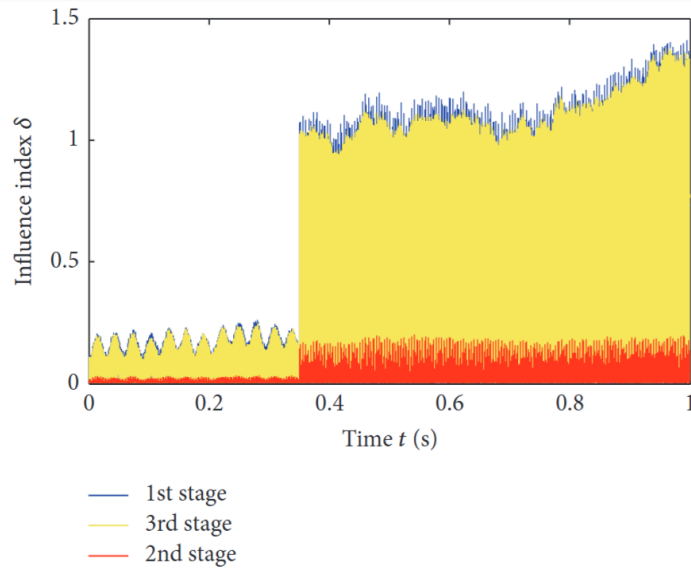
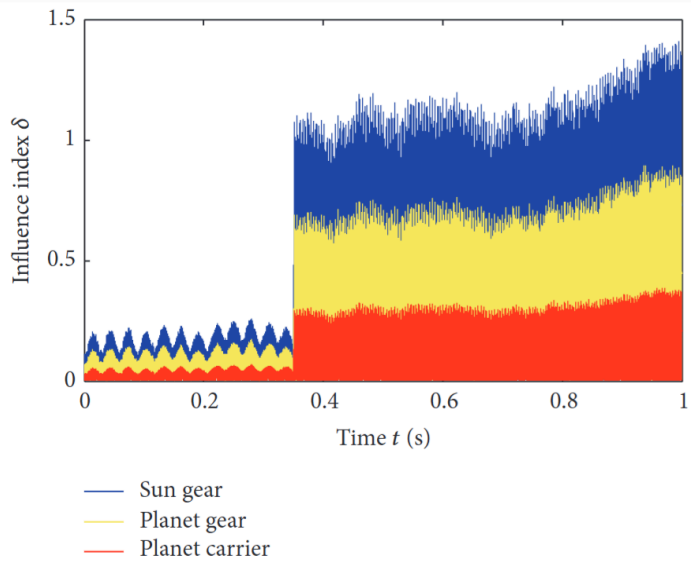
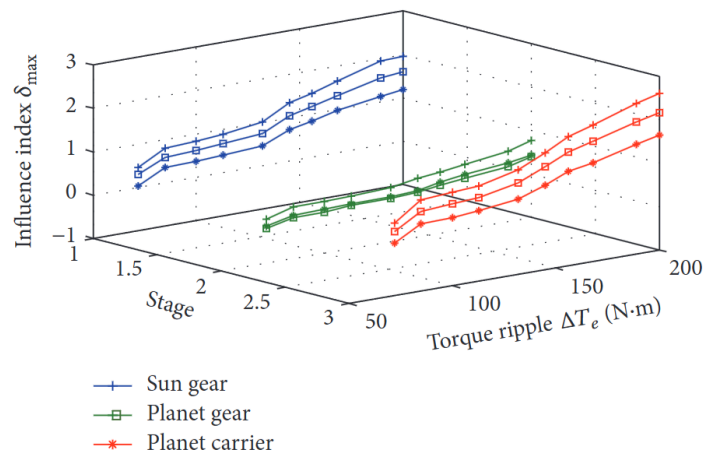


Figure 73: Influence of index δ on sun gear in first and second stage



3.7. Hydraulic Cylinders:

The transmission of forces and the generation of motion are both accomplished by hydraulic cylinders, which are linear actuators. They are able to transmit strong forces because of their high stiffnesses. Control is challenging due to the very nonlinear stiffness characteristics of hydraulic cylinder systems (Jelali and Kroll 2012). Specifically, the piston's location, or the variation in volume in each chamber, is the most well-known source of nonlinearity in hydraulic cylinder stiffness. Dynamic functionalities are demonstrated by hydraulic cylinders in their capacity as actuators. Therefore, for cylinders in dynamic applications, figuring out the static stiffness characteristics alone is insufficient. When flow is permitted via the intake ports, the stiffness properties that were computed under static circumstances are different. Spring-like behaviour is demonstrated by hydraulic cylinders when their inlet apertures are closed. Then, in addition to the characteristics of the sealing systems, the stiffness is controlled by fluid temperatures, pressure levels, and volumes. It is also necessary to think about the cylinder rod's and chamber's stiffness characteristics in certain high-pressure uses. Nonetheless, when flow is let via the input ports, the dynamic properties are significantly influenced by all components within the hydraulic system.

Stiffness is the ratio of applied force to elastic element translational deflection (McGraw-Hill 2002). Different environmental and dynamic situations affect system stiffness. The static stiffness (k) measured under a static load is specified by: (112) $k = \frac{\Delta F}{\Delta x}$ since $\Delta F = \text{static force}$,

$\Delta x = \text{corresponding deflection}$ Dynamic rigidity is tested at frequencies over 0.5 Hz under rapid periodic loads (Rivin and Kops 2010). Rotor and spinning machinery supports commonly experience periodic loads. As loads oscillate, vibration occurs. Vibration measurements are often processed using Fourier analysis. In dynamic settings, dynamic stiffness is the ratio of input force amplitude to output displacement amplitude:

(113) $k_{dyn} = \frac{F_a}{x_a}$ since $F_a = \text{load amplitude}$,
 $x_a = \text{resulting displacement response amplitude}$,

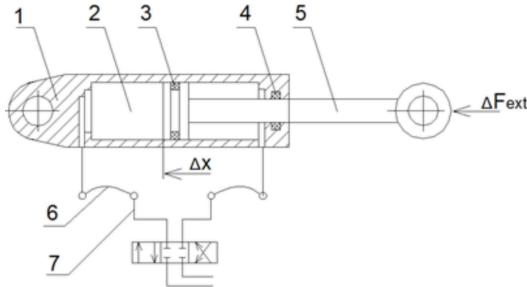


Figure 75: A hydraulic cylinder system consists of the following components: 1. Cylinder barrel, 2. Hydraulic oil, 3. Piston sealing, 4. Rod sealing, 5. Rod, 6. Hoses, 7. Metal pipes. (Feng et al. 2017)

The overall stiffness of hydraulic cylinder systems is influenced by the cylinder rod, cylinder chamber, seals, pipes, and hoses. A comprehensive stiffness model of a hydraulic cylinder has been introduced. The net static stiffness, or k_{st} , was calculated in the study by adding the reciprocals of the stiffnesses of the hydraulic fluid, piston rod, cylinder barrel, pipe, hose, and sealing rings.

$$(113) \frac{1}{k_{st}} = \frac{1}{k_o} + \frac{1}{k_r} + \frac{1}{k_c} + \frac{1}{k_p} + \frac{1}{k_h} + \frac{1}{k_s} \quad \text{since}$$

k_o = stiffness of fluid, k_r = axial cylinder rod stiffness,

k_c = cylinder barrel expansion stiffness,

k_p = piping expansion stiffness,

k_h = expansion stiffness of hoses, k_s = sealing ring stiffness. In the analysis of stiffness under dynamic loads, it is essential to evaluate the frequency responses of both the cylinder and the fluid lines. The system may react unexpectedly to natural resonances. Load masses and fluid volumes have an impact on hydraulic cylinder systems' natural resonance frequencies.

Power transmission, lubrication, heat transfer, and corrosion prevention are the primary goals of hydraulic fluids. Because of their affordable price, appropriate viscosity levels, and good stiffness performance in various applications, hydraulic fluids derived from minerals are the most often utilised. The fluid bulk modulus dominates the static hydraulic stiffness of cylinder systems in a closed hydraulic circuit. However, while the piston of the cylinder is in motion studies by (Kinker 2011), the flow alters the stiffness characteristics of the hydraulic cylinder. The dynamic impacts of transient flows and the impact of fluid medium and flow through orifices on hydraulic stiffness are discussed in this section. (114) $K_f = -V \frac{\Delta p}{\Delta V}$, The fluid bulk modulus (Kim and Murrenhoff 2012), or K_f , which is a measurement of a fluid's resistance to compressibility, is related to hydraulic stiffness. This can also be defined as a measure of fluid stiffness. Since V = initial volume, Δp = pressure difference, ΔV = difference in volume, before and after compression (Gholizadeh, Burton, and Schoenau 2011).

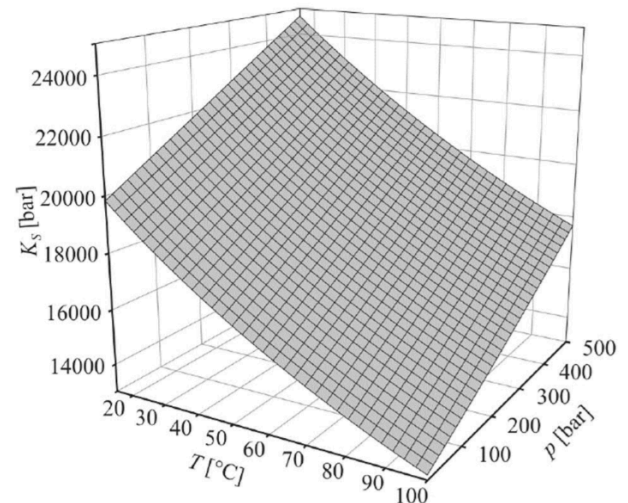


Figure 76: Temperature and pressure affect mineral oil bulk modulus (Kneževic et al. 2011).

The bulk modulus is a characteristic specific to fluids, influenced by both temperature and pressure. Figure above illustrates the dependence of the bulk modulus of a mineral oil on pressure and temperature. The bulk modulus decreases with increasing temperature and increases with increasing pressure, as the figure illustrates.

High bulk modulus in hydraulic fluids is advantageous as it enhances stiffness and stability. Oils derived from minerals typically have bulk moduli between 1.8 and 2.2 GPa. inside the context of practical applications, such as hydraulic cylinder systems, the presence of undissolved air that is trapped inside the hydraulic circuit results in a reduction in the effective bulk modulus of the fluid (Gholizadeh, Burton, and Schoenau 2011) (Kneževic et al. 2011) (X. Yuan et al. 2019). As seen in the picture below, trapped air has a major effect at lower working pressures (p 60 bar).

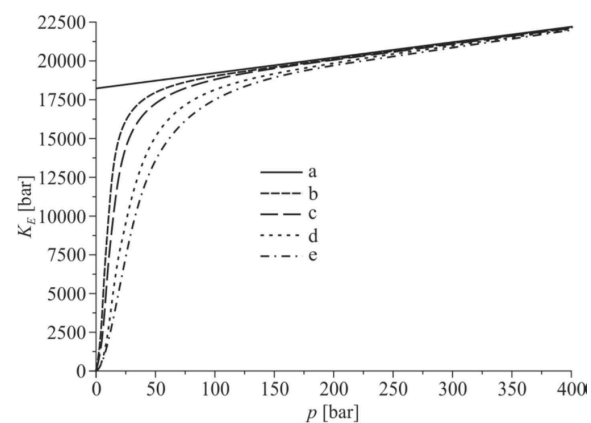


Figure 77: Utilisation of varying quantities of undissolved air at an oil temperature of 30°C, the effective bulk modulus is as follows

In the estimation of the effective bulk modulus, the undissolved air content is considered.

$$(115) K_E = K_f' [(1 + \alpha (\frac{p_a}{p_a + p})^{1/n}) \div (1 + \alpha K_f' \frac{p_a^{1/n}}{n(p_a + p)^{(n+1)/n}})] \quad \text{as the}$$

isentropic constant ($n = 1.4$) tells us how much undissolved air there is in the system compared to its volume. The atmospheric pressure is P_a and P refers to the working pressure, and the nominal bulk modulus of the fluid are also given as K_f when α is the the volume of undisolved air in atmospheric pressure.

$$v = 0$$

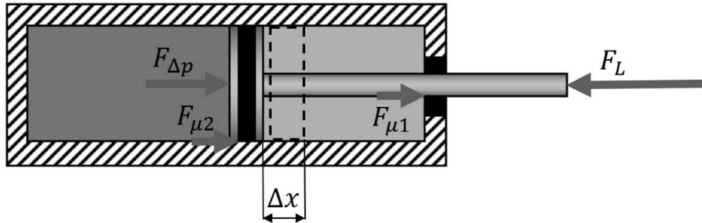


Figure 78: Static equilibrium free-body diagram of a hydraulic cylinder

The static load of FL induces a displacement of the piston, denoted by Δx , while the net hydraulic force, $F\Delta p$, is the result of the pressures operating on both sides of the piston surfaces. The seal friction forces for the rod and piston are denoted as F_{u1} and F_{u2} , respectively. The loading force is perpetually opposed by the seal friction forces which will be discussed in the following. And the hydraulic fluid stiffness, K_o , in a closed cylinder system can be calculated from the piston displacement Δx , which results in a proportional volume change in both chambers based on the effective piston area.

$$(116) k_o = K_{EA} \frac{A_A^2}{V_A + V_{AL}} + K_{EB} \frac{A_B^2}{V_B + V_{BL}} \text{ since } A_A = \text{head effective area} ,$$

A_B = Rod Effective area, V_A = piston position volume chamber,

V_p = piston position dependent rod chamber volume,

$V_{..}$ = head fluid line,

V_{rod} = rod end total volume line,

K_{AL} , K_{BL} \equiv effective bulk moduli for each chamber. Therefore

$$(117) V \equiv A \ x \quad \text{and} \quad (118) V \equiv A \ (l - x) \text{ since}$$

x = piston position, l = stroke of cylinder

x_p = piston position, t_s = stroke of cylinder

Flow occurs through inlet apertures when a cylinder piston is in motion, resulting in a change in fluid volumes. Furthermore, the discharge rate is affected by the pressure differential that external forces generate. Hydraulic inductance, which is also referred to as flow rate response to pressure fluctuations in a system, is determined by the fluid density, conduit lengths, and orifice flow areas. It is evident that the hydraulic inductance influences the system stiffness in dynamic conditions, as defined as the ratio of an external force to the resultant displacement. Fluid flow is induced by a static pressure difference in an open circuit cylinder. The cylinder ports facilitate the passage of fluid within the cylinder chambers. The free-body diagram of a hydraulic cylinder that is extending at a constant velocity of v is depicted in he (Figure 79) bellow:

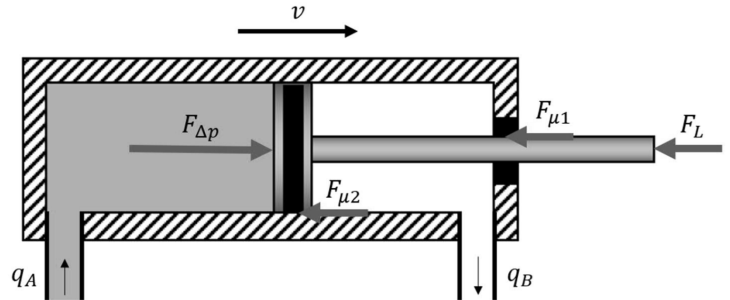


Figure 79: Free-body diagram of a hydraulic cylinder exhibiting constant flow and velocity.

The volumetric flow of the head chamber and rod end chamber is represented by q_A and q_B , respectively, while the net hydraulic force is represented by $F_{\Delta p}$, the loading force by F_L , and the rod and piston seal friction by F_{u1} and F_{u2} , respectively.

The steady state of volumetric flow is (119) $q_v = C_q A_o \sqrt{\frac{2\Delta p}{\rho}}$. The fluid density is represented by ρ , the pressure difference brought on by the load is represented by Δp , the flow coefficient by C_q , and the orifice's cross-sectional area by A_o . The flow coefficient is contingent upon the Reynolds number of the flow and the circularity of the orifice edges. The theoretical flow coefficient for a sharp-edged orifice is $C_q =$

0.611 (H. Lu 2022). (120) $R_e = \frac{U_{mean} d_h}{v}$ is the reynolds number.
 U_{mean} = average velocity of flow through orifice,
 d_h = hydraulic diameter, v = kinematic viscosity of the fluid (Watton 2009).

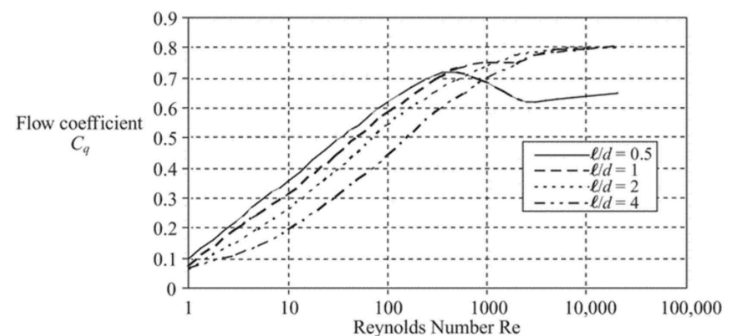


Figure 80: Source of flow coefficient variation in relation to Reynolds number (Watton 2009)

The piping dimensions, fluid density, bulk modulus, and viscosity are the primary factors influencing the dynamic response of pipelines. Density, in conjunction with bulk modulus, governs the inertial effects and dictates the speed of wave propagation in the fluid. The friction losses in the conduit are determined by the pipe dimensions and viscosity. To get a ballpark figure for the pressure drop caused by fluid-to-pipe wall friction in laminar flow, we can use: (121) $\Delta p_r = \frac{128\mu L}{\pi d^4} q_v$.

Where μ represents the dynamic viscosity and d_p represents the pipe diameter (Watton 2009). In many cases, the pressure loss

in a laminar flow in a pipe can be described by comparing it to an electrical circuit, where voltage represents pressure and current represents electrical current. This is followed by the hydraulic resistance, R_h . (122) $R_h = \frac{128 \nu p l}{\pi d_p^4}$, To employ kinematic viscosity (ν), μ is replaced by $\nu \rho$. The inertial effects of the fluid in a conduit are captured by (123) $\Delta p_i = \frac{l \rho}{A_p} \frac{d q_v}{dt}$. Fluid mass inertia, or hydraulic inductance L_h , is analogous to the electric circuit. Inductance is defined as the following and describes the impact of pressure difference on changes in flow rates: (124) $L_h = \frac{l \rho}{A_p}$, where the cross-sectional area of the pipe, A_p , is determined by the fluid density, ρ , and the length of the pipe, l . The change of volumetric flow is the quantity of compression of a fluid: (125) $\Delta q_v = q_{vin} - q_{Vout} = \frac{V_p}{K_f} \frac{dp}{dt}$, where K_f is the fluid bulk modulus and V_p is the pipe volume. The hydraulic capacitance C_h , or compressibility of fluid, is the ratio of volume to bulk modulus, following the same analogy: (126) $C_h = \frac{V_p}{K_f}$. Hydraulic resonators, like Helmholtz resonators, can be used to handle pressure pulsations and oscillations in fluid power applications. The components of a Helmholtz resonator are a tube and a cavity. A hydraulic resonator's operation is predicated on either attenuating the pressure pulsation through resonance or absorbing it. (Ortwig 2005) determined that the pressure amplitudes in particular frequency ranges can be attenuated or amplified using resonators. Nevertheless, experimental testing is frequently necessary for resonator sizing and tuning (Josef Mikota 2002). The rigidity of hydraulic cylinder systems would be reduced by reducing the pressure oscillation brought on by an external force. By using a reflecting resonator, such a T-pipe, to enhance the pressure oscillation, a cylinder's dynamic stiffness can be increased by resonance. However, the frequency range at which T-pipes operate is extremely limited. Additionally, a hydraulic cylinder system's stiffness is greatly decreased in all frequency ranges except for a particular one by the additional oil volume of resonators. When one end of a fluid line is plugged, antiresonances happen. The plugged end of the pipe reflects the pressure wave as it passes through it. Resonance is achieved by varying the length of the T-line. If a fluid line is half the wavelength or an even multiple of half, a plugged fluid line attenuates pressures, as (127) $l_f = \frac{n\lambda}{2} = \frac{na}{2f}$; $n = 1, 2, 3, 4, 6, \dots$ where the wavelength is represented by λ , the frequency is given by f , the wave propagation velocity by a , and the pipe length by l_f . When the T-line is in resonance, or when the T-line length is an odd multiple of the wavelength, the pressure oscillation is amplified: (128) $l_f = \frac{n\lambda}{4} = \frac{na}{4f}$; $n = 1, 3, 5, \dots$ The result is $l_f = 16,25$ m when a practical wave propagation velocity value of $a = 1300$ m/s and frequency of $f = 20$ Hz are substituted for mineral oil. The pipe length would therefore need to be 16.25 meters in order to improve the stiffness of a cylinder system and intensify the pressure pulsation at 20 Hz. Significant capacitances and inductances in hydraulic components can be handled using a lumped model technique.

The hydraulic resonant frequency is estimated as follows: (129) $f_n = \frac{1}{2\pi\sqrt{L_h C_h}}$. Throughout the volume and length of the components, the inductances and capacitance are distributed in practice. Any dynamic hydraulic system should be built to prevent unwanted vibrations in the hydraulic flow due to operational conditions, such as loads and structural vibrations. In hydraulics, transients are abrupt pressure waves or surges that follow an immediate change in fluid flow (Yuce and Omer 2019). Pump failures, fluid line openings or closures, and valve movement are common causes of pressure transients (Bosselman et al. 2008). In pipeline systems, particularly in water distribution networks, pressure transients are extensively researched (Ghidaoui et al. 2005). Potential pressure transients could harm the components and eventually lead to failure if they are not appropriately addressed in the design of pipeline systems. By (Funk, Wood, and Chao 1972), transient responses in fluid power systems are also examined. Transients should ideally travel through a fluid medium at the

speed of sound, which is: (130) $a = \sqrt{\frac{K_f}{\rho}}$. Transient pressure waves are reflected from closed-end pipes in a hydraulic system because of hydraulic capacitance and fluid compression. In hydraulic systems, the piping lengths primarily determine the frequency response of pressure transients.

3.7.2. One way flow control valve and mechanical stiffness:

The movement rate of hydraulic actuators in hydraulic systems is contingent upon the flow rate. Thus, regulating fluid flow is essential to controlling hydraulic system velocities. In hydraulic systems, flow control valves are frequently implemented to regulate flow. (Mobley 2000) demonstrated numerous varieties of flow control valves available, and the application must be taken into consideration while choosing a valve type. To modify the flow in a single direction, one-way flow control valves are used. One fluid line is furnished with an adjustable orifice, while the other is a flow bypass line with a check valve. The valves are composed of these two fluid lines. The check valve line permits unrestricted flow from 2 to 1, while the adjustable orifice permits control over flow from 1 to 2. After the valve, cavitation is usually avoided by the bypass line.

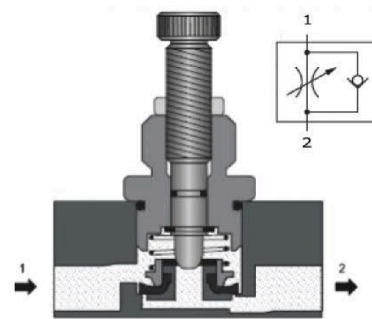


Figure 81: One-way flow control valve section and symbol

The most common components of check valves are a spring and a poppet. The geometry and shape of the poppet can vary, including spherical, conical, and planar forms. Poppet closes due to spring force. The valve opens, permitting flow through, when a specific pressure differential is achieved. Cracking pressure is the pressure differential required to overcome the spring's force. Pressure losses increase with high cracking pressures. An optimal check valve totally inhibits flow reversal; yet, the inertia, friction, and potential dampening effects of the poppet result in a slight closure of the valve following flow reverse.

In hydraulic cylinder systems, one-way flow control valves can be used to modify a cylinder piston's velocity. More flow can pass through to the other direction thanks to the integrated check valve, while the adjustable orifice limits flow to one direction. In order to prevent cavitation in fluid lines and cylinder chambers, appropriate flow control valves must be connected to both cylinder ports. The cylinder system becomes more rigid due to the flow limitation.

The steel joints and components that make up hydraulic cylinder systems are generally more stiffer than hydraulic fluids. As a result, although not always significant, mechanical stiffness components contribute little to the static net rigidity of hydraulic cylinder systems. This section discusses sealing system stiffnesses, cylinder rod stiffnesses, and pipe, hose, and cylinder chamber expansion stiffnesses.

A simple way to calculate the axial stiffness K_r of the solid steel cylinder rod is as follows: (131) $k_r = \frac{EA_r}{l_r}$ where E represents the

Young's modulus of steel, A_r denotes the cross-sectional area of the rod, and l_r indicates the length of the rod. The head and rod chambers have differing cylinder barrel expansion stiffness. The expansion stiffnesses of the head and rod chambers, k_{cA} and k_{cB} correspondingly, are determined in (Feng et al. 2017)

study as follows: (132) $k_{cA} = \frac{E_b A}{2l_A} \frac{1}{\lambda_c + v_b}$ and (133) $k_{cB} = \frac{E_b A}{2l_B} \frac{1}{\lambda_c + v_b}$

where E_b denotes the Young's modulus of the cylinder barrel, A represents the effective piston area, l indicates the effective chamber length, λ_c signifies the expansion coefficient of the cylinder barrel, and v_b is the Poisson's ratio of the cylinder barrel. For a cylindrical structure, the expansion coefficient is (134) $\lambda_c = \frac{D_1^2 + D^2}{D_1^2 - D^2}$, where D_1 represents the outer diameter and D denotes the inner diameter. The equation for the expansion stiffness of metal pipes is as follows (135) $k_p = \frac{2E_p A^2}{\pi D_p^2 l_p (\lambda_p + v_p)}$ where

E_p denotes the Young's modulus of the pipe, A represents the effective piston area, l_p indicates the length of the pipe, λ_p signifies the expansion coefficient of the pipe, and v_p is the Poisson's ratio of the pipe. Equation (136) can also be used to determine the expansion stiffness of hoses by replacing the pipe values with the appropriate hose parameters. The

expansion stiffness for hoses is as follows: (136) $k_h = \frac{2E_h A^2}{\pi D_p^2 l_p (\lambda_h + v_h)}$

The Young's modulus of the hose is represented by E_h . But

hydraulic cables have more than one layer. They usually have a rubber layer on the inside, a steel winding or braiding on the outside, and an anticorrosive rubber layer on top. Even the designs of steel braiding vary, as do the thicknesses and the amount of layers. Consequently, it is difficult to precisely determine the elasticity modulus E_h of a hydraulic hose since it is nonlinear. An estimated modulus of elasticity of 17.8 GPa was derived from experimental data. It should be mentioned that no information regarding the types of braiding was provided, and the figure was obtained from a single measurement made at a pressure of 160 bar. For hose stiffnesses in general, the resulting elasticity modulus can only be utilised to obtain an approximate value.

3.7.3. Friction effects models of hydraulic cylinder:

When two objects touch, friction is the force that acts in a tangential direction. It depends on many factors, including the shape and topology of the contact, the materials on the surfaces, the relative motion and displacement of the two things contacting each other, and the presence of lubrication (Olsson et al. 1998). This has resulted in challenges in formulating precise friction models and has introduced uncertainty in friction modelling (H. Lu 2022).

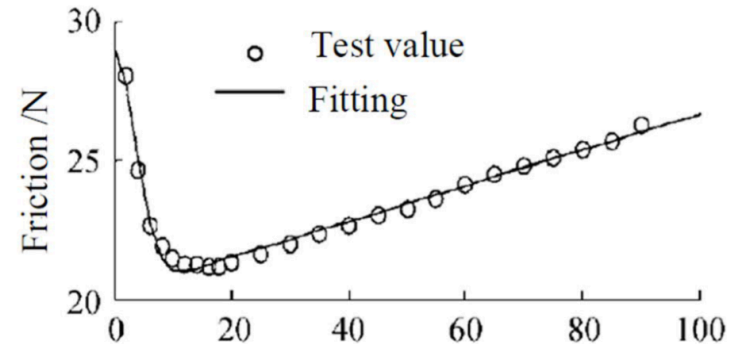


Figure 82: Comparison of LuGre Curve Fitting to Empirical Values (Wu et al. 2020)

Friction in hydraulic cylinders is mostly caused by the rod and piston sealing systems. The LuGre model is a commonly utilised dynamic friction model for hydraulic cylinders. When modelling friction properties, it provides a fair balance between accuracy and complexity. In the accompanying figure, the correctness of the LuGre model is demonstrated. The model accounts for the majority of the static and dynamic phenomena that result from friction.

The contacting surfaces in the LuGre model are simplified by viewing the friction surfaces as elastic bristles, which are represented as spring-damper systems in the figure below. Because of the surfaces' roughness, the bristles symbolise the microscopic peaks and valleys of the touching surfaces.

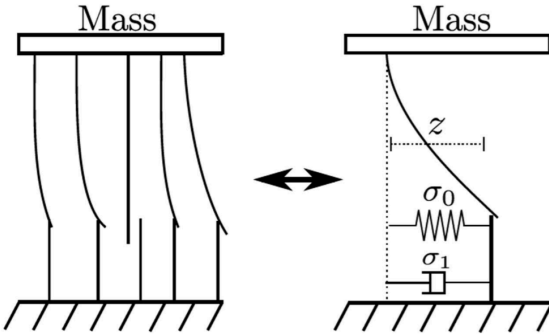


Figure 83: LuGre bristle modeling (Fuhg and Fau 2019)

(137) $z' = v - \sigma_0 \frac{|v|}{g(v)} z$, (138) $F = \sigma_0 z + \sigma_1 z' + f(v)$ where v is the relative velocity between the contacting surfaces, z is the average bristle deflection, F is the friction force, σ_0 is the bristle stiffness, σ_1 is the bristle damping, $f(v)$ is the viscous friction, also referred to as the damping term, and $g(v)$ is a velocity dependent function that accounts for the Stribeck effect and Coulomb friction. The viscous friction term $f(v)$ is frequently represented as a linear damping element: (139) $f(v) = \sigma_2 v$, where σ_2 represents damping. The function for Coulomb friction and the Stribeck effect, $g(v)$, is frequently approximated

by (140) $g(v) = F_c + (F_s - F_c) e^{-\left|\frac{v}{v_s}\right|^\alpha}$, where C is a geometry dependent coefficient, F_c is the Coulomb friction force, F_s is the static friction force, and v_s is the Stribeck speed, which indicates how quickly $g(v)$ approaches the Coulomb friction (Johanastrom and Canudas-de-Wit 2008).

By studying the steady state friction with constant velocities experimentally, the functions $f(v)$ and $g(v)$ can be obtained. (Johanastrom and Canudas-de-Wit 2008) is the formula that determines the steady state friction force F_{ss} for constant velocities:

$$(141) F_{ss} = g(v) \operatorname{sgn}(v) + f(v)$$

Subsequently, ascertaining the average spring and damping coefficients of the bristle, denoted as σ_0 and σ_1 correspondingly, results in the comprehensive friction model. Literature contains information on the material properties, the spring and damping coefficients.

Dynamic sealing systems, or reciprocating seals, are employed in hydraulics to avert hydraulic fluid leakage and to exclude pollutants. Efficiency, lifespan, and isolating qualities are always traded off in hydraulic cylinder sealing solutions. A higher level of seal squeezing, for instance, is necessary for effective isolation properties; however, this lowers lubrication, which accelerates seal wear. As a result of higher friction force, mechanical efficiency falls while volumetric efficiency rises. The increasing desire for more efficient systems has led to extensive study on sealing systems.

The guiding and sealing elements' contact surfaces of hydraulic cylinders rub against one another. As seen in (Figure 83-84), it should be mentioned that piston and rod sealing systems frequently have several sealing and guiding components, frequently made of various materials and profiles. Predicting

friction forces in hydraulic cylinders is challenging due to variations in material characteristics and cross-sectional shapes. Experimental investigation is thus necessary for an appropriate friction analysis.

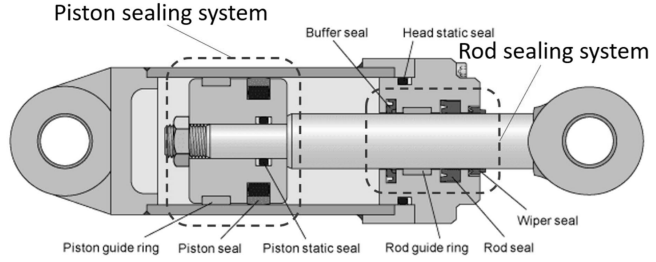


Figure 84: An example of both a rod and a piston sealing system

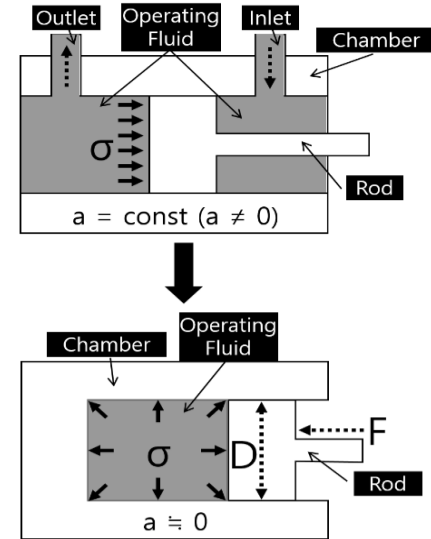


Figure 85: Equivalent condition of hydraulic cylinder to thrust force

One technique for numerically examining the fluid-structure interaction is FSI analysis. In other words, as illustrated in Figure above, the load, pressure, and temperature brought about by flow are transferred to a structure, and data regarding deformation is then reflected in the flow once more, which is then repeated.

This is identical to the way hydraulic cylinders work, in which motion is produced when the compressor introduces the cylinder's internal working fluid to the inlet and subsequently allows it to escape to the outlet. Thus, the fluid structure interaction (FSI) analysis is used to generally verify the working fluid flow characteristics and the stress applied to the structure. Nevertheless, this approach necessitates the assignment of all flow boundary conditions and the analysis of all dynamic features. Consequently, as analytical complexity and duration grow, analysis accessibility decreases. A streamlined approach to analysis can solve this issue.

In this context, this study examined the operational features of the TBM to compute the pressure generated in the cylinder's working fluid due to the thrust force. The company's TBM's

hydraulic cylinder has a forward speed of 57 mm/min, which propels the machine forward at a rate of about 1 mm per second.

Furthermore, aside from the initial acceleration, it advances at a steady pace, indicating that the acceleration converges on zero. Even in dynamic motion states, objects in motion can be statically analysed if their acceleration is zero, as illustrated in (Figure 85). This is employed to determine the pressure that is produced within the fluid. In a hydraulic cylinder, the area and force are often used to determine the pressure. This means that the entire chamber is under continual pressure. Pascal's principle, which is as follows, can be used to compute the pressure σ applied to the fluid, assuming that a constant pressure is applied to the whole area of the chamber.

(32) $\sigma = F/(0.25 \times \pi D^2)$ In this case, D stands for the chamber's internal diameter and F for the force. Table 1 lists the hydraulic cylinder parameters that the company uses. The thrust force that is used in a single cylinder ranges from 250 to 390 kN. This is used to determine the pressure caused by the thrust force, which is seen in Figure.

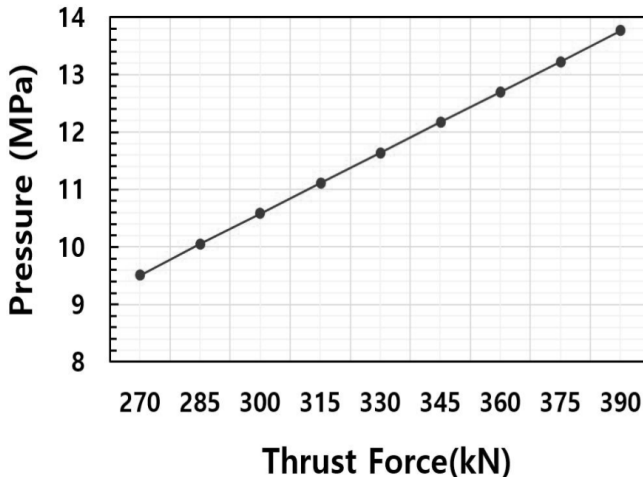


Figure 86: Pressure in theory based on thrust force

Table 13 : Specification of thrust jack

No.	Name	Unit	Value	Description
1	Number of cylinder	Set	12	-
2	Maximum Unit	kN	1000	-
	Thrust Force			
3	Stroke	mm	1750	-
4	Extending Speed	mm/min	57	All jacks extending
5	Inner Diameter	mm	95	-

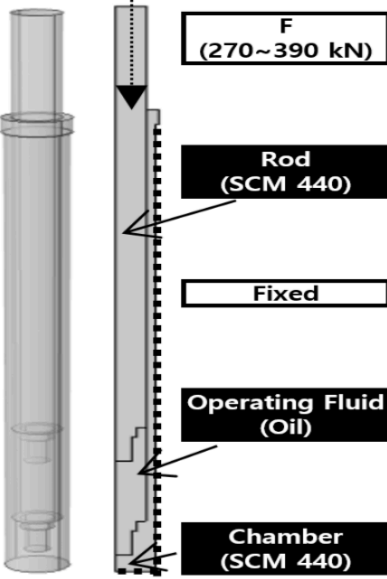


Figure 87: Analysis conditions

The hydraulic cylinder employed by the business, seen in figure above, had a chamber and rod that made up the analysis model. The purpose of this study was to examine the pressure that developed in the non-compressive oil working fluid inside the Software COMSOL Multiphysics. The cylinder was made of SCM 440. The physical properties are detailed in Table 13. The rod was moved solely in the direction of the chamber in this configuration, while the entire body remained fixed. The movement in the circumferential direction was restricted by the roller condition that was applied between the cylinder and chamber.

A thrust force was applied in the Y-axis direction, ranging from 270 kN to 390 kN, with increments of 15 kN. Figure below illustrates that the force was incrementally increased for a duration of 0.5 seconds and subsequently maintained after one second.

As seen in (Figure 87), the mesh has a free tetrahedral configuration. By the time the analysis values began to converge, it had 153,449 nodes. Furthermore, the mesh that had not achieved convergence was regenerated using the adaptive mesh refinement function to enhance the accuracy of the analysis. The analysis period, which did not include the working fluid's input and outlet, was zero to ten seconds with one-second chamber increments. It also included the stress caused by the pressure.

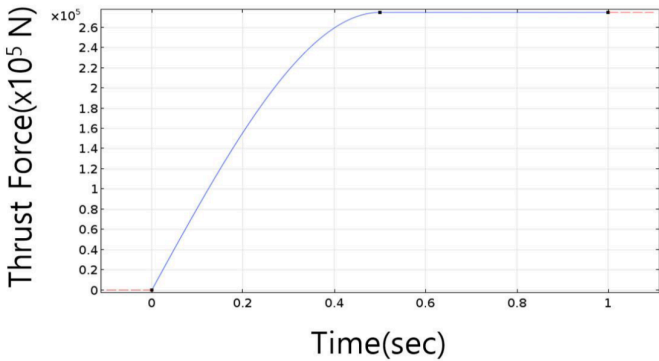


Figure 88: Graph representing thrust force with respect to time

Table 14: properties of the oil (SCM 440)

Property	Value	Property	Value
Elastic Modulus (GPa)	190	Dynamic Viscosity (Pa.s)	0.024
Poisson's Ratio	0.29	Dynamic Viscosity (Pa.s)	0.024
Density (kg/m ³)	7700	Density (kg/m ³)	880
Yield Strength (MPa)	590	Density (kg/m ³)	880

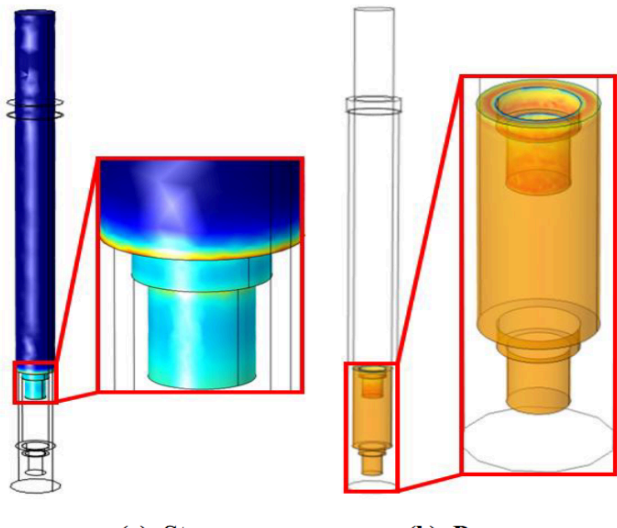


Figure 89: analysis results of cylinder thrust under stress and pressure.

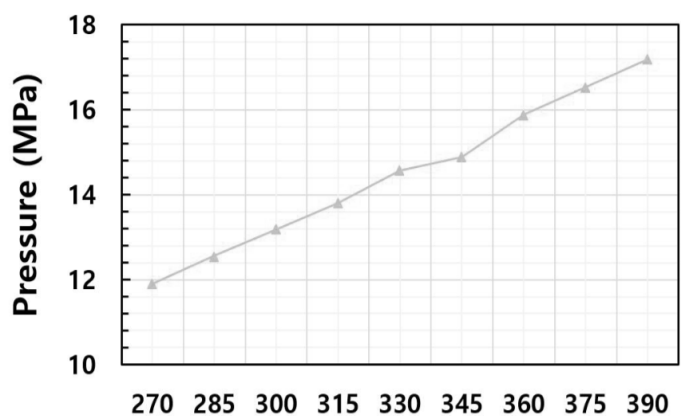


Figure 90: Analysis result according to thrust force

Pressure was generated when a force was exerted on a non-compressive fluid within the hydraulic cylinder utilised by the company. This pressure was determined during the FSI analysis, with the force fluctuating between 270 and 390 kN. At 390 kN, the study results confirmed that the maximum stress and fluid pressure were, respectively, 28 and 12 MPa. This cylinder was considered stable as the yield stress of SCM 440 was known to be 570 MPa. Experiments were conducted in accordance with this outcome, and the experimental results were compared to the theoretical and analytical results.

3.8 Power-hydraulic command and control system

With a high installed power, the shield tunnelling machine can operate under a variety of loads. A smooth and stepless modulation of the thrusting pressure and pace is highly desired (Maidl et al. 2013). This hydraulic system operates based on the principles of proportionate pressure and flow regulation, wherein the fluid flow into and out of each grouped cylinder is managed by suitable valve input configurations. As shown in Figure bellow, the output of variable displacement pump 1 in the main hypertension line is responsive to working pressure. The thrust system is divided into six identical groups to lower the control system's complexity and expense. Using electro-hydraulic proportional valves, one control group's control principle is shown in Figure 91 bellow.

A proportional flow control valve 3 and a proportional pressure relief valve 4 are included for each group, as seen in the figure below. Regardless of fluctuations in system or load pressure, the combination hydrostat maintains a steady level of pressure differential across the proportional valve, making the flow rate via valve 3 nearly constant. Additionally, the distributed fluid flow partially traverses valve 4 to maintain a consistent system pressure. By modulating the electric current through the coils of the valves, the system's pressure and flow rate can be calibrated to satisfy the thrust specifications. When the impetus is applied, the solenoid an of directional valve 2 is activated, causing the valve to move to the left in order to

propel the piston rod of the cylinder forward. Pressure sensor 7 and displacement sensor 6 continuously detect the pressure and displacement of the hydraulic cylinder. The programmable logic controller (PLC) 8 central control system receives the measured signals, which are then compared to reference input signals to apply flow control and pressure control, respectively. The valve 2 can be in the proper position *a* to propel the hydraulic cylinder rod when the shield stops to erect the tunnel lining.

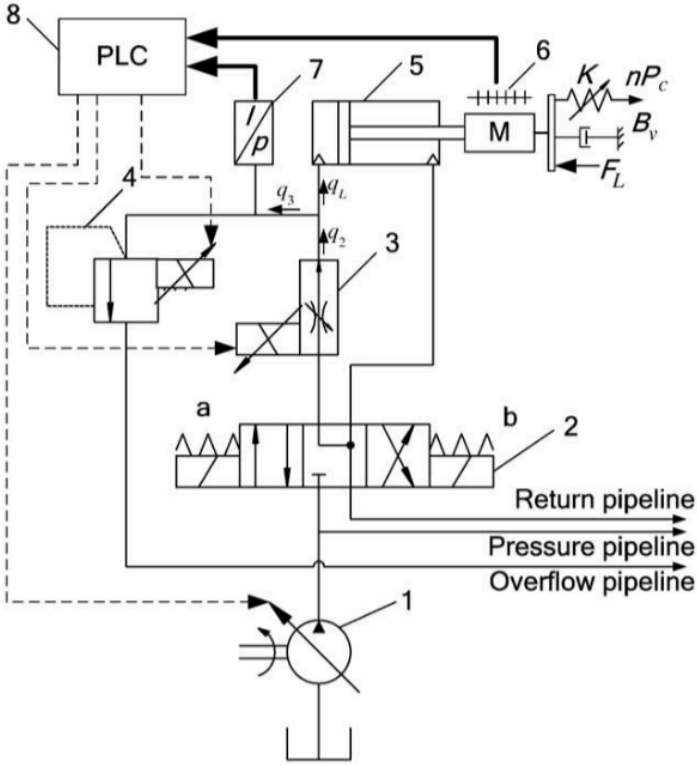


Figure 91: Thrust hydraulic system schematic diagram.

The thrust cylinders in each group are managed in a consistent manner; therefore, they can be regarded as a single cylinder with a sectional area that is the aggregate of the sectional areas of each cylinder in the group. As such, the mathematical model of a single group of cylinders can be derived as follows. As the oil flows through the orifice of the throttle valve, which is situated within valve 3, the propelling process can be represented as: (138) $q_2 = k_{q2}y_2$, q_2 = flow rate (m^3/s), k_{q2} = flow gain, pressure drop across the throttle valve.

$$(139) F_{M2} = m_2 \frac{d^2y_2}{dt^2} + D_2 \frac{dy_2}{dt} + k_2 y_2, \quad \text{since}$$

F_{M2} = output force of the solenoid valve 3,

m_2 = mass of the spool, D_2 = coefficient of viscous friction, k_2 = stiffness of spring. In the event that the outlet pressure is zero due to the overflow conduit being connected to the oil tank, the oil flow through valve 4 is (140) $q_3 = K_{q3}y_3 + K_{p3}p_L$ since K_{p3} = flow pressure coefficient, p_L = load pressure, the

dynamic equation of the spool is expressed as:

$$(141) p_L A_3 - F_{M3} = m_3 \frac{d^2y_3}{dt^2} + D_3 \frac{dy_3}{dt} + k_3 y_3,$$

A_3 = effective acting area (m^2) of the poppet,

F_{M3} = the acting force of the solenoid of valve 4, m_3 = mass of the moving body D_3 = coefficient of viscous friction, K_3 = total stiffness of the spring. The derived equation of the flow can be marked as: (142) $q_L = q_2 - q_3 = A \frac{dx}{dt} + C_{tc} P_L + \frac{V}{E} \frac{dp_L}{dt}$ where the cylinder flow is denoted by q_L , A is the effective working area, x is the cylinder displacement, C_{tc} is the coefficient of leakage, V is the total actuating volume, and E is the effective bulk modulus.. The dynamics equation of the cylinder is:

$$(143) A_{PL} = M \frac{d^2x}{dt^2} + B_v \frac{dx}{dt} + Kx + F_L \quad \text{the load force, } K, \text{ the viscous damping coefficient, and the total mass of the moving parts are all given by } M, B_v, \text{ and } K, \text{ respectively. The derivative equation can be used to characterise the current dynamics across the proportional solenoid coil the following way:}$$

(144) $u(t) = L \frac{di}{dt} + iR + K_v \frac{dy}{dt}$. where K_v is the coefficient of velocity back electromotive force caused by armature displacement, R is the total resistance of coils and amplifier, u is the voltage, L is the inductance, i is the current, and J is the current. The output electromagnetic force can be expressed as the following due to the proportional solenoid's approximately linear current-force characteristics: (145) $F_M = K_F i$ since F_M is the electro magnetic and K_F known for the current force gain.

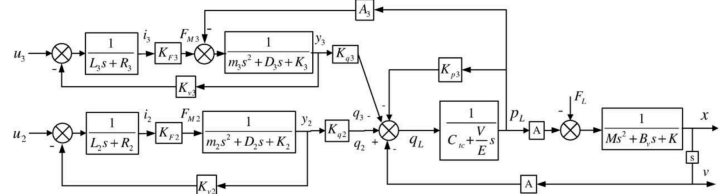


Figure 92: Block diagram of the thrust displacement/velocity system control.

The interaction between the tunnelling shield and the soil-ground-water conditions is a critical factor in the successful completion of EPB tunnelling. Typically, tunnelling must contend with a variety of soil types in order to achieve a planned alignment (Matsushita 1980). So, in order to accommodate the geological conditions, the thrust force and pace must be adjustable. Pressure, which is related to force, and flow, which is related to velocity, are intrinsically coupled in fluid power transmission. Consequently, when one is altered, the other is influenced. The pressure and flow compound control technique is essential for achieving a desirable performance in tunnel drive control. Additionally, the open-loop control is unable to ensure adequate accuracy in the presence of excavation uncertainties. Consequently, pressure and speed feedback are required to mitigate the impact of the various perturbations on the shield's performance (Hu 2006; H. Yang et al. 2009).

The thrust motion in the forward direction is depicted in Figure above, which is the control block diagram of one group in the propulsion system. Pressure and flow control are superfluous for the erection of the segments in order to facilitate the rapid return of the cylinder. A displacement sensor situated within the cylinder measures the thrust distance, which is subsequently converted to a velocity parameter that is transmitted back into the input signal of the flow control valve. In the same vein, the pressure sensor completes the closed-loop control. The errors are generated and subsequently transmitted to the controllers by comparing the reference signals and the feedback signals. The modifications to the flow rate and pressure are implemented simultaneously.

Because of its satisfactory performance, the conventional three-term PID strategy has been extensively implemented in industrial processes. Two PID controllers, as illustrated in Figure below, are employed in the thrust control system to mitigate the detrimental consequences of internal parameter changes, such as fluid volume in cylinders, and external disturbances, such as load variation. The next section's purpose is to look into a simple and effective driver for the system. If the error signal is denoted as $e(k)$, the conventional discrete PID can be expressed as:

$$(146) u(k) = K - pe(t) + K_i \sum_{j=0}^k e(j) + K_d(e(k) - e(k-1)) \text{ where}$$

K is the gain, k known for the integral factor, K_d derivative factor, $u(k)$ is the output of sample controller period k . $e(k)$ stands for the error in sampling period k and $e(k) = r(t) - y(t)$ since reference input signal and output signal for the control system respectively for $r(t)$ and $y(t)$.

$$(147) \Delta u(k) = Ae(k) - Be(k-1) + Ce(k-2) \text{ since}$$

$$A = K_p + K_i + K_d, B = K_p + 2K_d, C = K_d$$

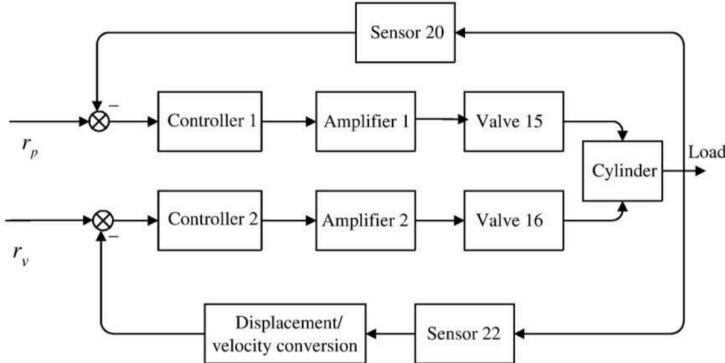


Figure 93: diagram of the thrust control system.

Nevertheless, the dynamic performance of the control system can be compromised by the large integral action, which can cause the system output to saturate. Consequently, the following equation can be obtained: sectional proportional integrated derivative (PID) control law is an appropriate solution to the issue.

$$(147) \Delta u(k) = \begin{cases} A_1 e(k) - B_e(k-1) + Ce(k-2), & |e(k)| > \varepsilon \\ Ae(k) - B_e(k-1) + Ce(k-2), & |e(k)| \leq \varepsilon \end{cases}$$

When ε is the integral threshold, $A_1 = K_p + K_d$

The standard Ziegler–Nichols closed-loop tuning approach (Nise 2019) can be employed to readily determine the optimal PID controller parameters. $G(s)$ is the system transfer function, $G_p(s)$ and $G_q(s)$ are the transfer functions of the pressure relief valve and flow control valve, respectively, and u_1 and u_2 are the reference input signals of pressure and flow rate, while p and v are the outputs. The velocity feedback gauge is denoted by K_2 , while the pressure feedback gain is denoted by K_1 .

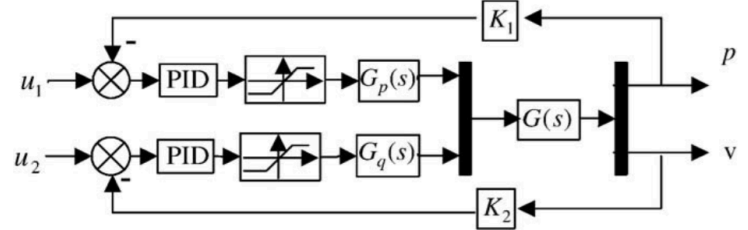
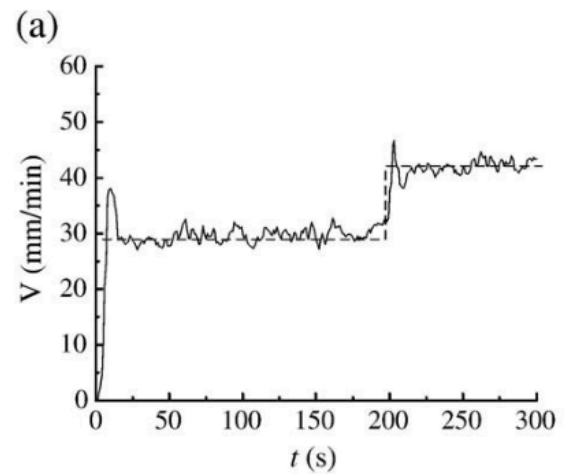


Figure 94: Pressure and velocity control system block diagram.

The experimental results of the thrusting velocity and pressure when the input value of velocity and pressure is shifted are illustrated in the figures below. The dashed lines are added to indicate the set value of the parameters. It is important to note that the curves are not smooth due to the uneven distribution of the tested soil in the experiment box (Hu Gl, Yang, and Others 2005). The findings imply that the shield's thrust hydraulic system, which was previously mentioned, may achieve its objectives with respectable dynamic performance. However, fluctuations and impacts are inevitable to a certain extent due to the nonlinearity of soil and the high weight of the shield.



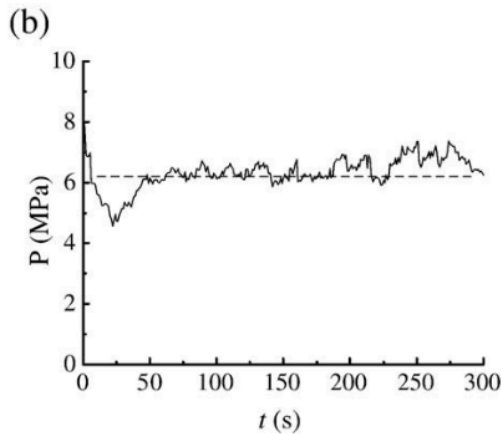


Figure 95: Velocity and pressure curves in the experiment of velocity adjustment.

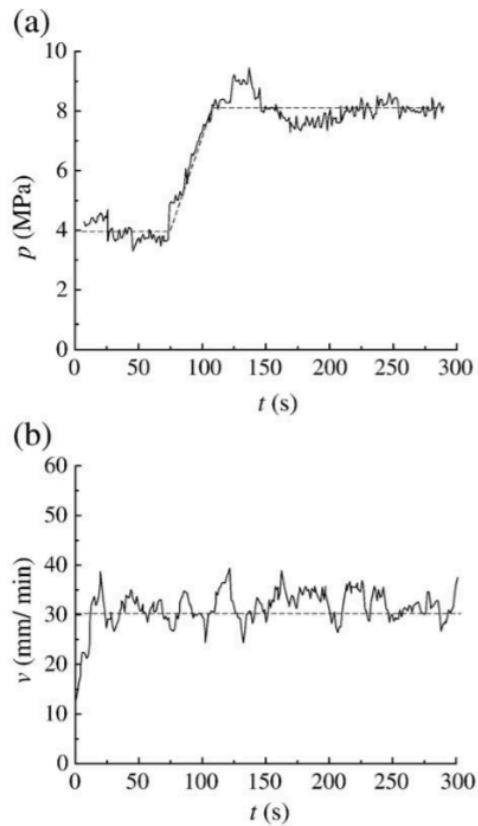


Figure 96: Pressure and velocity curves in the experiment of pressure adjustment.

In hydraulic-powered heavy-duty applications, synchronising several linear hydraulic actuators under load can significantly impact performance (H. Sun and Chiu 2002). While tunnelling in straight lines, hydraulically operated shield thrust systems experience this difficulty more while under strong loads. Typically, there are three techniques to handle the issue. Step one is to construct a flow divider circuit, which is limited by the flow divider and the compressibility of the working fluid. The

second option involves mechanically connecting actuators, raising system complexity. The closed-loop electro-hydraulic synchronisation system used in this paper is the third. To ease operation and improve precision the elast method is the most adequate one.

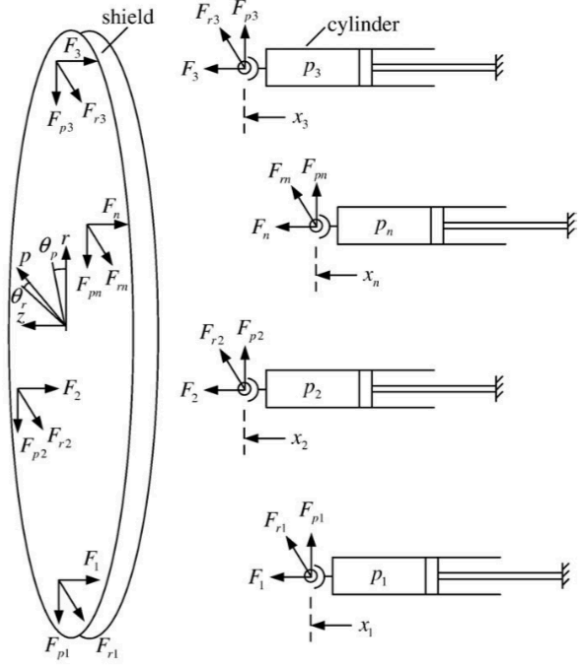


Figure 97: Force diagram for n-cylinder hydraulic thrust system.

$$\begin{aligned}
 (148) \quad & - \sum_{i=1}^n F_i - \sum_{i=1}^n F_{ri} \sin \theta_r - \sum_{i=1}^n F_{pi} \sin \theta_p = m \ddot{x}_p \\
 & \sum_{i=1}^n (F_i + F_{ri} \sin \theta_r (-1)^{\sigma_{ri}} l_{ri}) = J_r \ddot{\theta}_r \\
 & \sum_{i=1}^n (F_i + F_{pi} \sin \theta_p (-1)^{\sigma_{pi}} l_{pi}) = J_p \ddot{\theta}_p
 \end{aligned}$$

When the hydraulic cylinder extension is zero, the centre of the load is represented by $x_p = 0$. m represents the overall load mass. In Equation (148), F_i is the reaction force on cylinder i ($i = 1, 2, \dots, n$), and l_{ri} (or l_{pi}) is the moment arm for F_i with respect to rotational axis r (or axis p). σ_{ri} (or σ_{pi}) indicates the moment factor ($= 0$ when F_{ri} is left of axis r , 1 otherwise; σ_{pi} alike), J_r (or J_p) represents the load's rotational inertia about axis r , and θ_r (or θ_p) represents the rotation angle. F_{ri} (F_{pi}) indicates the friction force between load and cylinder along axis r (or p). To express the equations of motion for cylinders, consider the forces F_i ($i = 1, 2, \dots, n$) acting on them:

$$(149) \quad p_i A_i - F_i - F_{fi} - B_{pi} \dot{x}_i - \sum_{i=1}^n F_{ri} \sin \theta_r - \sum_{i=1}^n F_{pi} \sin \theta_p = m_i \ddot{x}_i$$

$i = 1, 2, \dots, n$. p_i is cylinder i is chamber pressure and A_i is its effective piston area. M_i denotes the piston mass of cylinder i .

F_{fi} represents stiction, whereas Bpi displays viscous friction and coefficient. Use the following equation to simulate the contacting effect of dirt ahead of the shield when thrust:

$$(150) F_i = F_{si} + k_i x_i + b_i \dot{x}_i,$$

where the force F_{si} is the force generated by earth pressure at rest in the vicinity of the acting point. i. x_i indicates the position of cylinder group i in relation to the tunnel lining ring. Each cylinder group's fluid flow is controlled by a flow control valve. The pressure dynamics in each cylinder can be described by the following equation, ignoring valve dynamics and leakages, but considering fluid compressibility:

$$(151) \dot{p}_i = \frac{\beta}{V(x_i)} [-A_i \dot{x}_i - K_{cei} p_i - K_{pqi} x_{pi} + K_{fqi} u_{qi}], \quad \text{where}$$

$K_{cei} = K_{ci} + C_{ti}$, $x_{pi} = \frac{K_{ui} u_{pi}}{s^2 + 2\xi_l \omega_n s + \omega_n^2}$. β denotes the working fluid's bulk modulus, V_i represents the entire fluid volume in a cylinder chamber, and C_{ti} indicates the leakage coefficient. K_{ci} and K_{pqi} represent the flow pressure and flow coefficients of the pressure relief valve in group i. Group i flow control valve flow coefficient is K_{fqi} . u_{pi} and u_{qi} are the pressure and flow valve control input signals. Group i pressure valve poppet displacement is x_{pi}

3.8.1. Synchronisation of motion control

The electro-hydraulic propulsion system of the shield utilises a closed-loop control technique with a master/slave strategy, as depicted in Fig. 8, accounting for fluctuations in loads, fluid volume in cylinders, and fluid viscosity.

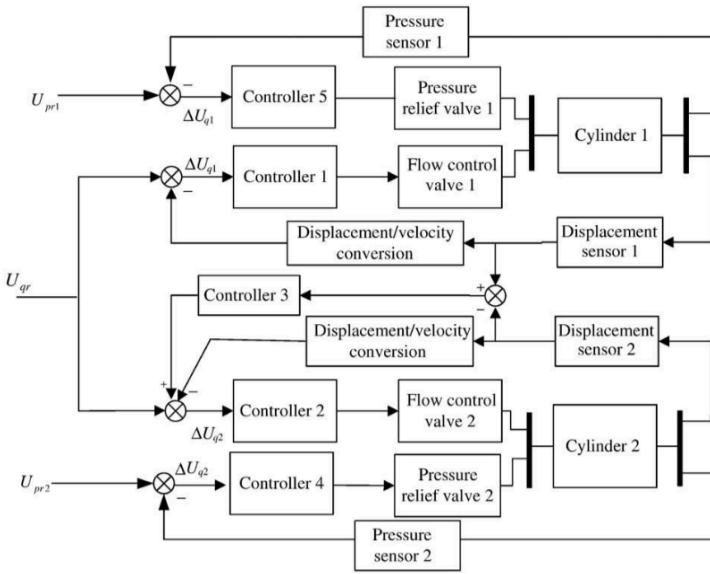


Figure 98: Diagram of the motion synchronization

This discussion pertains to two symmetric cylinders, as this method is particularly effective for managing multi-cylinder systems in which one cylinder serves as the master and the others as captives. The block diagram simultaneously achieves

synchronisation control in addition to the pressure and speed constraints previously mentioned. Cylinder 1 operates as the master, cylinder 2 as the slave, and controller 3 acts as a displacement compensator for synchronisation control. As the reference cylinder, Cylinder 1 must move in tandem with Cylinder 2. Controller 3 is a proportional integral derivative controller with a dead band that prevents oscillations that are the result of an excessive number of modifications. The control parameters, seen in (Figure 98), can be characterised as

$$p(t) = \begin{cases} e(t), & \text{When } |e(t)| = |y(t) - r(t)| > \varepsilon \\ 0, & \text{When } |e(t)| = |y(t) - r(t)| \leq \varepsilon \end{cases}$$

where ε is a variable band parameter, $r(t)$ is the input, $y(t)$ is the output, and $e(t)$ is the error signal. It fundamentally corresponds to a nonlinear control methodology. Two displacement sensors quantify the displacements of two cylinders, which are subsequently subtracted from each other. The displacement error provided to controller 3 will be verified to determine if it lies within the allowable error limit, sometimes referred to as the dead band. In order to accompany cylinder 1 in displacement, controller 3 uses an embedded proportional integral derivative control method to add its output value to the reference input of cylinder 2 flow regulation.

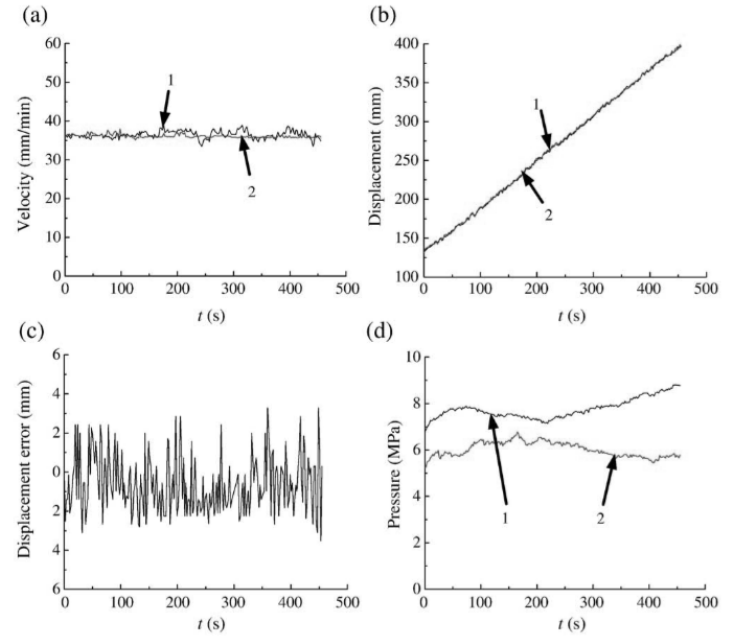


Figure 99: Two symmetric cylinders' synchronised motion behaviour was measured.

3.9 Ground Stability and Settlements

The goal of the numerical model is to replicate the movement and relaxation of the soil that results from a tunnel boring machine's overcutting and grouting of the tunnel void around the shield and lining annulus. In order to do this, the model makes use of a pressure relaxation technique that gradually

lowers the tunnel support pressure from the initial state of rest until a failure point is identified(Shiau et al. 2023).

It is crucial to assess the stability of tunnelling as it is being built. Equation (1) illustrates how this is most frequently determined using the stability number (N) that Broms and Bennermark (1967) (Broms and Bennermark 1967) suggested. They conducted a pilot study to investigate the clay soil's plastic movement through retaining wall vertical apertures. The experimental investigation of a tunnel face supported by internal air pressure was further expanded upon by Mair (1979) (R. J. Mair 1979):

$$(152) N = \frac{\sigma_s - \sigma_t + \gamma(C+D/2)}{s_u} \text{ where } \sigma_t \text{ indicates the interior tunnel}$$

pressure and s indicates the surface pressure. D is the diameter of the tunnel, and C is its cover. s_u and s stand for the soil's unit weight and undrained shear strength, respectively in equation (152). (R. J. Mair 1979) proposed upper and lower bound solutions for tunnel wall support with internal air pressure utilising dimensionless parameters. The goal was to determine the limiting value of a pressure ratio ($s = \sigma - \sigma_t + \gamma C + P/2 s t / s_u$) based on independent parameters like depth ratio (C/D) and strength ratio (D/s_u). (Sloan 2013)finite element limit analysis (FELA) techniques have been used in numerous studies on subsurface stability. Equation (2) defines a new stability number N for the tunnel, where s represents surface surcharge pressure and t represents interior tunnel pressure.

$$(153) N = \frac{\theta_s - \theta_t}{s_u} = f\left(\frac{C}{D}, \frac{\gamma D}{s_u}\right) \text{ The assurance ratio, defined as } (\sigma_s - \sigma_t)/s_u, \text{ is dependent on independent parameters such as:}$$

(155) $N = f\left(\frac{C}{D}, \frac{\gamma D}{s_u}\right)$. By structuring the equation in this manner, it facilitates the development of practical stability charts that are beneficial for design purposes. These dimensionless ratios enable the application of the findings from this study to various scenarios that may differ physically, yet where the soil strength ratio and depth ratio remain within the parametric domain. In accordance with the works of (Wilson et al. 2011)and (Shiau et al. 2023), the parameters utilised in this research are $D/s_u = 1-5$ and $C/D = 1-5$. This range encompasses the majority of realistic values, providing a thorough analysis and ensuring that the resulting design charts are relevant to a wide array of tunnel design and analysis challenges.

Conversely, ground surface settlement caused by tunnelling is a multifaceted phenomenon influenced by numerous factors, including soil and groundwater conditions, tunnelling dimensions, and construction methodologies. Consequently, contemporary tunnelling research has focused on enhancing the prediction of soil responses to stress alterations resulting from tunnel construction by deriving analytical solutions for these challenges mentioned by (Rankin 1988).

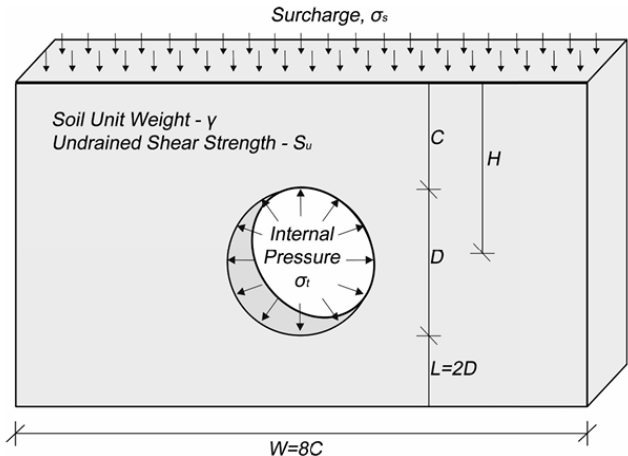


Figure 100: Calculation approach diagram(Shiau et al. 2023).

3.9.1. Pressure relaxation techniques:

Tunnelling, despite being a complex three-dimensional issue, can be effectively simplified to two-dimensional plane strain conditions by considering a transverse section and assuming the existence of a very long tunnel, as illustrated in (Figure 100) above. The tunnel is characterised by a soil overburden C and a diameter D . The soil mass is represented as a uniform Tresca material, possessing both an undrained shear strength (s_u) and a specific unit weight (γ).

In (Peck 1969) research, a strong correlation was observed between experimental and observational findings. The method relies on the input of a trough parameter (i_x), which impacts the physical width of the profile and links the volume loss to the maximum settlement, as outlined in Equation (4).

$$(156) S_x = S_{max} e^{-\frac{x^2}{2i_x^2}}, (157) V_S = \sqrt{2\pi} i_x S_{max}, (158) I_x = 0.5 D^{0.2} H^{0.8},$$

$$(159) I_x = 0.57 \left(\frac{C}{D}\right)^{0.8}, (160) I_x = 0.29 \left(\frac{H}{D}\right) + 0.5, (161) I_x = KH$$

Estimation of the inflection point parameter (i_x) have been attempted by many researchers, with the most notably by: (Clough and Schmidt 1981) for the equation (156), equation (157) by (Mair and Taylor 1999), also i_x is calculated by (C. J. Lee, Wu, and Chiou 1999) and ("Settlements above Tunnels in the United Kingdom-Their Magnitude and Prediction," n.d.) in equation (160).It proposed that i_x is linearly related to the to-axis tunnel depth after examining data gathered from London's tunnels shown in formulae (159).

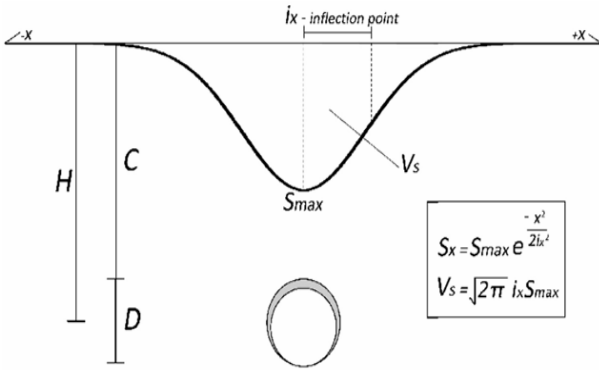


Figure 101: Typical tunnel settlement issues

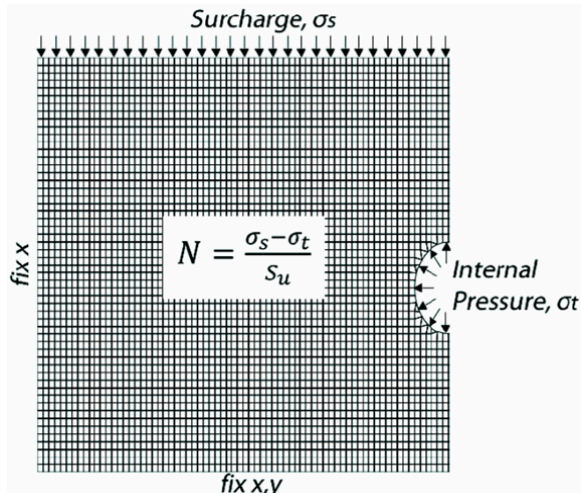


Figure 102: Typical mesh of the problem.

It is important to recognize that the aforementioned methods mentioned in the (Shiau et al. 2023) research are empirical in nature and lack comprehensive definitions based on pertinent design parameters. Consequently, designers may struggle to attain a high degree of confidence in their design endeavours. This paper aims to establish a numerical process that will facilitate a thorough investigation of the effects of the following dimensionless parameters: $D/S_u = 1-5$, $C/D = 1-5$, and $E/S_u = 100-800$. By utilising these dimensionless parameters, it will be possible to generate detailed design charts for practical applications within the specified range.

The breaking point takes place when, at a given relaxation stage, the unbalanced forces are unable to achieve a zero equilibrium. The collapse stage, or point instability, can be recognized by looking at the history of imbalanced forces. It can also be found using software tools like ANSYS, and it can be shown in velocity graphs and plasticity indicators.

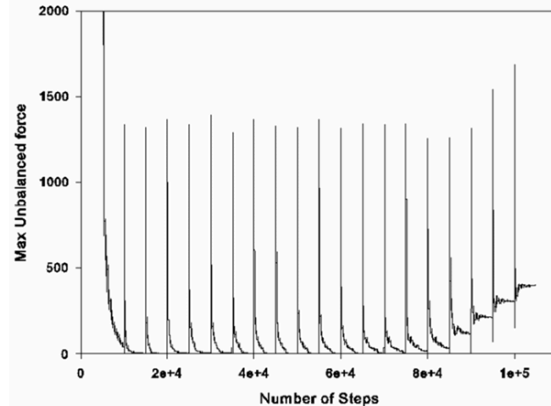


Figure 103 Unbalanced force history plot

$(C/D = 3, \gamma D/S_u = 4, E = 200S_u)$

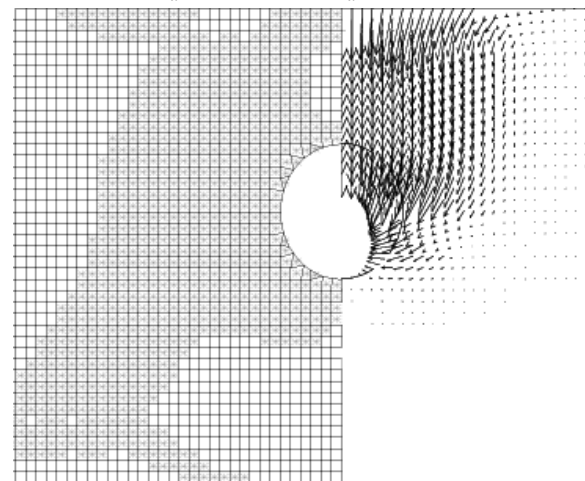


Figure 104: Plasticity (left), and velocity (right) plots at the stage of collapse $(C/D = 1, \gamma D/S_u = 3)$

3.9.2. Stability Results

Equation (157), which calculates the greatest stability number that leads to collapse, can be reasonably and accurately calculated using the internal pressure relaxation approach in conjunction with a small relaxation interval (amount relaxed per step). It should be noted that the pressure relaxation strategy will always overstate the stability number at collapse by a little amount since the internal pressure is lowered in discrete increments instead of continuously (Shiau et al. 2023). Unless the internal pressure at that point is higher, the pressure inside at the "collapse stage" will have been slightly more relaxed than necessary.

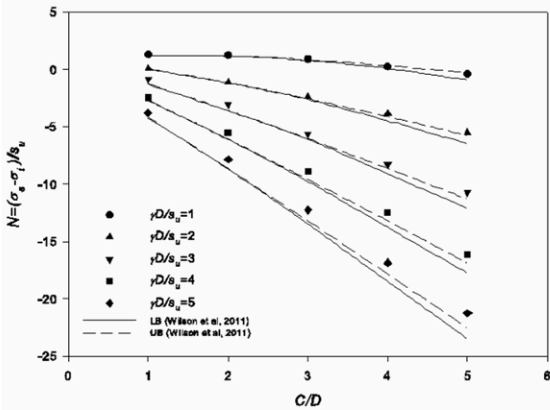


Figure 105: Comparison outcomes using additional proposed equations.

When comparing the stability numbers (N) at collapse, the pressure relaxation method is consistent with FELA solutions (Wilson et al. 2011), as (Figure 105) illustrates. Note that the tunnel would need a negative internal pressure σ_t (or a pulling pressure) to reach the point of impending collapse if the stability number were positive, e.g., if $\gamma D/S_u = 1$ for $C/D = 1, 2$, and 3 . It is regarded as stable in theory and doesn't need any internal pressure to stay that way. A reduction in soil strength, represented by a rise in $\gamma D/S_u$, results in negative values for the stability number. The equation $(\sigma_s - \sigma_t)/S_u$ indicates that in the case of a negative stability number, σ_t must have a positive value. This implies that a positive "pushing" pressure is necessary to avert an impending collapse.

Keep in mind that when C/D increases, the stability number (N) falls off assuming a fixed value of D/S_u . Additionally, it is evident that when the strength ratio D/S_u increases for a constant C/D , the stability number N drops. These findings suggest that higher values of the depth ratio C/D and strength ratio D/S_u (softer soils) would require higher levels of internal pressure management. Observe that when C/D increases, the stability number (N) falls for a fixed value of $\gamma D/S_u$. Additionally, it is evident that when the strength ratio $\gamma D/S_u$ increases, the stability number N falls for a constant C/D . These findings suggest that higher levels of the depth ratio C/D and strength ratio $\gamma D/S_u$ (softer) would need increased internal pressure control.

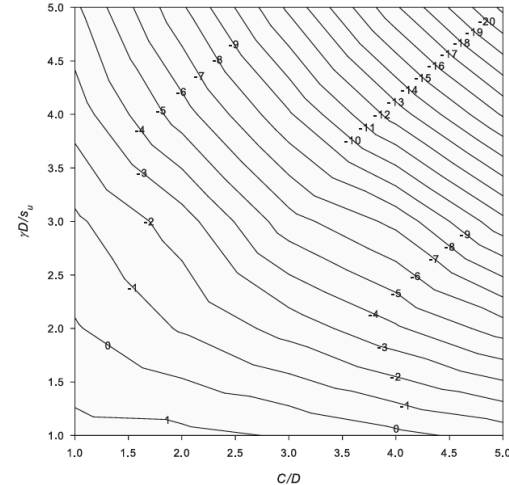


Figure 106 : $N = (\sigma_s - \sigma_t)/S_u$ is the contour plot of the crucial stability numbers found in this investigation.

The (Figure 106) above shows a design chart that has been constructed. With the strength ratio (D/S_u) and depth ratio (C/D) data, users may easily calculate the critical stability number $N=(s-t)/S_u$ for their design requirements. This is useful since it shows the collapse bound, which is one under the assumption of a safety factor. The surface regression of these data is given by (Equation 159), which shows these data with a $r^2 = 0.99$.

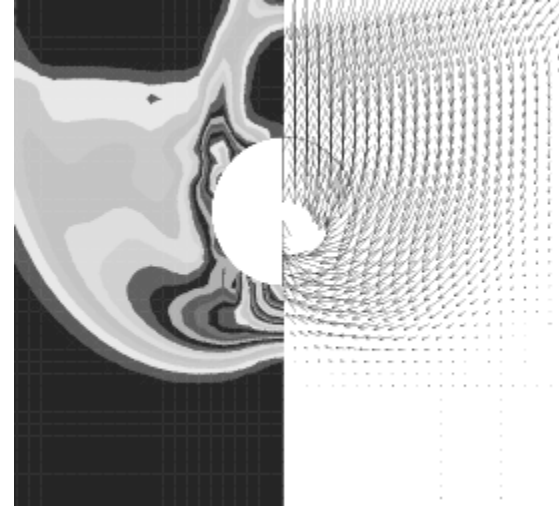


Figure 107: Shear strain rate (SSR) and velocity plot for $C/D = 1$, $\gamma D/S_u = 5$. (Shiau et al. 2023)

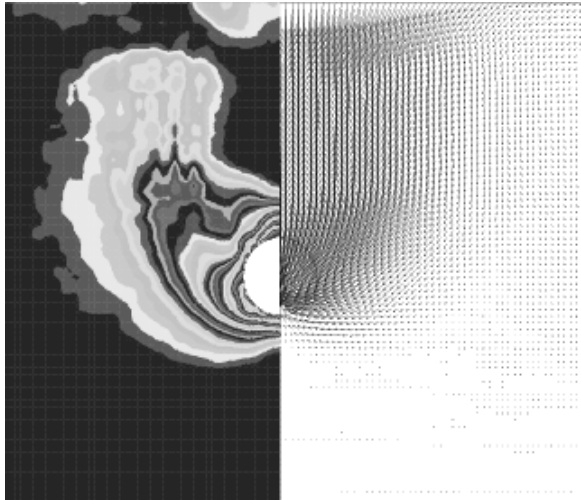


Figure 108: Shear strain rate (SSR) and velocity plot for $C/D = 3$, $\gamma D/Su = 5$. Figure 12. Shear strain rate (SSR) and velocity plot for $C/D = 3$, $D/Su = 1$

3.10. Prestressed anchors for tunnels and the design principles of arch effect.

A research conducted by (P. Li et al. 2023) The force distribution of the prestressed anchor and its parameter design are investigated. The surrounding rock is mechanically analysed using the bearing arch hypothesis. In order to confirm the prestressed anchor's ability to regulate the surrounding rock, the support structure created using this technology is then deployed to the engineering site for displacement monitoring. In order to control significant deformation of the surrounding rock, it offers a theoretical reference for prestressed anchor installation.

As seen in (Figure 109), the tunnel surrounding rock is separated into three zones based on the fracture of the surrounding rock: the elastic zone, the plastic softening zone, and the loose zone. After the tunnel is excavated, the shallow rock mass begins to fracture again, generating new fractures that eventually grow to create a loose circle (with a radius of R_0). If the stress is greater than the rock's bearing capacity, large plastic deformation occurs, which is mainly characterised by an area of devastation that reaches the deepest part of the surrounding rock (where R_p is the radius of the plastic zone).

Following this, the rock surrounding the tunnel enters an elastic stable region, which absorbs the remaining excess stress and primarily exhibits elastic deformation with a strong capacity for recovery. Based on the failure and deformation characteristics of the tunnel's surrounding rock, the support provided by anchors can be categorised into three scenarios. In the diagram, R_m represents the effective anchorage zone depth of the prestressed anchor. When the anchor's anchorage range exceeds the loose zone ($R_m > R_0$), the surrounding rock experiences a good support effect. (Figure 109) illustrates three elastic-plastic zoning modes of bolt support. As depicted in

(Figure 109a), when $R_m < R_0$, the bolt's anchorage range is less than that of the loose circle, rendering it insufficient to maintain the stability of the surrounding rock.

(Figure 109c) shows that as the bolt length increases, the support cost rises, and the effectiveness of bolt support becomes limited. Taking into account support costs and other factors, we believe that the second supporting situation (Fig. 109b) offers a more cost-effective solution whilst effectively controlling the stability of the surrounding rock.

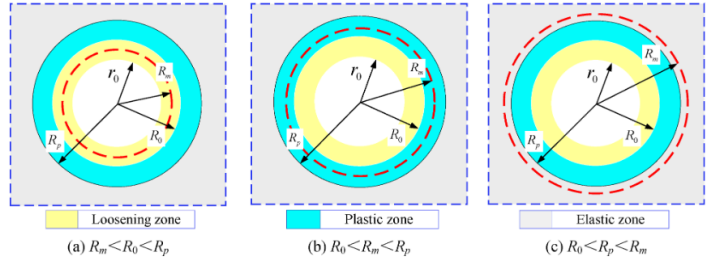


Figure 109: Three conditions of surrounding rock support

3.10.1. The Relationship Between Ground, Tunnel, and Shield Support

(Ramoni and Anagnostou 2006) used a numerical solution method that simulated tunnel excavation by monotonically emptying the tunnel border from its initial value, σ_0 , to zero. The stress-point algorithm was implemented by (Ramoni and Anagnostou 2008) to enhance this model in accordance with the "steady state method" of (D Minh and Corbetta 1991). This numerical procedure is used to solve problems with constant conditions in the tunnelling direction by taking into account a reference frame that is fixed to the advancing tunnel face. (Anagnostou 2007) and (Cantieni and Anagnostou 2009), respectively, provide a new description of the computational approach (including its continued development for poro-elastoplastic materials) and numerical comparisons with the sequential simulation of an advancing tunnel.

Instead of simulating many excavation and support installation processes, the steady state approach allows the advancing tunnel heading problem to be solved in a single computer step. The steady state approach is equivalent to the limit situation of an excavation with zero round length, as demonstrated by (Cantieni and Anagnostou 2009). As a result, it more accurately represents TBM advance than the step-by-step method that is frequently employed. The latter method necessitates the arbitrary selection of computationally manageable round length values of $s = 1-2$ m, which results in a significant underestimation of the shield and lining loading. The accuracy is enhanced, but the computer time is increased by selecting a reduced round length (e.g., $s = 0.5$ m, as discussed in Section 3.9.2). A thorough parametric study was conducted thanks to the steady state method's computational economy and numerical stability. Based on the study's numerical findings, design nomograms pertaining to shield loading and the thrust

force needed to overcome friction were developed for the various TBM types (Ramoni and Anagnostou 2010a). The ground behaviour was regarded as time-independent in each of these studies. While TBM advance is actually a continuous process, time effects were taken into consideration by (Einstein and Bobet 1997), and (Sterpi and Others 2007), who emphasised the fundamental effect of creep. These studies examined the consolidation processes related to the development and subsequent dissipation of excess pore pressures around the tunnel in a low-permeability water-bearing ground.

3.11. Computational Model of Tunnel Lining

This research presents numerical investigations utilising an axially symmetric model illustrated in the (Figure 110). Assuming a hydrostatic, isotropic, and uniform stress field, the criterion of rotational symmetry states that the tunnel must be deepseated. It is described as a flat, linearly elastic, perfectly plastic material that follows the Mohr–Coulomb yield criterion and a flow rule that is not connected to it.

Creep and consolidation processes have been overlooked.

Accordingly, the progressive advancement of the working face is thought to be the only cause of the spatial stress redistribution that causes the ground pressure and ground deformations to gradually grow in the longitudinal direction (Lombardi 1973). Similar to previous studies by the authors (refer to Sect. 2.3), the numerical calculations were conducted utilising the steady state method (D Minh and Corbetta 1991). (Ramoni and Anagnostou 2010a) are recommended reading for those interested in learning more about the computational model and a discussion of the underlying assumptions. The current section of the paper concentrates on the modelling of the interface between the barrier or lining and the ground.

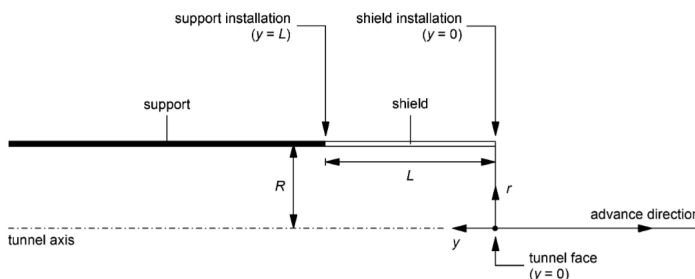


Figure 110: Layout of the issue differential lining installation of the shield (Ramoni and Anagnostou 2011).

An accurate simulation of the two support elements "shield" and "tunnel support" must consider the following: (161) their distinct installation points ($y = 0$ and $y = L$ in Figure bellow respectively) and (162) the fact that the shield and tunnel support experience smaller displacements than the ground at any given point y in the tunnel wall. The pre-deformation of the ground advance of the tunnel face $u(0)$ and the overcut ΔR that is typically present between the shield and the excavation

boundary are the reasons for this. To account for these factors, a mixed and non-uniform boundary condition is implemented for the tunnel wall. This condition is generally expressed as:

$$(161) p(y) = \begin{cases} f_s(u(y)) & \text{if } 0 \leq y \leq L \\ f_s(u(y)) & \text{if } y > L \end{cases}$$

Where $p(y)$ represents the ground pressure that develops on the shield or lining, $u(y)$ represents the radial displacement of the earth at the tunnel boundary, and L represents the shield length.

and the displacement is described by the functions f_s and f_r the shield's resistance is contingent upon penetration. Consideration is given to the fact that the ground begins to apply a load on the shield only when the radial gap around it is closed, that is, when additional deformation of ΔR behind the face occurs, where ΔR is the size of the radial gap Figure bellow. The developing ground pressure p and the shield stiffness k_s are linearly dependent after the gap is closed, provided that the shield is capable of bearing the burden without being overstressed.

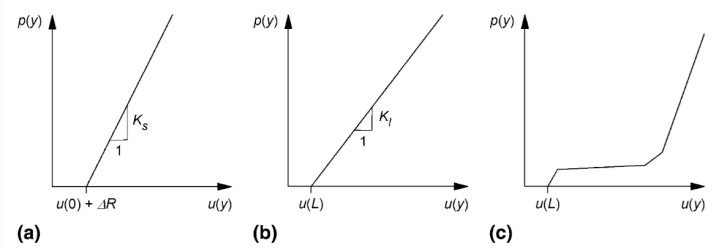


Figure 111: Boundary condition at the tunnel boundary for the simulation of: a shield, b stiff supports, c yielding supports

Shields may possess a "conical" shape. The shield's "conicity" is achieved through a gradual reduction in its diameter (Herrenknecht, Bäppler, and Burger 2010). This can be considered in the computational model by establishing a variable radial gap size, $\Delta R(y)$. For instance, the non-uniform mixed boundary conditions of Eq. 1 are generally expressed as follows: When the shield's conicity is achieved in two stages (Figure 111),

$$(162) p(y) =$$

$$\begin{cases} 0 & \text{if } 0 \leq y \leq L \text{ and } u(y) - u(0) \leq \Delta R(y) \\ K_s(u(y) - u(0) - \Delta R(y)) & \text{if } 0 \leq y \leq L \text{ and } u(y) - u(0) \leq \Delta R(y) \\ K_1(u(y) - u(l)) & \text{if } y > L \end{cases}$$

since :

$$(163) \Delta R(y) = \begin{cases} \Delta R_1 & \text{if } 0 \leq y \leq L_1 \\ \Delta R_2 & \text{if } L_1 < y \leq L_2 \\ \Delta R_3 & \text{if } L_1 < y \leq L_2 \end{cases}$$

(164) $u_{1,1-2} = \varepsilon_{t,1-2} R$ where R is the tunnel radius and $\varepsilon_{t,1-2}$ is the hoop strain. The hoop strain $\varepsilon_{t,1-2}$ is the ratio of the ring's initial circumference C to the reduction in circumference ΔC_{1-2} caused by the tangential deformation of both elements (161) and (162).

$$(165) \varepsilon_{t,1-2} = \frac{\Delta C_{1-2}}{C} = \frac{\Delta C_{sc} + \Delta C_{ce}}{2R\pi},$$

$$(166) \Delta C_{sc} = \varepsilon_{t,sc} C_{sc} = \frac{\sigma_{t,sc}}{E_{sc}} (2R\pi - n_{ce} d_2),$$

E_{sc} = young's modulus of shotcrete ,

n_{ce} = number of deformable concrete elements ,

d_e = height of deformable elements all incorporate into the shotcrete. $\sigma_{t,sc}$ = hoop stress, N_{sc} = hoop forces ,

$$(167) \sigma_{t,sc} = \frac{N_{sc}}{b'd_1} \leq f_{s,sc},$$

b = width of shotcrete, between steel sets

d_1 = thickness of shotcrete layer ,

$f_{c,sc}$ = uniaxial compressive strength of shotcrete ,

ΔC_{ce} = reduction of the arc length, (168) $\Delta C_{ce} = \varepsilon_{t,ce} C_{ce} = \varepsilon_{t,ce} n_{ce} d_2$,

The hoop strain $\varepsilon_{t,ce}$ depends on the hoop stress $\sigma_{t,ce}$,

$$(169) \varepsilon_{t,ce} = f(\sigma_{t,ce}),$$

$$(170) \sigma_{t,ce} = \frac{N_{ce}}{b'd_1} \leq f_{c,ce},$$

$f_{c,ce}$ = maximum compressive stress, (171) $N_{1-2} = N_{sc} = N_{ce}$

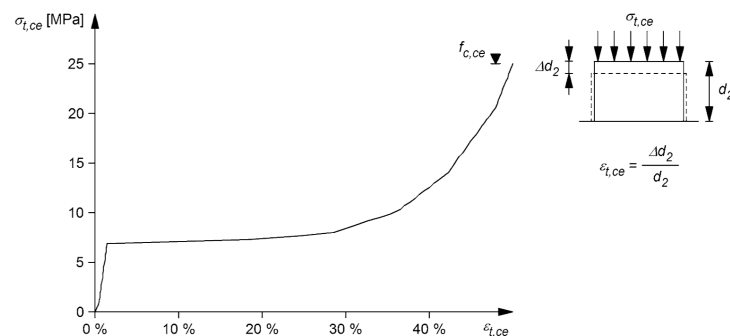


Figure 112: The anticipated load deformation behaviour of the high-ductility concrete elements

$$(172) u_{1,3} = \varepsilon_{t,3} R,$$

$$(173) \Delta u_{1,3,i} = \Delta \varepsilon_{t,3,i} R$$

$\Delta u_{1,3,i}$ = the increase of the radial deformation, $\Delta \varepsilon_{t,3,i} = \frac{\Delta C_{3,i}}{C}$, As previously indicated, the steel set is the sole component that undergoes deformation during phase A.

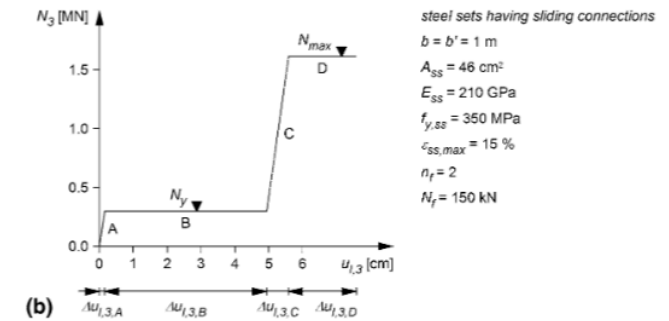
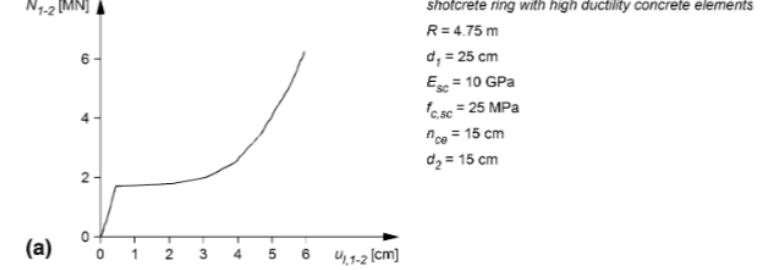
Consequently, $\Delta C_{3,A}$ is contingent upon the Young's modulus of the steel set E_{ss} and the increase in the hoop stress $\Delta \sigma_{t,ss,A}$ in the steel set (occurred in phase A). (174) $\Delta C_{3,A} = \varepsilon_{t,ss,A} C_{ss} = \frac{\Delta \sigma_{t,ss,A}}{E_{ss}} 2R\pi$,

(175) $\sigma_{t,ss,A} = \frac{N_y}{A_{ss}}$ The cross-sectional area of the steel set is denoted as A_{ss} . The yield load N_y is contingent upon the friction loop resistance N_y and the number of friction loops n_f of each sliding connection: $N_y = n_f N_f$. The sliding connections undergo deformation and closure during phase B. The circumference

$\Delta C_{3,B}$ is subsequently reduced in accordance with the maximum slot deformation and the number of slots: (176) $\Delta C_{3,B} = n_{ce} \frac{d_2}{2}$, In this instance, the number of spaces is equivalent to the number of deformable concrete elements, as the steel sets are utilised in conjunction with high ductility concrete elements. Their deformability must be taken into account when selecting the permissible slot deformation. The maximal slot deformation is equivalent to half of the height d_2 of the deformable concrete elements, as they become nearly rigid at a strain of $\varepsilon_{t,ce} = 50\%$ (see figure above). The reduction of the circumference $\Delta C_{3,C}$ is as follows for phase C, in which only the steel set deforms (the sliding connections are closed at the conclusion of phase B). (177) $\Delta C_{3,C} = \varepsilon_{t,ss,C} C_{ss} = \frac{\Delta \sigma_{t,ss,C}}{E_{ss}} 2R\pi$,

(178) $\Delta \sigma_{t,ss,C} = \frac{N_{max} - N_y}{A_{ss}}$ The yield load of the steel set N_{max} can be determined by multiplying the yield stress $f_{y,ss}$ by the cross-sectional area, A_{ss} , of the steel set: (179) $N_{max} = f_{y,ss} A_{ss}$. The steel set undergoes plastic deformation in phase D until the failure strain $\varepsilon_{ss,max}$ is attained. The reduction of the circumference $\Delta C_{3,D}$ is calculated by considering the elastic deformations that have already occurred in phases A and C, and presuming that the steel set does not experience hoop strain changes in phase B. (180) $\Delta C_{3,D} = \Delta C_{ss,max} - (\Delta C_{3,A} + \Delta C_{3,C})$, $\Delta C_{ss,max}$ is the utmost circumference reduction that the steel set can tolerate until it fails: (181) $\Delta C_{ss,max} = \varepsilon_{ss,max} 2R\pi$.

YS25/C15 Support System The parallel connection between the subsystems (161–162) and (163) can be accounted for by combining their hoop forces and equating their deformation: the relationship between hoop force N and radial displacement u for the entire system (161–162//163) can now be calculated.



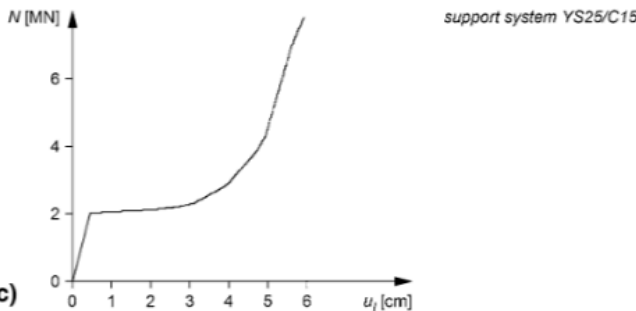


Figure 113: Hoop force N as a function of radial displacement u_l : a shotcrete ring with high ductility concrete elements, b steel sets with movable connections, and c YS25/C15 support system

$$(182) p \quad \boxed{N = N_{1-2} + N_3} \\ u_1 = u_{1,1-2} = u_{1,3}$$

$$(183) p = \frac{N}{Rb} \text{ when } b \text{ is the steel set spacing}$$

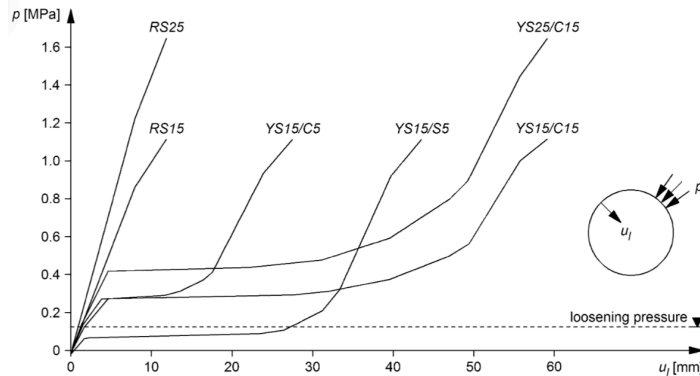


Figure 114: The investigated support systems' characteristic lines (ground pressure p as a function of the radial displacement of the lining u_l) are as follows:

3.11.1. Effect of Short Weaker Zones

The last section's numerical computations were predicated on the assumption of homogeneous ground in the longitudinal direction. However, the ground behaviour, as evidenced by the thrust force required to maintain the TBM's advancement during the TBM's drive in Uluabat, fluctuated at frequent intervals, suggesting a succession of unstable zones separated by periods of more competent ground.

The adjacent competent rock also has a stabilising effect with respect to the fault zone, as indicated by previous research on the mechanics of deformation in brief geological fault zones (Kovářík and Anagnostou 1995). The shear stresses are mobilised at the interface of the adjacent competent rock with the solitary weak zone when it is traversed, as the latter undergoes smaller deformations. The convergences within the weakened zone are diminished by the shear stresses, particularly when its length is short. This "wall effect" is also advantageous in terms of the risk of TBM blocking, as

demonstrated by (Matter et al. 2007) and in greater detail by (Graziani, Capata, and Romualdi 2007).

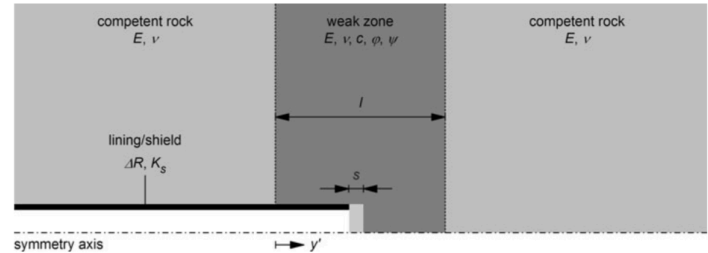


Figure 115: Step-by-step calculations were conducted to investigate the layout of the brief fault zone problem.

Contrary to the preceding section, the fundamental assumptions remain unchanged. Assuming linear elastic behaviour of the competent rock before and after the weak zone was a computational cost reduction strategy employed in the numerical investigations. The steady state numerical solution method was unable to be applied due to the non-uniformity of the conditions in the longitudinal orientation. Consequently, the tunnel excavation and support installation were modelled step-by-step using a step length s of 0.5 or 1.0 m.

In light of these factors, an investigation was conducted to determine whether the variability of the ground behaviour observed in Uluabat could be attributed to the presence of weak zones of varying extent. Additionally, an analysis was conducted to determine the impact of the length of a weak zone on the necessary thrust force.

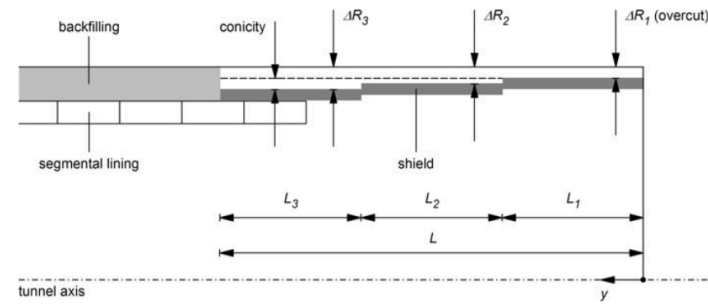


Figure 116: step reduction into shield diameter

The shield loading and, consequently, the thrust force necessary to overcome shield skin friction are underestimated as a result of the overestimation of the support pressure exerted by the lining behind the shield, which is caused by the longitudinal arch action in the ground around the shield. In addition, the simplified boundary condition assumes that the gap size ΔR remains constant throughout the shield and the lining. Consequently, it is incapable of mapping the perfect contact between the lining and ground that exists in certain instances from the outset (e.g., in the case of a gripper TBM with shotcrete support or a shielded TBM with annulus grouting occurring concurrently with the TBM's advance via the shield tail).

Numerical examples will be employed to analyse the interaction between the shield, the ground, and the tunnel support in the hypothetical scenario of a 400 m deep tunnel with a 10 m drilling diameter. A TBM with a single shield that is 10 meters long excavates the tunnel. The support is made of a segmental lining that is 30 cm thick and backfilled right away. Table 15 (Set 1) specifies the material constants.

The ground pressure exerted on the shield is critical for the structural design of the machine and for overcoming the frictional resistance during the advancement of the TBM.

Table 15 : Assumed parameters values based on recorded data

Set Figures

	1 (5-10)	2 (11)	3 (12)	4 (14-15)	5 (18)
$R (m)$	5.00	5.00	2.50	2.5	4.75
$\Delta R (mm)$	0-200	50	30/60/90/120	30	120
$L (m)$	6-12/ ∞	0-12	10/12	12	5
$K_s (MPa/m)$	1,008	1,008	2,688	2,688	558
$K_i (MPa/m)$	360	0/ ∞	2,688	2,688	Variable
$\sigma_0 (MPa)$	10	10	3	3	40
$E (MPa)$	1,000	2,000	200-1,000	2000 ^a 400 ^b	3,235
$\nu (-)$	0.25	0.25	0.2	0.20	0.3
$f_c (MPa)$	3.0	4.5	-	-	5.5
$c (kPa)$	-	-	500-400	200 ^b	-
$\varphi (\circ)$	25	25	20	20 ^b	35
$\Psi (\circ)$	5	5	1	1 ^b	5
$\mu (-)$	0.15/0.25/ 0.3/0.45	0.45	0.25/50	0.50	0.3
$F_i (MN)$	150	-	30/60	30	27.5
$F_b (MN)$	0/18	0	0	0	17
$s (m)$	-	-	-	0.5/1.0	-

a rock component *b* Weak Zone

When $L = \text{length of the shield}$, $K_s = \text{stiffness of the shield}$,

$K_i = \text{stiffness of the lining}$,

$f_c = \text{uniaxial compressive strength of the ground}$,

$\nu = \text{poisson's ratio of the ground}$, $c = \text{cohesion of the ground}$,

$\varphi = \text{Angle of internal friction of the ground}$,

$\Psi = \text{dilatancy angle of the ground}$,

$\mu = \text{shield skin friction coefficient}$, $F_i = \text{installed thrust force}$,

$F_b = \text{boring thrust force}$,

$s = \text{step length (step - by - step calculations)}$, $\sigma_0 = \text{initial stress}$

3.11.2. Effect of Shield Diameter

This section begins by discussing the convergences and pressures that develop along the tunnel, noting that the ground exerts pressure on the shield only after a specific amount of deformation has occurred. It also examines how the geometrical parameters of the shield affect the level of overstressing and the thrust force necessary to overcome friction. The purpose of this section is to demonstrate that the ground at the excavation boundary undergoes numerous discharging and reloading cycles, and that a gradual reduction

in the shield diameter is highly advantageous in terms of the ground pressure. Additionally, a quantitative discussion of the shield-ground interface's simplified model highlights the significance of accurately accounting for the geometrical features and the order of installation of the tunnel support and shield. The tunnel support's installation position and stiffness are crucial for both loading and shield pressure.

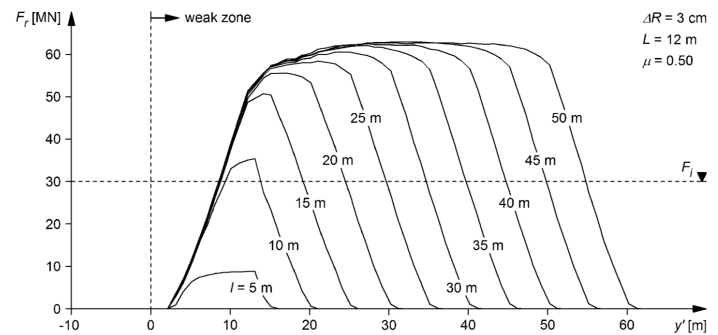


Figure 117: The required thrust force F_r is calculated as a function of the position y' of the tunnel face for varying lengths l of the vulnerable zone (step length $s = 1$ m, radial gap size $\Delta R = 3$ cm, shield length $L = 12$ m, skin friction coefficient $\mu = 0.50$, safety factor for the required thrust force SF = 1.0).

The required thrust force F_r is depicted in (Figure 117) above as a function of the tunnel face position y' , which is indicative of the onset of the critical zone. The contours are applicable to weak zones of varying lengths l . When the TBM enters the weak zone, the required propulsion force increases, as anticipated, and decreases when it exits. Given that the TBM is capable of managing a 5–10 m thick vulnerable zone, it would be able to overcome skin friction with nearly the entire installed thrust force of $F_i = 30$ MN. However, the TBM may become confined in the event of a weak zone that extends beyond approximately 10 meters. It is therefore possible that the observed variability is connected to a progression of rock zones that are weaker and stronger in succession. For step lengths s of 0.5 or 1 m, Figure below illustrates the maximal required thrust force F_r as a function of the length l of the weak zone. The wall-effect will be more pronounced and the danger of shield jamming will be lower as the weak zone becomes shorter. The wall-effect is particularly noteworthy in critical zones that are shorter than approximately 10–15 meters, which is equivalent to two or three tunnel diameters, as illustrated in (Figure 117). The results of the step-by-step solution are consistent with those obtained by the steady state method for lengthy fault zones and a step length of $s = 0.5$ m. Conversely, the adoption of a longer round length (e.g., $s = 1$ m) results in an underestimation of the required thrust force F_r (by 15% in this example) for the reasons outlined.

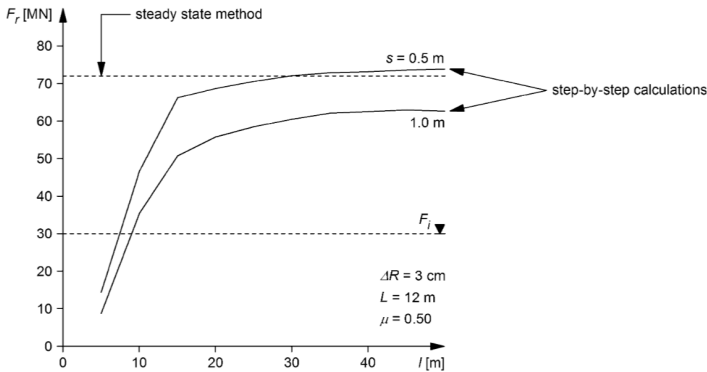


Figure 118: Maximum required thrust force F_r in the vulnerable zone as a function of their length l (radial gap size $\Delta R = 3$ cm, shield length $L = 12$ m, skin friction coefficient $\mu = 0.50$, safety factor for the required thrust force SF = 1.0)

Numerical examples will be employed to analyse the interaction between the shield, the ground, and the tunnel support in the hypothetical scenario of a 400 m deep tunnel with a 10 m drilling diameter. A TBM with a single shield that is 10 meters long excavates the tunnel. The support is made of a segmental lining that is 30 cm thick and backfilled right away. Table 1 above specifies the material constants.

The ground pressure exerted on the shield is critical for the structural design of the machine and for overcoming the frictional resistance during the advancement of the TBM. This section begins by discussing the convergences and pressures that develop along the tunnel (Sect. 3.11.2), noting that the ground exerts pressure on the shield only after a specific amount of deformation has occurred. It also examines how the geometrical parameters of the shield affect the level of overstressing and the thrust force necessary to overcome friction. The purpose of this section is to demonstrate that the ground at the excavation boundary undergoes numerous discharging and reloading cycles, and that a gradual reduction in the shield diameter is highly advantageous in terms of the ground pressure. Additionally, a quantitative discussion of the shieldground interface's simplified model highlights the significance of accurately accounting for the geometrical features and the order of installation of the tunnel support and shield. The tunnel support's installation position and stiffness are crucial for both loading and shield pressure.

3.11.3. Shield-Ground Interaction

For three values of the size ΔR of the radial gap between the shield and the ground, (Figure 119a) displays the radial displacement u of the ground at the tunnel boundary. The latter establishes the permissible level of convergence.

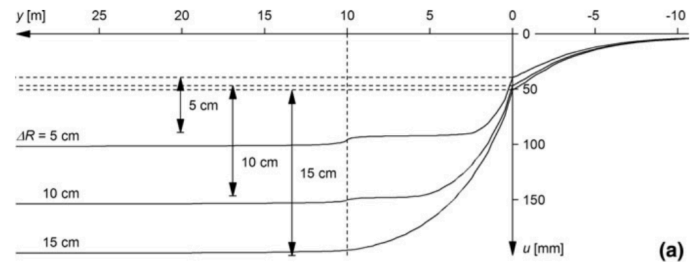


Figure 119 a: The radial displacement u of the ground at the tunnel boundary is the result of numerical computations for a 10 m long shield and an overboring ΔR of 5, 10, or 15 cm.

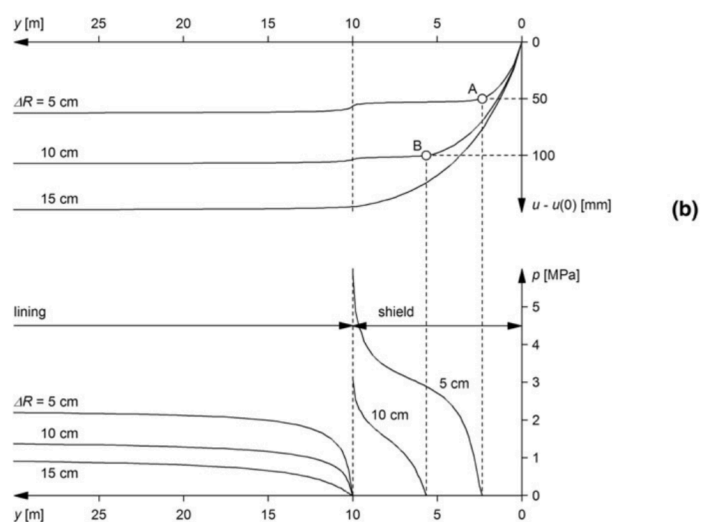


Figure 120 b: convergence of the weary profile $u - u(0)$

The convergence of the boring profile, denoted as $u - u(0)$ in (Figure 120b), is the sum of the radial displacements u , minus the so-called "pre-deformation" $u(0)$ that happens before the tunnel face. The ground closes the opening near the face (at point A, (Figure 120 b) in the event of a normal overcutting ($\Delta R = 5$ mm). For a prolonged period (up to point B, Figure 120b), a gap that is larger ($\Delta R = 100$ mm) remains open. The shield begins to be loaded by the earth after the gap is closed.

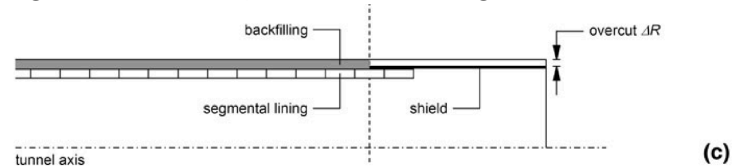


Figure 120 c: The shield and the lining are subject to ground pressure p , while the other parameters are as specified in Table 15.

Ground pressure pacing distribution on the shield and liner is illustrated in (Figure 120c). The ground pressure increases as the distance from the tunnel face decreases, as the stabilising effect of the core upstream of the face becomes less pronounced. It is possible to trace the load concentration at the

shield's end to the full unloading of the tunnel border at the lining installation site.

When a larger overboring is applied, the ground pressure p decreases for both the barrier and the lining, as anticipated. In this numerical example, the distance between the ground and shield would not close at all as a result of a very large overboring of $\Delta R = 15$ cm, and the shield would remain unloaded. It is important to acknowledge, however, that overboring technology is not yet fully developed and, as evidenced by the tunnelling experience, may be of limited reliability (Ramoni and Anagnostou 2010b). It is imperative to thoroughly evaluate the feasibility and reliability of a large overboring, particularly in the presence of hard rocks, as the extended gauge cutters may be subjected to extremely high pressures, which could jeopardise their structural integrity.

3.11.4. Thrust force:

The ground pressure P can be integrated over the shield surface, and the resulting integral can be multiplied by the skin friction coefficient μ to determine the thrust force F_r necessary to surmount shield skin friction. For two operating stages, "ongoing excavation" and "restart after a standstill," (Figure 9a) demonstrates how the required thrust force F_r changes as a function of the radial gap size ΔR . The TBM must surmount sliding during ongoing excavation, as opposed to static friction. However, additional thrust force F_b is required for the boring process (F_b was set to 18 MN in this example).

Following (Gehring 2020), the skin friction coefficient was determined to be $\mu = 0.15\text{--}0.30$ for sliding friction and $\mu = 0.25\text{--}0.45$ for static friction. The reduced friction coefficient values are intended to demonstrate the beneficial effects of lubricating the shield extrados, such as with bentonite. A thrust force of 150 MN is indicated by the line marked by F_r , which is both high and feasible. The required thrust force F_r is depicted in (Figure 9b) as a function of the shield length L for the two operational phases, with an overcut of $\Delta R = 50\text{--}150$ mm. The beneficial impact of a shortened shield is illustrated in the diagram. It is important to acknowledge that the relationship between the shield length and the propulsion force is generally non-linear.

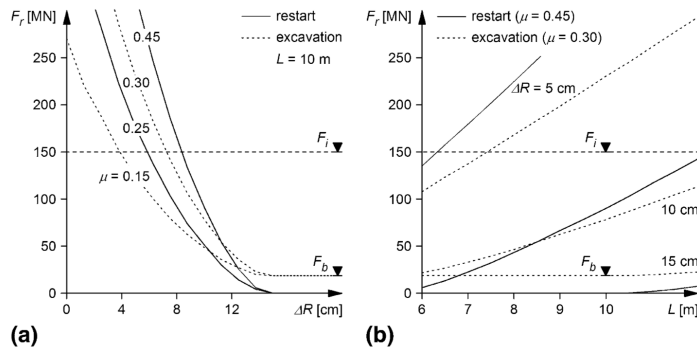


Figure 121: Thrust force F_r is required for the ongoing excavation (thrust force for the boring process $F_b = 18$ MN)

For the restart after a standstill with (skin friction coefficient $\mu = 0.15$ or 0.25 , respectively) or without (skin friction coefficient $\mu = 0.30$ or 0.45 , respectively) lubrication of the shield extrados: a as a function of the overboring ΔR for a 10 m long shield, and b as a function of the shield length L for an overboring ΔR of 50, 100, or 150 mm. The required thrust force F_r is significantly influenced by the shield length L , the skin friction coefficient μ , and the overcut ΔR , as illustrated in a condensed form in (Figure 120). The shield's "conicity" which is the variation ΔR , of the radial gap size along the shield, is another critical TBM design parameter (see Section 3.11.3). (Figure 122) illustrates the ground pressure p that acts on the shield and the lining for three distinct shield configurations that share an average radial gap size of $\Delta R = 50$ mm. Comparing the average ground pressure P (which regulates the required thrust force) acting upon the shield, the beneficial impact of a stepwise shield construction is demonstrated. Where the shield is constructed in two or three phases, it decreases by 16 or 28%, respectively (Figure 122).

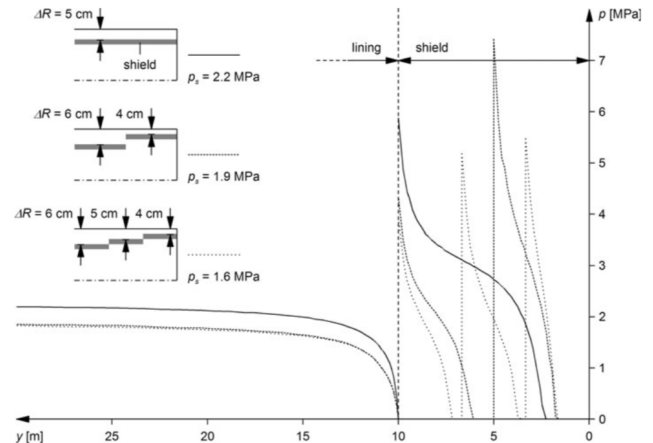


Figure 122: The shield and the lining are subjected to ground pressure for three distinct shield configurations with an average radial gap size of 40–60 mm (shield length $L = 10$ m).

The posterior portion of the shield is more critical to have a wide gap, as the ground's convergence increases as the distance from the face increases. The computational model can be simplified by modelling the shield and the lining as a single indefinitely long cylindrical body of constant stiffness and radial gap size. The longitudinal distribution of the ground pressure p in the simplified model is in comparison to a pressure distribution based on the more accurate model discussed in the previous sections (for a 10 m long shield) in Figure 10a. The ground pressure that develops upon the lining is overestimated by the simplified computational model (by 56% in the final state, which emerges far behind the face). Consequently, the sustaining effect of the lining in the area

immediately behind the shield (the diagonally dashed region in Figure 123 a) is overestimated.

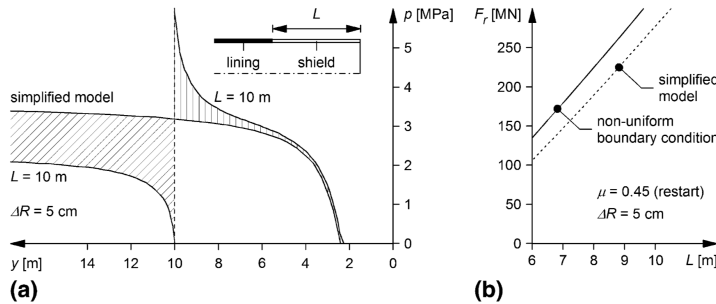


Figure 123: Distribution of the ground pressure p acting on the shield and the lining (a) and the required thrust force F_r as a function of the shield length L (b) based on the simplified model and a model that employs a non-uniform boundary condition (radial gap size $\Delta R = 50$ mm, skin friction coefficient $\mu = 0.45$).

This results in a lower shield loading (the vertically dashed region in (Figure 123 a) as a result of the load transfer in the longitudinal direction, thereby underestimating the thrust force necessary to surmount friction. The thrust force F_r required to resume TBM advance after a standstill is depicted in (Figure 123b) as a function of the shield length L in the simplified model and based upon the more accurate model with the non-uniform boundary condition (Eq. 161). In this instance, the thrust force is estimated to be approximately 40 MN lower by the simplified model. It is therefore crucial to accurately model the characteristics and installation point of the tunnel support, not only from the perspective of structural assessment but also with regard to the TBM's design.

3.11.5. Shield-Support Interaction

The shield loading and thrust force requirement are reduced by the implementation of a stiff support in close proximity to the shield, as it enhances load transfer in the longitudinal direction. The longitudinal arching effect will be more pronounced and the shield burden will be reduced to a greater extent as the lining becomes stiffer and its distance from the face decreases.

This effect is illustrated in the upper portion of (Figure 11a), which displays the thrust force F_r (required to restart TBM advance after a standstill) as a function of the shield length L for two borderline cases with regard to support stiffness: a rigid support $K_1 = \infty$ and an unsupported tunnel $K_1 = 0$. The discharge effect is more pronounced for short shields, as anticipated. However, despite the fact that it is advantageous with regard to the shield, a rigid support that is put close to the face attracts a higher ground load. In reality, the final ground pressure p that develops upon the rigid support $K_1 = \infty$ approaches values that are unsustainable by the standard linings (Figure 124a, lower part) for short shields, where the

longitudinal arching effect is particularly pronounced. As anticipated, the tunnel support p experiences a decrease in load as the shield length L increases, leading to a reduction in the arching effect.

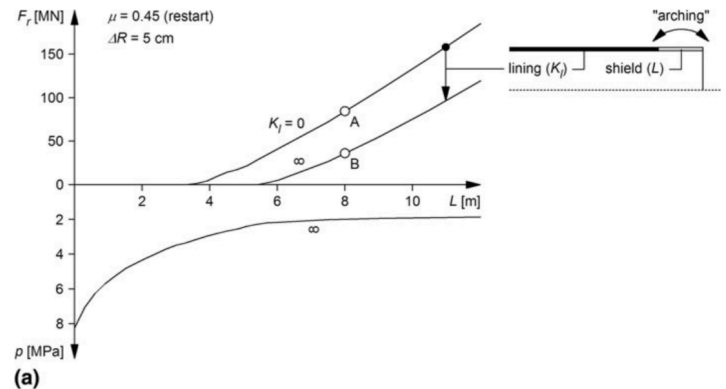


Figure 124: The required thrust force F_r and final ground pressure p acting upon the lining as a function of the shield length L for a rigid support $K_1 = \infty$ and an unsupported tunnel $K_1 = 0$ are as follows: radial gap size $\Delta R = 50$ m, skin friction coefficient $\mu = 0.45$.

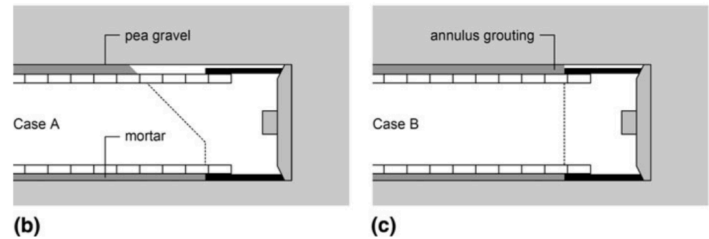


Figure 125: b single shielded TBM in rock with delayed backfilling of the segmental lining (case A of a); c single shielded TBM with annulus grouting via the shield tail (case B of a)

Notably, the scenario of an unsupported tunnel is not merely hypothetical. Indeed, the segmental lining is backfilled with pea gravel at a specific distance behind the shield during shield tunnelling through rock. Consequently, the rock behind the shield is left unsupported (Figure 125 b). Naturally, there is no discharge effect in this scenario (point A in Figure 125 a). The reduction of shield load (point B in Figure 125 a) through longitudinal arching between the face and the segmental lining necessitates the simultaneous grouting of the annulus and the advancement of the TBM through the shield tail (Figure 125 c). (Lavdas 2010) has conducted an analysis of the unique characteristics of segmental lining installation.

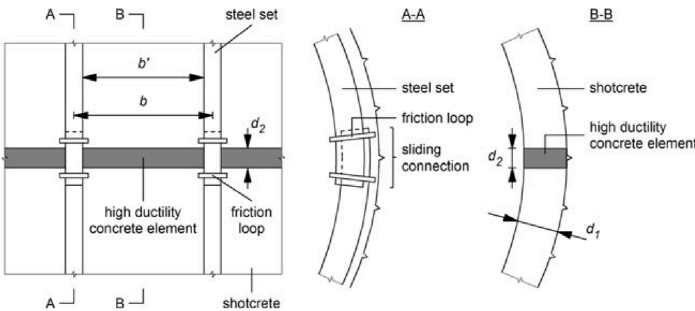


Figure 126: Sketch of the supporting system

Nevertheless, the step-by-step method that is frequently employed in the investigation of heterogeneous ground conditions must be implemented. A comparative analysis that involves a brief critical zone (striking orthogonally to the tunnel axis) has demonstrated that a reduction in the step length enhances accuracy in relation to the required thrust force. However, this improvement is accompanied by a higher computational cost. The latter is especially high for fractures that strike at a small angle to the tunnel axis and for non-hydrostatic initial stress conditions, as these scenarios necessitate genuine three-dimensional numerical analyses.

3.12 Concrete Segment Erector synchronization

The lifting gantry of a conventional segment erector, which is the primary subject of this study, is powered by twin cylinders to produce the necessary substantial lifting force and maintain motion stability. Consequently, the synchronisation of motion between the dual cylinders at an advanced level is important. In contrast to the dual-cylinder mechanism employed in other machinery, such as forklifts (H. Sun and Chiu 2002), (Ge et al. 2017) the lifting gantry often operates at an inclined angle, resulting in unequal loads on either side. The segment's substantial weight and the gantry's crossbeam length, ranging from 3 m to 7 m based on the tunnel's diameter, result in significant variability in the forces acting on the twin cylinders, complicating motion synchronisation. Even though the lifting gantry has sturdy guide rails to guarantee synchronisation, the gantry occasionally experiences chattering, 'pull-and-drag', or even being stuck in practice as a result of inadequate synchronisation under loads that are significantly out of balance. Therefore, the foundation of the segment erector's high-precision closed-loop control is a motion synchronisation control method for the lifting gantry under unbalanced loads. Indeed, there have been numerous research on the synchronisation control of dual actuators, including redundant hydraulic cylinders in aeroplanes (T. Li et al. 2019), dual motors in automobiles (Zou and Zhao 2020), and the linear motor gantry (C. Li et al. 2018), (Z. Chen, Li, et al. 2020). The dynamics of hydraulic systems exhibit significant nonlinearity, characterised by intrinsic nonlinearities and uncertainties, making high-level synchronisation control of hydraulic cylinders more complex than that of other actuators. Regarding the control techniques, earlier implementations utilised

identical control signals for the dual cylinders. It would appear that this technique can achieve reasonable precision with appropriate mechanical couplings to guarantee motion synchronisation if the gantry is horizontal or vertical with balanced loads for both sides.

To resolve issues such as extended design periods, complex interference, and increased restriction conditions in the design process of the segment erector for the Tunnel Boring Machine, it is imperative to conduct a study on the kinematics simulation of the TBM segment erector. The dynamic simulation is completed after the kinematics characteristics of the segment erector are analysed, the 3-D model is designed in the Pro/E environment, and the model is imported into ADAMS. The maximal speeds of the driving parts are identified using the space search technology method after the analysis of the simulation of this mechanism. The speed curves for the driving parts are obtained.

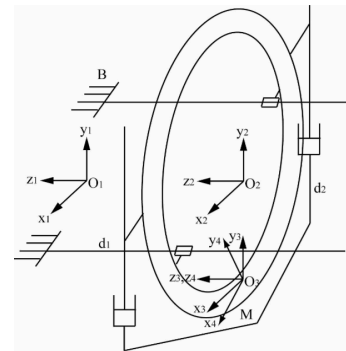


Figure 127: Configuration scheme for segment erector (G. Li et al. 2012).

$$(184) M_4 = M_{2-1} M_{3-2} M_{4-3} M_0, (185) M_4 = T_{2-1} T_{3-2} R_{4-3} M_0$$

$$T_{2-1} = \begin{bmatrix} 1 & 0 & 0 & 0 \\ 0 & 1 & 0 & 0 \\ 0 & 0 & 1 & V_{21}t \\ 0 & 0 & 0 & 1 \end{bmatrix}$$

$$T_{3-2} = \begin{bmatrix} 1 & 0 & 0 & 0 \\ 0 & 1 & 0 & 0 \\ 0 & 0 & 1 & V_{32}t \\ 0 & 0 & 0 & 1 \end{bmatrix}$$

$$R_{4-3} = \begin{bmatrix} \cos\omega_{43}t & -\sin\omega_{43}t & 0 & 0 \\ \sin\omega_{43}t & \cos\omega_{43}t & 0 & 0 \\ 0 & 0 & 1 & 0 \\ 0 & 0 & 0 & 1 \end{bmatrix}$$

$$M_0 = \begin{bmatrix} 1 & 0 & 0 & 0 \\ 0 & 1 & 0 & 0 \\ 0 & 0 & 1 & 0 \\ 0 & 0 & 0 & 1 \end{bmatrix}$$

$$R_{4-3} = \begin{bmatrix} \cos\omega_{43}t & -\sin\omega_{43}t & 0 & 0 \\ \sin\omega_{43}t & \cos\omega_{43}t & 0 & V_{32}t \\ 0 & 0 & 1 & V_{21}t \\ 0 & 0 & 0 & 1 \end{bmatrix}$$

3.12.1. Three-Dimensional Solid Model Establishment

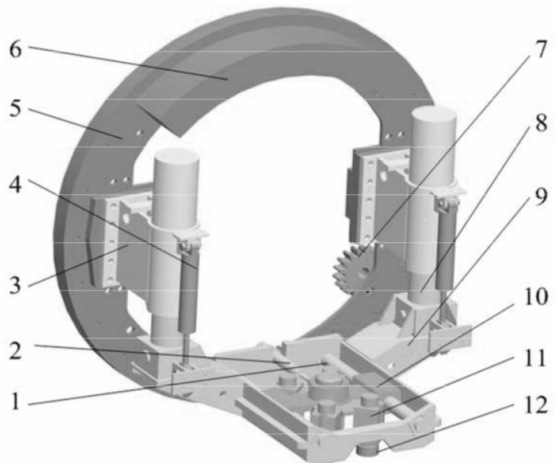


Figure 128: segment erector model components: 1- Horizontal guide rail, 2- horizontal cylinder, 3- beam, 4-lifting cylinder, 5-rotating disk body, 6-balance weight, 7-pinion, 8-orientation column, 9- lifting beams, 10-mobile rack, 11- micro-adjustment bracket, 12-micro-adjustment cylinder

The six-DOF segment erector for tunnel boring machine is represented in a three-dimensional solid model through

feature simplification and part combination. This model is suitable for kinematics simulation and accurately represents the actual working conditions of the segment erector. The segment erector's three-dimensional solid representation

However, without any controller effort, the synchronisation performance can only rely on the mechanical connections if the loads go significantly out of balance. In essence, the two cylinders in such an intuitive scheme do not share any information, such as motion differences, which could result in subpar synchronisation in practice (C. Li et al. 2018). Following the principle of contouring control for a multi-axis system, another prevalent approach is cross-coupled control (F.-J. Lin et al. 2012). This scheme involves the construction of a synchronisation compensator based on the kinetic data between the two cylinders, including their relative position and velocity, resulting in enhanced synchronisation performance across varying drive characteristics and loading conditions of each cylinder (J. Yao et al. 2018). This technique attempts to address the motion synchronisation issue at the kinetics level, neglecting the impact of mechanical coupling, which may result in additional internal forces and diminished performance (C. Li et al. 2018).

In essence, a component that is not sufficiently rigid is implied by the lifting gantry's poor synchronisation even though there is a strong mechanical coupling between the two cylinders. In summary, with the fundamental linear motion, the gantry must facilitate a degree of rotational motion, which elucidates the nature of inadequate synchronisation about the rotation of the crossbeam. Both (C. Li et al. 2018) and (García-Herreros et al. 2013) have conducted modelling of a linear dual-drive gantry, incorporating rotational motion and developed model-based controllers to address the additional degree of freedom. For the lifting gantry to be controlled with great precision under unbalanced loads, a comprehensive model that incorporates both rotational and linear motions must be built. Furthermore, the substantial mass and rotational inertia of the segment, along with the mechanical coupling exhibiting high stiffness, must be taken into account when constructing the dynamics model. Few research have proposed a full model of a dual-cylinder lifting gantry working at an inclined angle, to our knowledge.

Inadequate synchronisation of the dual cylinders will lead to the rotation of the crossbeam, subsequently generating excessive internal forces due to the mechanical linkage. Furthermore, "pull-and-drag" and chattering that follow have a negative impact on the segment erector's overall stability and accuracy. This work proposes a model-based synchronisation control technique for achieving high-precision motion tracking of the dual-cylinder lifting gantry of the segment erector under unbalanced loads. As the fundamental control theory in the design of the suggested controller, adaptive robust control (ARC), with a rigorous mathematical theoretical framework, is used to ensure the tracking performance in the presence of diverse nonlinearities and uncertainties of the system. The ARC was proposed by Yao (B. Yao and Tomizuka 1997), and its superior performance has been validated in numerous practical

applications over the past two decades by (M. Yuan et al. 2021),(Y. Lin, Chen, and Yao 2020),(Deng and Yao 2021) and (Z. Chen, Huang, et al. 2020). The ARC demonstrated its efficacy in addressing the nonlinear control challenges of hydraulic systems, as seen in both the authors' prior research (Helian, Chen, and Yao 2020),(S. Chen et al. 2021) and further pertinent studies (Lyu, Chen, and Yao 2021),(Lyu, Chen, and Yao 2019). A practical thrust allocation mechanism is proposed alongside the linear motion tracking as part of the overall controller. In order to control internal forces and motion differences within a narrow range, the thrust allocation is intended to coordinate the twin cylinders. Together with the theoretical performance and supporting evidence, the meticulous theoretical design procedures are described in full. The results of comparative simulations demonstrate that the suggested controller can achieve both high levels of motion synchronisation and high precision motion tracking capabilities.

In reality, the lifting gantry will not experience any synchronisation issues if the connection between the crossbeam and the guide rails is flawlessly rigid. It is well-established that there should be certain components that are comparatively elastic, which enable motion discrepancies between dual cylinders. The crossbeam will rotate at a very small angle as a consequence of the dual cylinders' poor synchronisation. The guide rails, which are stout and relatively long, are illustrated in Figure above. Consequently, they will not permit such rotation. Additionally, the crossbeam is exceedingly robust and cannot be bent by conventional working forces. Consequently, the elasticity may be attributed to the connections between the guide rails and the crossbeam.

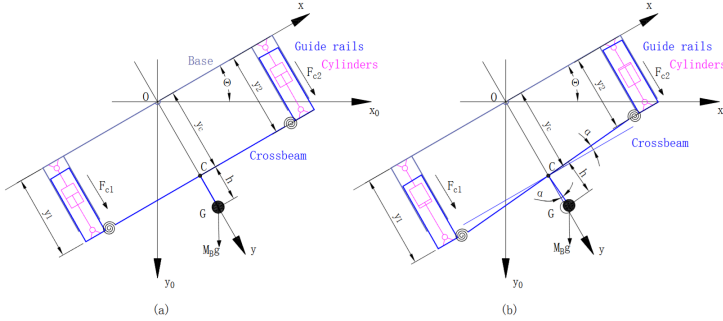


Figure 129: a schematic diagram of the dual-cylinder lifting gantry at a specific rotational angle of Θ . (a) The hoisting gantry's general configuration. (b) The hoisting gantry's linear and rotational motions.

Crossbeam rotation is confirmed by the practical synchronisation challenge of the lifting gantry in segment erectors. Since the suggested schematic model fully incorporates both linear and rotating motions, it can therefore be utilised to investigate the gantry. It is difficult to achieve precise control of a lifting gantry, especially when it operates at an inclined inclination. To handle the 2-DOF model, hardware-level twin cylinders should be controlled by independent proportional valves in the hydraulic circuit, providing two independent control inputs. Key contributions of

this project include thorough modelling and model-based motion control design for the lifting gantry.

3.12.1. Mathematical model of the lifting gantry

(Figure 129) above shows lifting gantry modelling. The dual side locations (y_1 and y_2) are defined individually, whereas the output cylinder rod forces (F_{c1} and F_{c2}) are defined with positive Y-axis directions. Point C, often known as y_c , is the midpoint of the crossbeam and follows the Y-axis. Point G represents the crossbeam centroid, which includes both the crossbeam mass and the section being lifted. Therefore, point G should have a distance h from point C. The crossbeam's rotating motion is described by the angle α between the crossbeam and the X-axis. The following practical assumptions can be made in addition to the above definition.

The linear motion along the Y-axis and an additional rotation around the midpoint C of the crossbeam comprise the complete planar motions of the entire moving body in the frame OXY, as predicated on the aforementioned definitions and assumptions. Consequently, the 2-DOF motions can be described using the generalised coordinates $q = [y_c, \alpha]^T$. In practice, it is inconvenient to explicitly measure y_c and α . Consequently, the following geometrical relationships can be employed to calculate them by measuring y_1 and y_2 .

(186) $y_c = \frac{1}{2}(y_1 + y_2)$; $\alpha \approx \sin\alpha = \frac{1}{l_c}(y_1 - y_2)$ while assuming the following: Assumption 1. The crossbeam with the attached segment is a body that is entirely rigid. Consequently, the crossbeam is perpendicular to the line that runs between the centroid G and the midpoint C. The crossbeam and segment are particularly massive, which allows for the disregard of the mass of other components, including the guide rails and cylinders. Assumption 2. The elasticity is solely derived from the connections between the crossbeam and the guide rails, despite the fact that the rigidity of the connection is extremely high, resulting in a very small rotational angle α . This is the actual case. Assumption 3. The midpoint C is consistently located on the Y-axis as a result of the hoisting gantry's symmetrical design.

l_c = length of the cross beam , centroid coordinations are defined as: $G[x_G, y_G]^T$, (187) $x_G = h\sin\alpha$, $y_G = y_c + h\cos\alpha$ the velocity of the centroid

$$(188) v_G = [x'_G, y'_G]^T = [hsoc\alpha\dot{\alpha}, y_c - hsin\alpha\dot{\alpha}]^T,$$

(189) $E_k = \frac{1}{2}m_G v_G^T v_G + \frac{1}{2}J_G \dot{\alpha}^2 = \frac{1}{2}m_G y_G^2 + \frac{1}{2}m_G h^2 \dot{\alpha}^2 + \frac{1}{2}J_G \dot{\alpha}^2 - m_G h\sin\alpha y_G^2 \dot{\alpha}$ where J_G is the rotational inertia of the entire moving body around the centroid G, and m_G is the mass of the moving body, including the segment and the crossbeam. Furthermore, the potential energy, comprising gravitational energy $E_p G$ and elastic energy $E_p E$, can be computed as:

$$(190) E_p = E_{pG} + E_{pE} = -m_{Gg} [y_c \cos\theta + h\cos(\theta + \alpha)] + \frac{1}{2}k_e \dot{\alpha}^2, \text{ when } k_e = \text{effective elastic stiffness of the connection between}$$

the crossbeam and guide rails. By using the langrangian equation $\frac{d}{dt}(\frac{\partial E}{\partial q_i}) - \frac{\partial E}{\partial q_i} = F_i$ $i = 1, 2$ by defining $E = E_k - E_p$ the following equation can be defined; (191) $m y_c'' - m_g g \cos\Theta - m_g h \sin\alpha \cdot \alpha'' - m_g h \cos\alpha \cdot \alpha'^2 = F_1$ and $(J_g + m_g h^2) \alpha'' + k_e \alpha - m_g h \sin\alpha \cdot y_c'' - m_g h \cos\alpha \cdot \alpha \cdot y_c' + m_g h \sin(\Theta + \alpha) = F_2$, since F_1 and F_2 are the general forces moduled as: (192) $F_1 = F_{c1} + F_{c2} - F_{r1} - F_{r2}$, $F_2 = (F_{c1} - F_{c2} - F_{r1} + F_{r2}) \frac{l_c}{2}$ since F_r is the viscous coulomb friction of two sides noted as: (193) $F_{r1} = B_1 y_1 + A_1 S(y_1)$, $F_{r2} = B_2 y_2 + A_2 S(y_2)$, the coefficient of viscous and coulomb friction are B_i and A_i . Also to approximate the sign function $\text{sgn}(\bullet) \cdot S(\bullet)$ is used as a continuous function. Each hydraulic cylinder that produces F_{c1} and F_{c2} is managed by a proportional valve. Using cylinder C1 as a reference, the force exerted by the output rod can be represented as (194) $p_{A1} A_{A1} - p_{B1} A_{B1}$ with p_{A1} and p_{B1} representing each chamber's pressure, and A_{A1} and A_{B1} representing the piston areas of the head-end and rod-end chambers, respectively. The dynamics of these chambers can be further described as: (195) $\dot{p}_{A1} = -\frac{A_{A1}}{V_{A1}} \beta_e y_1 + \frac{1}{V_{A1}} \beta_e Q_{A1} + d_{A1}$, $\dot{p}_{B1} = -\frac{A_{B1}}{V_{B1}} \beta_e y_1 + \frac{1}{V_{A1}} \beta_e Q_{B1} + d_{B1}$. In this context, $V_{A1} = V_{A10} + A_{A1} y_1$ and $V_{B1} = V_{B10} + A_{B1} y_1$ denote the total hydraulic compressible volumes associated with the head-end and rod-end chambers at position y_1 , where V_{A10} and V_{B10} represent the initial volumes. The symbol β_e signifies the effective bulk modulus, Q_{A1} indicates the inflow into the head-end chamber, and Q_{B1} denotes the outflow from the rod-end chamber, while d_{A1} and d_{B1} reflect the inevitable modelling inaccuracies. Consequently, the dynamics of F_{c1} can be computed as (196) $F_{c1} = p_{A1} A_{A1} - p_{B1} A_{B1} = -\left(\frac{A_{A1}^2}{V_{A1}} + \frac{A_{B1}^2}{V_{B1}}\right) \beta_e y_1 + \beta_e \left(\frac{A_{A1}}{V_{A1}} Q_{A1} + \frac{A_{B1}}{V_{B1}} Q_{B1}\right) + A_{A1} d_{A1} - A_{B1} d_{B1}$.

We can write Q_{A1} and Q_{B1} as follows, using the features of a common proportional directional valve:

$$(197) \Delta p_{A1} = \begin{cases} p_s - p_{A1} & \text{if } u_1 \geq 0 \\ p_{A1} & \text{if } u_1 < 0 \end{cases}$$

$$\Delta p_{B1} = \begin{cases} p_{B1} & \text{if } u_1 \geq 0 \\ p_s - p_{B1} & \text{if } u_1 < 0 \end{cases}$$

(Deng and Yao 2021) reserahced the proportional valve's control signal is denoted by u_1 , the flow gains of the valve are k_{qA1} and k_{qB1} , and the pressures of the pump and tank are p_s and p_r . The

dynamics between the valve filament position and the control signal u_1 are disregarded due to the high bandwidth, as has been observed in numerous other existing works. The intermediate flow rate (198) $Q_{c1} = \frac{A_{A1}}{V_{A1}} Q_{A1} + \frac{A_{B1}}{V_{B1}} Q_{B1} = \left(\frac{A_{A1}}{V_{A1}} k_{qA1} \sqrt{|\Delta p_{A1}|} + \frac{A_{B1}}{V_{B1}} k_{qB1} \sqrt{|\Delta p_{B1}|}\right) u_1$. similar for the other cylinder can be modeled as: (199) $F_{c2} = p_{A2} A_{A2} - p_{B2} A_{B2} = -\left(\frac{A_{A2}^2}{V_{A2}} + \frac{A_{B2}^2}{V_{B2}}\right) \beta_e y_2 + \beta_e Q_{c2} + A_{A2} d_{A2} - A_{B2} d_{B2}$ and $Q_{c2} = \left(\frac{A_{A2}}{V_{A2}} k_{qA2} \sqrt{|\Delta p_{A2}|} + \frac{A_{B2}}{V_{B2}} k_{qB2} \sqrt{|\Delta p_{B2}|}\right) u_2$. The lifting gantry's dynamics can be rearranged in the following way to incorporate the aforementioned modelling processes while taking modelling faults into account: (200) $m y_c'' = F_{c1} + F_{c2} - F_{r1} - F_{r2} + m_g g \cos\Theta + m_g h (\sin\alpha \cdot \alpha'' + \cos\alpha \cdot \alpha'^2 + d_{\alpha})$, $(J_g + m_g h^2) \alpha'' = (F_{c1} - F_{c2} - F_{r1} + F_{r2}) \frac{l_c}{2} - k_e \alpha + m_g h (\sin\alpha \cdot y_c'' + \cos\alpha \cdot y_c') - m_g h \sin(\Theta + \alpha) + d_\alpha$, $F_{c1} = -\left(\frac{A_{A1}^2}{V_{A1}} + \frac{A_{B1}^2}{V_{B1}}\right) \beta_e y_1 + \beta_e Q_{c1} + A_{A1} d_{A1} - A_{B1} d_{B1}$, $F_{c2} = -\left(\frac{A_{A2}^2}{V_{A2}} + \frac{A_{B2}^2}{V_{B2}}\right) \beta_e y_2 + \beta_e Q_{c2} + A_{A2} d_{A2} - A_{B2} d_{B2}$, $d_{yc}, d_\alpha, d_{A1}, d_{B1}, d_{A2}, d_{B2}$ denote the modelling errors associated with the respective dynamic equations, whereas Q_{c1} and Q_{c2} can be regarded as the accessible control inputs, as they are directly linked to the actual control inputs u_1 and u_2 .

13.12.2. Synchronisation controls

To achieve high-precision motion tracking performance of the dual-cylinder lifting gantry, while keeping the internal forces and rotational angle within a small range, a modelbased motion synchronization control scheme is proposed in this study. The controller should synthesize the valve control signals u_1 and u_2 such that the following objectives can be fulfilled by; High motion tracking precision: The midpoint position yc tracks the reference trajectory $yd(t)$ as precisely as possible, which is assumed to be known, bounded, and at least third-order differentiable; and Rotation regulation: The dual cylinders should be properly coordinated so that the rotational angle of the crossbeam can be guaranteed within a very small range.

In (Figure 130), the suggested controller's structure is displayed. The controller receives input signals including the reference trajectory signals $y_d(t)$, the rotational angle Θ of the entire lifting gantry, and state feedback signals from both the hydraulic system and the gantry. Utilising the signals and the system model, the controller synthesises the control signals u_1 and u_2 . Part one of the controller is responsible for tracking motion, and part two for allocating thrust. The thrust

allocation component coordinates the dual cylinders by receiving the angle Θ and the desired total force F_{cd} from the motion tracking controller, subsequently synthesising the individual desired forces F_{c1d} and F_{c2d} for the dual cylinders.

The motion tracking controller serves as the fundamental component of the overall system, developed in accordance with the adaptive robust control theory introduced by (B. Yao et al. 2000). This design ensures the achievement of the desired tracking precision despite the presence of parametric uncertainties and modelling errors. The subsequent subsections present the details of the thrust allocation and motion tracking controller.

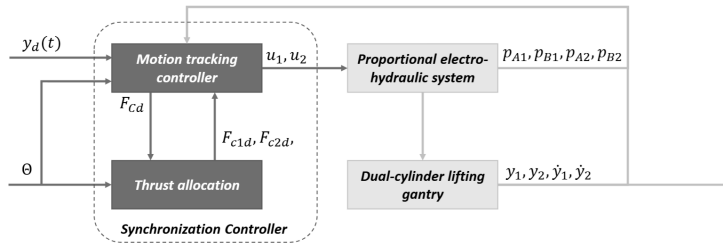


Figure 130: Structure of the synchronization controller model

The proportional feedback term $ke\alpha$ can be viewed as having a very big gain ke . Maintaining the expression (201) $(F_{c1} - F_{c2} - F_{r1} + F_{r2}) \frac{l_c}{2} - m_g g \sin(\Theta + \alpha)$ within a limited range allows for the regulation of the angle α to remain small in steady state, facilitated by the presence of $k_e \alpha$. As a result, the internal forces brought on by the mechanical coupling and the rotational angle will both be controlled to a level close to zero. The following is a design for a workable thrust allocation scheme based on the aforementioned concept.

As explained in the following subsection, define F_{cd} as the force that F_c should have in order to ensure that the linear motion tracks y_d accurately. The intended forces F_{c1d} and F_{c2d} of F_{c1} and F_{c2} for the dual cylinders must meet the subsequent requirement: (202) $F_{c1d} + F_{c2d} = F_{cd}$, to ensure the precision of linear motion tracking. Simultaneously, to regulate the rotational angle, F_{c1d} and F_{c2d} must also meet the following

criteria. (203) $(F_{c1} - F_{c2} - F_{r1} + F_{r2}) \frac{l_c}{2} - m_g g \sin(\Theta + \alpha) \approx 0$

F_{c1d} and F_{c2d} can be accurately calculated using the pre-estimated friction forces. Taking into account Assumption 3 and the fact that F_{r1} and F_{r2} are significantly smaller than F_{c1d} and F_{c2d} in practice, the following approximation can be used because the large feedback gain ke can also control the angle within a narrow range even when there are some approximation errors: (204) $(F_{c1d} - F_{c2d}) \frac{l_c}{2} - m_{gpre} g \sin(\Theta) \approx 0$, The moving body's pre-estimated mass is m_{gpre} . Thus, the appropriate forces for the dual cylinder can be apportioned

using the relationships in (202) and (204) as follows:

$$(205) F_{c1d} = \frac{1}{2} F_{cd} + \frac{1}{l_c} m_{gpre} g \sin(\Theta),$$

$F_{c2d} = \frac{1}{2} F_{cd} + \frac{1}{l_c} m_{gpre} g \sin(\Theta)$. The thrust allocation system above works for engineering. The open-loop control of rotational motion eliminates the need for measurement signals of α , which often contain noise. The research reveals that the thrust distribution technique regulates rotational motion due to the connection's intrinsic stiffness. In the next subsection, the relationship in (204) will be used to synthesise control signals u_1 and u_2 . The linear motion along the Y-axis dynamics control design can be tweaked as :

$$(206) \ddot{y}_c = g \cos \Theta + \frac{1}{m_g} F_c - \frac{B_r}{m_g} \dot{y}_c - \frac{A_r}{m_g} S(\dot{y}_c) + D_{1n} + \Delta D_1$$

since it is inconvenient to directly correct the coupling term $m_g h(\sin \alpha \cdot \ddot{\alpha} + \cos \alpha \cdot \dot{\alpha}^2)$ in the control rule since it includes the second derivative of α . Furthermore, the angle is diminutive and may be affected by measurement noise in actuality, thus the attainable precision of the direct model adjustment may be inadequate. When $F_c = F_1 + F_2$, $B_r = B_1 + B_2$, $A_r = A_1 + A_2$, \dot{y}_c is used instead of y_1 and y_2 to approximate the frictions for simplicity since $y_c \approx y_1 \approx y_2$

With D_{1n} as its nominal value, $D_1 = D_{1n} + \Delta D_1$ is the lumped disturbance component that includes the modelling mistakes, coupling terms, and the previously indicated friction errors.

$$(207) \dot{F}_{c1} = - \left(\frac{A_{A1}^2}{V_{A1}} + \frac{A_{B1}^2}{V_{B1}} \right) \beta_e \dot{y}_1 + \beta_e Q_{c1} + A_{A1} d_{A1n} - A_{B1} d_{B1n} + \Delta d_{c1}$$

$$\dot{F}_{c2} = - \left(\frac{A_{A2}^2}{V_{A2}} + \frac{A_{B2}^2}{V_{B2}} \right) \beta_e \dot{y}_2 + \beta_e Q_{c2} + A_{A2} d_{A2n} - A_{B2} d_{B2n} + \Delta d_{c2}$$

where Δd_{c1} and Δd_{c2} stand for the remaining lumped modelling errors, and d_{A1n} , d_{B1n} , d_{A2n} , and d_{B2n} are the nominal values of the modelling error terms in (207). It is not necessary to parameterise the dynamics of the rotating motion since, as was mentioned in the previous part, the thrust allocation would only employ the static solution of the dynamics.

$$(208) \ddot{y}_c = g \cos \Theta + \theta_1 F_c - \theta_2 \dot{y}_c - \theta_3 S(\dot{y}_c) + \theta_4 + \Delta D_1,$$

$$\dot{F}_{c1} = - \left(\frac{A_{A1}^2}{V_{A1}} + \frac{A_{B1}^2}{V_{B1}} \right) \theta_5 \dot{y}_1 + \theta_5 Q_{c1} + A_{A1} \theta_6 - A_{B1} \theta_7 + \Delta d_{c1},$$

$$\dot{F}_{c2} = - \left(\frac{A_{A2}^2}{V_{A2}} + \frac{A_{B2}^2}{V_{B2}} \right) \theta_5 \dot{y}_2 + \theta_5 Q_{c2} + A_{A2} \theta_8 - A_{B2} \theta_9 + \Delta d_{c2},$$

$\theta = [\theta_1, \theta_2, \dots, \theta_9]^T$, $\theta_1 = 1/m_g$, $\theta_2 = B_r/m_g$, $\theta_3 = A_r/m_g$, $\theta_4 = D_{1n}$, $\theta_5 = \beta_e$, $\theta_6 = d_{A1n}$, $\theta_7 = d_{B1n}$, $\theta_8 = d_{A2n}$, $\theta_9 = d_{B2n}$. This study uses the following nomenclature: With $\tilde{\bullet}$ representing the estimation error, $\tilde{\bullet}^\Delta$ represents the estimates of \bullet ; that is, $\tilde{\bullet} = \bullet^\Delta - \bullet$; where \bullet_{\min} and \bullet_{\max} represent the lowest and maximum values of $\bullet(t)$ for all time t , respectively. The lumped modelling errors ΔD_1 , Δd_{c1} , and Δd_{c2} in (22), as well as the unknown parameter θ , are all affected by practical

uncertainties. The following practical assumption results from the fact that the modelling mistakes and parametric uncertainties are constrained by recognised bounds: Assumption 4: The modelling errors and parametric uncertainties' magnitudes are known, i.e.

$$(209) \theta_i \in \Omega_{\theta_i} = \{\theta_i : \theta_{i \min} \leq \theta_i \leq \theta_{i \max}\}, \Delta D_i \in \Omega_{D_i} = \{\Delta D_i : |\Delta D_i| \leq \delta_i\}, \Delta d_i \in \Omega_{dci} = \{\Delta d_{ci} : |\Delta d_{ci}| \leq \delta_{ci}\} \quad \text{since}$$

$$\theta_{i \min} = [\theta_{1 \min}, \theta_{2 \min}, \dots, \theta_{9 \min}]^T, \theta_{i \max} = [\theta_{1 \max}, \theta_{2 \max}, \dots, \theta_{9 \max}]^T, \text{ are known the bounds and } \delta_i \text{ and } \delta_{ci} \text{ are the functions.}$$

(210) $\hat{\theta} = \text{Proj}_{\theta}(T\tau)$ The Adaptive Robust Control (ARC) proposed by (B. Yao et al. 2000) is used to synthesize the motion tracking controller. The parameters will be updated online by the use of the following discontinuous projection-type adaption law.

$$(211) \text{Proj}_{\theta_i}(\cdot, i) = \begin{cases} 0, & \text{if } \hat{\theta}_i = \theta_{i \max} \text{ and } \cdot_i > 0 \\ 0, & \text{if } \hat{\theta}_i = \theta_{i \min} \text{ and } \cdot_i < 0 \\ \cdot_i & \text{otherwise} \end{cases}$$

Consequently, using the above equation guarantees the following characteristics for every adaptation function τ :

$$(212) (P1): \hat{\theta} \in \Omega_{\theta} = \{\hat{\theta}_i : \theta_{i \min} \leq \hat{\theta}_i \leq \theta_{i \max}\},$$

(P2) $\theta^{\sim T}(T^{-1}\text{Proj}_{\hat{\theta}}(T\tau) - \tau) \leq 0, \forall \tau$ The adaptive robust motion tracking controller's backstepping design will then be created. To achieve the highest degree of accuracy, the controller must combine the valve control signals u_1 and u_2 in such a way that the crossbeam's midpoint, y_c , follows the reference trajectory, $y_d(t)$. Step 1: Use $z_1 = y_c - y_d$ to define the motion tracking error. The ensuing quantity can be defined in a manner similar to a toggling function (213) $z_2 = z_1 + k_1 z_1 = \dot{y}_c - \dot{y}_{eq}, \ddot{y}_{eq} = \ddot{y}_d - k_1 z_1$ where k_1 is greater than 0. It appears that the reduction of z_1 or its convergence to zero is equivalent to the reduction of z_2 or its convergence to zero.

Taking into account (214), the dynamics of z_2 can be calculated as (214) $\dot{z}_2 = g\cos\theta + \theta_1 F_c - \theta_2 \dot{y}_c - \theta_3 S(\dot{y}_c) + \theta_4 + \Delta D_1 - \ddot{y}_{eq}$ In order to reduce z_2 or achieve convergence to zero, F_c can be used as the virtual control input. Consequently, the virtual control law F_{cd} for F_c can be synthesised in accordance with the ARC design procedure. (215) $F_{cd} = F_{cda} + F_{cds}$

$$F_{cda} = \frac{1}{\theta_1} [-g\cos\theta + \hat{\theta}_2 \dot{y}_c + \hat{\theta}_3 S(\dot{y}_c) - \hat{\theta}_4 + \ddot{y}_{eq}], F_{cds} = F_{cds1} + F_{cds2}, F_{cds} = -k_{2s1} \frac{1}{\theta_{1\min}} z_2, k_{2s1} \geq \frac{\omega_3}{\omega_2} g_1 |T\phi_1 \omega_2|^2 + k_2,$$

$$\phi_1 = [F_{cda}, \dot{y}_c - S(\dot{y}_c), 1, 0, 0, 0, 0, 0]^T \text{ where } k_{2s1} > 0 \text{ is the feedback gain, } k_2 > 0 \text{ and } g_1 > 0, T > 0 \text{ is the adaptation rate matrix, } \omega_2 > 0 \text{ and } \omega_3 > 0 \text{ are the weighting coefficients, and } F_{cds2} \text{ is the nonlinear robust feedback term meeting the following dual}$$

robust performance conditions. The control law F_{cd} comprises the adaptive model compensation law F_{cd} and the robust control law

$$(216) (i) z_2 F_{cds2} \leq 0,$$

(ii) $z_2 (\theta_1 F_{cds2} - \phi_1^T \hat{\theta} + \Delta D_1) \leq \varepsilon_1$. With the design parameter ε_1 being used.

As $z_3 = F_c - F_{cd}$, we may express the difference between the real cylinder force F_c and the virtual control law F_{cd} . After substituting (215) into (214) the error dynamics of z_2 can be calculated

$$(217) \dot{z}_2 = -\frac{\theta_1}{\theta_{1\min}} k_{2s1} z_2 + (\theta_1 F_{cds2} - \phi_1^T \hat{\theta} + \Delta D_1) + \theta_1 z_3. \quad \text{Step}$$

Two: The purpose of this phase is to generate the control signals u_1 and u_2 for the proportional valves. The following tracking defects are defined as: (218) $z_3 = z_{31} + z_{32}$,

$$z_{31} = F_{c1} - F_{c1d}, \quad z_{32} = F_{c2} - F_{c2d} \quad (219) z_{31} = F_{c1} - F_{c1d} = -\left(\frac{A_{A1}^2}{V_{A1}} + \frac{A_{B1}^2}{V_{B1}}\right) \theta_5 \dot{y}_1 + \theta_5 Q_{c1} + A_{A1} \theta_6 - A_{B1} \theta_7 + \Delta d_{c1} - \frac{1}{2} F_{cd},$$

$$(220) F_{cd} = F_{cdc} + F_{cdv}, \quad F_{cdc} = \frac{\partial F_{cd}}{\partial y_c} \dot{y}_c + \frac{\partial F_{cd}}{\partial \dot{y}_c} \ddot{y}_c + \frac{\partial F_{cd}}{\partial t},$$

$$\ddot{y}_c = g\cos\theta + \hat{\theta}_1 F_c - \hat{\theta}_1 \dot{F}_c - \hat{\theta}_2 \dot{y}_c - \hat{\theta}_3 S(\dot{y}_c) + \hat{\theta}_4,$$

$$F_{cdi} = \frac{\partial F_{cd}}{\partial y_c} (y_c - \hat{y}_c) + \frac{\partial F_{cd}}{\partial \hat{\theta}} \hat{\theta},$$

$$= \frac{\partial F_{cd}}{\partial y_c} [-\theta_1^T F_c + \theta_2^T \dot{y}_c + \theta_3^T S(\dot{y}_c) - \theta_4^T + \Delta D_1] + \frac{\partial F_{cd}}{\partial \hat{\theta}} \hat{\theta}. \text{ where } F_{cdi}$$

represents the calculable portion of F_{cd} , which can be compensated through an adaptive robust control law, \hat{y}_c denotes the estimate of y_c based on the measured states and parameter estimates, and F_{cdi} is the incalculable portion that must be managed through a specific robust feedback approach. The control law Q_{c1d} for Q_{c1} can be synthesised by following the ARC design procedure and taking into account the error dynamics in (221). (222) $Q_{c1d} = Q_{c1da} + Q_{c1ds}$,

$$Q_{c1da} = \frac{1}{\hat{\theta}_5} \left[\left(\frac{A_{A1}^2}{V_{A1}} + \frac{A_{B1}^2}{V_{B1}} \right) \hat{\theta}_5 \dot{y}_1 - A_{A1} \hat{\theta}_6 - A_{B1} \hat{\theta}_7 + \frac{1}{2} F_{cdc} - \frac{\omega_2}{2\omega_3} \hat{\theta}_1 z_2 \right],$$

$$Q_{c1ds} = Q_{c1ds1} + Q_{c1ds2}, \quad Q_{c1ds1} = -k_{3s1} \frac{1}{\theta_{5\min}} z_{31},$$

$k_{3s1} \geq g_2 \|T\phi_2 \omega_3\|^2 + c_1 \left\| \frac{\partial F_{cd}}{\partial \hat{\theta}} \right\|^2 + k_3$ where the adaptive model compensation law Q_{c1da} and the robust control law Q_{c1ds} are included in the control law Q_{c1d} . The feedback gain is represented by $k_{3s1} > 0$, the adaptation rate matrix by $d_1 > 0$, $g_2 > 0$, and the nonlinear robust feedback term, Q_{c1ds2} is to be described later. Likewise, with respect to the error z_{32} , the control rule Q_{c2da} for Q_{c2d} can similarly be synthesised as follows; the specific steps are not included here: (223) $Q_{c2d} = Q_{c2da} + Q_{c2ds}$,

$$Q_{c2da} = \frac{1}{\theta_5} \left[\left(\frac{A_{A2}^2}{V_{A2}} + \frac{A_{B2}^2}{V_{B2}} \right) \widehat{\theta}_5 y_2 - A_{A2} \widehat{\theta}_8 - A_{B1} \widehat{\theta}_8 + \frac{1}{2} F_{Cdc} - \frac{\omega_2}{2\omega_3} \widehat{\theta}_1 z_2 \right],$$

$$Q_{c2ds} = Q_{c2ds1} + Q_{c2ds2},$$

$$Q_{c2ds1} = -k_{3s1} \frac{1}{\theta_{5min}} z_{32},$$

$k_{3s1} \geq g_2 \|T\Phi_2 \omega_3\|^2 + c_1 \left\| \frac{\partial F_{cd}}{\partial \theta} \right\|^2 + k_3$. Noting that $z_3 = z_{31} + z_{32}$, the error dynamic can be calculated as:

$$(224) \begin{aligned} z_3^* &= (F_{c1}^* - F_{c1d}) + (F_{c2}^* - F_{c2d}) \\ &= -k_{3s1} \frac{\theta_5}{\theta_{5min}} z_3 + [\theta_5 (Q_{c1ds2} + Q_{c2ds2}) \\ &\quad - \Phi_2^T \theta^* + \Delta d_{c1} + \Delta d_{c2}] - \frac{\partial F_{cd}}{\partial \theta} \widehat{\theta} - \frac{\omega_2}{\omega_3} \theta_1 z_2, \end{aligned}$$

$$(225) \Phi_2 = \begin{bmatrix} \frac{\omega_2}{\omega_3} z_2 - \frac{\partial F_{cd}}{\partial y_c} F_c \\ \frac{\partial F_{cd}}{\partial y_c} y_c \\ \frac{\partial F_{cd}}{\partial y_c} S(y_c) \\ -\frac{\partial F_{cd}}{\partial y_c} \\ -(\frac{A_{A1}^2}{V_{A1}} + \frac{A_{B1}^2}{V_{B1}}) y_1^* - (\frac{A_{A2}^2}{V_{A2}} + \frac{A_{B2}^2}{V_{B2}}) y_2^* + Q_{c1da} + Q_{c2da} \\ A_{A1} \\ A_{B1} \\ A_{A2} \\ A_{B2} \end{bmatrix}$$

$$(226) (i) z_3 (Q_{c1ds2} + Q_{c2ds2}) \leq 0,$$

(ii) $z_3 \left| \theta_5 (Q_{c1ds2} + Q_{c2ds2}) - \Phi_2^T \theta^* + \Delta d_{c1} + \Delta d_{c2} \right| \leq \varepsilon_2$, the adaptation function is defined as (224) $\tau = \omega_2 \phi_1 z_2 + \omega_3 \phi_2 z_3$,

$$(227) u_1 = \frac{Q_{c1d}}{\frac{A_{A1}}{V_{A1}} k_{A1} \sqrt{|\Delta p_{A1}|} + \frac{A_{B1}}{V_{B1}} k_{B1} \sqrt{|\Delta p_{B1}|}}, u_2 = \frac{Q_{c2d}}{\frac{A_{A2}}{V_{A2}} k_{A2} \sqrt{|\Delta p_{A2}|} + \frac{A_{B2}}{V_{B2}} k_{B2} \sqrt{|\Delta p_{B2}|}}$$

13.12.3 Theoretical performance and simulation results

In (220) the resulting control law guarantees the theoretical performance as follows. Theorem 1. The control law in (227) and the adaptation law in (210) result in assured tracking errors that are bounded by if the controller parameters g_1 , g_2 , and c_1 satisfy

$$g_1 > \frac{2}{4c_1} \quad \text{and} \quad g_2 > \frac{2}{4c_1}.$$

$$(226) V(t) \leq \exp(-\lambda t) V(0) + \frac{\varepsilon}{\lambda} [1 - \exp(-\lambda t)], \quad \text{since}$$

$$V = \frac{1}{2} \omega_2 z_2^2 + \frac{1}{2} \omega_3 z_3^2, \quad \lambda = 2 \times \min\{k_2, k_3\} \varepsilon = \omega_2 \varepsilon_1 + \omega_3 \varepsilon_2$$

Furthermore, if $\Delta D_1 = \Delta d_{c1} = \Delta d_{c2} = 0$ after a finite time t_0 , i.e., in the presence of parametric uncertainties only, asymptotic output tracking is achieved, i.e., $z_1 \rightarrow 0$ as $t \rightarrow \infty$. Proof of Theorem 1: By differentiating $V(t)$ and observing the error dynamics that follow in (214) and (220), one can get

$$(227) \begin{aligned} V^* &= \omega_2 z_2 z_2^* + \omega_3 z_3 z_3^* \\ &= -\omega_2 \frac{\theta_1}{\theta_{1min}} k_{2s1} z_2^2 + \omega_2 z_2 (\theta_1 F_{Cds2} - \Phi_1^T \theta^* + \Delta D_1) - \omega_3 \frac{\theta_5}{\theta_{5min}} k_{3s1} z_3^2 \\ &\quad + \omega_3 z_3 [\theta_5 (Q_{c1ds2} + Q_{c2ds2}) - \Phi_2^T \theta^* + \Delta d_{c1} + \Delta d_{c2}] - \omega_3 z_3 \frac{\partial F_{cd}}{\partial \theta} \widehat{\theta} \end{aligned}$$

$$(229) \left\| \widehat{\theta} \right\|^2 = \left\| Proj_{\theta} [T(\omega_2 \phi_1 z_2 + \omega_3 \phi_2 z_3)] \right\|^2$$

$$\leq \left\| T(\omega_2 \phi_1 z_2 + \omega_3 \phi_2 z_3) \right\|^2 \leq 2(\|T\Phi_1\|^2 \omega_2^2 z_2^2 + \|T\Phi_2\|^2 \omega_3^2 z_3^2)$$

$$(230) \left\| z_3 \frac{\partial F_{cd}}{\partial \theta} \widehat{\theta} \right\| \leq c_1 \left\| \frac{\partial F_{cd}}{\partial \theta} \right\|^2 + \frac{1}{4c_1} \left\| \widehat{\theta} \right\|^2 \leq d_1 \left\| \frac{\partial F_{cd}}{\partial \theta} \right\|^2 +$$

$$g_1 \|T\Phi_1\|^2 \omega_2^2 z_2^2 + g_2 \|T\Phi_2\|^2 \omega_3^2 z_3^2)$$

$$(231) V \leq -\omega_2 \frac{\theta_1}{\theta_{1min}} k_2 z_2^2 + \omega_2 z_2 (\theta_1 F_{Cds2} - \Phi_1^T \theta^* + \Delta D_1) - \omega_3 \frac{\theta_5}{\theta_{5min}} k_3 z_3^2$$

$$+ \omega_3 z_3 [\theta_5 (Q_{c1ds2} + Q_{c2ds2}) - \Phi_2^T \theta^* + \Delta d_{c1} + \Delta d_{c2}]$$

$$\leq -\omega_2 \frac{\theta_1}{\theta_{1min}} k_2 z_2^2 - \omega_3 k_3 z_3^2 + \omega_2 \varepsilon_1 + \omega_3 \varepsilon_2 = -\lambda V + \varepsilon$$

$$(232) V_{\theta} = V^* + \theta^T T^{-1} \theta^*$$

$$= -\omega_2 \frac{\theta_1}{\theta_{1min}} k_{2s1} z_2^2 + \omega_2 z_2 \theta_1 F_{Cds2} - \omega_3 \frac{\theta_5}{\theta_{5min}} k_{3s1} z_3^2$$

$$+ \omega_3 z_3 [\theta_5 (Q_{c1ds2} + Q_{c2ds2})]$$

$$\leq -\omega_2 k_2 z_2^2 - \omega_3 k_3 z_3^2 + \theta^T [T^{-1} Proj_{\theta} (T\tau) - \tau] \leq -\omega_2 k_2 z_2^2 - \omega_3 k_3 z_3^2$$

. As a result, z_2 and z_3 are bounded, and z_2 and $z_3 \in L_2$. According to the Barbalat Lemma, as t approaches ∞ , $z_2 \rightarrow 0$. One can determine that $z_1 \rightarrow 0$ as $t \rightarrow \infty$ by taking into account the steady transfer function between z_1 and z_2 in (213).

In Matlab/Simulink, the dynamics of the lifting gantry to be controlled, i.e., the plant, were established using the complete dynamics model created in (200). The gantry's fundamental parameters are as follows: $m_g = 2200$ kg, $B_1 = 1200$ N/(m/s), $B_2 = 800$ N/(m/s), $A_1 = 2000$ N, $A_2 = 1400$ N, $I_m = 3$ m, $J_g = 4000$ kg·m², $ke = 1 \times 107$ Nm/rad, and $h = 0.2$ m. The pistons and rods have diameters of 80 mm and 56 mm, respectively. In addition, the controller's parameters deviate from the plant's actual values, and modelling errors were incorporated into all equations.

The theoretically rigorous method of selecting controller parameters is illustrated by (B. Yao et al. 2000), but it may significantly increase the complexity of the resultant control law. Therefore, in accordance with our previous research (Lyu, Chen, and Yao 2021) (Lyu, Chen, and Yao 2019), an alternative method was employed for gain tuning in this study. This involved selecting k_{2s1} and k_{3s1} that were sufficiently large, without regard for the precise values of the nonlinear robust feedbacks in (215) and (224). Additionally, this methodology was implemented in (B. Yao et al. 2000) (Helian, Chen, and Yao 2020). This ensured that, at least in the immediate vicinity of the reference trajectory, the robust performance requirements (215) and (224) were still met.

The simulation contrasted the following three control schemes:

• C1: the proposed controller The pre-estimated mass of the entire moving body was selected as $m_{Gpre} = 2000$ kg for the thrust allocation, which differed from the actual value in the plant. The feedback gains in the motion tracking controller were adjusted to $k_1 = k_{2s1} = k_{3s1} = 50$. The adaption rate matrix was $T = \text{diag}\{5 \times 10^{-17}, 1 \times 10^{-9}, 1 \times 10^{-9}, 5 \times 10^{-9}, 4 \times 107, 1 \times 107\}$,

$1 \times 107, 1 \times 107, 1 \times 107\}$, and the weighting coefficients were $\omega_2 = 1 \times 1010$ and $\omega_3 = 1$.

- C2: Without adaptation, the controller The sole distinction from C1 was that the motion tracking controller's adaptation was disabled, resulting in a value of zero for T .

- C3: the device that doesn't assign thrust The dual cylinders were typically operated by identical signals, as is customary in the field of engineering. Consequently, the controller performed no synchronisation efforts. The high-stiffness mechanical coupling was required to synchronise the dual cylinders. The motion tracking controller was identical to the one in C1.

For the following reasons, the control schemes noted above were selected for comparison.

C2 behaves similarly to a typical robust controller with only offline model compensation, as the adaptation is disabled. Consequently, the impact of parameter adaptation can be evaluated by comparing C1 and C2, for example, in terms of steady-state tracking error or positioning error. In the realm of practical engineering, C3 can be regarded as a control scheme that is frequently employed. One the one hand, the dual cylinders in the hoisting gantry are currently controlled by a single human-operated proportional valve in nearly all engineering applications. This implies that the synchronisation is solely mechanically maintained by the guide rails and crossbeam, with no software or control-level efforts involved. The crossbeam will rotate by a small angle, resulting in synchronisation issues, as the forces of the dual cylinders should be equal under these circumstances.

Therefore, in C3, the desired cylinder forces are generated by setting $F_{c1d} = F_{c2d} = \frac{1}{2}F_{cd}$ instead of the proposed thrust allocation in (204). This will result in cylinder output forces that are similar to those of the aforementioned practical situation. Conversely, the PID control is frequently implemented in practice, and it appears that the PID control should also be implemented in C3. The ideal parameter tweaking of PID is laborious and task-dependent, however numerous previous investigations have confirmed that ARC outperforms PID (B. Yao et al. 2000). It may be challenging to determine whether the enhancement is a result of the proposed propulsion allocation scheme or ARC's superiority over PID if C3 employs PID.

Consequently, in order to evaluate the synchronisation performance, C3 implements the motion tracking controller that was proposed, but without the allocation of propulsion. The proposed control scheme is compared to the representative control schemes C2 and C3, which are based on the aforementioned analyses, in terms of specific aspects.

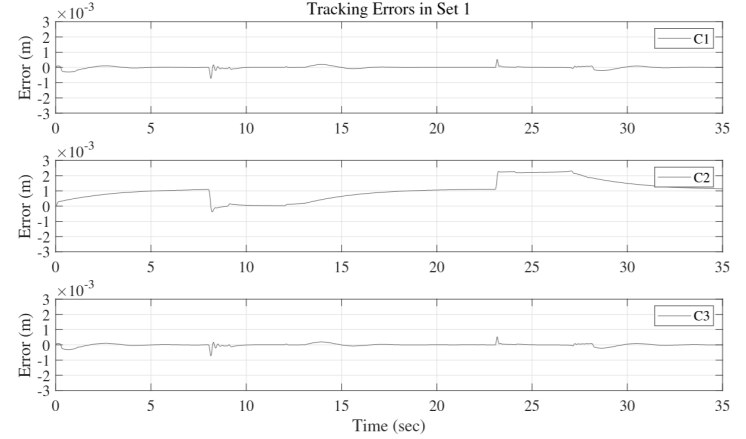


Figure 131: Motion tracking errors comparison in Set 1.

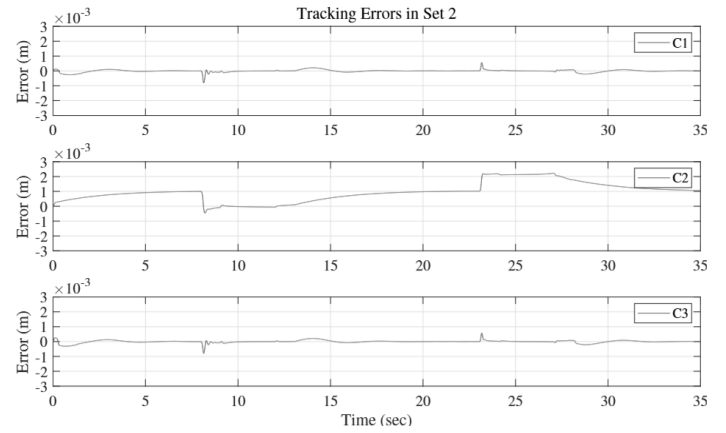


Figure 132: Motion tracking errors comparison in Set 2.

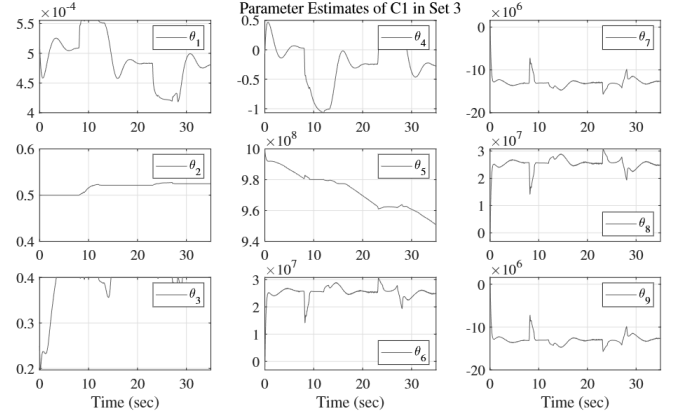


Figure 133: Parameter estimation results of C1 in Set 3.

Synchronisation performance is compared based on the calculated crossbeam rotational angle α . Refer to Set 1 for the rotating angles of C1, C2, and C3, with the inclined angle Θ of the lifting gantry set to zero. Ideal operational conditions load the dual cylinders equally.

As expected, all three control methods can regulate angles to zero following brief transient processes, but C1 and C2 are slightly faster.

However, under imbalanced load conditions (Set 2 and Set 3 with inclined angles $\Theta = 0.5$ rad, 1 rad), synchronisation performance differs. After rapid transient processes, the angles of C1 and C2 converge to very tiny values. This is due to the intended thrust allocation in both C1 and C2. The allocation of forces in the rotational motion, as defined in (202), allows for a small range of rotational angle regulation due to the stiffness of the connections between the crossbeam and guide lines. When unbalanced loads apply on dual cylinders, the rotational angle of C3 increases significantly without thrust allocation. Compared to traditional methods, the suggested thrust distribution methodology effectively regulates imbalanced loads on dual cylinders, resulting in high synchronisation performance.

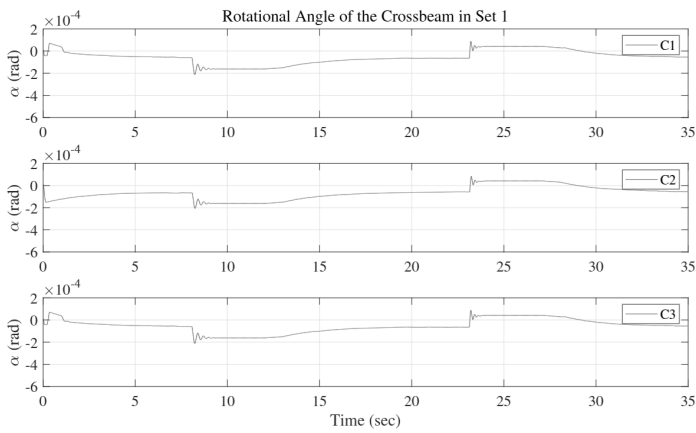


Figure 134: Rotational angles comparison in Set 1.

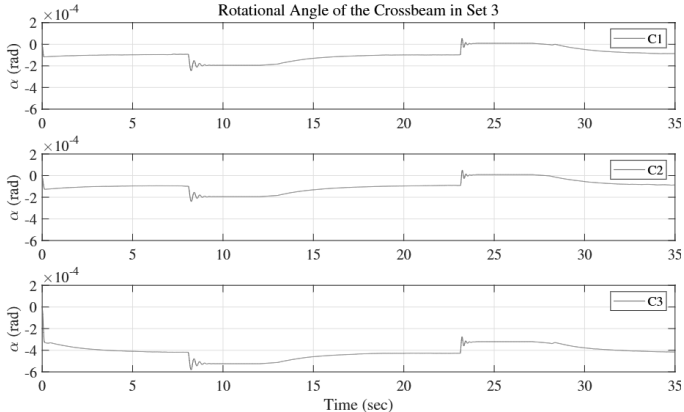


Figure 135: Rotational angles comparison in Set 3.

In conclusion, the comparative simulation results indicate that the proposed control schemes C1 are capable of achieving high-precision motion tracking performance and simultaneous high-level synchronisation of the dual cylinders in the hoisting gantry under unbalanced loads.

13.13. TBM manoeuvring through a curve

The narrow tail clearances in planar curves are located on the outer side of the ring diameter, which is parallel to the curve's plane, due to the predominantly inward (positive) tail

eccentricities relative to the lining (Figure 136 a). The TBM construction scenario, which is defined by an outward shield tail angle α and an inward tail eccentricity e , can be maintained while travelling around curves and is classified as a "eccentric" scenario (Saleta Gil Lorenzo 2022). The equilibrium can be achieved at a significant relative eccentricity between the shield tail and the touching rings in the "eccentric" scenarios (Figure bellow), as the net transverse component of the jack forces counteracts the action of the unbalanced sealing pressures. Specifically, the hydraulic thrust jacks lock the sealing pressure gradients. The position of the rings in contact is restricted at the cost of activating ring distortion (Saleta Gil Lorenzo 2022), as evidenced by field (Fig bellow) and numerical studies (Saleta Gil Lorenzo 2021). In contrast, the touching rings are prompted to adjust to a more concentric position by both TBM transverse actions when the tail shield eccentricity is negative. Only the underground tunnel structure resists lining correction. In that case, it would be anticipated that the distortion of the rings in contact would be reduced.

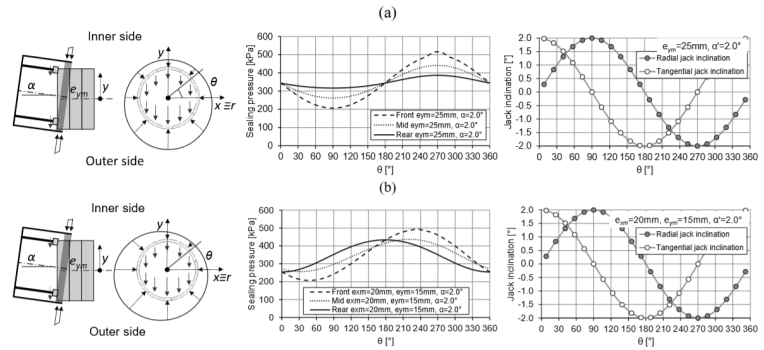


Figure 136: Example of eccentric tail seal passage that is typical of (a) steady and (b) incipient TBM steering around a curve (Saleta Gil Lorenzo 2022); e_{ym} represents the average eccentricity in the y axis aligned with the shield symmetry axis; exm represents the average eccentricity in the x axis.

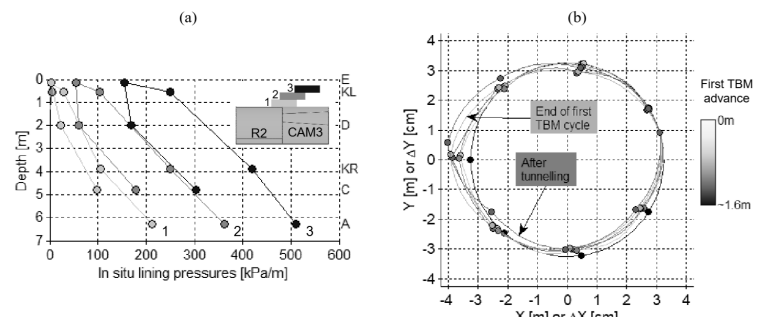


Figure 137: (a) Average lining pressures acting on the CAM3 instrumented ring of the Crossrail's Thames tunnel during the first TBM advance after ring erection; (b) in situ cross-sectional CAM3 ring distortion

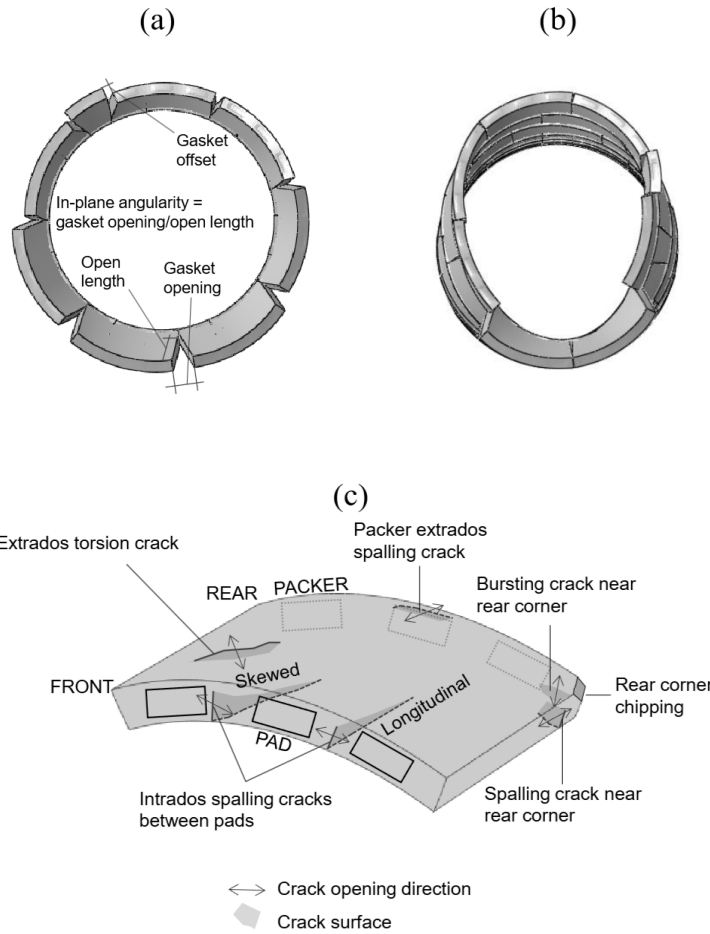


Figure 138: (a) The typical tulip shape in concentric scenarios (Saleta Gil Lorenzo 2021); (b) An example of R1 ring distortion mode for sealing pressures with vertical gradient and thrust jack transverse restraints at the invert (Saleta Gil Lorenzo 2021); (c) Concrete damage modes in the R1 ring identified during tail seal passage.

The in situ response research of the CAM4 instrumented ring in the Thames tunnel (CTT) of Crossrail is thoroughly investigated during tailseal passage at incipient TBM steering around a left curve. The extensive field data set collected on location must be carefully interpreted in order for the research to proceed. A Brillouin Optical Time Domain Reflectometer (BOTDR) was used to successfully equip the CAM4 ring segments with (i) distributed fibre optic sensors (DFOS) embedded in the concrete segments, (ii) embedded vibrating wire strain gauges (VWSGs), and (iii) a biaxial micro-electro-mechanical system (MEMS) tiltmeter. The results of the FE modelling carried out in conjunction with the field data are compared.

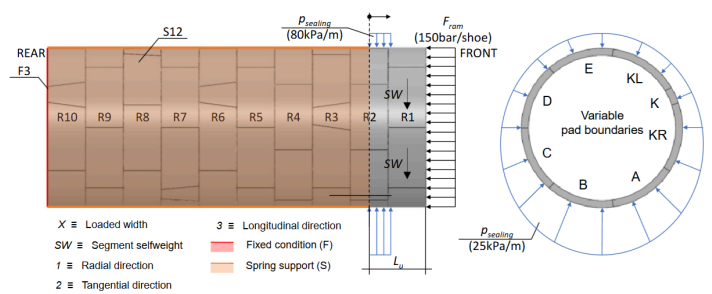


Figure 139: Single TBM advance sequential loading ABAQUS/Standard solid spring model.

A cell sensor topology was replicated in every instrumented segment of the ring sensor network, with the exception of the keystone. The deployment of the Neubrescope-5000X as the BOTDR interrogator for data collecting as a field monitoring instrument and the installation of fibre optic sensing cables embedded in the instrumented segments made it possible for the DFOS to sense temperature and tension. Parallel sensor topologies were implemented in the two primary directions of anticipated axial loading and bending, namely the hoop and longitudinal directions, to facilitate the calculation of mean strain and curvature. The principal instrumented parts consisted of a front and central hoop section, as well as a longitudinal section at the midpoint of the segment.

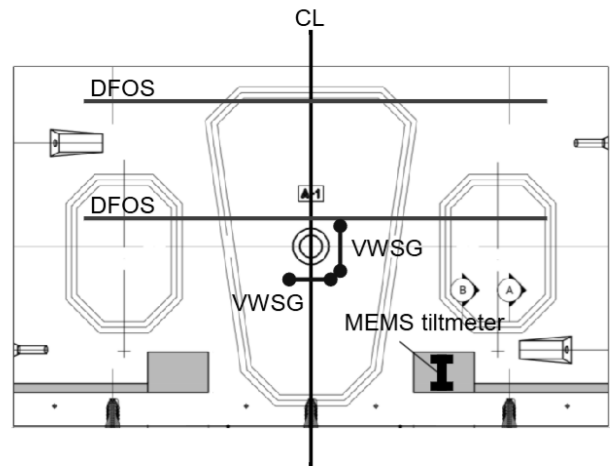


Figure 140: standard segment layout for instrumentation. MEMS stands for micro-electro-mechanical system, DFOS for distributed fibre optic sensor, and VWSG for vibrating wire strain gauge.

The calculated transverse jack forces should be regarded as indicative of trends. The graph indicates that the vertical moments were negative, necessitating the TBM operator to adjust the jack forces of the lower cylinder groups to be marginally greater than those of the top groups during uphill driving. Prior to manoeuvring around the left curve, the TBM operated with an elevated stance as the vertical jack forces were concurrently negative. The horizontal moments were

insignificant, and hence, the horizontal transverse forces were absent. From 0MNm to nearly 25MNm, the horizontal moments rose as the TBM went farther around the curve. With the active curve steering, the horizontal jack forces increased, indicating the development of an inward TBM position. In the initial two advancements following the erection of the CAM4 ring, AD1 and AD2, the vertical moments were minimal, approximately 5MNm, while the positive horizontal moments increased from around 10MNm to almost 20MNm, and the shield's inclination relative to the lining transitioned from primarily vertical to horizontal.

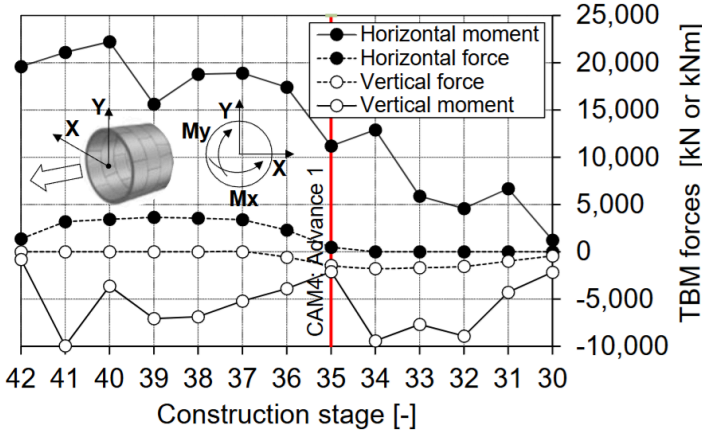
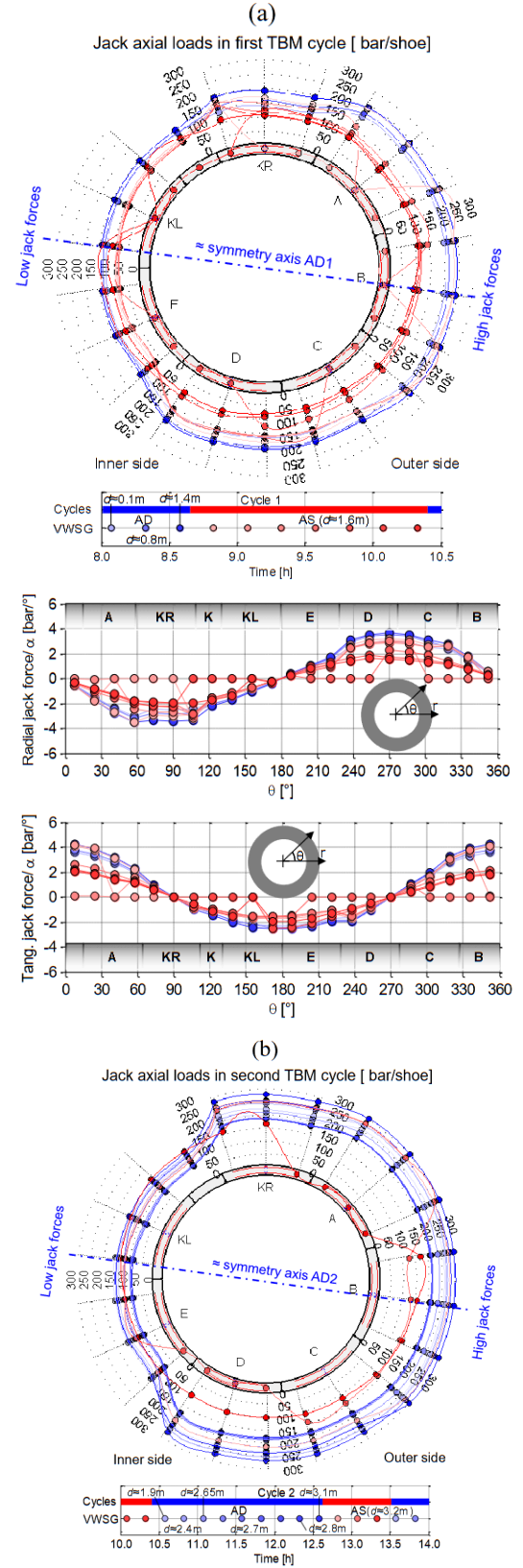


Figure 141: TBM forces adjacent to the CAM4 instrumented ring.

This is followed by the crown segment KR and the keystone K. In general, the hydraulic jacks that were released at each step of assembly were those that were absolutely necessary for the erection of segments. The axial loads of the reinstated jack were higher than those of the previous stages, with the exception of the first two assembled segments. This may have been done to assure the insertion of the segment and to balance the axial load distribution in the subsequent stage. After the keystone was erected, the maximum load per ram shoe—roughly 1,060 kN/shoe—was applied. Except for segments A and K, which were loaded by over 500kN/shoe, the ram loads oscillated about the value of 100bar/shoe, or 625kN/shoe, as soon as the ring assembly was finished. The loads just before the commencement of the first advance fluctuated around 50bar/shoe, which is equivalent to 312kN/shoe, as the jack forces relaxed over time during the stationary period.



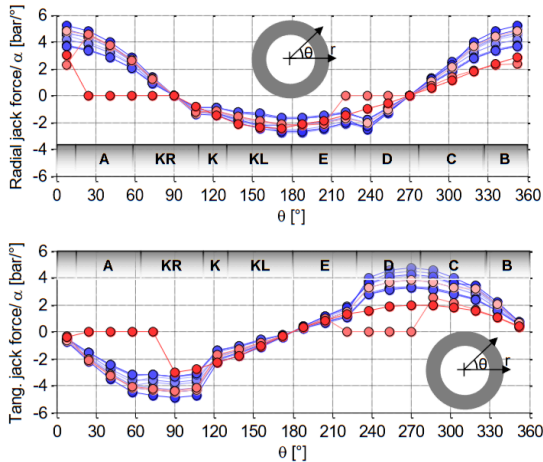


Figure 142: Axial jack loads and jack transverse forces in the (a) first and (b) second TBM cycles

The above study delineates the radial and tangential jack forces resulting from the machine's stance concerning the front ring. The shield angle α was considered positive vertical during the initial TBM cycle and negative horizontal during the subsequent cycle, resulting in negative and positive total transverse forces in the x and y axes, respectively. Both the first and latter phases of the shift to a steady steering along the left curve are reflected in the chosen shield poses. Since the shield tail angle's magnitude is unknown, the jack forces are expressed in bar/°. There were no additional TBMor line deviations taken into account. An inclined shield's geometry problem was used to determine the transverse forces using the approach suggested in Appendix A. The graphs indicate that the highest positive (outward) radial forces in the initial TBM cycle were experienced by the inversion segments C and D, measuring 4 bar/shoe/° or 25 kN/shoe/° during the first advance, and 2 bar/shoe/° by the conclusion of the subsequent ring's assembly. The outer springline segment B experienced the maximum tangential forces during the advance (4 bar/shoe/°) and the standstill (2 bar/shoe/°). During the second cycle, segment B had high radial outward forces of 6 bar/shoe/°, equivalent to 38 kN/shoe/°, during the advance phase, which subsequently decreased to around 2 bar/shoe/° during the assembly period. This time, the uppermost tangential forces were delivered to the crown and invert segments, varying between 4 bar/shoe/° during the advance and 2 bar/shoe/° during assembly.

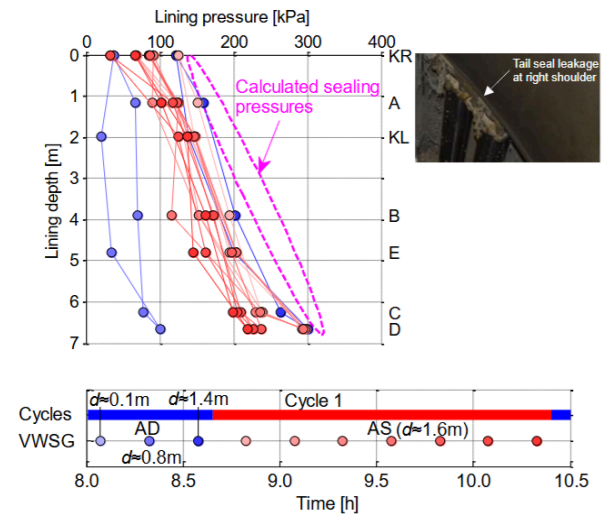
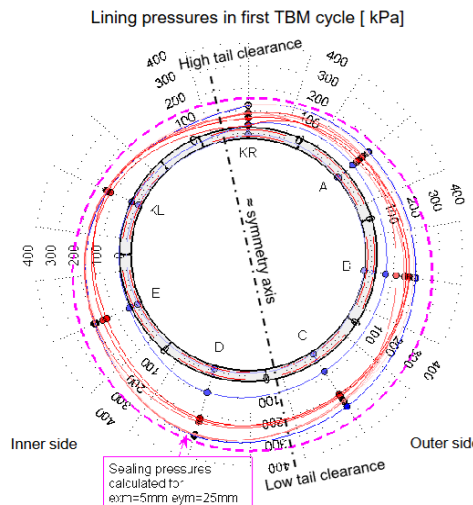


Figure 143: CAM4 lining pressures in the first TBM cycle

Similar to the other instrumented ring of the CTT tunnel, the CAM3 ring (Lorenzo 2023), the chronological analysis of the CAM4 lining pressures demonstrates that the eccentric passage of the tail seal was the primary cause of the highest pressures and pressure gradients observed during the initial two TBM cycles (Figure 143). Since the ring had not yet touched the tail seal when the first AD1 data set was taken at $d \approx 0.1$ m, the pressures were almost zero (Figure 142). The ring received almost half of the grease pressure when it was ≈ 0.8 m. The lining pressures exhibited an almost linear gradient with a depth of ~ 10 kPa/m, with elevated pressures on the outside side compared to the inner side of the ring. At $d \approx 1.4$ m, the complete sealing system had shifted onto the instrumented ring, with the majority of its breadth exerting pressure on the rear of the ring. The grout pressures in the rear encompassed a width of less than 0.1 meters. The lining pressures escalated to 120 kPa at the crown and 300 kPa at the invert, the vertical pressure

gradient climbed to 25 kPa/m, while the horizontal gradient became negligible. After the first advance ended, some ten minutes later, the next pressure profile was taken at $d \approx 1.6$ m. In accordance with prior research (Bezuijen et al. 2004; Talmon and Bezuijen 2009; "Processes around a TBM" 2008); , the annular pressures dissipate gradually during the tail stagnation periods as a result of grout consolidation and, ultimately, grout hardening. In bicomponent grouts, the hardening process generally commences within thirty minutes (Peila, Borio, and Pelizza 2011), and the compressive strength after one hour may vary from 30 kPa to 300 kPa (Hashimoto et al. 1995; Peila, Borio, and Pelizza 2011).

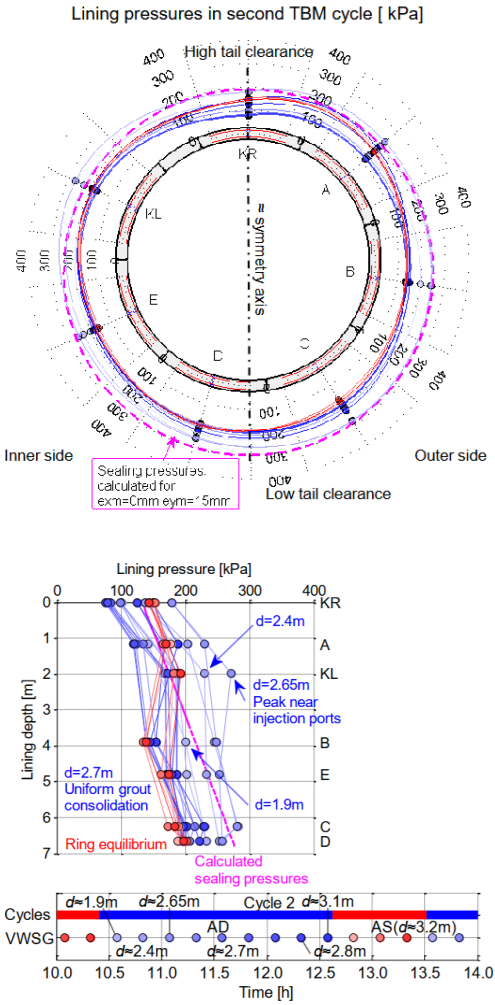


Figure 143: CAM4 lining pressures in the second TBM cycle

The initial pressure profile at $d \approx 1.6$ m during AS1 can be interpreted as a representation of the lining pressures at the end of AD1 since it is plausible to believe that the grout strength gain in the first 10 minutes of AS1 was minimal. At a depth of approximately 1.6 meters, the complete sealing system was in contact and approximately centred with the ring, while the rear of the ring was encircled by the annular grout for a width of approximately 0.3 meters. The lining pressures for swept

distances of $d \approx 1.4$ m and $d \approx 1.6$ m are nearly indistinguishable, indicating that a 0.2m increase in loaded breadth due to grout pressures resulted in an insignificant variation in average pressures. The contribution of the grout pressures to the lining pressures at this phase of the tail seal passage was consequently minimal. The void pressures behind the TBM are maintained throughout advancement with the continual injection of supplementary grout.

The thrust jack deviations of radial ram shoe offset and radial jack inclination can initiate the longitudinal curvatures, or moments, at the segment centroids during the tail seal passage. Although not very much, the longitudinal curvatures can also be altered by the increase in sealing pressures (S. Gil Lorenzo 2018). After subtracting the influence of the radial jack inclination associated with a specific shield body angle, Figure bellow estimates the ram shoe offset needed to approximate the field curvatures in the first TBM cycle. The computed ram shoe offset, α , is therefore:

(233) $\alpha = -\frac{kE_c I}{F} - \sin\varphi \frac{W}{2} + t \tan\varphi$ as the concrete is E_c . The following values are used to calculate the Young's modulus: I is the segment moment of inertia, F is the axial thrust load, φ is the jack radial inclination relative to the segment, taking outward jack rotations as positive, W is the segment width, and t is the ram pad thickness. This calculation was conducted with the shield body angles that were in alignment with the initial shield symmetry axis. (234) $\beta_r = \frac{\omega}{\sin\theta}$ where the polar coordinate of the centroid of the segment is denoted by θ . As a result of these segment rotations, the tail clearance ΔC at the ring front can be calculated as: (235) $\Delta C = -W \sin\left(\frac{\omega}{\sin\theta}\right)$

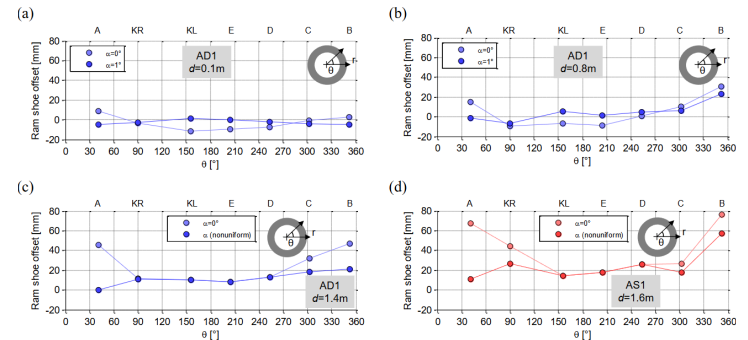


Figure 144 : Required ram shoe offset in the first TBM cycle.

The longitudinal vertical tilt increases following MEMS biaxial sensor in situ adjustment are shown. The tilt adjustment before the first advance was slight. Except for segments A and B, all segments' longitudinal tilt was negative throughout AD1, peaking around the crown and invert, consistent with the shield body and jacks' downward inclination. The $\sim 0.04^\circ$ vertical tilt at the invert matched the FE-calculated tilts from the eccentric tail seal passage simulation with invert ram pad restraints. Under thrust jack and selfweight downward forces, the top segments with the largest tail clearance rotated less

restrictively. Thus, the maximum negative tilt was near -0.06° . No downward force was provided at the crown segments in the FE model with invert constraints, hence the numerical tilt was positive. The early in situ tilt and vertical tilt increments developed at the second ring of the FE model coincide well in the second TBM cycle, except for segment A.

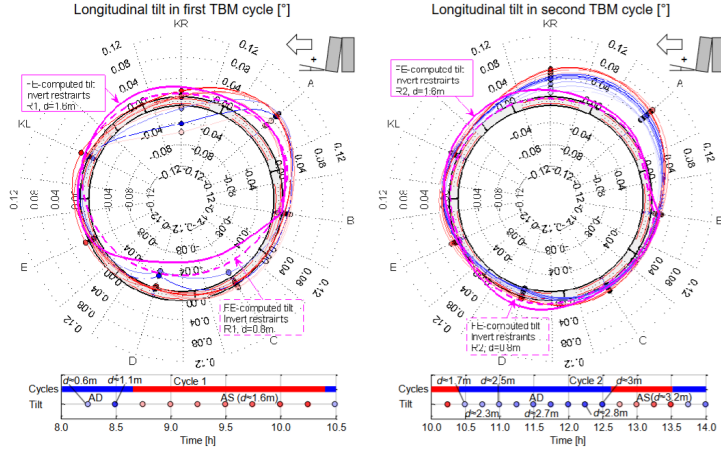


Figure 145: Longitudinal tilt in the first (a) and (b) second TBM cycles.

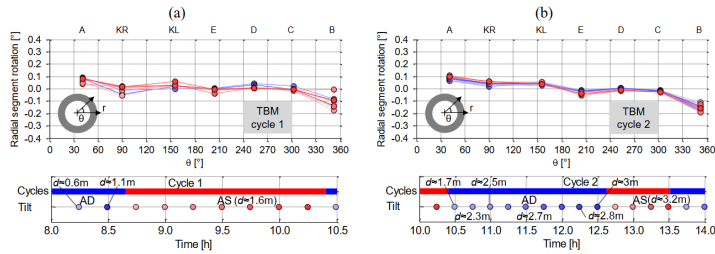


Figure 146: Radial segment rotation in the first (a) and (b) second TBM cycles.

The springline segment B turned inwards by $\sim-0.1^\circ$ during the initial advance, while the shield was tilted downwards. The rotation angle varied during the installation of the next ring. AS1 segment rotation matched ram loads and longitudinal curvatures. For instance, at the initial measurements at $d \approx 1.6m$, the longitudinal curvature and inward rotation exceeded -1.00° and nearly -0.2° , respectively. The negative curvature subsided by more than 0.25% , and the rotation decreased to zero in the third data set. The rotation returned to $\sim-0.15^\circ$ in the fourth data set, whereas the curvature fell to less than -0.50% . The rotations and curvatures were stabilised at approximately -0.10° and -0.75% , respectively, after the assembly of the exterior segments in the subsequent ring was done. These longitudinal numbers show that the interfacial quality between ram shoe and segment first and between segments after the next ring is erected greatly affects the outer springline's radial rotations and curvatures. Rotation of the following ring's segments during AD2 could affect thrust load transfer at the CAM4 ring's front ring joint. The considerable decline in segment B's longitudinal curvature may have been produced by front segment rotation in response to changing loading circumstances, as the outer springline segments are more prone

to radial rotations. Once segment cooperation was obtained in the following ring by rear hoop compression, curvature increments stabilised.

The minor changes indicate that the pressures were already stable. The concrete creep deformations resulted in an apparent rise in mean pressures. As in the initial two TBM cycles, the left segments displayed pressures above those of the right segments, correlating with the horizontal displacement of the tunnel tube and the offset ring position during the CAM4 tail seal passage. The transverse displacement $\Delta\delta$ of a ring embedded in elastic ground induces a total ground reaction F_g that is proportional to the variation in pressure gradient Δg : (236) $F_g = -K_{tot}\Delta\delta = \Delta g\pi R_e^2$. k_{tot} is the foundation modulus (Saleta Gil Lorenzo 2019) and R_e the tunnel's exterior radius. After the second TBM cycle, the residual horizontal pressure gradient was insignificant and became -12.0kPa/m in the eighth progression.

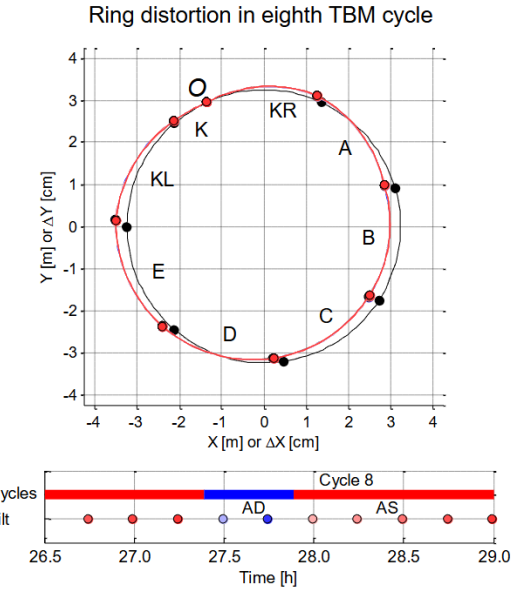


Figure 147: Ring distortion in the eighth TBM cycle

This gradient increment increases horizontal displacement by $+0.7\text{mm}$ for chalk elastic characteristics (Saleta Gil Lorenzo 2019) and CTT (cross rail thames tunnel) tunnel geometry. The sequential beam model projected a $+4\text{mm}$ displacement after the second TBM cycle, which would have increased horizontal gradients. Ground penetration of shields on the outer side of curves (D. Festa 2015; Alsahly, Marwan, and Meschke 2019) reduces the horizontal effective foundation modulus, which may explain the discrepancy between the two numbers. In Equation (236), a lower K_{tot} would increase horizontal displacements. Vertical pressure gradients were difficult to identify due to the lining pressure distribution's skewness. Between AS2 and the ninth TBM cycle, gradients increased from 0kPa/m to -14kPa/m in D, the inversion pressure segment.

Increased pressure gradients cause a +0.9mm displacement closer to the +3mm vertical deflection.

3.14. TBM Steering Simulator Geometric Model around Concrete Rings

The excavation efficiency of TBMs is significantly influenced by the proficiency of its operators, making TBM operator training an increasingly critical concern. Thus, TBM simulators for operator training have lately been developed by a couple of the world's top research universities in the TBM sector (Park et al. 2023). This study sought to construct a geometrical model for TBM steering simulation in curved excavation as part of the research project for the TBM steering simulator. The TBM steering system's concept and mechanism were examined first, and then mathematical formulae for simulation based on the steering mechanism—including articulation and shield jack operations—were derived. To validate the mathematical formulas, curved excavations were simulated using a Python software. In order to ascertain the impact of two articulation angles and two rotation angles on horizontal and vertical tendency, simulations of various cases were implemented. A actual TBM simulation of articulation operations was conducted using the proposed formulae.

TBM steering is accomplished by thrust and articulation jacks. The thrust jack is the sole tool that may be used for straight or almost straight excavation. The TBM can advance by simultaneously extending the jacks at the same rate. Nevertheless, depending on the characteristics of the tunnel line, both thrust and articulation jacks are utilised in tandem if the tunnel alignment consists of a straight line with a tightly curved line. The articulation jacks adjust to a specified articulation angle prior to the extension of the thrust jacks.

A copy cutter, an articulation jack, and a shield jack operation are typically included in curved excavation with a TBM steering system. In order to steer the front shield with the cutterhead in the desired direction, the articulation jacks are extended after the initial overcutting ensures sufficient space for curved excavation. The extension of the shield jacks propels the TBM forward. The following procedures are frequently carried out in curved excavation, although copy cutter operation was not taken into account in this study: 1. Extension of the articulation jacks to the desired articulation angle; 2. Extension of the shield jacks to the segment width; 3. Alignment of the articulation jacks; 4. Alignment of the shield jacks; 5. Installing the segment ring; 6. Repeating step 1.

For curved excavation to be successful, shield jack extension differences must be made by using tapered segments and one-sided extension (Chanchaya and Suwansawat 2014). We made the assumption that the shield jacks were stretched uniformly, concurrently, and at the same speed in this instance. The placement of the articulation point is the primary distinction between the two types of articulation systems, known as the "V" and "X" types. In the V-type system, articulation jacks are extended in the direction opposite to that of the curve, with the articulation point situated opposite the

extended jack. The X-type mechanism entails the simultaneous extension and retraction of the articulation jack during articulation, with the articulation point consistently positioned at the centre of the shield.

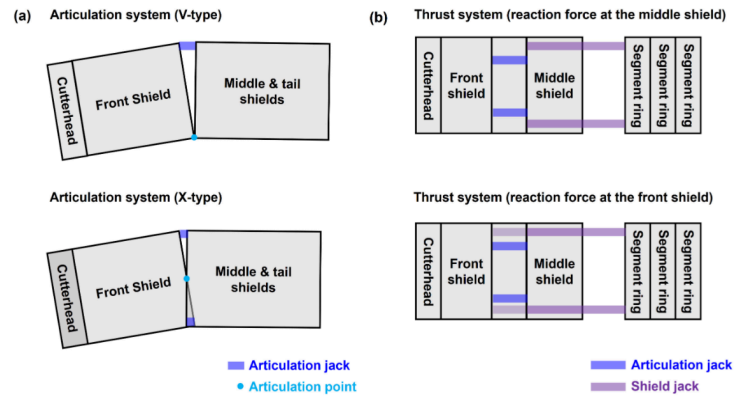


Figure 148: Different types of steering system (a) articulation system; (b) thrust system (S. O. Kang et al. 2017)

The front and middle shields are connected by a rotation pin at the articulation position in the X-type. The pin's position at the articulation point allows for the preservation of the space between both shields during articulation, facilitating effective sealing and water resistance, albeit with a reduced range of controllable articulation angles compared to the V-type. The shield skin plate serves as the articulation point in the V-type system. Due to the absence of connecting pins in the system, it is straightforward to rotate through any articulation angle in either direction. However, it becomes more difficult to stop water and dirt from entering during articulation as the articulation angle increases because of the wider spaces between shields (S. H. Kang et al. 2017). Figure b above illustrates two types of thrust systems: response force at the front shield and reaction force at the middle and tail shields. Regardless of the front shield's rotation, the latter may provide a steady thrust force to the segment ring without eccentric force, making it generally more suitable for curved excavation (Brundan and Danno 2020).

TBM positioning systems should use a minimum of three reference locations in three-dimensional space to report TBM behaviour as it advances. (Figure 149) bellow shows that the front reference point is on the shield face's plane, while the rear left and right points are on the plane of the shield face on the back of each side.

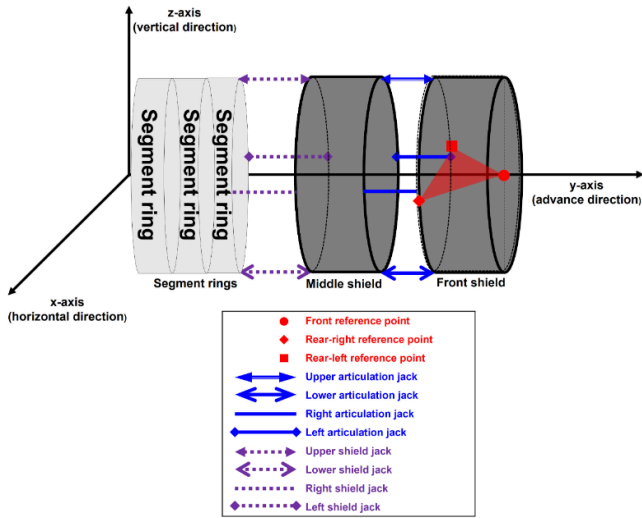


Figure 149: TBM steering system with TBM position

By keeping an eye on reference points, TBM operators try to maintain the intended alignment. During TBM advance, pitch, yaw, and roll rotations are unavoidably produced because of ground characteristics and machine weight (Figure 150 a). Pitching is the result of vertical deviations caused by an up or down deviation in the shield advance direction (Figure 150 b). Yawing refers to the departure of direction to the right or left, resulting in horizontal displacement (Figure 150c). Rolling refers to the inclination of the shield body to rotate in the opposite direction of the cutterhead's rotation (Figure 150d). During pitch and yaw, tail clearance between the shield machine and the segments is not guaranteed. Before they go above the maximum value, this should be fixed by extending a set of shield jacks, depending on the direction of rotation. There will be issues with muck discharge if rolling takes place since the released soil won't be properly placed onto the conveyor. Additionally, this puts an undue strain on the segment ring or screw conveyor, which eventually fails. Before it reaches its maximum value, rolling should also be adjusted by rotating the cutterhead in the rolling direction.

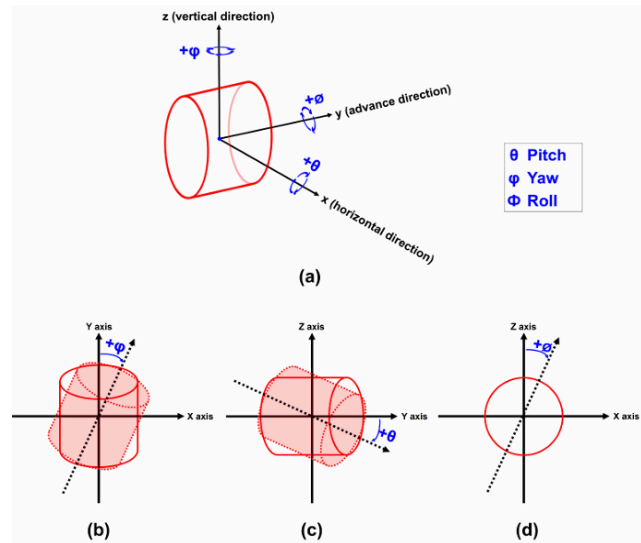


Figure 150: Three rotation angles (Xuesong Shen, Lu, and Chen 2011) : (a) three rotations; (b) yaw; (c) pitch; (d) roll

In an excavation simulation, the path is initially planned, using a TBM tunnel alignment that includes both a straight line and a curved line, utilising parallel rings for straight line excavation and tapered segments to the left or right for curved excavation (Poncetti et al. 2025). Presumably, each segment ring's cross section is situated at the centre of each monitoring point. The following is the mathematical model for the curved line based on this idea (Figure bellow) : (238) $T_x^i = T_x^{i-1} + d_r \cos(b_i) \sin(a_i)$, (239) $T_y^i = T_y^{i-1} + d_r \cos(b_i) \sin(a_i)$, (240) $T_z^i = T_z^{i-1} + d_r \sin(b_i)$ since $i = \text{ring number}$, $T_x^i = \text{the } i^{\text{th}} \text{ term of tracking point } T_x^i$ of the segment ring on x coordinate, $T_y^i = \text{the } i^{\text{th}} \text{ term of tracking point } T_y^i$ on y coordinates, $T_z^i = \text{the } i^{\text{th}} \text{ term of tracking point } T_z^i$ on z coordinates. a_i is the horizontal angle in the $x - y$ plane at the position of i , b_i is the vertical angle on the $y - z$ plane at the position i ; d_r = average width of the tapered segment rings

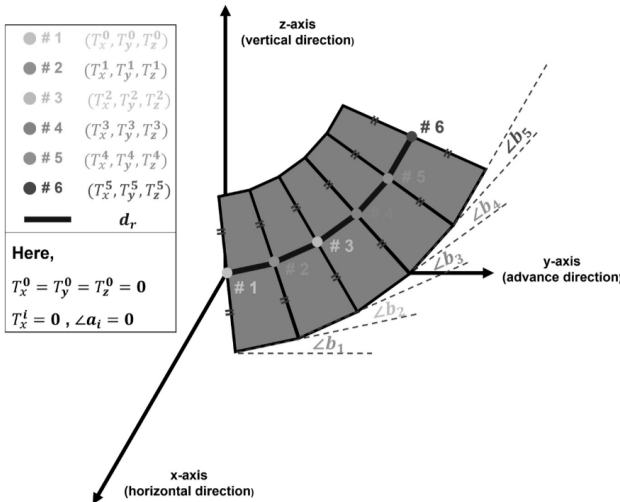


Figure 151: Illustration of a designed vertical curving trajectory

3.14.1 Operation of the Articulation Jack in the X-Type System

In order to manoeuvre the front shield in a curved excavation, articulation jacks are extended first.

The TBM is moved forward in the target alignment by extending shield jacks after the direction has been determined. The calculation of reference points entails several assumptions: the four articulation jacks (upper, lower, left, and right) are configured in a circular arrangement; the distance from each jack position to the centre is equivalent to the shield radius; the distance between the two rear reference points is equal to the shield diameter; and the distance between the rear and front reference points corresponds to the length of the front shield. Figure below depicts the X-type articulation system. It is possible to retract the articulation jack that is pointing in the direction of the target while concurrently extending the other jacks. While the other jacks automatically extend, only the upper articulation jack retracts if the TBM is to be guided upward. The following formula is used to calculate each articulation jack's length in the X-type system based on this principle:

$$(241) l = \begin{vmatrix} l_u \\ l_d \\ l_l \\ l_r \end{vmatrix} = \begin{vmatrix} -t_u v_u + t_d v_d + t_1 v_1 + t_r v_r \\ t_u v_u + t_d v_d + t_1 v_1 + t_r v_r \\ t_u v_u + t_d v_d + t_1 v_1 + t_r v_r \\ t_u v_u + t_d v_d + t_1 v_1 - t_r v_r \end{vmatrix}$$

In this context, l_u , l_d , l_l and l_r denote the length variations of the upper, lower, left, and right articulation jacks, respectively; t_u , t_d , t_l and t_r represent the operational durations for adjusting the articulation jacks in the upper, lower, left, and right orientations, respectively; and v_u , v_d , v_l and v_r indicate the extension velocities of the upper, lower, left, and right articulation jacks, respectively. The articulation angle is determined by the varying length of articulation jacks:

$$(242) \alpha = \tan^{-1}(\frac{l_l - l_r}{D}) = \tan^{-1}(\frac{l_{lr}}{D}),$$

$$(243) \beta = \tan^{-1}(\frac{l_d - l_r}{D}) = \tan^{-1}(\frac{l_{du}}{D}),$$

$$(244) l_r = \begin{vmatrix} l_{x^r} \\ l_{y^r} \\ l_{z^r} \end{vmatrix} = \begin{vmatrix} L_x^0 + \frac{D}{2}(\cos a_0 - \cos(a_0 + \alpha)) \\ L_y^0 + \frac{D}{2}(\sin(a_0 + \alpha) - \sin a_0) \\ L_z^0 \end{vmatrix}$$

$$(245) R_r = \begin{vmatrix} R_{x^r} \\ R_{y^r} \\ R_{z^r} \end{vmatrix} = \begin{vmatrix} R_x^0 + \frac{D}{2}(\cos a_0 - \cos(a_0 + \alpha)) \\ R_y^0 + \frac{D}{2}(\sin(a_0 + \alpha) - \sin a_0) \\ R_z^0 \end{vmatrix}$$

$$(246) F_r = \begin{vmatrix} F_{x^r} \\ F_{y^r} \\ F_{z^r} \end{vmatrix} = \begin{vmatrix} \frac{(L_x^0 + R_x^0)}{2} + l_F \cos(b_0 + \beta) \sin(a_0 + \alpha) \\ \frac{(L_y^0 + R_y^0)}{2} + l_F \cos(b_0 + \beta) \cos(a_0 + \alpha) \\ \frac{(L_z^0 + R_z^0)}{2} + l_F \sin(b_0 + \beta) \end{vmatrix}$$

(a) X-type (horizontal steering)

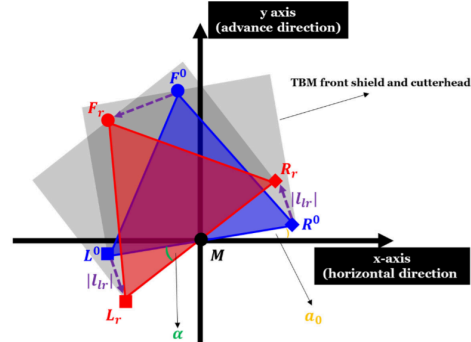


Figure 152: X-type system: (a) horizontal steering:

when F^0 = initial front reference point, R^0 = initial rear right reference point, L^0 = initial rear left reference point, F_r = front reference point after articulation work, R_r = rear-right reference point articulation work, L_r = rear-left reference point after articulation work, M = rear middle reference point (articulation point) α = articulation angle in horizontal direction, α_0 = initial angle in horizontal direction of planned route, $\overline{F^0 M} = \overline{F_r M} = l_F$ (length of front shield and cutterhead) $\overline{L^0 R^0} = \overline{L_r R_r} = D$ (TBM shield diameter), l_{lr} = length difference between left and right articulation jack.

(b) X-type (vertical steering)

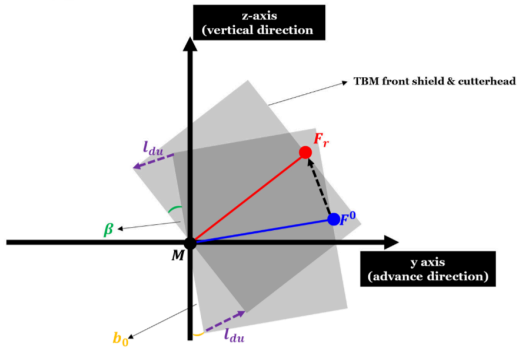


Figure 153: X-type system: (b) vertical steering;

F^0 = initial front reference point, F_r = front reference point after articulation work, M = rear middle reference point (articulation point = $R^0 = L^0 = R_r = L_r$), β = articulation angle in the vertical direction (yz plane), b_0 = Vertical angle on the yz plane at the initial position of planned route l_{du} = length difference between upper and lower articulation jack.

3.14.2 Operation of the Articulation Jack in the V-Type System:

Here, the other articulation jacks are stretched, leaving only the one in the target direction unaltered. Only the upper articulation joint remains unaltered in order to direct the TBM upward, while the others are retracted. The length of each articulation jack is established as follows:

$$(247) \quad l = \begin{vmatrix} l_u \\ l_d \\ l_l \\ l_r \end{vmatrix} = \begin{vmatrix} t_d v_d + t_1 v_1 + t_1 v_r \\ t_u v_u + v_1 + t_r v_r \\ t_u v_u + t_d v_d + t_r v_r \\ t_u v_u + t_d v_d + t_1 v_1 \end{vmatrix}$$

Regardless of the direction of horizontal steering, two reference points change simultaneously, with the front reference point shifting to new coordinates. However, since the articulation point is situated within the articulation jack, the reference points at the rear right and left may either vary or remain constant, contingent upon the goal direction. Auxiliary variables are initially determined to ascertain the new reference points in horizontal steering. (248) $d_{FR} = \sqrt{l_F^2 + \left(\frac{D}{2}\right)^2}$,

$$(249) d_r = \sqrt{2(d_{rp})^2(1 - \cos\alpha)}, \text{ Given that } d_{rp}, \text{ which is the}$$

distance between $R_r(R^0)$ and $F_r(F^0)$, and d_{Fa} , which is the distance between F^0 and F_r , are both dependent on the horizontal articulation angle. Reference points are recalibrated based on these auxiliary variables, contingent upon the rotation direction of the articulation angle and the angle of the

intended trajectory. If the horizontal articulation angle (α) is negative, the reference points are established as follows:

$$(250) \quad l_r = \begin{vmatrix} l_x \\ l_y \\ l_z \end{vmatrix} = \begin{vmatrix} L_x^0 \\ L_y^0 \\ L_z^0 \end{vmatrix}$$

$$(251) R_r = \begin{vmatrix} R_x^r \\ R_y^r \\ R_z^r \end{vmatrix} = \begin{vmatrix} R_x^0 + |l_{tr}| \cos(b_0 + \beta) \sin(a_0 + \frac{\alpha}{2}) \\ R_y^0 + |l_{tr}| \cos(b_0 + \beta) \cos(a_0 + \frac{\alpha}{2}) \\ R_z^0 + d_{F\alpha} \sin(b_0 + \beta) \end{vmatrix}$$

$$(252) F_r = \begin{vmatrix} F_x^r \\ F_y^r \\ F_z^r \end{vmatrix} = \begin{vmatrix} F_x^0 + d_{F\alpha} \cos(b_0 + \beta) \sin(-c + a_0 + \frac{\alpha}{2}) \\ F_y^0 + d_{F\alpha} \cos(b_0 + \beta) \sin(-c + a_0 + \frac{\alpha}{2}) \\ F_z^0 + d_{F\alpha} \sin(b_0 + \beta) \end{vmatrix}$$

where, according to the reference line at the back, c is the base angle of an isosceles triangle with three reference points ($\text{angle } F^0 L^0 R^0 = F_r^0 R_r^0 L_r^0 = F^0 R^0 L^0 = F_r^0 L_r^0 R_r^0$).

(a) V-type (horizontal steering, when $\alpha < 0$)

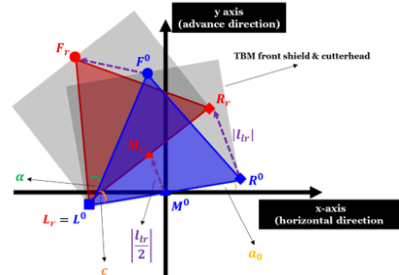


Figure 154: V-type system: (a) horizontal steering

When M_r = rear middle reference point after articulation work
 M^0 = initial rear-middle reference point α = articulation angle in horizontal direction, α_0 = initial angle in horizontal xy direction of planned route, α = articulation angle in the horizontal direction (xy plane) $\overline{L^0 R^0} = \overline{L_r R_r} = D$ (TBM shield diameter), $\overline{L^0 R^0} = \overline{F_r R_r} = d_{FR}$ (distance between $R_r(R^0)$ and $F_r(F^0)$), $\overline{F^0 F_r} = (d_{Fa})$ distance between F^0 and F_r caused by articulation angle in horizontal direction. $c = \text{angle } F^0 L^0 R^0 = \text{angle } F_r R_r L_r$

(b) V-type (vertical steering, when $\beta > 0$)

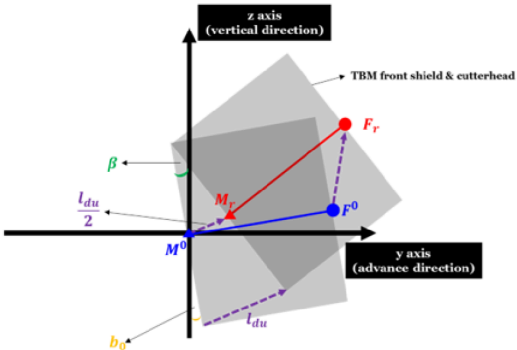


Figure 155: V-type system (b) vertical steering

M_r = rear middle reference point after articulation work M^0 = initial rear-middle reference point β = articulation angle in vertical direction (yz plane), b_0 = vertical angle in the horizontal direction (xy plane) at the initial position of planned route $F^0 M^0 (= \overline{F_r M_r}) = l_f$ (length of the front shield cutterhead), $F^0 F_r = (d_{F\beta})$ (distance between F^0 and F_r caused by articulation angle in horizontal direction). l_{du} = length difference between upper and lower articulation jack.

The three reference points shift in tandem for vertical steering, with the front reference points moving more than the rear and the rear reference points moving to new locations by the same amount:

(253) $d_{F\beta} = \sqrt{2(d_{FR})^2(1 - \cos\beta)}$, $d_{F\beta}$ = distance between F^0 and F_r caused by the articulation angle in the vertical direction. Based on the intended route's angle and the rotation direction of the articulation angle, the reference points are subsequently recalculated. The reference points are established in this manner if the articulation angle (β) in the vertical direction is positive.

$$(254) l_r = \begin{vmatrix} l_x^r \\ l_y^r \\ l_z^r \end{vmatrix} = \begin{vmatrix} L_x^0 + \frac{|l_{du}|}{2} \sin(a_0 + \alpha) \cos(b_0 + \frac{\beta}{2}) \\ L_y^0 + \frac{|l_{du}|}{2} \cos(a_0 + \alpha) \cos(b_0 + \frac{\beta}{2}) \\ L_z^0 + \frac{|l_{du}|}{2} \sin(b_0 + \frac{\beta}{2}) \end{vmatrix}$$

$$(255) R_r = \begin{vmatrix} R_x^r \\ R_y^r \\ R_z^r \end{vmatrix} = \begin{vmatrix} R_x^0 + \frac{|l_{du}|}{2} \sin(a_0 + \alpha) \cos(b_0 + \frac{\beta}{2}) \\ R_y^0 + \frac{|l_{du}|}{2} \cos(a_0 + \alpha) \cos(b_0 + \frac{\beta}{2}) \\ R_z^0 + \frac{|l_{du}|}{2} \sin(b_0 + \frac{\beta}{2}) \end{vmatrix}$$

$$(256) F_r = \begin{vmatrix} F_x^r \\ F_y^r \\ F_z^r \end{vmatrix} = \begin{vmatrix} F_x^0 + d_{F\beta} \sin(a_0 + \alpha) \cos(c + b_0 + \frac{\beta}{2}) \\ F_y^0 + d_{F\beta} \cos(a_0 + \alpha) \cos(c + b_0 + \frac{\beta}{2}) \\ F_z^0 + d_{F\beta} \sin(c + b_0 + \frac{\beta}{2}) \end{vmatrix}$$

If $\beta < 0$ then

$$(257) F_r = \begin{vmatrix} F_x^r \\ F_y^r \\ F_z^r \end{vmatrix} = \begin{vmatrix} F_x^0 + d_{F\beta} \sin(a_0 + \alpha) \cos(-c + b_0 + \frac{\beta}{2}) \\ F_y^0 + d_{F\beta} \cos(a_0 + \alpha) \cos(-c + b_0 + \frac{\beta}{2}) \\ F_z^0 + d_{F\beta} \sin(-c + b_0 + \frac{\beta}{2}) \end{vmatrix}$$

Extended shield jacks follow articulation. The shield jack mechanism works similarly to the V-type articulation system, extending just selected jacks while leaving others unaffected. For successful curved excavation during articulation, shield jack differences from one-sided extension are necessary. Assuming equal and simultaneous extension of shield jacks at the same speed, the length is determined as follows:

$$(258) ll = \begin{vmatrix} ll_u \\ ll_d \\ ll_l \\ ll_r \end{vmatrix} = \begin{vmatrix} tt \cdot V \end{vmatrix}$$

tt = operation time of the jack extensions, V = speed of jack extensions. During TBM advancement, the shield jack extension changes three reference locations by the same distance. These new reference points are calculated as follows following articulation work:

$$(260) R_r = \begin{vmatrix} L_x \\ L_y \\ L_z \end{vmatrix} = \begin{vmatrix} L_x^r + ll \cos(b_0 + \beta) \sin(a_0 + \alpha) \\ L_y^r + ll \cos(b_0 + \beta) \sin(a_0 + \alpha) \\ L_z^r + ll \sin(b_0 + \beta) \end{vmatrix}$$

$$(261) R_r = \begin{vmatrix} R_x \\ R_y \\ R_z \end{vmatrix} = \begin{vmatrix} R_x^r + ll \cos(b_0 + \beta) \sin(a_0 + \alpha) \\ R_y^r + ll \cos(b_0 + \beta) \cos(a_0 + \alpha) \\ R_z^r + ll \sin(b_0 + \beta) \end{vmatrix}$$

$$(262) R_r = \begin{vmatrix} F_x \\ F_y \\ F_z \end{vmatrix} = \begin{vmatrix} F_x^r + ll \cos(b_0 + \beta) \sin(a_0 + \alpha) \\ F_y^r + ll \cos(b_0 + \beta) \sin(a_0 + \alpha) \\ F_z^r + ll \sin(b_0 + \beta) \end{vmatrix}$$

The TBM advance shifts the front reference point F_x^r, F_y^r, F_z^r , rear right point R_x^r, R_y^r, R_z^r and rear left point L_x^r, L_y^r, L_z^r . To compensate for pitch, yaw, and roll deviations during TBM advancement, reference points are regenerated as per (Xuesong Shen, Lu, and Chen 2011).

$$(263) T = \begin{vmatrix} \cos\phi \cos\varphi & -\cos\phi \sin\varphi & \sin\phi & -\sin\phi \cos\theta \\ -\cos\theta \sin\varphi \cos\theta \cos\varphi & \sin\theta & \sin\phi \cos\varphi & +\cos\phi \sin\varphi + \cos\phi \cos\phi \cos\theta \end{vmatrix}$$

$$(264) LL = \begin{vmatrix} LL_x \\ LL_y \\ LL_z \end{vmatrix} = T \cdot L$$

$$(265) RR = \begin{vmatrix} RR_x \\ RR_y \\ RR_z \end{vmatrix} = T \cdot R$$

$$(266) FF = \begin{vmatrix} FF_x \\ FF_y \\ FF_z \end{vmatrix} = T \cdot F$$

T =matrix transformation of three rotational angles, θ =pitch angle φ =yaw angle, ϕ =roll angle FF = front reference point affected by the three rotational angles, RR = rear right reference point attached to the three rotational angles and LL = rear-left reference point due to the effect of three rotation angles.

(D. Festa, Broere, and Bosch 2015) research undermined the vertical and horizontal deviations caused by pitch and yaw when the TBM is assumed to move along the planned route:

$$(267) d_h = \left(\frac{(MM_x - M_x) - (FF_x - F_x)}{l_F} \right) \cdot 100,$$

$$(268) d_v = \left(\frac{(MM_z - M_z) - (FF_z - F_z)}{l_F} \right) \cdot 100$$

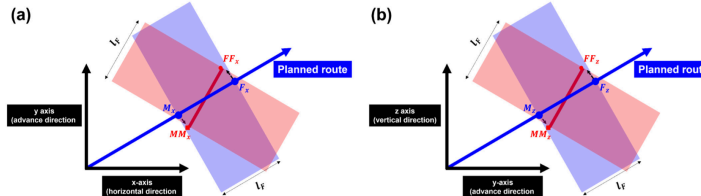


Figure 156: Deviation tendencies: (a) horizontal tendency; (b) vertical tendency.

Python programming was used to simulate curved excavations based on the mathematical models. Two procedures make up the curved simulation. After articulation, shield jacks are stretched to match segment length. After TBM advancement, a segment ring is formed and articulation and shield jacks are reset to their initial locations. Cycle operations consist of a sequence of processes, repeated until the simulation is complete.

Table 16: Example of simulation conditions for curved excavation.

Parameters	Value
TBM shield diameter (D)	8000 mm
Length of front shield and cutterhead (l_F)	3000 mm
Average thickness of segment ring (d_r)	1500 mm
Articulation jack speed ($= v_u = v_d = v_1 = v_r$)	1 mm/s
Shield jack speed (vv)	10 mm/s

Initial front reference point (F_x^0, F_y^0, F_z^0)	0 mm, 300 mm, 0 mm
Initial rear-right reference point (R_x^0, R_y^0, R_z^0)	4000 mm, 0 mm, 0 mm
Initial rear-left reference point (L_x^0, L_y^0, L_z^0)	-4000 mm, 0 mm, 0 mm

According to TBM manuals, the maximum articulation angle in the vertical direction is around 0.5° , while the horizontal angle varies based on the manufacturer and TBM size, ranging from 0.5° to 5.4° . As a result, the simulation's intended trajectory had both horizontal and vertical angles set at 0.5° . The horizontal and vertical variations resulting from two rotation degrees are critical metrics that the TBM operator must monitor in real time. In order to ascertain the impact of horizontal and vertical deviation, simulations with varying rotation angles ($0 - 2.5^\circ$) and articulation angles in the horizontal ($0 - 2.5^\circ$) and vertical ($0 - 0.5^\circ$) directions were tested.

The benefits of articulation sealing and water resistance during articulation make the X-type system evidently more suitable for use in curved excavation. Also, in comparison to the V-type, the X-type system's mathematical model is simpler. As a result, our primary focus was on X-type articulation system simulations of curved excavations under certain simulation settings. These simulations involved 100 cycles (100 rings) and took pitch and yaw into account.

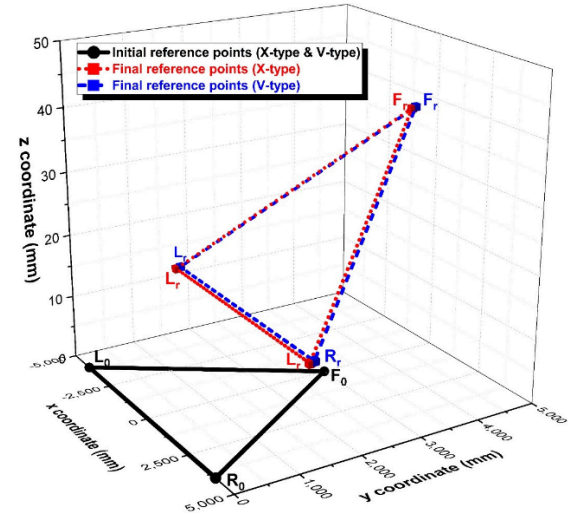


Figure 157: Comparison of reference points from a singular cycle simulation including X- and V-type systems.

Horizontal (a_i) and vertical (b_i) angles of 0.5° were used to generate the intended route in the upper-right direction. Therefore, a and b were set to be the same as a_i and b_i , respectively, to proceed along this path. Then, as indicated by Equations (5) and (6) in the table below, the articulation jacks were stretched.

The curved excavation process flow chart is displayed in the simulated curved excavation.

Location of Jack	Required length of articulation
	jack $\alpha = 0.5^\circ$ and $\beta = 0.5^\circ$
Upper	0 mm
Lower	70 mm
Left	70 mm
Right	0 mm

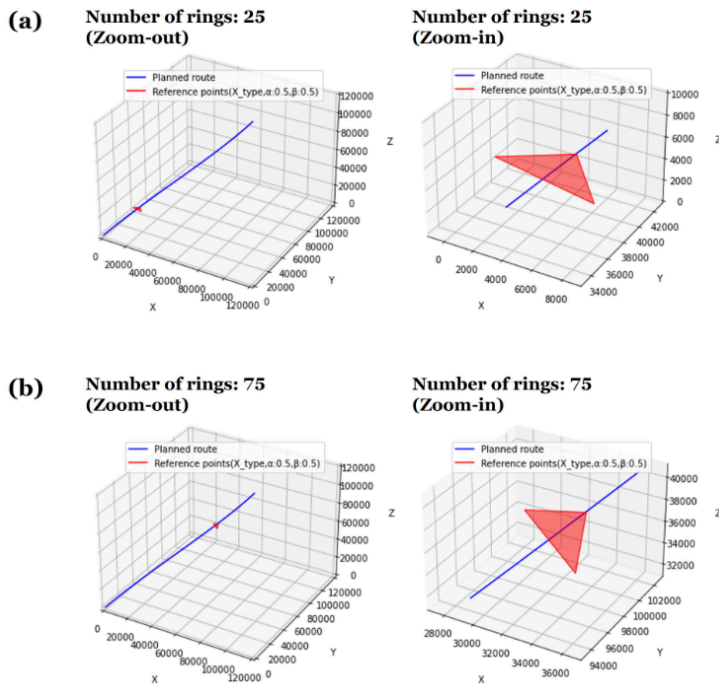


Figure 158: Simulated curved excavation in top-right direction without consideration of rotation angles: (a) simulation with 25 cycles; (b) simulation with 75 cycles.

(Figure 158) above illustrates the simulated advancement of curved excavation in the top-right direction, accounting for rotation angles (pitch = yaw = 1.0°) during 25 and 75 cycles.

In this case, during the simulation, the red triangle does not entirely follow the path. During the excavation process, the TBM is bound to vibrate due to pitch and yaw, which could result in deviations.

The final reference sites are listed in Table 17 bellow, and the TBM's total distance travelled is once more around 150 meters.

Table 17: Site references

Location of the reference point	Position (x;y;z)
L	(48, 299; 119, 800, 62, 117)
R	(53, 427; 113, 659; 62, 117)
F	(52, 339; 117, 962; 64, 420)
LL	(50, 383; 120, 004; 60, 032)
RR	(55, 403; 113, 776; 60, 141)
FF	(53, 390; 118, 137; 62, 368)

Figure bellow illustrates the difference, taking into account the rotation angles, between the rear reference point (M_{xx} , M_{yy} , M_{zz}) and the tracking locations of the intended route (T_x , T_y , T_z). The calculated deviations of 15,000 show an almost straight line, indicating that the estimated rear reference points and the tracking point are different. Despite the alignment of articulation angles with the direction angles of the planned route, deviations occur during curved excavation due to pitch and yaw when considering the rotation angles. Thus, following or during one cycle of curved excavation, the TBM operator would try to regulate the shield or articulation jacks to minimise deviations.

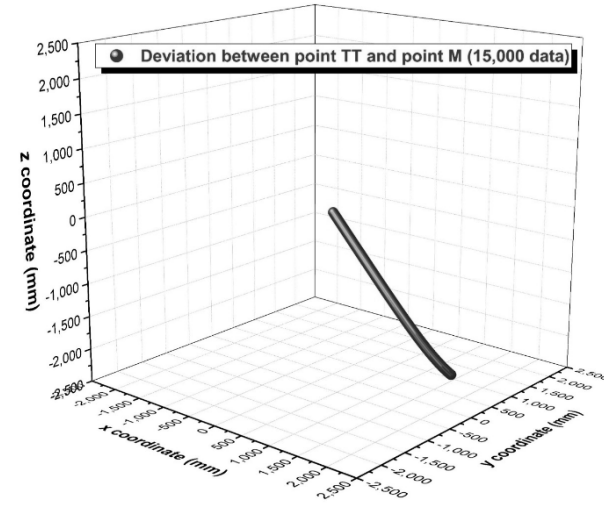


Figure 159: Simulated variations between the top-right tracking points of the intended route and the rear reference points, taking into account two rotation angles

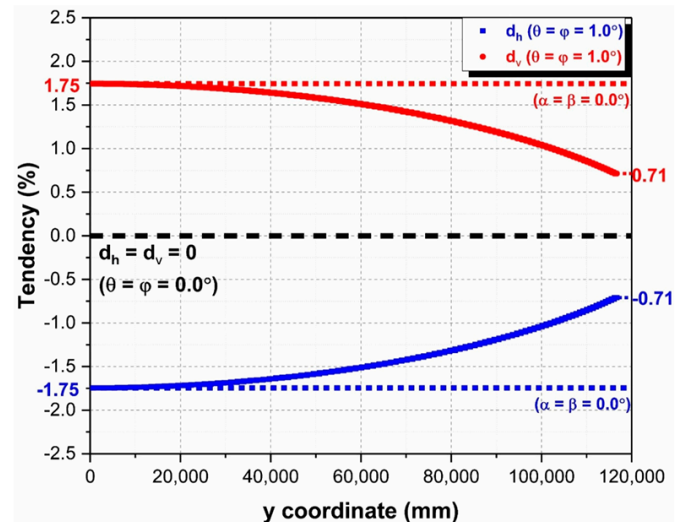


Figure 160: The top-right direction of the simulated curved excavation was used to determine the horizontal and vertical tendencies.

The horizontal and vertical tendencies shift from 1.75 and -1.75 to 0.71 and -0.71, respectively, as the total angle of the intended path grows. The TBM's forward motion causes a change in its y-coordinate advance direction, which in turn alters the direction of both tendencies, the magnitude of which approaches zero. When both α and β are equal to zero, the articulation angles are -1.75 and +1.75, respectively, and neither tendency changes. Since yaw and pitch are both identical at 1.0 degrees, the values of α and β are 0.5 degrees, and both tendencies align with the y symmetry axis.

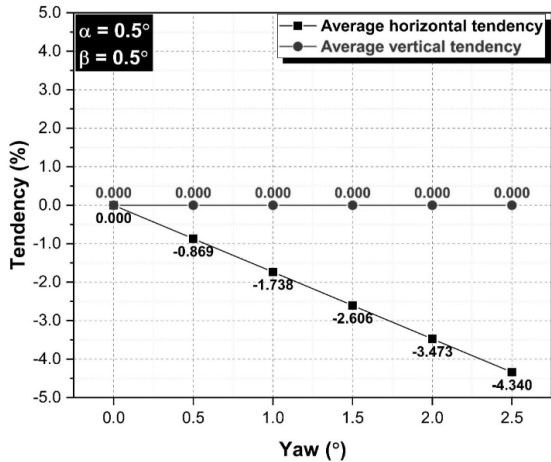


Figure 160: The yaw angle affects the horizontal and vertical tendencies differently.

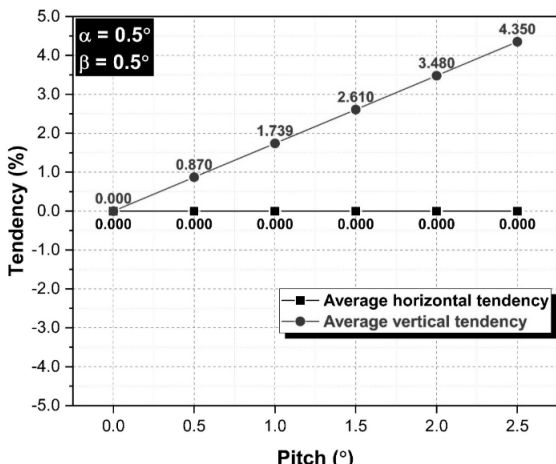


Figure 170: Variation of horizontal and vertical tendency with pitch angle

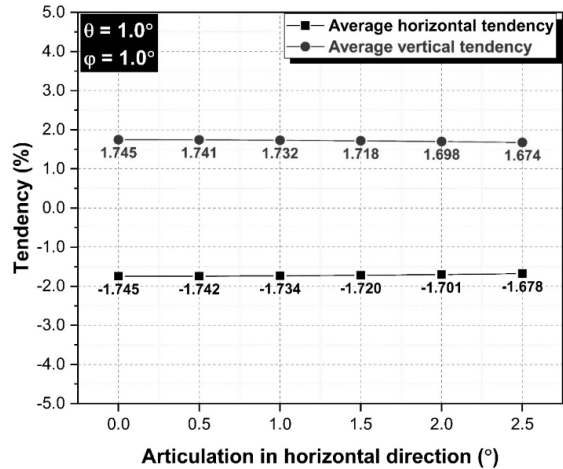


Figure 171: Propensity to lean horizontally or vertically varies with angle of horizontal articulation.

This study set out to instruct TBM operators, using a simulator, how to utilise the steering system for curved excavation. Consequently, the last step of the research was to apply and test the mathematical models that were proposed using the TBM simulator. Adobe Air, with its native scripting language Adobe ActionScript 3.0, was used to develop the TBM simulator. The software development kit (SDK) for Adobe Air was version 32.0, and the integrated programming environment (IDE) utilised was IntelliJ IDEA. Adobe Air is able to create applications with low capacity and excellent performance since it employs vector graphics. Easy platform access is a result of the lack of installation-related pre-configuration effort. The simulations included the test circumstances provided in order to compare the findings with Python.



Figure 172: Simulation progress of the curved excavation at 25 rings without considering rotation angles in top-right direction.

The graphic above illustrates the simulation in the top-right direction across five cycles, excluding the rotation angles, to demonstrate the adjustment of the articulation jacks during excavation. As illustrated in the above figure, discrepancies between the intended trajectory and the rear-middle reference point build throughout excavation due to the variance in articulation angles (0.2°) and the angles along the route (0.2°).

With both articulation angles elevated to 0.5°, the deviations are significantly reduced, allowing the TBM to traverse nearly the whole route once more.

Table 18: Direction angle in the x-z plane calculated from articulation jack lengths.

Condition	Direction Angle (Clockwise)
$l_u \leq l_d, l_l = l_r$	0° (= 360°)
$l_u > l_d, l_l = l_r$	180°
$l_u = l_d, l_l > l_r$	90°
$l_u = l_d, l_l < l_r$	270°
$l_u < l_d, l_l < l_r$	$\tan^{-1}(\frac{l_l - l_r}{l_d - l_u}) + 360°$
$l_u < l_d, l_l > l_r$	$\tan^{-1}(\frac{l_l - l_r}{l_d - l_u})$
$l_u > l_d, l_l \neq l_r$	$\tan^{-1}(\frac{l_l - l_r}{l_d - l_u}) + 180°$

During excavation, variations between the planned route and the rear-middle reference point are measured due to the rotation angles. As the entire excavation distance escalates, the deviations augment, as evidenced by the distance between the pale green dot and the crossline. Due to the progressive accumulation of induced deviation, the TBM operator must adjust the pitch and yaw utilising the shield jacks and articulation jacks. The varied nature of soil grounds means that variations are often inevitable during excavation. As a result, the operator uses the navigation panel to monitor the TBM position in real time and makes adjustments to the articulation and shield jacks based on deviations. The operator, on the other hand, is less worried by variations during rock extraction because most rocks exhibit more uniform properties than soil. Thus, the operator just needs to modify the shield jacks to be stretched during the excavation once the articulation jacks have been established beforehand. The excavation simulation in real time allows for the indirect experience of curved excavation in both soil and rock, contingent upon the designated rotation angles for the TBM simulator.

3.16. Anchorage length of the anchor

The free piece of the anchor can create prestress by increasing torque, and the anchor section can retain the anchor rod firmly inside the surrounding rock. The length of the anchorage section is often assumed to be around 0.4 times the length of the anchor, and the amplitude of the prestress is typically not greater than 2/3 of the anchor rod's tensile strength. This is the anchorage section's stress diagram.

(267) $\int_0^{L_1} 2\pi a \tau(x) dx - P = 0$, Establish the equilibrium equation as follows by taking a tiny force unit dx in the direction of the anchoring length and taking the prestressed anchor's anchorage length as L_1 . (268) $\tau(x) = Ax^2 + Bx + C$, anchorage section can be determined by fitting a

three-parameter quadratic polynomial as follows. (269) $2AL_1^3 + 3BL_1^2 + 6CL_1 = \frac{3P}{\pi a}$ The distribution law function of shear stress $\tau(x)$ in the where A, B, and C are constants to be calculated. L_1 is the length of the anchorage section, a is its radius, P is the prestressed anchor tension load, and $\tau(x)$ is the shear stress distribution function. From equations (267) and (268), we obtain (270) $2AL_1^2 + BL_1 + C = 0$ The maximum shear stress in the anchorage section of the prestressed anchor should be less than the shear strength of the anchorage interface when the anchoring force is supplied in that section. A safety factor is added to guarantee that the anchorage portion can function as intended, as indicated by the following equation. (271) $\tau_{max} = \frac{-B^2}{4A} + C \leq [\tau]/K$ where $[\tau]$ is the anchorage interface shear strength, τ_{max} is the maximum shear stress at the anchorage interface, and $1/K$ is the safety factor. By combining the aforementioned formulas (272) $L_1 \geq \frac{3P}{2\pi a(K[\tau] + C + \sqrt{K^2[\tau]^2 - K[\tau]C})}$ The physical meaning of constant C is residual strength τ_r when the loading end of the bolt enters the debonding stress condition. The shear strength of the anchorage interface should be greater than the maximum shear stress of the anchorage section. The embedded end shear stress value is still very small, almost negligible, when compared to the maximum shear stress of the bolt interface, meaning that the loaded end's residual strength can be disregarded. In the event that the field pullout test is unable to monitor the entire load-displacement curve of the loading end, the residual strength is set to zero and the parameter C 's influence on the anchorage length can be disregarded (273) $L_1 \geq \frac{3KP}{4\pi a[\tau]}$ Thus, equations (272) and (273) can be used to calculate the minimum anchorage section length of a r.prestressed anchor

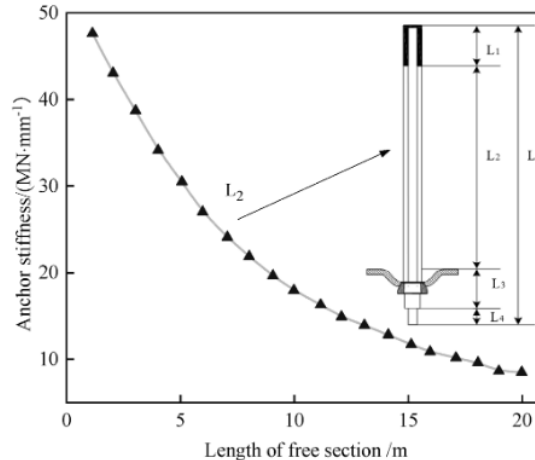


Figure 173: Effect of free section length on anchor stiffness

Anchor stiffness and bearing capacity are significantly increased by free section leading, and as free section length grows, so does bearing capacity, but overall anchor stiffness decreases. The bolt's stiffness value decreases with increasing free segment length. As a result, while designing and building a

prestressed anchor, it is crucial to choose the right anchor free length.

The utilisation of prestressed anchors in tunnel construction has seen a gradual increase. (Q. Wang et al. 2024) categorised prestressed bolts and validated their efficacy in maintaining surrounding rock stability under various anchoring techniques through on-site engineering tests. (Zhenyu Sun et al. 2024) examined the impact of different anchor support methods on tunnel yield zones and deformation, taking into account the interplay between grouting anchors and surrounding rock, and corroborated their findings at the construction site. (Cai et al. 2015) conducted a comparative analysis of plastic zone distribution and stress change characteristics in surrounding rock under diverse anchoring conditions. Field results demonstrate that the combined use of bolts and anchor cables effectively controls surrounding rock. These outcomes indicate the successful application of prestressed anchor bolts in practical engineering scenarios. Employing the prestressed anchor design method outlined in this paper, engineering calculations were performed within the context of the actual Badaling tunnel project.

To determine the length of the anchor The radius of the surrounding rock's plastic zone must first be calculated. The modified Fenner formula could be used to determine the radius of the plastic zone based on the elastic-plastic theory and the Mohr-Coulomb criterion.

$$(274) R_p = r_0 \left[\frac{(p_0 + c \cot \varphi)(1 - \sin \varphi)}{(p_1 + c \cot \varphi)} \right]^{\frac{1 - \sin \varphi}{2 \sin \varphi}}, r_0 = \text{circle radius of tunnel}$$

, $p_0 = \text{original rock stress}$, $C = \text{cohesiveness of soil}$,
 $p_1 = \text{Prestressed anchor force}$

R_p = Is the radius plastic zone, To get R_p (9) $L_2 \geq R_p - R_0$

(275) $L = L_1 + L_2 + L_3 + L_4$ where L is the exposed tension length, L_2 is the free section length, L_3 is the thickness of the pallet and anchorage, and L is the entire length of the prestressed anchor.

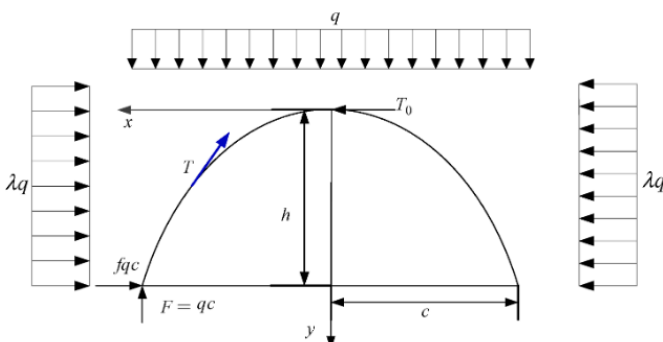


Figure 174: Mechanical bearing load on the arch

(276) $T_0 \cdot h - \lambda \cdot q \cdot h^2/2 - q \cdot c^2/2 = 0$ According to the balance of the force system:

$q = \text{vertical stress}$, $\lambda = \text{lateral pressure coefficient}$,
 $2c = \text{span of the bearing arch}$ (277) $T_0 - fqc - \lambda qh = 0$

$h = \text{height of the bearing arch}$

, $f = \text{solidity coefficient of the surrounding rock}$,
 $fqc = \text{horizontal shear force at the bearing arch}$

$$(278) T = \sqrt{T_x^2 + T_y^2} = \sqrt{(T_0 - \lambda \cdot q \cdot y)^2 + (q \cdot x)^2}$$

$T_0 = \text{axial force at the top of the rock}$

$T = \text{axial force at any point of the arch}$,

$$(279) T_0 = q(\lambda \cdot h^2/2 + q \cdot c^2/2)/h,$$

$$(280) T = \sqrt{(q \cdot (\lambda \cdot h^2/2 + c^2/2)/h - \lambda \cdot q \cdot y)^2 + (q \cdot x)^2}$$

$$(281) T_a = \frac{q \lambda \cdot h^2 + q \cdot c^2}{2h} = T_0$$

$x = c$, $y = h$, the side wall axial force is

(282) $T_b = \sqrt{\left(\frac{q \cdot c^2}{2h} - \frac{\lambda \cdot q \cdot h}{2}\right)^2 + (q \cdot c)^2}$ The axial force of the side wall and vault can be determined by analysing the surrounding rock bearing arch. The bearing capacity of the surrounding rock can be ascertained by further obtaining the bearing arch thickness of the surrounding rock by stress analysis.

3.16.1. Calculating the thickness of the bearing arch.

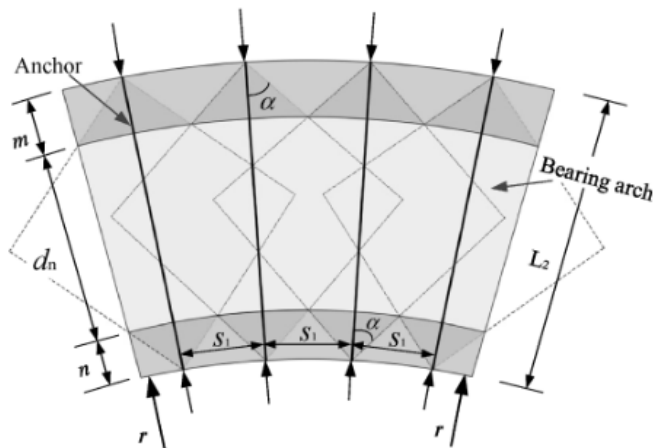


Figure 175: Schematic diagram of reinforcement bearing arch

$$(283) \frac{r}{L_2 + r} = \frac{s_1}{2m \cdot \tan \alpha}$$

$L_2 = \text{Length of the free section}$,

$d_n = \text{thickness of bearing arch}$,

$$r = \text{radius of curvature of cavity wall} \quad (284) n = \frac{s_1}{2 \tan \alpha}$$

$s_1 = \text{annular spacing of anchor}$

$$\alpha = 45^\circ \quad (285) d_n = L_2 - m - n \quad (286) d_n = L_2 - \frac{r + L_2}{2r \cdot \tan \alpha} s_1 - \frac{s_1}{2 \tan \alpha}$$

$$\text{Reinforcement diameter formed by the anchor} \quad (287) P_b = \frac{F_b}{S_1 s_1}$$

$$F_b = \text{Anchor preStress} \quad (288) [\sigma_c] = P_b \tan^2 \left(\frac{\pi + 2\phi}{4} \right) + 2c \cdot \tan \left(\frac{\pi + 2\phi}{4} \right)$$

$[\sigma_c] = \text{compressive strength bearing arch load (surrounding)}$

$$P_b = \text{Anchor prestressed}, \quad S_1 = \text{Annular spacing},$$

$$s_2 = \text{longitudinal Spacing} \quad (289) \sigma_a = \frac{q \lambda \cdot h^2 + q \cdot c^2}{2d_n \cdot h} < [\sigma_c]$$

$[\sigma_a] = \text{compressive strength bearing arch load}$

$$(290) \sigma_b = \frac{\sqrt{(q \lambda \cdot h)^2 + (q \cdot c)^2}}{d_n} < [\sigma_c]$$

Using the minimum uniaxial

compressive strength ($[\sigma_c]$) of the surrounding rock, the minimum bearing thickness of the tunnel vault and side walls can be calculated as follows (291) $d_a = \frac{T_a}{[\sigma_c]}$ (292) $d_b = \frac{T_b}{[\sigma_c]}$ By incorporating equations (293) and (294) into the safety coefficients of the vault and side walls, we obtain (293) $K_a = \frac{2d_n h [\sigma_c]}{q\lambda h^2 + qc^2}$, (294) $K_b = \frac{d_n [\sigma_c]}{\sqrt{(qc^2/2h - \lambda qh/2)^2 + (qc)^2}}$

3.16.2. Anchor length and spacing calculation:

(P. Li et al. 2023) was able to demonstrate from equation (273), it is evident that K equals 1.5, and P is contingent on the bolt's tensile strength, typically set at 10% by the designer, amounting to 18 kN. The shear strength of the anchorage interface, $[\tau]$, is 240 kPa, as determined by field pullout tests measuring the average cohesive force of the stratum. With a being 0.01 m, the final calculation yields: $L1 \geq 2.69$ m.

Equation (275) demonstrates that $L2 \geq RpR0$. The surrounding rock's cohesion, c , varies based on its properties. For grade IV and V surrounding rock, c is 0.3 MPa. The internal friction angle, ϕ , is 32°, while the original rock stress, $P0$, is 2.75 MPa. The prestressed anchor supporting force is 0.2 MPa. Inserting these values into equation (275) results in: $r0 = 19.11$ m and $Rp = 26.65$ m. Consequently, $L2 \geq RpR0 = 7.54$ m.

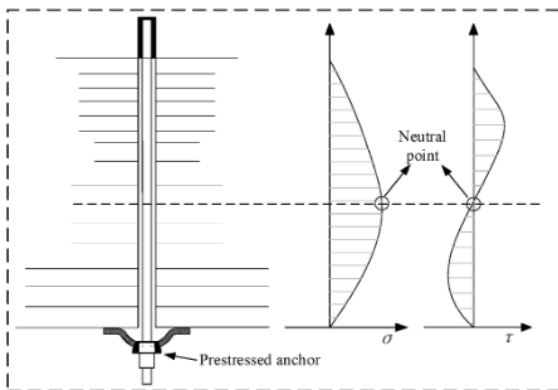


Figure 176: Axial force of an anchor diagram

$L3$ represents the pallet and anchorage thickness, typically ranging from 0.2 to 0.3 m. $L4$ denotes the exposed tension length, usually 0.15 m, which depends on the anchor type and anchorage method. The total prestressed anchor length is thus calculated as: $L = L1 + L2 + L3 + L4 \geq 10.68$ m. In this case, the prestressed anchor length, L , is set at 11 m.

As anchor density increases, the stress fields generated by the bolts overlap, resulting in a thicker bearing arch. For grade III and IV surrounding rock, it is suitable to consider a thickness of 0.8 to 1.5 m for grade IV. In the Badaling tunnel project, the transverse bolt spacing is 1.2 m. However, as the tunnel excavation's impact on the surrounding rock is less significant along the tunnel axis compared to the transverse direction, and the anchor rod forms the bearing arch transversely, the transverse bolt spacing can be slightly larger than the longitudinal spacing.

3.16.3 Calculation explanatory of anchor axial force and applied load of the bearing arch

The bearing arch thickness for various surrounding rock grades is determined by calculating the axial force using formulae (278) to (289), considering the differing bearing capacities. Utilising equations (290) to (294), the minimum bearing arch thickness for the vault and side wall is derived, as shown in (Figure 175). (Figure 176) illustrates the correlation between surrounding rock strength and bearing arch thickness.

The calculations reveal that bearing arch thickness decreases as surrounding rock strength increases. For surrounding rock strength below 5 MPa, the vault requires a minimum bearing arch thickness exceeding 10 m. When the strength reaches 8 MPa, the required minimum thickness ranges from 2.96 to 5.41 m. At 20 MPa strength, the minimum thickness is approximately 3 m.

Grade I surrounding rock typically has a bearing arch thickness under 3.5 m, while grade II ranges from 3 to 6 m. Grade III requires a minimum thickness of 6 to 16 m. Due to their low strength, grades IV and V necessitate a bearing arch thickness surpassing 16 m to maintain stability.

Consequently, grade I, II, and some grade III surrounding rock can maintain stability using their own bearing arch and bolt support. However, grades IV and V require more robust support measures to enhance the surrounding rock's compressive strength and bearing arch thickness, thereby ensuring stability. The surrounding rock bearing arch thickness (d_n) can be increased by modifying anchor length and judiciously adjusting spacing. Preliminary design parameters for prestressed anchors are determined by comparing the bearing arch thickness with the minimum bearing arch (d_a , d_b) through theoretical calculations.

3.17. Rail system

The wheelset, consisting of two wheels connected by a cylindrical rod (the axle), rotates at a uniform angular velocity (ω) due to the rigid connection between the components. This wheelset moves along a steel guideway formed by two parallel rails, separated by a predefined distance known as the rail inside face. This configuration is commonly referred to as the conventional "wheel-axle" system (Figure 177). The rail itself consists of three primary structural elements: the foot, the web, and the head, each contributing to the stability, strength, and functionality of the track system.

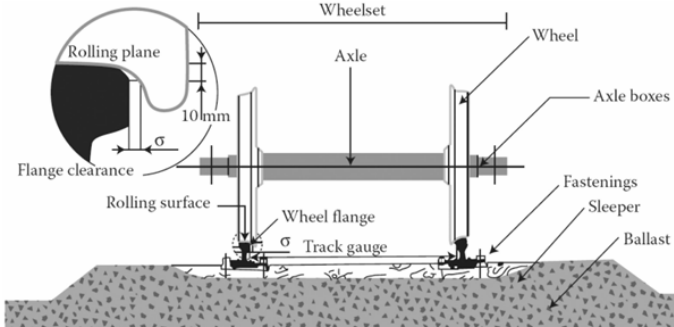


Figure 177: Wheelset railway conventional rolling rails(Pyrgidis 2021).

Elastic forces, including creep and gravitational forces, are generated at the wheel-rail contact interface during wheel rolling. Under favorable operating conditions—such as high-quality track alignment, compliance with speed limits, and well-maintained rolling stock—these forces play a crucial role in maintaining vehicle stability and ensuring precise guidance along both straight sections and curves of the railway.

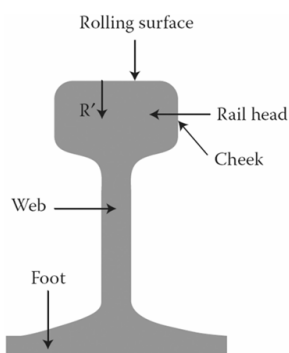


Figure 178: Applied load direction on track

Rail operating on a straight path: A conventional railway wheelset, running at a constant speed (V) along a straight track, maintains equilibrium when centered on the rails. However, any transverse displacement of the axle from its initial equilibrium position—due to factors such as track irregularities or wheel asymmetry—alters the rolling radii of the two wheels, resulting in unequal radii ($r_1 \neq r_2$). In such a scenario, as shown in (Figure 180), the relationship ($r_2 > r_0 > r_1$) holds, where r_0 represents the rolling radius at equilibrium.

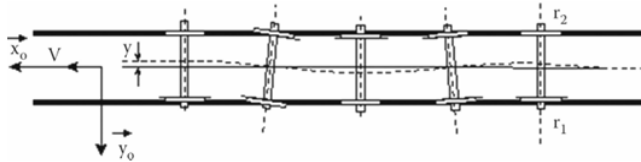


Figure 179: Sinusoidal motion of a railway wheelset(Pyrgidis 2021)

Since both wheels are rigidly connected to the axle, they rotate with the same angular velocity ω . Consequently, the following relationship emerges:

$$(295) \omega r_2 > \omega r_0 > \omega r_1 \text{ where } V_2 > V_1 > v$$

Where V_2, V_1 relative velocities of the wheels

Here, the wheel with the larger rolling radius r_2 travels faster than the smaller-radius wheel r_1 , causing the axle to rotate about the transverse axis y_0 . As the wheelset continues moving forward, the rolling radius r_1 of the slower wheel (wheel 1) gradually increases, while r_1 of the faster wheel (wheel 2) decreases. This dynamic reversal, where wheel 1 begins to overtake wheel 2, initiates a cyclical process known as hunting oscillation.

In practice, the motion of the wheelset—and particularly of the complete vehicle system, including the car body and bogies—is more complex. At constant speed V , if the rolling direction of the wheels deviates from the direction of vehicle movement, creep forces develop at the wheel-rail interface. These forces alter the kinematics, imparting a dynamic behavior to the wheelset (Giannakos 2012).

At low speeds, this mechanism ensures vehicle stability (Joly and Pyrgidis 1990). However, at higher speeds, the amplitude of oscillations increases, and the wheelset motion becomes unstable. Stability under such conditions is maintained through the primary suspension system, which provides longitudinal elastic connections between the bogies and wheelsets, thus limiting oscillation amplitudes.

If the wheelset's lateral displacements exceed the allowable flangeway clearance, the wheel flanges ensure continuous wheel-rail contact and prevent derailment as shown in figure 7. These flanges play a critical role in maintaining safe operation, especially under dynamic conditions.

Wheelset Dynamics in Curved Track Sections: Consider the scenario depicted in Figure 8, where a wheelset enters a curve and experiences a lateral displacement 'y' relative to its outer face. Due to the conical shape of the wheel profiles, the original rolling radius r_0 for both wheels changes to r_1 and r_2 for the outer and inner wheels, respectively. The rolling radius of the outer wheel becomes larger, satisfying the condition $r_1 > r_2$, which results in higher linear velocity for the outer wheel $V_1 > V_2$. Since the two wheels are rigidly connected to a common axle, the wheelset tends to rotate towards the inner side of the curve by a transverse displacement y_0 , seeking a radial alignment along the curve, with each wheel covering a different path length. However, if this transverse offset y_0 exceeds the available flangeway clearance σ , the wheel flanges ensure that the wheels remain securely on the rails, preventing derailment.

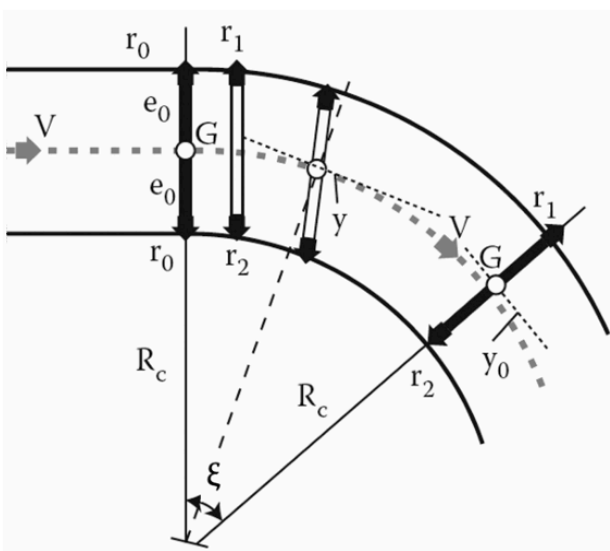


Figure 180: Single railway wheelset movement in a track curvature(Pyrgidis 2021).

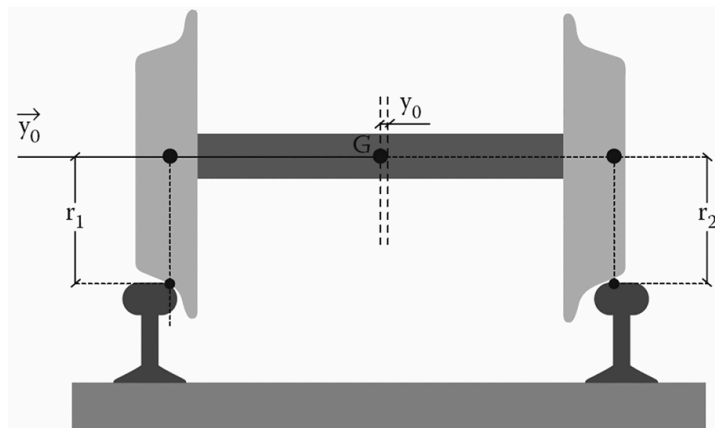


Figure 181: Cross section illustration(Pyrgidis 2021).

Although the description above focuses on the behaviour of a single wheelset, curve negotiation by the bogie and vehicle as a whole involves more complex dynamics. The positioning of the axles is influenced by the interaction between the motions of the bogies and the car body. Despite these complexities, the fundamental mechanism of wheelset guidance in curves follows the same principle.

Since the inception of railways in 1825, this wheelset guidance mechanism has served as the foundation for maintaining the stability and alignment of railway vehicles on both straight and curved tracks. Unlike other modes of transport, rail vehicles do not rely on human input, such as steering, nor do they require complex guidance systems.

To further analyse curve negotiation, horizontal curves can be categorised based on the range of their radii values R_c , offering insight into the challenges involved in vehicle dynamics along different track geometries.

- $R_c \geq 5,000 \text{ m}$ Very large curve radii
- $2,000 \text{ m} \leq R_c < 5,000 \text{ m}$ Large curve radii
- $500 \text{ m} \leq R_c < 2,000 \text{ m}$ Medium curve radii
- $250 \text{ m} \leq R_c < 500 \text{ m}$ Small curve radii
- $100 \text{ m} \leq R_c < 250 \text{ m}$ Very small curve radii
- $20 \text{ m} \leq R_c < 100 \text{ m}$ Tramway network curve radii

6) $V_{ar} \leq V_{maxtr} \leq V_d V_{maxtr} = \text{Speed at individual track segment}$
 $= \text{Average running speed}$

57) $t = \frac{s}{V_{ar}} + n_s t_s = \text{Target time,}$
 $= \text{Connection length (Km)} n_s = \text{number of intermediate stops,}$
 $= \text{Average running speed, (257)} V_d = V_{ar} \cdot k_v,$
 $= \text{Track design speed coefficient, (258)} 2\sigma = 2e - (2d_a + 2f_a)$

With the exception of curved alignment sections with small curvature radii ($R_c < 150\text{--}200\text{ m}$), where a widening of the track gauge is frequently permitted to facilitate the inscription of vehicle wheelsets (gauge widening), the distance between the rails is constant throughout the network length regardless of the type of track gauge. In the case of standard track gauge, the arrangement of the rails and the wheels that run on them automatically.

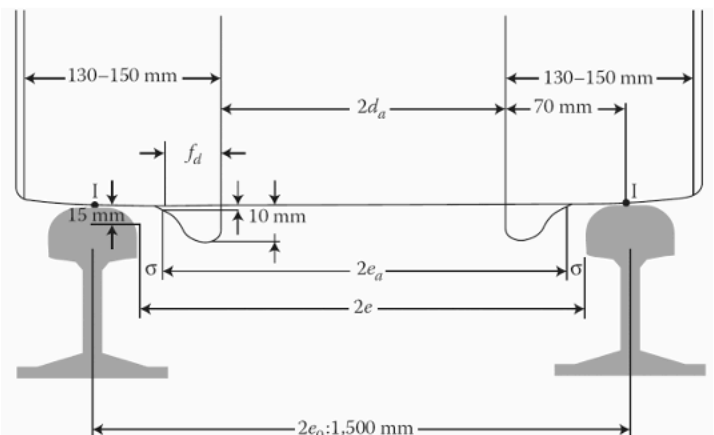
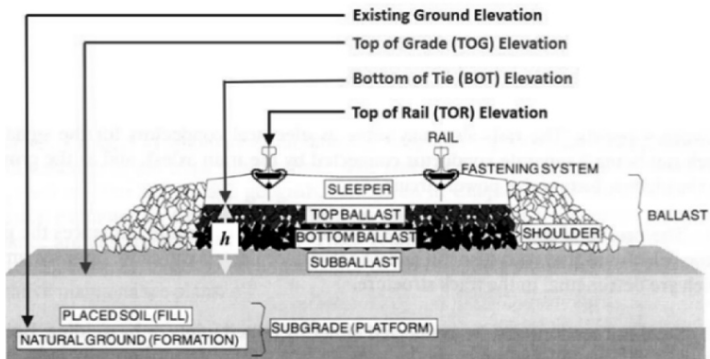


Figure 182: Standard gauge railway track with wheels on rails: geometrical and constructional dimensions (Pyrgidis 2021).

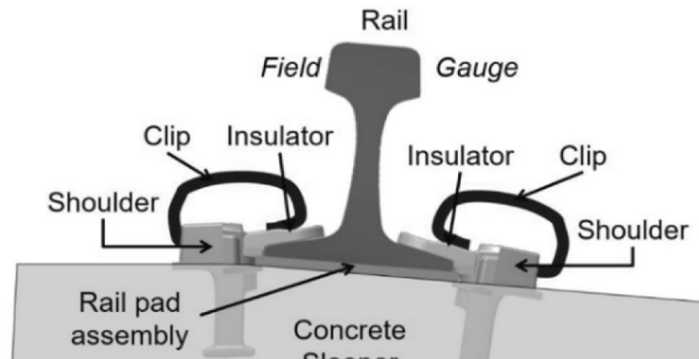
2e represents the track gauge= 1,432 – 1,470 (mm), $2e_a$ outer flange edge-to-edge distance (flange gauge) = 1,426(mm) – 16 + 3, $2d_a$ is the back to back wheel distance (inside gauge)= 1,360 (mm) – 3, $2e_0$ is the theoretical distance between the running surface of the right and the left wheel between centred \approx 1,500 (mm), f_d is the flange thickness = 33 – 25 (mm) (wear limit = 25 mm, σ is the flange ay clearance = $(2e - 2e_a)/2$ (mm). 2σ is the total flange way clearance= $2e - 2e_a$ (mm).

The rail fastener system (Figure 183) serves to anchor the rail to the sleepers, playing a crucial role in maintaining gauge and

limiting rail movement. The complexities of this system were reduced to its essential translational restraining function. To avoid geometric bias in thermal expansion, a straight track was chosen for the study, as curved track introduces additional effects on Rail Neutral Temperature (RNT). The investigation utilised the standard 132 RE rail section, assuming no manufacturing or welding defects. Whilst concrete sleepers and the e-clip rail fastening system were selected, their properties had minimal impact on the analysis presented. An RNT of 17 °C (0 °F) was chosen to align with previous literature (Knopf et al. 2021). Although this RNT is not realistic, it does not affect the study's outcomes, as thermal stress develops due to temperature changes post-installation rather than the initial temperature. The maximum deviation from the RNT was set at 60 °C (140 °F), which exceeds typical field conditions but allows for investigation of extreme scenarios in simulations..



(a)



(b)

Figure 183: Cross section illustration demonstrating the rail angle

3.17. Railway Automation

As the primary executive component of the railway automation system, the work aims to establish a mathematical and simulation model of a switch's electric drive in the form of a two- and three-mass electromechanical system based on DC

and AC motors. Research material. A significant issue in the mathematical modelling of switches' electric actuators was that the load was not considered in the existing models, which were regarded as single-mass electromechanical systems. The most prevalent switches in Ukraine's railway transport system are SP-6 switches and variations based on them. The main structural components of the switch are illustrated in Figure below: the frictional connection 4 is constructed within the same block, the main shaft with gate gear is 5 and the autoswitch block is 6, and the gate with cam locking mechanism is 7. Increased switching time and accelerated wear of the kinematic system's links are caused by the SP-6 switch's design features and associated drawbacks (the need for frequent friction protective device adjustments, the intricacy of the autoswitch design, and the existence of a technological clearance in the gearbox's gear gear transmission), which generally compromise railway traffic safety.

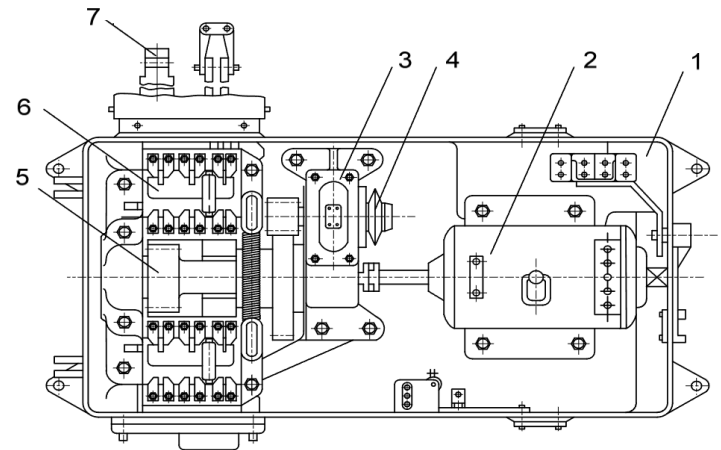


Figure 184: A SP-6m form of design (Buriakovskiy et al. 2020).

1. The body; 2. The electric motor; 3. The reducer with frictional connection, which is integrated into the same block; 4. The main shaft with gate gear; 5. The autoswitch block; 6. The gate with cam locking mechanism; and 7. The gate.

The SP-6 switch's design features and the associated disadvantages (such as the necessity for periodic adjustment of the friction protective device, the complexity of the autoswitch design, and the presence of a technological clearance in the gear gearbox of the gearbox) result in an increase in the switching time and accelerated wear of the links of the kinematic system, which generally impacts railway traffic safety.

The mechanical (friction clutch, technological clearance) and electrical (position sensor, uncontrolled switching) disadvantages that have been identified can be conditionally divided (Kuznetsov et al. 2018). In order to investigate the processes that transpire within the switch's electric motor, it is suggested that the system be regarded as an interconnected electromechanical system. Furthermore, in order to investigate the impact of clearances and control methods on the reliability of the switching process (Buriakovskiy et al. 2019), it is

advisable to view a switch as a multimass electromechanical system that accounts for the masses of an electric motor, wings, and elastic connections, as a result of its design features. The mechanical (friction clutch, technological clearance) and electrical (position sensor, uncontrolled switching) disadvantages that have been identified can be conditionally divided. The electric drive of the switch is suggested to be studied as an integrated electromechanical system. Furthermore, in order to investigate the impact of clearances and control methods on the reliability of the switching process, it is advisable to view a switch as a multimass electromechanical system that accounts for the masses of an electric motor, wings, and elastic connections, as a result of its design features.

The first mass J_1 is the entire moment of inertia of the motor, gearbox, and gate in a two-mass electromechanical system (Figure 185 a). The total mass of intelligence and inter-edge thrust is represented by the second mass, m_2 . c_{12} is an elastic connection that is formed by the working thrust from the gate to the first blade. The gearbox is responsible for converting the rotary motion of the motor shaft into the translational movement of the gate. The model considers the clearances in the kinematic transmission, including the technological clearance φ_{tz} and the clearances l_z in the cotter-pin connections of the thrust attachment with the gate and the blade. In a two-mass system, the existence of an interstellar thrust indicates the presence of elastic connections between the first and second wits.

Consequently, the authors further examine the switch as a three-mass system (Figure 185 b, c). The primary rationale for this method is that the dynamic processes in the mechanism are significantly affected by the presence of elastic coupling elements (Lagos et al. 2014; Papacek 2000; Krishnan 2001). Therefore, it is recommended to employ the two-mass model for engineering calculations.

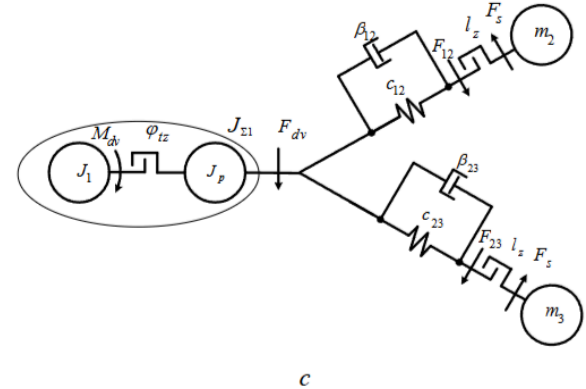
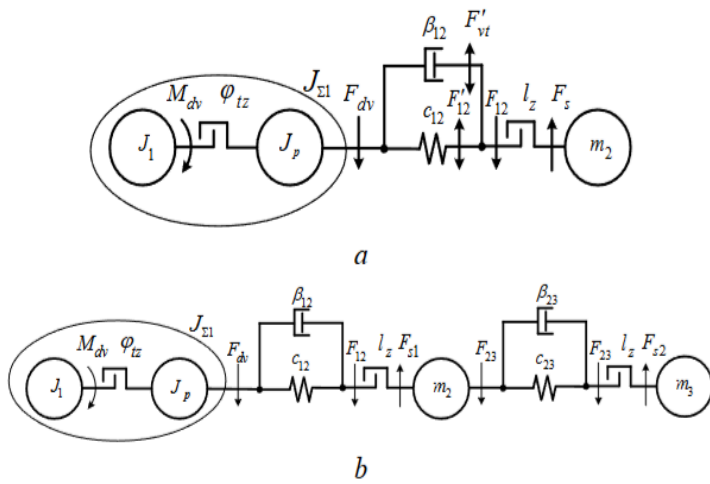


Figure 185: The switch's two-mass calculation scheme (a); three-mass calculation scheme with an elastic mass connection in series (b); and three-mass calculation strategy with an elastic mass connection in parallel.

As previously mentioned, the first mass in the calculation scheme with series connection of elastic masses (Figure 184,b) of such a system is composed of the motor shaft's moment of inertia and the gearbox's moment of inertia decreased to the motor shaft. The interstitial thrust serves as an extra elastic link, while the second and third masses are the first and second wits, respectively c_{23} . As can be seen from the switch's kinematic diagram (Figure 186), the working rod is attached to the first wit via the inter-turn rod rather than resting directly on it. According to the authors, it is most practical to think of the switch's mechanical component as a three-mass design scheme with a series connection of elastic masses, where J_1 is the motor rotor's moment of inertia, J_p is the gearbox's moment of inertia reduced to the motor shaft, and $J_{\Sigma 1}$ is the first mass's total moment of inertia; The motor's electromagnetic torque and thrust force are denoted by M_{dv} and F_{dv} , respectively; the technological clearance and inter-shaft rods by φ_{tz} and l_z ; the elasticity of the working and inter-shaft rods by F_{12} and F_{23} ; the resistance forces of the first and second wits by F_{s1} and F_{s2} ; the elasticity of the working and interstellar rods by c_{12} and c_{23} ; the coefficients of internal viscous friction of the working and intershaft rods by β_{12} and β_{23} ; and the second and third masses, respectively, are represented by m_2 and m_3 (Figure 185,b). It is not feasible to depict the switch as a four-mass system.

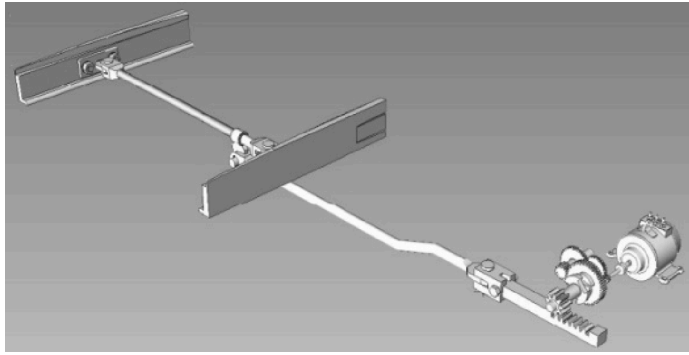


Figure 186: Diagram illustrating the SP-6m switch's kinetics

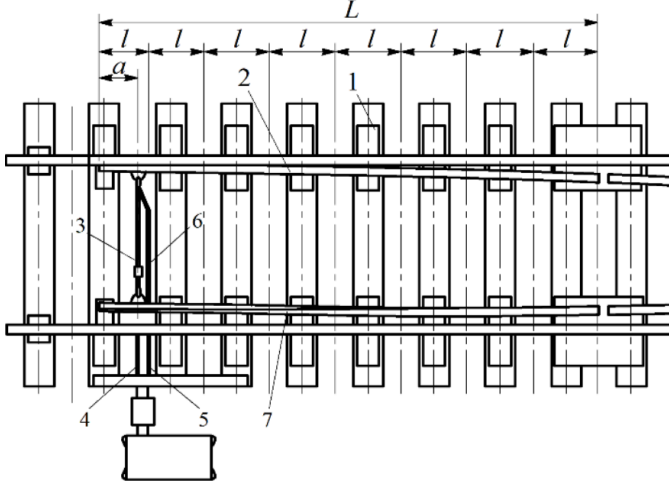


Figure 187: The general mechanism for determining switching effort is as follows: 2 wits; 3 connecting thrust; 4 working thrust; 1 switching surface; The first control rod is number five; the second is number six.

length of the wit and is equal to ψ , we find the elementary friction forces: (259) $F_1 = \psi q_1$, $F_2 = \psi q_2$, ..., $F_k = \psi q_k$ moment of element forces relative to the root of wits: (260) $M_1 = \psi q_1 \frac{1}{2} l$,

$$M_2 = \psi q_2 \frac{3}{2} l, \dots, M_k = \psi q_k \frac{2k-1}{2} l,$$

$$(261) M_1 = \sum_{k=1}^n M_k = \frac{1}{2} \psi l \sum_{k=1}^n q_1 + 3q_2 + \dots + (2k-1)q_k, \quad \text{Thus,}$$

when applied at a distance $L-a$ from the root (beginning) of the wit, the force necessary to overcome the frictional forces of the moving components is

$$(262) F = \frac{M_r}{L-a} = \frac{1}{2} \psi \frac{l}{L-a} \sum_{k=1}^n q_1 + 3q_2 + \dots + (2k-1)q_k, \quad \text{Assuming that } q_1 = q_2 = \dots = q_k = q \text{ and doing approximations of the force } F,$$

$$\text{we get: (263) } F = \frac{1}{2} \psi q \frac{l}{L-a} \sum_{k=1}^n 2 + 3 + \dots + (2k-1) = \frac{1}{2} \psi q n^2 \frac{1}{L-a}$$

as $L = l \cdot n$ and $Q = q \cdot n$ then (264) $F = \frac{1}{2} \psi \cdot Q \frac{L}{L-a}$ since L is the wit length and Q . Typically, 1.1 is used as the coefficient that accounts for the impact of friction forces in the joints. Using the following formula, we compute the estimated effort required to switch between a pivot and an inlay-onlay mount:

(265) $F = 1, 1 \frac{1}{2} \psi \cdot Q \frac{L}{L-a} = 0, 55 \psi \cdot Q \frac{L}{L-a}$, According to the preceding calculation, the switching force is dependent on the weight of the switch's moving parts, the kind of rails, where the switching rods are fixed, and the coefficient of friction of the cushions' wits. All given quantities, with the exception of the final one, are ascertainable. The value of the coefficient of friction is contingent upon the condition of the switch, the quality of lubrication of the switch pads, the purity of the treatment of their surfaces, the soles of the feet, and other factors, and can range from 0.05 to 0.3.

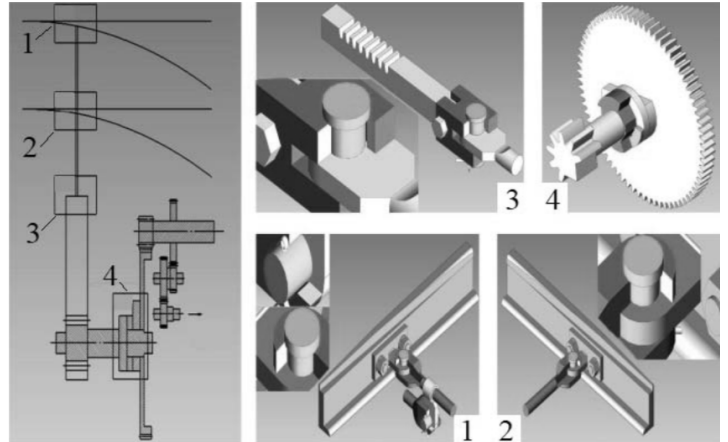


Figure 188: Kinematic line clearances of the switch: 1, 2, 3 - at the rods' attachment locations, 4 - technological authority

The permissible distance for the safe movement of the wheels of the rolling stock must not exceed 4 mm (Rubanenko, Labzun, and Hryshchuk 2017); otherwise, emergency situations may occur, such as "cutting the switch," resulting in derailment and damage to both the roadbed and the associated infrastructure. Because of the effects of friction, uncontrolled switching speed, and the influence during technical clearance development, the rod links gradually break and clearances rise. The average rate of increase in the size of the clearance is 0.05 mm per month.

The SP-6m switches are distinguished by the 46 technological clearance between the third and fourth stages of the gearbox (Figure 187, 188). This clearance is essential for the motor's acceleration and the accumulation of kinetic energy, which is needed to disrupt the switching process at the outset (Resnikov 1975). The modelling of the mechanical component of the electric drive is conducted using the actual values of clearances and the influence of internal viscous friction forces. The total elastic viscous force is determined as:

$$F_{12} = \begin{cases} 0, & \text{if } \text{sign} \Delta l \neq \text{sign} \Delta v \text{ and } |F_{vt}| > |F_{12}| \\ F_{vt} + F_{12}, & \text{if } \text{sign} \Delta l = \text{sign} \Delta v \text{ and } |F_{vt}| > |F_{12}| \end{cases}$$

$F_{12} = c_{12} \cdot F_1(l)$ is the elastic force; $F_{vt} = \beta_{12} \cdot \Delta v \cdot F_2(l)$ is the viscous friction force, $F_1(l)$ and $F_2(l)$ are the non-linear functions:

$$(266) F_1(l) = \begin{cases} 0 \text{ at } |\Delta l| \leq \frac{\Delta l_3}{2} \\ \Delta l - \frac{\Delta l_3}{2} \text{ at } \Delta l > \frac{\Delta l_3}{2} \\ \Delta l + \frac{\Delta l_3}{2} \text{ at } \Delta l < -\frac{\Delta l_3}{2} \end{cases}$$

$$(267) F_2(l) = \begin{cases} 0 \text{ at } |\Delta l| \leq \frac{\Delta l_3}{2} \\ 1 \text{ at } |\Delta l| > \frac{\Delta l_3}{2} \end{cases}$$

A similar method is used to compute the elastic viscous force F_{23} in the three-mass model (Figure 190). The mathematical model was implemented in the Simulink environment of MATLAB for engineering purposes. The model was constructed incrementally, adhering strictly to the calculation methods: motor block, reducer block, first wit block, second wit block. Clearances – technological clearances one and two at the joints, reduced to the fastening of the first and second rail, are indicated with separate blocks. The weight and dimensions of the gear stages are used to compute the numerical values of their moments of inertia. The viscous friction coefficients c_{12} , β_{12} , c_{23} , and β_{23} , as well as the stiffness of the working and connecting thrusts, are also necessary for modelling. Along the longitudinal axis, the deformation of a metal rod is the thrust:

(268) $c_{12} = c_{23} = E \frac{\pi \left(\frac{d}{2}\right)^2}{l}$. where d is the thrust diameter, l is the thrust length, and E is the steel modulus of elasticity. Because the direct connecting thrust and the working thrust in the model have the same length and diameter, it is assumed that their rigidities are equivalent. The internal viscous friction coefficient is calculated to be between 1×10^3 and 1×10^4 based on the research findings (Akimov, Kolotilo, and Markov 2000). Currently, a lot of systems use both an induction motor (IM) and a DC motor (DCM). The frequency converter (FC) can be powered by direct current (DC) from an autonomous voltage inverter or alternating current (AC) from a rectifier. Consequently, the system under development can be integrated into a switch control circuit utilising both direct current motors (DCM), such as the sequential excitation motors MSP-0.1, MSP-0.15, and MSP-0.25, commonly employed in Ukraine, as well as induction motors (IM). In the DCM of sequential excitation, the electromagnetic and electromechanical processes are described by the following equations:

$$u = (L_a + L_v) \frac{di}{dt} + (r_a + r_v)i + e_a$$

$$(268) \quad J \frac{d\omega}{dt} = M_d - M_s$$

$$e_a = k\omega\Phi_v$$

$$M_d = ki\Phi_v$$

$$\text{As } k = \frac{pN}{2\pi a}$$

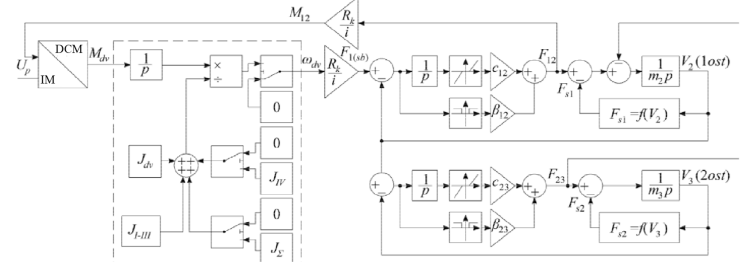


Figure 189: Block diagram of a switch with a three-mass model and serial mass connection

The electric drive of a switch can be replaced from a DCM to an IM with frequency control using the model presented in this paper. A mathematical model of a switch is proposed as a solution, which is based on a structural diagram figure above. Rather than a DCM/IM block, an FC-IM block is employed. Because an induction motor is a nonlinear, three-dimensional object with a pretty complicated structure, the given set of equations (268) for DCM does not accurately describe or model an electric drive with an IM in the (Figure 190) bellow illustrates the equivalent circuit of the IM in the electric drive.

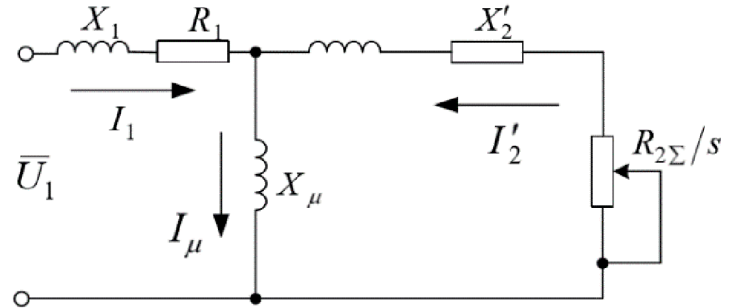


Figure 190: Phase-equivalent induction motor circuit

To accurately describe the IM mathematically, the coordinate system and model configuration are crucial, as they depend on the input and output signals, control system structure, and motor power source characteristics.

This study modelled an electric drive setup using a coordinate system orientated along the rotor flux linkage. For the simulation, the following assumptions were made: In a three-phase induction motor, the stator and rotor have symmetrical windings, air gap is uniform, magnetic field is sinusoidal, and rotor and stator axes do not align, resulting in an arbitrary angle. To transition from multiphase harmonic signal mathematical description to orthogonal two-phase coordinates, a generalised vector notion is utilised.

(269) $i = \frac{2}{3}(i_A + a \cdot i_B + a^2 \cdot i_C)$, $a = e^{j\frac{2\pi}{3}}$, $a^2 = e^{j\frac{4\pi}{3}}$ are the vectors taken into the account of spacial displacement of the windings; $i_A = I_m \cos \omega t$, $i_B = I_m \cos(\omega t - \frac{2\pi}{3})$, $i_C = I_m \cos(\omega t + \frac{2\pi}{3})$, the following equation is obtain by substituting the values of the instantaneous current into the equation above to obtain:

$$(270) i_S = \frac{2}{3}I_m(\cos \omega t + e^{j\frac{2\pi}{3}} \cdot \cos(\omega t - \frac{2\pi}{3}) + e^{j\frac{2\pi}{3}} \times \cos(\omega t + \frac{2\pi}{3})) =$$

, For an arbitrary-speed rotating coordinate system, the equations can be stated as:

$$(271) \begin{cases} u_S = R_S i_S + \frac{d\psi_S}{dt} + j\omega_k \psi_S \\ u_R = R_R i_R + \frac{d\psi_R}{dt} + j(\omega_k - \omega_R) \psi_R \\ \psi_S = L_S i_S + L_m i_R \\ \psi_R = L_m i_S + L_R i_R \\ M = \frac{3}{2} p k_R \cdot \text{Mod}(\psi_R \times i_S) \\ \int \frac{d\omega_m}{dt} = M - M_n \end{cases}$$

Where $\omega = p\omega_n$; as p is the number of pole in the machine; J is the moment of inertia of the rotor. In a squirrel-cage motor, the vectors ψ_S and ψ_R diverge due to scattering of the stator and rotor windings. The following applies to them: (272) $\psi_S = (L_m + L_{sl})i_S + L_m i_R$; $\psi_R = (L_m + L_{rl})i_S + L_m i_R$, where the leakage inductance of windings is L_{sl} , and the leakage inductance of the main leak is L_m . In this context, it is considered the inductances associated with the stator and rotor windings. (273) $L_S = (L_m + L_{sl})$, $L_R = (L_m + L_{rl})$. Control systems for AC electric drives typically contain coordinate converters to convert three-phase variables to two-phase model variables and vice versa. The direct transformation for the coordinate system α, β as: (274) $i_A = i_\alpha i_\beta = -\frac{1}{2}i_\alpha + \frac{\sqrt{3}}{2}i_\beta$, $i_C = -\frac{1}{2}i_\alpha - \frac{\sqrt{3}}{2}i_\beta$ and the opposite one is: $i_\alpha = i_A i_\beta = \frac{i_B - i_C}{\sqrt{3}}$ (19) $i_\alpha = i_A i_\beta = \frac{i_B - i_C}{\sqrt{3}}$

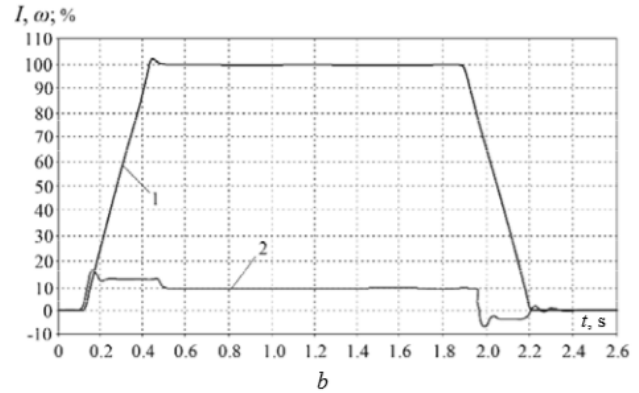
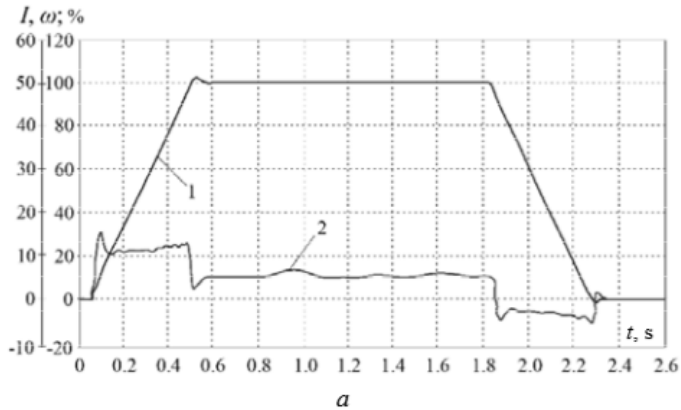


Figure 191: Movement oscillogram of switching drive: A Siemens equipment; B mathematical model

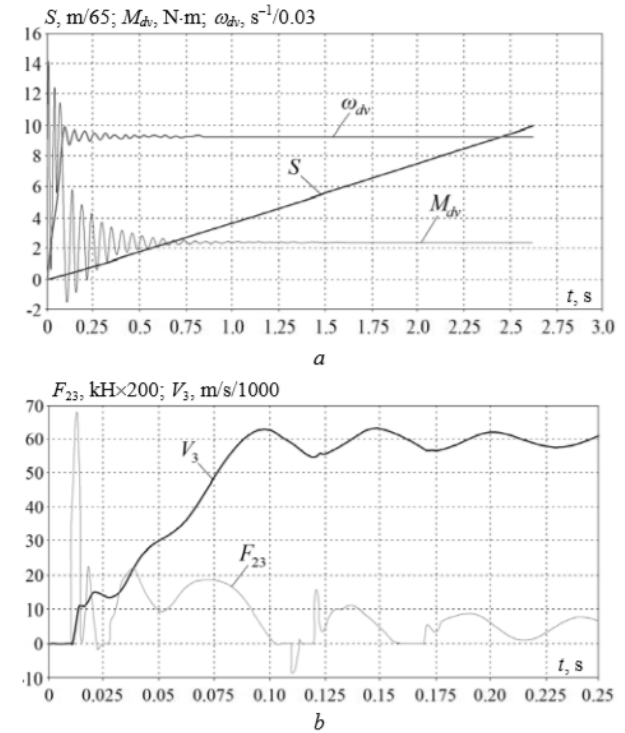


Figure 192: A three-mass structure with a series connection of masses is represented by oscillograms of transients as follows: The angular speed, displacement, and torque of the IM are denoted by the letters a and b, respectively.

Studies of the condition of the switching surfaces, where wave-like traces are visible, corroborate the existence of oscillations in the switch's kinematic line. The presence of characteristic mats on both pillows is indicative of the emergence of elastic vibrations in both thrusts. These vibrations, in turn, lead to vibrations of both wits, which substantiates the necessity of considering the electric drive of the switch as a three-mass electromagnetic switch (EMS). Based on the observations made by the service workers, the depth and width of undulating formations are determined by

the existence of "backlashes" in the kinematic line of the switch as well as the magnitude of those backlashes.

Conclusion

The study evaluated thrust and torque prediction models for TBM cutterhead design. The Japanese method derives equations incorporating vertical stress relaxation from tunnel crown to ground surface, showing that effective vertical stress decreases with increasing active earth pressure coefficient. The Modified Japanese method employs a polar coordinate framework to explicitly calculate water and earth pressures relative to TBM diameter, producing higher thrust and torque estimates than the Japanese method, with ~2 MN difference in shield-soil frictional resistance (F_2) and ~0.2 MN·m difference in frontal and cutter edge resistance torques (T_2, T_3). The CSM model, applicable to rock TBMs, formulates thrust and torque from cutter penetration mechanics, where penetration depth directly increases the cutting coefficient; under identical penetration depth, uniform pressure distribution (shape coefficient = 0) yields relatively higher values.

TBMs are marvels of modern engineering, capable of excavating tunnels through diverse geological environments with precision and efficiency. The cutting-edge technology employed in their design—from the cutting head to the spoil removal system and advanced control mechanisms—ensures safe and efficient tunnelling. As tunnel projects continue to increase in complexity, TBMs will remain essential for overcoming the challenges of underground construction.

the surface and extends to the surface along a horizontal angle of 45°, gradually forming fatigue spalling. Damage to the main bearing will not only lead to the increase in the peak vibration response of the TBM, but also cause the response of more frequency components. The kurtosis, impulse factor and margin factor of vibration signal can characterise the damage degree of bearing. By monitoring the time-domain indexes of vibration signals, the damage degree of the main bearing can be mastered in real time, providing a reference for the maintenance of the main bearing.

It is clear that the likelihood of the soil collapsing decreases with the depth of the tunnel boring machine since it will be farther below the water table and avoid the relaxation mode. To prevent water table intrusion when navigating the TBM to the upper surface, an injectable boring machine with bentonite must be used. However, this will significantly increase the cost of building the TBM because the bentonite-mixed soil requires a separate factory to separate it from the soil and enable safe disposal.

A theoretical examination of prestressing anchor lengths, both anchorage and free, is conducted to establish design parameters. The mechanical model of the bearing arch is utilised to derive formulae for calculating axial force in tunnel vaults and side walls, as well as bearing arch thickness. This design approach may serve as a reference for similar support projects.

The prestress time-change curve can be broadly categorised into two phases: a rapid decline phase followed by a stable

phase. Higher design prestress values correlate with more pronounced axial force decay. Increasing prestress effectively enhances the proportion of active support force relative to total support force, thereby diminishing passive support effects and achieving the desired support outcome.

Utilising field engineering case studies, calculations are performed for the thickness and axial force of surrounding rock vaults and sidewalls under five distinct surrounding rock conditions. The bearing arch thickness diminishes as surrounding rock strength increases. For lower-grade surrounding rock and soil, when the bearing arch thickness surpasses 16 m, additional robust support measures become necessary to maintain surrounding rock stability.

The current research examined the rockbreaking process of TBM disc cutters using the ABAQUS-based VUMAT subroutine in conjunction with the Lemaitre damage model and the D-P yield criteria. Twenty-five sets of orthogonal numerical simulations were run, together with a full-scale rockbreaking test on the RCM. The ideal values of the specified parameters D_{c1} , k , and B were found to be 9×10^{-4} , 0.1, and 0.8, respectively, after comparing the errors of the normal force, rolling force, and specific energy between the experimental and numerical findings.

The normal force, rolling force, and specific energy were investigated in relation to the cutter spacing, as determined by the parameters and the numerical method presented. While the forces of the second cut grew linearly with the cutter spacing, the normal and rolling forces of the first cut tended to stay constant. In line with the cutter spacing of the TBM used in this tunnel project, the ideal cutter spacing for the kind of rock under study (hard sand rock taken from the West Qinling tunnel) was around 72 mm.

Whenever there is a change in load torque or electromagnetic torque, the DTC drive system reacts rapidly. A torque ripple of approximately 120 N·m is present in T_e . Factors such as sample duration, motor velocity, flux, and voltage vector—all of which are correlated with the digital controller's processing capacity and switching frequency—fluence torque ripple.

There are three distinct vibration modes that can occur in a gear gearbox system, as determined by dynamic analysis: rigid motion, rotational, and planet. The vibration amplitude of the second stage component is the smallest of the three stages when comparing vibration displacements.

The low frequency domain, which is close to the mesh frequency and the low-order natural frequency ($Z2 = 308$ Hz, $Z3 = 529$ Hz), is where meshing forces mostly vibrate. At the changing point of load torque, the meshing forces of the first stage of planet gears change more visibly than those of the other two stages, and they rise with each stage according to the gear ratio.

The torque ripple worsens the vibration displacements of the gear transmission system under electromagnetic torque T_e , in comparison to the dynamic responses under idealised piecewise torque (3). To demonstrate the effect of electromagnetic torque T_e , the dynamic index δ is suggested and examined. At the same point, the sun gear δ is at its

biggest. The effects on components in the second stage are minimal compared to those in earlier stages. Also, when torque increases, the vibration levels of all the parts get much worse. The 2-DOF dynamics of the hoisting gantry are meticulously modelled in this study. The connections between the crossbeam and guide lines are modelled as high-stiffness rotational springs to introduce the supplementary rotational motion. Subsequently, a synchronisation control scheme that is model-based is devised. Within it, the propulsion allocation is intended to regulate the rotational angle within a very narrow range, and the motion tracking controller is synthesised using the ARC theory to ensure the desired motion tracking precision. Extensive analysis and demonstration of theoretical performance. In conclusion, the proposed scheme's efficacy in managing dual-cylinder synchronisation and linear motion tracking is confirmed by comparative simulations. From comprehensive modelling to control design and validation, the work provides a viable control solution for the dual-cylinder mechanisms under unbalanced loads. Thrust allocation is simple to understand and independent of exact measurement signals, making it easy to implement and achieve high-level synchronisation. Experiments will be conducted in the future to further validate the performance in an actual lifting gantry. The CAM4 ring tail seal passage in the first two TBM cycles caused high vertical pressures (~300 kPa) from eccentric shield alignment during curve steering. Jack forces shifted orientation, concentrating loads on the outer curve side. Grout effects were minor initially but later altered gradients. Eccentric loading produced small but permanent ring distortions (<0.03%D) and minor skew, with behaviour matching FE models. The unbedded ring acted arch-like, with ovalisation under modest pressure gradients dominating curvature. DFOS mapping detected a longitudinal crack at the outer springline from combined ram shoe spalling stresses and hoop tension, plus near-opening of left-side joints. Deformation patterns stabilised by the end of cycle two.

A smooth, clog-free rock flow was observed in the short screw conveyor, with efficiency stabilising over time; durability should be reinforced at high-wear zones, optimal performance achieved at 10–13 rpm rotational speed and 0.6–0.9 pitch-to-diameter ratio, while larger particle size, higher installation angles, and extreme speeds reduce efficiency.

Typically, there are four categories for the selection of shield jacks. The velocity of each shield jack group can regulate the duration of each shield jack group. The segment plane remains perpendicular to the back shield axis throughout the curved excavation process. Consequently, each shield jack group should be augmented with varying jack speeds based on the curvature direction. However, the assumption made in this study was that the extension speed of a group of shield jacks was the same. Consequently, it is challenging to evaluate the unilateral extension of the shield jack concurrently with articulation jack operations during excavation.

The paper offers an electro-hydraulic thrust system to control shield driving speed, thrust pressure, and cylinder motion synchronously. A closed-loop control approach with a proportional pressure relief valve and flow control valve is

effective for achieving target thrust performance. The technology further reduces synchronous error by adjusting for displacement errors between the reference and following cylinders using a controller. The test findings indicate a ± 3 mm synchronous error under high pressure differences. Overall, the study shows that the proposed tunnel drive shield advance control methods are effective in theory and practice. Research on this project is ongoing, considering unknown geological conditions, nonlinear soil dynamics, and the electro-hydraulic system in situ tunnelling.

A mathematical and simulation model of an electric switching drive has been constructed in the form of a two- and three-mass electromechanical system based on DC and AC motors. This system serves as the primary executive component of the automation system that is utilised by Ukrainian railways. As the goal of modelling, the starting data came from the SP-6m turnout switch, which is the most prevalent type of turnout switch. In order to take into consideration the activities that are taking place in the mechanical subsystem, it is demonstrated that while designing an electromechanical system of a switch, it is necessary to take into account the size of the clearances as well as the dynamics of their change. It has been determined through both simulation and experimentation that the spread of the deviation values of the main coordinates of the electric switching drive during transients does not exceed 5%. This was calculated using the approach of simulation.

References

Abdollahi, M. S., M. Najafi, A. Y. Bafghi, and M. F. Marji. 2019. "A 3D Numerical Model to Determine Suitable Reinforcement Strategies for Passing TBM through a Fault Zone, a Case Study: Safaroud Water Transmission Tunnel, Iran." *Tunnelling and Underground Space Technology* 88:186–99. <https://www.sciencedirect.com/science/article/pii/S0886779818305078>.

Abdullah, Muhammad U., and Zulfiqar A. Khan. 2022. "A Multiscale Overview of Modelling Rolling Cyclic Fatigue in Bearing Elements." *Materials* 15 (17): 5885. <https://doi.org/10.3390/ma15175885>.

Acaroglu, O., L. Ozdemir, and B. Asbury. 2008. "A Fuzzy Logic Model to Predict Specific Energy Requirement for TBM Performance Prediction." *Tunnelling and Underground Space Technology* 23 (5): 600–608. <https://www.sciencedirect.com/science/article/pii/S0886779807001137>.

Afshani, A., H. Dobashi, K. Komiya, and H. Akagi. 2014. "Numerical Analysis of the Effect of Earth Pressure Balanced Shield Tunneling on Soil Stress-Deformation Behavior." *Journal of JSCE* 2:224–38. https://doi.org/10.2208/JOURNALOFJSCE.2.1_224.

Akimov, L. V., V. I. Kolotilo, and V. S. Markov. 2000. *Dinamika Dvuhmassovyh Sistem S Netradicionnymi Reguljatorami Skorosti I Nabljudateljami Sostojanija* [Dynamics of Two-Mass Systems with Nontraditional Regulators of Speed and Observers of State].

Systems with Non-Traditional Speed Controllers and State Observers. Vol. 93. Kharkiv: KhSPU Publ.

Alsahly, A., A. Marwan, and G. Meschke. 2019. "TBM Drive along Curved Alignments: Model Based Prognosis of Shield Movement." *Tunnels and Underground Cities: Engineering and Innovation Meet Archaeology, Architecture and Art*, April. <https://doi.org/10.1201/9780429424441-173>.

Anagnostou, G. 2007. "Continuous Tunnel Excavation in a Poro-Elastoplastic Medium." In *Numerical Models in Geomechanics*. Taylor & Francis. <https://doi.org/10.1201/noe0415440271.ch27>.

Anastasopoulos, I., N. Gerolymos, and V. Drosos. n.d. "Nonlinear Response of Deep Immersed Tunnel to Strong Seismic Shaking." [https://doi.org/10.1061/\(ASCE\)1090-0241\(2007\)133:9\(1067\)](https://doi.org/10.1061/(ASCE)1090-0241(2007)133:9(1067)).

Ates, Ugur, Nuh Bilgin, and Hanifi Copur. 2014. "Estimating Torque, Thrust and Other Design Parameters of Different Type TBMs with Some Criticism to TBMs Used in Turkish Tunneling Projects." *Tunnelling and Underground Space Technology* 40 (February):46–63. <https://doi.org/10.1016/j.tust.2013.09.004>.

Baek, S. H., and H. K. Moon. 2003. "A Numerical Study on the Rock Fragmentation by TBM Cutter Penetration." *Tunn Undergr Space (J Korean Soc Rock Mech)*. <https://scholar.google.com.au/citations?user=tFbR4T4AAA AJ&hl=en&oi=sra>.

Balci, C. 2009. "Correlation of Rock Cutting Tests with Field Performance of a TBM in a Highly Fractured Rock Formation: A Case Study in Kozyatagi-Kadikoy Metro Tunnel, Turkey." *Tunnelling and Underground Space Technology* 24 (4): 423–35. <https://doi.org/10.1016/j.tust.2008.12.001>.

Bezuijen, A., A. M. Talmon, F. J. Kaalberg, and R. Plugge. 2004. "Field Measurements of Grout Pressures during Tunnelling of the Sophia Rail Tunnel." *SOILS AND FOUNDATIONS* 44 (1): 39–48. <https://doi.org/10.3208/sandf.44.39>.

Biggart, A. 2010. "The 2010 British Tunnelling Society (BTS) Harding Lecture." *Tunnels & Tunnelling International*.

Bilgin, N., M. A. Demircin, H. Copur, C. Balci, H. Tuncdemir, and N. Akcin. 2006. "Dominant Rock Properties Affecting the Performance of Conical Picks and the Comparison of Some Experimental and Theoretical Results." *International Journal of Rock Mechanics and Mining Sciences (Oxford, England: 1997)* 43 (1): 139–56. <https://doi.org/10.1016/j.ijrmms.2005.04.009>.

Bilgin, N., H. Tuncdemir, C. Balci, H. Copur, and S. Eskikaya. 2000. "A Model to Predict the Performance of Tunneling Machines under Stressed Conditions." In *Proceedings, AITES-ITA 2000 World Tunnel Congress*, 47–53.

Bilgin, Nuh, and Melih Algan. 2012. "The Performance of a TBM in a Squeezing Ground at Ulubat, Turkey." *Tunnelling and Underground Space Technology* 32 (November):58–65. <https://doi.org/10.1016/j.tust.2012.05.004>.

Billig, B., C. Gipperich, M. Wulff, and A. Schaab. 2008. "Ausbauysteme Für Den Maschinellen Tunnelbau in Druckhaftem Gebirge." *Taschenbuch Für Den Tunnelbau* 32:223–62.

Bosserman, Bayard E., II, William A. Hunt, Robert C. Glover, Joseph R. Kroon, M. Steve Merrill, and Gary Z. Watters. 2008. "Fundamentals of Hydraulic Transients." In *Pumping Station Design*, edited by Garr M. Jones, Robert L. Sanks, George Tchobanoglous, and Bayard E. Bosserman, 6.1–6.13. Elsevier. <https://doi.org/10.1016/b978-185617513-5.50013-5>.

Broms, Bengt B., and Hans Bennermark. 1967. "Stability of Clay at Vertical Opening." *Journal of the Soil Mechanics and Foundations Division* 93 (1): 71–94. <https://doi.org/10.1061/jsfea.0000946>.

Bruland, A. 1998. "Hard Rock Tunnel Boring: Drillability Test Methods." *Project Report 13A-98, NTNU Trondheim*. https://www.researchgate.net/profile/Amund-Bruland/publication/275540702_Hard_Rock_Tunnel_Boring_Vol_8_-_Drillability_-Test_Methods/links/553f50130cf24c6a05d1fd9a/Hard-Rock-Tunnel-Boring-Vol-8-Drillability-Test-Methods.pdf.

———. 2000. "Hard Rock Tunnel Boring." <https://ntnuopen.ntnu.no/ntnu-xmlui/handle/11250/231256>.

Brundan, William, and Hitoshi Danno. 2020. "Tunnel Boring Machines for Extremely Tight Radius Curves." In *Lecture Notes in Civil Engineering*, 241–48. Singapore: Springer Singapore. https://doi.org/10.1007/978-981-15-2184-3_30.

Buriakovskiy, S., A. Maslii, O. Pasko, and V. Smirnov. 2020. "Mathematical Modelling of Transients in the Electric Drive of the Switch – the Main Executive Element of Railway Automation." *Electrical Engineering & Electromechanics*, no. 4 (eng) (August), 17–23. <https://doi.org/10.20998/2074-272x.2020.4.03>.

Buriakovskiy, S., V. Smirnov, L. Asmolova, I. Obruch, O. Rafalskyi, and A. Maslii. 2019. "Analysis of Optimization Criteria for the Process of Switch Displacement in a DC Railroad Turnout." *Eastern-European Journal of Enterprise Technologies* 6 (2): 58–69. <https://www.neliti.com/publications/308448/analysis-of-optimization-criteria-for-the-process-of-switch-displacement-in-a-dc>.

Cai, Yue, Yujing Jiang, Ibrahim Djamaruddin, Tomomi Iura, and Tetsuro Esaki. 2015. "An Analytical Model Considering Interaction Behavior of Grouted Rock Bolts for Convergence–confinement Method in Tunneling Design." *International Journal of Rock Mechanics and Mining Sciences (Oxford, England: 1997)* 76 (June):112–26. <https://doi.org/10.1016/j.ijrmms.2015.03.006>.

Cantieni, Linard, and Georgios Anagnostou. 2009. "The Effect of the Stress Path on Squeezing Behavior in Tunneling." *Rock Mechanics and Rock Engineering* 42 (2): 289–318. <https://doi.org/10.1007/s000603-008-0018-9>.

Chanchaya, C., and S. Suwansawat. 2014. "Directional Control of EPB Shield in Spiral Curve," August, 561–66. <https://doi.org/10.1201/b17240-105>.

Chang, S. H., S. W. Choi, G. P. Lee, and G. J. Bae. 2011. "Statistical Analysis of NTNU Test Results to Predict Rock TBM Performance." *Journal of Korean Tunnelling and Underground Space Association* 13 (3): 243–60. <https://www.jkta.or.kr/articles/xml/gnem/>.

Chang, S. H., Y. T. Park, G. P. Lee, and G. J. Bae. 2013.

“Experimental Evaluation of the Effects of Cutting Ring Shape on Cutter Acting Forces in a Hard Rock.” *Journal of Korean Tunnelling and Underground Space Association* 15 (3): 225–35. <https://www.jkta.or.kr/articles/xml/onRw/>.

Chao, Wang yu, He Yuan Xin, Weng Wei, and Liu Jia Rong. 2017. “Frictional Analysis of Deep-Groove Ball Bearings with Varying Circumference Radial Preloads.” *Advances in Mechanical Engineering* 9 (5): 168781401770389. <https://doi.org/10.1177/1687814017703895>.

Cheng, Yuping, and T. Lim. 2003. “Dynamics of Hypoid Gear Transmission with Nonlinear Time-Varying Mesh Characteristics.” *Journal of Mechanical Design* 125 (June):373–82. <https://doi.org/10.1115/1.1564064>.

Cheng, Yuping, and Teik C. Lim. 2000. “Dynamics of Hypoid Gear Transmission with Non-Linear Time-Varying Mesh.” In *Volume 6: 8th International Power Transmission and Gearing Conference*, 611–17. American Society of Mechanical Engineers. <https://doi.org/10.1115/detc2000/ptg-14432>.

Chen, J. S., and H. H. Mo. 2009. “Numerical Study on Crack Problems in Segments of Shield Tunnel Using Finite Element Method.” *Tunnelling and Underground Space Technology* 24 (1): 91–102. <https://doi.org/10.1016/j.tust.2008.05.007>.

Chen, Shan, Tenghui Han, Fangfang Dong, Lei Lu, Haijun Liu, Xiaoqing Tian, and Jiang Han. 2021. “Precision Interaction Force Control of an Underactuated Hydraulic Stance Leg Exoskeleton Considering the Constraint from the Wearer.” *Machines* 9 (5): 96. <https://doi.org/10.3390/machines9050096>.

Chen, Zheng, Fanghao Huang, Wenjie Chen, Junhui Zhang, Weichao Sun, Jiawang Chen, Jason Gu, and Shiqiang Zhu. 2020. “RBFNN-Based Adaptive Sliding Mode Control Design for Delayed Nonlinear Multilateral Telerobotic System with Cooperative Manipulation.” *IEEE Transactions on Industrial Informatics* 16 (2): 1236–47. <https://doi.org/10.1109/tnii.2019.2927806>.

Chen, Zheng, Chao Li, Bin Yao, Mingxing Yuan, and Can Yang. 2020. “Integrated Coordinated/synchronized Contouring Control of a Dual-Linear-Motor-Driven Gantry.” *IEEE Transactions on Industrial Electronics* (1982) 67 (5): 3944–54. <https://doi.org/10.1109/tie.2019.2921287>.

Choi, Jung-In, and Seok-Won Lee. 2010. “Influence of Existing Tunnel on Mechanical Behavior of New Tunnel.” *KSCE Journal of Civil Engineering* 14 (5): 773–83. <https://doi.org/10.1007/s12205-010-1013-8>.

Cho, Jung-Woo, Seokwon Jeon, Ho-Young Jeong, and Soo-Ho Chang. 2013. “Evaluation of Cutting Efficiency during TBM Disc Cutter Excavation within a Korean Granitic Rock Using Linear-Cutting-Machine Testing and Photogrammetric Measurement.” *Tunnelling and Underground Space Technology* 35 (April):37–54. <https://doi.org/10.1016/j.tust.2012.08.006>.

Cho, Jung-Woo, Seokwon Jeon, Sang-Hwa Yu, and Soo-Ho Chang. 2010. “Optimum Spacing of TBM Disc Cutters: A Numerical Simulation Using the Three-Dimensional Dynamic Fracturing Method.” *Tunnelling and Underground Space Technology* 25 (3): 230–44. <https://doi.org/10.1016/j.tust.2009.11.007>.

Chunyu, M., T. Zhengjun, and C. Mingxiang. 2019. “A Large Deformation Elastoplastic Model Based on the Intermediate Configuration.” *Chinese Journal of Theoretical and Applied Mechanics* 51 (1): 182–91. <https://doi.org/10.6052/0459-1879-18-138>.

Cigla, M., S. Yagiz, and L. Ozdemir. 2001. “Application of Tunnel Boring Machines in Underground Mine Development.” In *17th International Mining Congress and Exhibition of Turkey*, 155–64.

Clough, G. W., and B. Schmidt. 1981. <https://www.sciencedirect.com/science/article/pii/B97804417848500113/pdf?md5=f3a913c1ae81bbaa2bef95813ce1bd09&pid=1-s2.0-B9780444417848500113-main.pdf>.

Cobreros, J. A., Manuel Moreno Cervera, M. Herrera, Carlos Conde, and C. Oteo. 2005. “Tunnels de Guadarrama : Problèmes Géotechniques Rencontrés Dans Un Double Tunnel de 27 Km : Espagne.” *Tunnels et Ouvrages Souterrains*, no. 190, 5–12. <https://pascal-francis.inist.fr/vibad/index.php?action=getRecordDetail&idt=17183206>.

Cundall, P. A., and O. D. L. Strack. 1979. “A Discrete Numerical Model for Granular Assemblies.” *Géotechnique* 29 (1): 47–65. <https://doi.org/10.1680/geot.1979.29.1.47>.

Dajun, Y. 2008. “Research on Distribution Regularities of Grain Size of Rock Detritus from Discoid Cutters.” *Chinese Journal of Rock Mechanics and Engineering*.

Debrock, Shana, Maarten Van Acker, and Han Admiraal. 2023. “Design Recommendations for Sustainable Urban Underground Spaces.” *Tunnelling and Underground Space Technology* 140 (105332): 105332. <https://doi.org/10.1016/j.tust.2023.105332>.

Deng, Wenxiang, and Jianyong Yao. 2021. “Asymptotic Tracking Control of Mechanical Servosystems with Mismatched Uncertainties.” *IEEE/ASME Transactions on Mechatronics* 26 (4): 2204–14. <https://doi.org/10.1109/tmech.2020.3034923>.

Ding, Cheng, Hai-Dong Tu, and Hao Wang. 2010. “Hydraulic-Mechanical Coupling Model and Load Characteristic Analysis of Shield Thrust System with Redundant Drive.” *China Mechanical Engineering* 21 (03): 258. <https://www.cmemc.org.cn/EN/abstract/abstract1828.shtml>.

D Minh, Nguyen, and F. Corbetta. 1991. “Nouvelles Méthodes de Calcul Des Tunnels Revêtus Incluant L’effet Du Front de Taille.” In *International Conference on Rock Mechanics*, 1335–38. pascal-francis.inist.fr/vibad/index.php?action=getRecordDetail&idt=6524897.

Dunne, Fionn, and Nik Petrinic. 2005. *Introduction to Computational Plasticity*. London, England: Oxford University Press. [https://books.google.com.au/books?hl=en&lr=&id=GwVREAAAQBAJ&oi=fnd&pg=PR9&dq=F.+Dunne+and+N.+Petrinic,+Introduction+to+computational+plasticity,+Oxford+University+Press,+New+York+\(2005\).&ots=WBNetNdW6W&sig=X-B-x_sSksaqIYS_s-Esa78fW5t4](https://books.google.com.au/books?hl=en&lr=&id=GwVREAAAQBAJ&oi=fnd&pg=PR9&dq=F.+Dunne+and+N.+Petrinic,+Introduction+to+computational+plasticity,+Oxford+University+Press,+New+York+(2005).&ots=WBNetNdW6W&sig=X-B-x_sSksaqIYS_s-Esa78fW5t4).

Edelin, Denis, Pierre-Clement Czujko, Cathy Castelain, Christophe Josset, and Francine Fayolle. 2015. "Experimental Determination of the Energy Optimum for the Transport of Floating Particles in Pipes." *Experimental Thermal and Fluid Science* 68 (November):634–43. <https://doi.org/10.1016/j.expthermflusci.2015.06.018>.

Einstein, H. H. 2001. "The Decision Aids for Tunnelling (DAT)-a Brief Review." *Magazine of Korean Tunnelling and Underground Space Association* 3 (3): 37–49. <https://koreascience.kr/article/JAKO200108823587171.page>.

Einstein, H. H., and A. Bobet. 1997. "Mechanized Tunnelling in Squeezing rock—From Basic Thoughts to Continuous Tunnelling." *Tunnels for People, ITA World Tunnel Congress*. <https://scholar.google.com.au/citations?user=HevRHcIAAAAJ&hl=en&oi=sra>.

Elbaz, Khalid, Shui-Long Shen, Wen-Chieh Cheng, and Arul Arulrajah. 2018. "Cutter-Disc Consumption during Earth Pressure Balance Tunnelling in Mixed Strata." *Proceedings of the Institution of Civil Engineers - Geotechnical Engineering* 171 (4): 363–76. <https://doi.org/10.1680/jgeen.17.00117>.

Elbaz, Khalid, Shui-Long Shen, Wen-Juan Sun, Zhen-Yu Yin, and Annan Zhou. 2020. "Prediction Model of Shield Performance during Tunneling via Incorporating Improved Particle Swarm Optimization into ANFIS." *IEEE Access: Practical Innovations, Open Solutions* 8:39659–71. <https://doi.org/10.1109/access.2020.2974058>.

Elbaz, Khalid, Shui-Long Shen, Annan Zhou, Da-Jun Yuan, and Ye-Shuang Xu. 2019. "Optimization of EPB Shield Performance with Adaptive Neuro-Fuzzy Inference System and Genetic Algorithm." *Applied Sciences (Basel, Switzerland)* 9 (4): 780. <https://doi.org/10.3390/app9040780>.

Elbaz, K., S. L. Shen, A. Zhou, Z. Y. Yin, and H. M. Lyu. 2021. "Prediction of Disc Cutter Life during Shield Tunneling with AI via the Incorporation of a Genetic Algorithm into a GMDH-Type Neural Network." *Engineering* 7 (2): 238–51. <https://www.sciencedirect.com/science/article/pii/S2095809920302332>.

Engineering Committee, Tunnel. 2007. "Standard Specifications for Tunneling-2006: Shield Tunnels." *Jpn. Soc. Civ. Eng.*

Entacher, Martin, and Erik Schuller. 2018. "Angular Dependence of Rock Cutting Forces due to Foliation." *Tunnelling and Underground Space Technology* 71 (January):215–22. <https://doi.org/10.1016/j.tust.2017.08.009>.

Farrokh, E. 2012. *Study Utilization Factor Advance Rate Hard Rock TBMs*.

Farrokh, Ebrahim. 2020. "A Study of Various Models Used in the Estimation of Advance Rates for Hard Rock TBMs." *Tunnelling and Underground Space Technology* 97 (103219): 103219. <https://doi.org/10.1016/j.tust.2019.103219>.

Feng, H., Q. Du, Y. Huang, and Y. Chi. 2017. "Modelling Study on Stiffness Characteristics of Hydraulic Cylinder under Multi-Factors." *Journal of Mechanical Engineering*.

Festa, D. 2015. "On the Interaction between a Tunnel Boring Machine and the Surrounding Soil." <https://repository.tudelft.nl/record/uuid:f52c59d9-9aa0-4dc4-a44b-d953fa7f639f>.

Festa, Daniele, Wout Broere, and Johan W. Bosch. 2013. "On the Effects of the TBM-Shield Body Articulation on Tunnelling in Soft Soil." <https://repository.tudelft.nl/record/uuid:17bf3e8a-4637-47a6-84bc-59c1cd0eaf09>.

Festa, D., W. Broere, and J. W. Bosch. 2012. "An Investigation into the Forces Acting on a TBM during Driving-Mining the TBM Logged Data." *Tunnelling and Underground Space Technology* 32:143–57.

———. 2015. "Kinematic Behaviour of a Tunnel Boring Machine in Soft Soil: Theory and Observations." *Tunnelling and Underground Space Technology* 49 (June):208–17. <https://doi.org/10.1016/j.tust.2015.03.007>.

Fuhg, Jan N., and Amelie Fau. 2019. "Surrogate Model Approach for Investigating the Stability of a Friction-Induced Oscillator of Duffing's Type." *arXiv [eess.SY]*. arXiv. <https://doi.org/10.1007/s11071-019-05281-2>.

Funk, J. E., D. J. Wood, and S. P. Chao. 1972. "The Transient Response of Orifices and Very Short Lines." *Journal of Basic Engineering* 94 (2): 483–89. <https://doi.org/10.1115/1.3425456>.

Gao, Min-Yu, Ning Zhang, Shui-Long Shen, and Annan Zhou. 2020. "Real-Time Dynamic Earth-Pressure Regulation Model for Shield Tunneling by Integrating GRU Deep Learning Method with GA Optimization." *IEEE Access: Practical Innovations, Open Solutions* 8:64310–23. <https://doi.org/10.1109/access.2020.2984515>.

Gao, Xianjie, Maolin Shi, Xueguan Song, Chao Zhang, and Hongwei Zhang. 2019. "Recurrent Neural Networks for Real-Time Prediction of TBM Operating Parameters." *Automation in Construction* 98 (February):225–35. <https://doi.org/10.1016/j.autcon.2018.11.013>.

García-Herreros, Iván, Xavier Kestelyn, Julien Gomand, Ralph Coleman, and Pierre-Jean Barre. 2013. "Model-Based Decoupling Control Method for Dual-Drive Gantry Stages: A Case Study with Experimental Validations." *Control Engineering Practice* 21 (3): 298–307. <https://doi.org/10.1016/j.conengprac.2012.10.010>.

Gehring, K. H. 2020. "Design Criteria for TBM's with Respect to Real Rock Pressure." In *Tunnel Boring Machines*, 43–53. CRC Press. <https://doi.org/10.1201/9781003078081-6>.

Ge, Lei, Long Quan, Xiaogang Zhang, Bin Zhao, and Jing Yang. 2017. "Efficiency Improvement and Evaluation of Electric Hydraulic Excavator with Speed and Displacement Variable Pump." *Energy Conversion and Management* 150 (October):62–71. <https://doi.org/10.1016/j.enconman.2017.08.010>.

Geng, Q., Z. Wei, H. Meng, and F. J. Macias. 2016. "Mechanical Performance of TBM Cutterhead in Mixed Rock Ground Conditions." *Tunnelling and Underground Space Technology* 57:76–84. <https://www.sciencedirect.com/science/article/pii/S0886779815300894>.

Geng, Zhe, Dalong Jin, and Dajun Yuan. 2023. "Face Stability Analysis of Cohesion-Frictional Soils Considering the Soil Arch Effect and the Instability Failure Process." *Computers and Geotechnics* 153 (105050): 105050. <https://doi.org/10.1016/j.compgeo.2022.105050>.

Gharahbagh, E. A., M. A. Mooney, G. Frank, B. Walter, and M. A. DiPonio. 2013. "Periodic Inspection of Gauge Cutter Wear on EPB TBMs Using Cone Penetration Testing." *Tunnelling and Underground Space Technology* 38:279–86. <https://www.sciencedirect.com/science/article/pii/S0886779813001090>.

Ghidaoui, Mohamed S., Ming Zhao, Duncan A. McInnis, and David H. Axworthy. 2005. "A Review of Water Hammer Theory and Practice." *Applied Mechanics Reviews* 58 (1): 49–76. <https://doi.org/10.1115/1.1828050>.

Gholizadeh, Hossein, Richard Burton, and Greg Schoenau. 2011. "Fluid Bulk Modulus: A Literature Survey." *Journal of Fluid Power* 12 (3): 5–15. <https://doi.org/10.1080/14399776.2011.10781033>.

Giannakos, Konstantinos. 2012. "Modern Railway Infrastructure: Resilient Fastenings Improve Track's Life-Cycle." *Procedia, Social and Behavioral Sciences* 48:3538–47. <https://doi.org/10.1016/j.sbspro.2012.06.1317>.

Gil Lorenzo, S. 2018. "Structural Behaviour of Concrete Segmental Lining Tunnels: Towards Design Optimisation." <https://www.repository.cam.ac.uk/items/8b1f1f23-a7b3-4df8-b64a-c8e8df36ac6b>.

Gil Lorenzo, Saleta. 2019. "Longitudinal Beam Response of Concrete Segmental Linings Simultaneously Backfilled with Bicomponent Grouts." *Tunnelling and Underground Space Technology* 90 (August):277–92. <https://doi.org/10.1016/j.tust.2019.05.007>.

———. 2021. "Structural Response of Concrete Segmental Linings in Transverse Interaction with the TBM. Part 2: Non-Axisymmetric Conditions." *Tunnelling and Underground Space Technology* 116 (104024): 104024. <https://doi.org/10.1016/j.tust.2021.104024>.

———. 2022. "Design Guidelines for Concrete Segmental Linings in Transverse Interaction with the TBM." *Tunnelling and Underground Space Technology* 122 (104388): 104388. <https://doi.org/10.1016/j.tust.2022.104388>.

Gong, Qiuming, Fan Wu, Dujuan Wang, Haifeng Qiu, and Lijun Yin. 2021. "Development and Application of Cutterhead Working Status Monitoring System for Shield TBM Tunnelling." *Rock Mechanics and Rock Engineering* 54 (4): 1731–53. <https://doi.org/10.1007/s00603-021-02380-8>.

Gong, Qiu-Ming, Jian Zhao, and Yu-Yong Jiao. 2005. "Numerical Modeling of the Effects of Joint Orientation on Rock Fragmentation by TBM Cutters." *Tunnelling and Underground Space Technology* 20 (2): 183–91. <https://doi.org/10.1016/j.tust.2004.08.006>.

Gong, Q. M., Y. Y. Jiao, and J. Zhao. 2006. "Numerical Modelling of the Effects of Joint Spacing on Rock Fragmentation by TBM Cutters." *Tunnelling and Underground Space Technology* 21 (1): 46–55. <https://www.sciencedirect.com/science/article/pii/S088677980500056>.

Graziani, A., A. Capata, and P. Romualdi. 2007. "Analysis of Rock-TBM-Lining Interaction in Squeezing Rock." *Felsbau Magazin* 25 (6): 23–31. https://www.researchgate.net/profile/Alessandro-Graziani-5/publication/288764948_Analysis_of_rock-TBM-lining_interaction_in_squeezing_rock/links/62c6dcb7d7bd92231f9e48b2/Analysis-of-rock-TBM-lining-interaction-in-squeezing-rock.pdf.

Graziani, A., R. Ribacchi, and A. Capata. 2007. "3D-Modelling of TBM Excavation in Squeezing Rock Masses." <https://scholar.google.com.au/citations?user=w--I0f4AAAAJ&hl=en&oi=sra>.

Gruebl, Fritz. 2006. "Segmental Rings (critical Loads and Damage Prevention)." In *International Symposium on Underground Excavation and Tunnelling, Bangkok, Thailand*, 9–19.

Guo, Yidong, Dalong Jin, Xinggao Li, Panpan Cheng, Guogang Qiao, Quanxian Wang, and Yi Yang. 2023. "Effect of Cutting Blind Zones on the Performance of the Rectangular Pipe Jacking Machine with Multiple Cutterheads: A DEM Study." *Tunnelling and Underground Space Technology* 134 (104984): 104984. <https://doi.org/10.1016/j.tust.2023.104984>.

Guo, Yidong, Xinggao Li, Dalong Jin, Hongzhi Liu, Yi Yang, Yingran Fang, and Lunmeng Cui. 2023. "Assessment on the Reverse Circulation Performance of Slurry Shield Pipeline System Assisted with CFD-DEM Modeling under Sandy Cobble Stratum." *Powder Technology* 425 (118573): 118573. <https://doi.org/10.1016/j.powtec.2023.118573>.

Guo, Yidong, Xinggao Li, Yu Sun, Yi Yang, Yingran Fang, and Hanyuan Li. 2023. "Investigation into the Flow Characteristics of Slurry Shield Pipeline System under Sandy Pebble Stratum: Model Test and CFD-DEM Simulation." *Powder Technology* 415 (118149): 118149. <https://doi.org/10.1016/j.powtec.2022.118149>.

Haeri, H., K. Shahriar, and M. F. Marji. 2013. "Simulating the Bluntness of TBM Disc Cutters in Rocks Using Displacement Discontinuity Method," October. https://scholar.google.com.au/citations?user=QL3_VGsAAAJ&hl=en&oi=sra.

Hansen, A. 1998. *The History of TBM Tunnelling in Norway. Norwegian TBM Tunnelling*. Oslo: Norwegian Tunnelling Society.

Harding, Doug. n.d. "Soft Ground Tunneling on a Mexico City Wastewater Project." [books.google.com](http://www.robbinstbm.com/wp-content/uploads/2010/09/EmisorOriente_NAT_2010.pdf). http://www.robbinstbm.com/wp-content/uploads/2010/09/EmisorOriente_NAT_2010.pdf.

Hashimoto, T., T. Konda, J. Brinkman, and A. Feddema. 1995. "Simultaneous Backfill Grouting, Pressure Development In. Tunnelling. A Decade of Progress." *GeoDelft*.

Hassanpour, Jafar. 2018. "Development of an Empirical Model to Estimate Disc Cutter Wear for Sedimentary and Low to Medium Grade Metamorphic Rocks." *Tunnelling and Underground Space Technology* 75 (May):90–99. <https://doi.org/10.1016/j.tust.2018.02.009>.

Hassanpour, Jafar, Jamal Rostami, Jian Zhao, and Sadegh Tarigh Azali. 2015. "TBM Performance and Disc Cutter Wear Prediction Based on Ten Years Experience of TBM Tunnelling in Iran." *Geomechanics and Tunnelling* 8 (3): 239–47. <https://doi.org/10.1002/geot.201500005>.

Hassanpour, J., J. Rostami, S. Tarigh Azali, and J. Zhao. 2014. "Introduction of an Empirical TBM Cutter Wear Prediction Model for Pyroclastic and Mafic Igneous Rocks; a Case

History of Karaj Water Conveyance Tunnel, Iran." *Tunnelling and Underground Space Technology* 43 (July):222–31. <https://doi.org/10.1016/j.tust.2014.05.007>.

Hauge, E. H., and J. A. Støvneng. 1989. "Tunneling Times: A Critical Review." *Reviews of Modern Physics*. <https://doi.org/10.1103/RevModPhys.61.917>.

Heitkamp, H., and R. Stoltz. 1978. "Method Of, and Apparatus For, Controlling the Advance of a Tunnel Drive Shield." U.S. Patent 4.

Helian, Bobo, Zheng Chen, and Bin Yao. 2020. "Precision Motion Control of a Servomotor-Pump Direct-Drive Electrohydraulic System with a Nonlinear Pump Flow Mapping." *IEEE Transactions on Industrial Electronics* (1982) 67 (10): 8638–48. <https://doi.org/10.1109/tie.2019.2947803>.

Herrenknecht, Martin, K. Bäppler, and W. Burger. 2010. "Tunnelling through Squeezing Rock with TBM." *Brenner Base Tunnel and Access Routes, BrennerCongress*, 45–54.

Huang, Hongwei, Jiaqi Chang, Dongming Zhang, Jie Zhang, Huiming Wu, and Gang Li. 2022. "Machine Learning-Based Automatic Control of Tunneling Posture of Shield Machine." *Journal of Rock Mechanics and Geotechnical Engineering* 14 (4): 1153–64. <https://doi.org/10.1016/j.jrmge.2022.06.001>.

Huayong, Yang, Shi Hu, Gong Guofang, and Hu Guoliang. 2009. "Electro-Hydraulic Proportional Control of Thrust System for Shield Tunneling Machine." *Automation in Construction* 18 (7): 950–56. <https://doi.org/10.1016/j.autcon.2009.04.005>.

Hu Gl, Gong G. F., H. Y. Yang, and Others. 2005. "Electro-Hydraulic Control System of Shield Tunnel Boring Machine for Simulator Stand: LU YX, WANG QF, LI W, et Al." In *Proceedings of the Sixth International Conference on Fluid Power Transmission and Control (ICFP'2005)*, 94–99. Hangzhou, China: International Academic Publishers.

Hu, Guoliang. 2006. "Thrust Hydraulic System of Shieid Tunnel Boring Machine with Pressure and Flow Compound Control." *Chinese Journal of Mechanical Engineering* 42:124. <https://doi.org/10.3901/JME.2006.06.124>.

Huo, Jun-Zhou, Xiao-Long Sun, Guang-Qing Li, Tao Li, and Wei Sun. 2015. "Multi-Degree-of-Freedom Coupling Dynamic Characteristic of TBM Disc Cutter under Shock Excitation." *Journal of Central South University* 22 (9): 3326–37. <https://doi.org/10.1007/s11771-015-2873-3>.

Januário, J. R., and C. Maia. 2020. "CFD-DEM Simulation to Predict the Critical Velocity of Slurry Flows." *Journal of Applied Fluid Mechanics* 13 (1): 161–68. https://www.jafmonline.net/JournalArchive/article_908.html.

Jelali, M., and A. Kroll. 2012. "Hydraulic Servo-Systems: Modelling, Identification and Control." https://www.researchgate.net/profile/Mohieddine-Jelali/publication/236893628_Hydraulic_servo-systems_modelling_identification_and_control/links/0c96053b5b14f93c4400000/Hydraulic-servo-systems-modelling-identification-and-control.pdf.

Jiang, L. J. 2013. "Structure Design for Main Bearing of Full Face Rock Tunnel Boring Machine Oriented to Reliability and Vibration Behavior."

Jin, Dalong, Yidong Guo, Xinggao Li, Yi Yang, and Yingran Fang. 2023. "Numerical Study on the Muck Flow Behavior in the Screw Conveyor during EPB Shield Tunneling." *Tunnelling and Underground Space Technology* 134 (105017): 105017. <https://doi.org/10.1016/j.tust.2023.105017>.

Johanastrom, Karl, and Carlos Canudas-de-Wit. 2008. "Revisiting the LuGre Friction Model." *IEEE Control Systems* 28 (6): 101–14. <https://doi.org/10.1109/mcs.2008.929425>.

John, M., and E. Schneider. 2007. "TBM Tunnelling in Squeezing Rock." *Felsbau-Magazin*.

Joly, R., and Christos Pyrgidis. 1990. "Circulation D'un Véhicule Ferroviaire En Courbe." *IKEEART-2016-630*. Vol. 21. Αριστοτέλειο Πανεπιστήμιο Θεσσαλονίκης. <https://ikee.lib.auth.gr/record/282940>.

Josef Mikota, Linz Mai. 2002. "Contributions to the Development of Compact and Tuneable Vibration Compensators for Hydraulic Systems." Doctoral, Austria: Johannes Kepler University. https://www.academia.edu/download/42115340/Contributions_to_the_deveopment_of_compa20160204-30232-7q98yz.pdf.

Jung, H. S., J. M. Choi, B. S. Chun, J. S. Park, and Y. J. Lee. 2011. "Causes of Reduction in Shield TBM Performance-A Case Study in Seoul." *Tunnelling and Underground Space Technology* 26 (3): 453–61.

Kahraman, A. 1993. "Effect of Axial Vibrations on the Dynamics of a Helical Gear Pair." *Journal of Vibration and Acoustics* 115 (1): 33–39. <https://doi.org/10.1115/1.2930311>.

Kanaan, Hadi Youssef, Kamal Al-Haddad, and Gilles Roy. 2003. "Analysis of the Electromechanical Vibrations in Induction Motor Drives due to the Imperfections of the Mechanical Transmission System." *Mathematics and Computers in Simulation* 63 (3–5): 421–33. [https://doi.org/10.1016/s0378-4754\(03\)00086-7](https://doi.org/10.1016/s0378-4754(03)00086-7).

Kang, S. H., D. H. Kim, H. T. Kim, and S. W. Song. 2017. "Study on the Structure of the Articulation Jack and Skin Plate of the Sharp Curve Section Shield TBM in Numerical Analysis." *Journal of Korean Tunnelling and Underground Space Association* 19 (3): 421–35. <https://www.jkta.or.kr/articles/pdf/W1AA/JKTUS-2017-019-03-0.pdf>.

Kang, S. O., H. Kim, Y. M. Kim, and S. H. Kim. 2017. "Application Technique on Thrust Jacking Pressure of Shield TBM in the Sharp Curved Tunnel Alignment by Model Tests." *Journal of Korean Tunnelling and Underground Space Association* 19 (2): 335–53. <https://www.jkta.or.kr/articles/xml/1vXE/>.

Karami, Morteza, Shokrollah Zare, and Jamal Rostami. 2021. "Tracking of Disc Cutter Wear in TBM Tunneling: A Case Study of Kerman Water Conveyance Tunnel." *Bulletin of Engineering Geology and the Environment* 80 (1): 201–19. <https://doi.org/10.1007/s10064-020-01931-7>.

Kaushal, D. R., T. Thinglas, Yuji Tomita, Shigeru Kuchii, and Hiroshi Tsukamoto. 2012. "CFD Modeling for Pipeline Flow of Fine Particles at High Concentration." *International Journal of Multiphase Flow* 43 (July):85–100. <https://doi.org/10.1016/j.ijmultiphaseflow.2012.03.005>.

Kaushal, D. R., and Yuji Tomita. 2002. "Solids Concentration

Profiles and Pressure Drop in Pipeline Flow of Multisized Particulate Slurries." *International Journal of Multiphase Flow* 28 (10): 1697–1717. [https://doi.org/10.1016/s0301-9322\(02\)00047-2](https://doi.org/10.1016/s0301-9322(02)00047-2).

Kim, Sunghun, and Hubertus Murrenhoff. 2012. "Measurement of Effective Bulk Modulus for Hydraulic Oil at Low Pressure." *Journal of Fluids Engineering* 134 (2): 021201. <https://doi.org/10.1115/1.4005672>.

Kinker, B. G. 2011. "4 Fluid Viscosity and Viscosity." *Handbook of Hydraulic Fluid Technology*. https://books.google.com.au/books?hl=en&lr=&id=yKZwwWAuNlsC&oi=fnd&pg=PA181&dq=Kinker,+B.G.,+2011.+4+Fluid+Viscosity+and+Viscosity.+Handbook+of+Hydraulic+Fluid+Technology,+p.181.&ots=tHD96WZsFe&sig=2s6QHgo_QjqA7y8216erV-60FvM.

Knežević, D., A. Milašinović, Z. Milovanović, and V. Savić. 2011. "Analysis of Changes of Bulk Modulus of Mineral oil—Effects on the Dynamic Behavior of Hydraulic Actuators." In *12th International Conference on Tribology—Serbiatrib'11*, 370–75. <https://scholar.google.com.au/citations?user=lpXIOUIAAAAJ&hl=en&oi=sra>.

Knopf, Katelyn, Dimitris C. Rizos, Yu Qian, and Michael Sutton. 2021. "A Non-Contacting System for Rail Neutral Temperature and Stress Measurements: Concept Development." *Structural Health Monitoring* 20 (1): 84–100. <https://doi.org/10.1177/1475921720923116>.

Kök, M. V., T. Batmaz, and I. H. Gücüyener. 2000. "Rheological Behavior of Bentonite Suspensions." *Petroleum Science and Technology* 18 (5–6): 519–36. <https://doi.org/10.1080/10916460008949858>.

Komiya, Kazuhito, Kenichi Soga, Hirokazu Akagi, Toshiyuki Hagiwara, and Malcolm D. Bolton. 1999. "Finite Element Modelling of Excavation and Advancement Processes of a Shield Tunnelling Machine." *SOILS AND FOUNDATIONS* 39 (3): 37–52. https://doi.org/10.3208/sandf.39.3_37.

Kong, Suk-Min, Hyuk-Sang Jung, and Yong-Joo Lee. 2017. "Investigation of Ground Behaviour Adjacent to an Embedded Pile according to Various Tunnel Volume Losses." *International Journal of Geo-Engineering* 8 (1). <https://doi.org/10.1186/s40703-017-0043-1>.

Kovářík, K., and G. Anagnostou. 1995. "The Ground Response Curve in Tunnelling through Short Fault Zones" 2:611–14. <https://doi.org/10.3929/ETHZ-A-010819319>.

Koyama, Y. 2003. "Present Status and Technology of Shield Tunneling Method in Japan. Tunnelling and Underground Space Technology" 18:145–59.

Koyama, Yukinori. 2003. "Present Status and Technology of Shield Tunneling Method in Japan." *Tunnelling and Underground Space Technology* 18 (2–3): 145–59. [https://doi.org/10.1016/s0886-7798\(03\)00040-3](https://doi.org/10.1016/s0886-7798(03)00040-3).

Krishnan, R. 2001. *Switched Reluctance Motor Drives: Modeling, Simulation, Analysis, Design, and Applications*. Industrial Electronics. Boca Raton, FL: CRC Press. <https://doi.org/10.1201/9781420041644>.

Kuznetsov, B., T. Nikitina, V. Kolomietz, and I. V. Bovdyj. 2018. "Improving of Electromechanical Servo Systems Accuracy." *Electrical Engineering & Electromechanics*, no. 6 (December), 33–37. <https://doi.org/10.20998/2074-272X.2018.6.04>.

Labra, Carlos, Jerzy Rojek, and Eugenio Oñate. 2017. "Discrete/finite Element Modelling of Rock Cutting with a TBM Disc Cutter." *Rock Mechanics and Rock Engineering* 50 (3): 621–38. <https://doi.org/10.1007/s00603-016-1133-7>.

Lagos, R. F., A. San Emeterio, J. Vinolas, A. Alonso, and M. Aizpun. 2014. "The Influence of Track Elasticity When Travelling on a Railway Turnout." In *Proceedings of the Second International Conference on Railway Technology: Research, Development and Maintenance*. Stirlingshire, UK: Civil-Comp Press. <https://doi.org/10.4203/ccp.104.208>.

Lan, H., Y. Xia, Z. Ji, J. Fu, and B. Miao. 2019. "Online Monitoring Device of Disc Cutter wear—Design and Field Test." *Tunnelling and Underground Space Technology* 89:284–94. <https://www.sciencedirect.com/science/article/pii/S0886779818301652>.

Lavdas, N. 2010. "Einsatzgrenzen Vom Tübbingausbau Beim TBM-Vortrieb in Druckhaftem Gebirge." *Masterarbeit*, ETH Zürich.

Lee, C. J., B. R. Wu, and S. Y. Chiou. 1999. "Soil Movements around a Tunnel in Soft Soils." *PROCEEDINGS-NATIONAL SCIENCE COUNCIL REPUBLIC OF CHINA PART A PHYSICAL SCIENCE AND ENGINEERING* 23:235–47. https://www.researchgate.net/profile/Chung-Jung-Lee-2/publication/255660738_Soil_Movements_Around_a_Tunnel_in_Soft_Soils/links/02e7e528c13df831600000000/Soil-Movements-Around-a-Tunnel-in-Soft-Soils.pdf.

Lee, Gi-Jun, Hee-Hwan Ryu, Tae-Hyuk Kwon, Gye-Chun Cho, Kyoung-Yul Kim, and Sungyun Hong. 2021. "A Newly Developed State-of-the-Art Full-Scale Excavation Testing Apparatus for Tunnel Boring Machine (TBM)." *KSCE Journal of Civil Engineering* 25 (12): 4856–67. <https://doi.org/10.1007/s12205-021-2347-0>.

Lemaître, Jean. 1985. "A Continuous Damage Mechanics Model for Ductile Fracture." *Journal of Engineering Materials and Technology* 107 (1): 83–89. <https://doi.org/10.1115/1.3225775>.

Li, Chao, Cong Li, Zheng Chen, and Bin Yao. 2018. "Advanced Synchronization Control of a Dual-Linear-Motor-Driven Gantry with Rotational Dynamics." *IEEE Transactions on Industrial Electronics* (1982) 65 (9): 7526–35. <https://doi.org/10.1109/tie.2018.2795522>.

Li, Fukai, Weiping Hu, Qingchun Meng, Zhixin Zhan, and Fei Shen. 2018. "A New Damage-Mechanics-Based Model for Rolling Contact Fatigue Analysis of Cylindrical Roller Bearing." *Tribology International* 120 (April):105–14. <https://doi.org/10.1016/j.triboint.2017.12.001>.

Li, G., L. D. Zhu, J. Y. Yang, and W. S. Wang. 2012. "Research of Kinematics Simulation of TBM Segment Erector Based on Virtual Prototype." *Applied Mechanics and Materials* 236:418–21. <https://www.scientific.net/amm.236-237.418>.

Li, H. L. 2010. "Troubleshooting for Cutter Disk Cracking of Model TB880 Rock Tunneler." *Construction Machinery and Equipment* 41 (3): 62–67.

Lin, Faa-Jeng, Po-Huan Chou, Chin-Sheng Chen, and Yu-Sheng Lin. 2012. "DSP-Based Cross-Coupled Synchronous Control for Dual Linear Motors via Intelligent Complementary

Sliding Mode Control.” *IEEE Transactions on Industrial Electronics* (1982) 59 (2): 1061–73. <https://doi.org/10.1109/tie.2011.2157286>.

Lin, Tianliang, Yuanzheng Lin, Haoling Ren, Haibin Chen, Qihuai Chen, and Zhongshen Li. 2020. “Development and Key Technologies of Pure Electric Construction Machinery.” *Renewable and Sustainable Energy Reviews* 132 (110080): 110080. <https://doi.org/10.1016/j.rser.2020.110080>.

Lin, Tianliang, Yuanzheng Lin, Haoling Ren, Haibin Chen, Zhongshen Li, and Qihuai Chen. 2021. “A Double Variable Control Load Sensing System for Electric Hydraulic Excavator.” *Energy (Oxford, England)* 223 (119999): 119999. <https://doi.org/10.1016/j.energy.2021.119999>.

Lin, Yinjie, Zheng Chen, and Bin Yao. 2020. “Decoupled Torque Control of Series Elastic Actuator with Adaptive Robust Compensation of Time-Varying Load-Side Dynamics.” *IEEE Transactions on Industrial Electronics* (1982) 67 (7): 5604–14. <https://doi.org/10.1109/tie.2019.2934023>.

Li, Pengfei, Yang Chen, Jingluo Huang, Xinyu Wang, Jianyou Liu, and Jie Wu. 2023. “Design Principles of Prestressed Anchors for Tunnels Considering Bearing Arch Effect.” *Computers and Geotechnics* 156 (105307): 105307. <https://doi.org/10.1016/j.comgeo.2023.105307>.

Li, Ting, Ting Yang, Yuyan Cao, Rong Xie, and Xinmin Wang. 2019. “Disturbance-Estimation Based Adaptive Backstepping Fault-Tolerant Synchronization Control for a Dual Redundant Hydraulic Actuation System with Internal Leakage Faults.” *IEEE Access: Practical Innovations, Open Solutions* 7:73106–19. <https://doi.org/10.1109/access.2019.2920415>.

Liu, G. 2007. *Nonlinear Dynamics of Multi-Mesh Gear Systems* (Doctoral Dissertation).

Liu, H. Y., S. Q. Kou, P. A. Lindqvist, and C. A. Tang. 2002. “Numerical Simulation of the Rock Fragmentation Process Induced by Indenters.” *International Journal of Rock Mechanics and Mining Sciences* 39 (4): 491–505. <https://www.sciencedirect.com/science/article/pii/S1365160902000436>.

Liu, Jie, Shijie Wang, Shihua Zhou, and B. Wen. 2014. “Nonlinear Behavior of a Spur Gear Pair Transmission System with Backlash.” *Journal of Vibroengineering* 16 (December):3850–61. <https://www.extrica.com/article/15315>.

Liu, Quansheng, Xing Huang, Qiuming Gong, Lijie Du, Yucong Pan, and Jianping Liu. 2016. “Application and Development of Hard Rock TBM and Its Prospect in China.” *Tunnelling and Underground Space Technology* 57 (August):33–46. <https://doi.org/10.1016/j.tust.2016.01.034>.

Liu, Quansheng, Jianping Liu, Yucong Pan, Xiaoping Zhang, Xingxin Peng, Qiuming Gong, and Lijie Du. 2017. “A Wear Rule and Cutter Life Prediction Model of a 20-In. TBM Cutter for Granite: A Case Study of a Water Conveyance Tunnel in China.” *Rock Mechanics and Rock Engineering* 50 (5): 1303–20. <https://doi.org/10.1007/s00603-017-1176-4>.

Liu, R., J. Z. Sun, Y. Q. Luo, W. Sun, and W. D. Li. 2011. “Research on Multi-Motor Synchronization Control Based on the Ring Coupling Strategy for Cutterhead Driving System of Shield Machines.” *Applied Mechanics and Materials* 52:65–72. <https://www.scientific.net/AMM.52-54.65>.

Liu, R., D. Y. Yu, W. G. Zhao, W. D. Li, and J. Z. Sun. 2014. “Research on Adaptive Load Sharing Control for Multi-Motor Synchronous Driving System of Shield Machine.” *Applied Mechanics and Materials* 667:417–20. <https://www.scientific.net/AMM.667.417>.

Liu, Wenlian, Sugang Sui, Hanhua Xu, Jinchao Wang, and Feng Wang. 2023. “Exploration Technology of Adverse Geological Body in Karst Development Area Based on Borehole Multi-Source Data.” *Applied Sciences (Basel, Switzerland)* 13 (5): 2955. <https://doi.org/10.3390/app13052955>.

Liu, Yang, Shuaiwen Huang, Di Wang, Guoli Zhu, and Dailin Zhang. 2022. “Prediction Model of Tunnel Boring Machine Disc Cutter Replacement Using Kernel Support Vector Machine.” *Applied Sciences (Basel, Switzerland)*, February. <https://doi.org/10.3390/app12052267>.

Liu, Zhiwei, Hongliang Zhang, and Chuanyong Qu. 2023. “An Investigation into Fatigue Damage and Clearance Evolution of TBM Main Bearings.” In *Lecture Notes in Computer Science*, 242–53. Lecture Notes in Computer Science. Singapore: Springer Nature Singapore. https://doi.org/10.1007/978-981-99-6480-2_20.

Li, W., C. Zhang, D. Zhang, Z. Ye, and Z. Tan. 2022. “Face Stability of Shield Tunnels Considering a Kinematically Admissible Velocity Field of Soil Arching.” *Journal of Rock Mechanics and Geotechnical Engineering* 14 (2): 505–26. <https://www.sciencedirect.com/science/article/pii/S1674777521001797>.

Li, X., D. Yuan, D. Jin, J. Yu, and M. Li. 2018. “Twin Neighboring Tunnel Construction under an Operating Airport Runway.” *Tunnelling and Underground Space Technology* 81:534–46. <https://www.sciencedirect.com/science/article/pii/S0886779817310507>.

Lombardi, G. 1973. “Dimensioning of Tunnel Linings with Regard to Constructional Procedures.” *Tunnels and Tunnelling International* 5. <https://trid.trb.org/View/26218>.

—. 1981. “Bau von Tunneln Bei Grossen Verformungen Des Gebirges.” *Tunnel 81, Internationaler Kongress, Düsseldorf*.

Lombardi, G., and A. Panciera. 1997. “Problems with TBM and Linings in Squeezing Ground.” *Tunnels & Tunnelling*. <https://pascal-francis.inist.fr/vibad/index.php?action=getRecordDetail&idt=5874044>.

Lorenzo, S. G. 2023. “In Situ Behaviour of an Instrumented Ring Subjected to Active Eccentric Tail Seal Passage. *Tunnelling and Underground Space Technology*” 131.

Lu, F., C. Zhang, J. Sun, J. X. Tian, M. Liu, and Y. H. Wu. 2016. “Study on Rock-Breaking Simulation and Experiment of Double Disc Cutter of TBM.” *International Journal of Engineering Research in Africa* 23:80–88. <https://www.scientific.net/jera.23.80>.

Lu, Heikki. 2022. “Stiffness Characteristics of Hydraulic Cylinder System Subjected to Dynamic Loading.” <https://aaltodoc.aalto.fi/items/06e3d303-ae4e-4cff-bd5f-07d8c1614b86>.

Luo, J. W., and T. Y. Luo. 2009. *The Calculation and Application of*

Rolling Bearings. Beijing: Chinese.

Lu, Ping, Dajun Yuan, Dalong Jin, Weiping Luo, and Minggao Liu. 2022. "Centrifugal Model Tests on the Structural Response of the Shield Tunnel When Constructing Cross Passages by Mechanical Methods." *Tunnelling and Underground Space Technology* 128 (104621): 104621. <https://doi.org/10.1016/j.tust.2022.104621>.

Lyu, Litong, Zheng Chen, and Bin Yao. 2019. "Development of Pump and Valves Combined Hydraulic System for Both High Tracking Precision and High Energy Efficiency." *IEEE Transactions on Industrial Electronics* (1982) 66 (9): 7189–98. <https://doi.org/10.1109/tie.2018.2875666>.

———. 2021. "Advanced Valves and Pump Coordinated Hydraulic Control Design to Simultaneously Achieve High Accuracy and High Efficiency." *IEEE Transactions on Control Systems Technology: A Publication of the IEEE Control Systems Society* 29 (1): 236–48. <https://doi.org/10.1109/tcst.2020.2974180>.

Ma, Chen-Xiao, and Fang-Le Peng. 2023. "Evaluation of Spatial Performance and Supply-Demand Ratios of Urban Underground Space Based on POI Data: A Case Study of Shanghai." *Tunnelling and Underground Space Technology* 131 (104775): 104775. <https://doi.org/10.1016/j.tust.2022.104775>.

Maidl, Bernhard, Martin Herrenknecht, Ulrich Maidl, and Gerhard Wehrmeyer. 2013. *Mechanised Shield Tunnelling*. Translated by David S. Sturge. 2nd ed. Berlin, Germany: Wilhelm Ernst & Sohn Verlag fur Architektur und technische Wissenschaften.

Mair, R. J. 1979. "Centrifuge Modelling of Tunnel Construction in Soft Clay." *Ph. D Thesis, University of Cambridge*. <https://cir.nii.ac.jp/crid/1573668924330473600>.

Mair, R. J., and R. N. Taylor. 1999. "Bored Tunnelling in the Urban Environments." In *Fourteenth International Conference on Soil Mechanics and Foundation Engineering. Proceedings International Society for Soil Mechanics and Foundation Engineering*. Vol. 4. <https://trid.trb.org/View/500762>.

Marji, Mohammad Fatehi. 2015. "Simulation of Crack Coalescence Mechanism underneath Single and Double Disc Cutters by Higher Order Displacement Discontinuity Method." *Journal of Central South University* 22 (3): 1045–54. <https://doi.org/10.1007/s11771-015-2615-6>.

Matsushita, H. 1980. "Earth Pressure Balanced Shield Method." *Tunnels and Tunnelling International* 12 (January). <https://trid.trb.org/View/153957>.

Matter, J., A. Stauber, F. Bauer, and J. Daller. 2007. "OBB Wienerwaldtunnel—Erfahrungen Aus Dem Vortrieb." In *FGU-Fachtagung Für Untertagbau, Swiss Tunnel Congress*, 101–12.

McGraw-Hill. 2002. *Harris' Shock And Vibration Handbook*. Edited by Allan G. Piersol Cyril M. Harris. Columbia University New York, New York. <http://ndl.ethernet.edu.et/bitstream/123456789/25591/1/309.pdf>.

Mindlin, R. D., and H. Deresiewicz. 1953. "Elastic Spheres in Contact under Varying Oblique Forces." *Journal of Applied Mechanics* 20 (3): 327–44. <https://doi.org/10.1115/1.4010702>.

Min, Fanlu, Hangbiao Song, and Nan Zhang. 2018. "Experimental Study on Fluid Properties of Slurry and Its Influence on Slurry Infiltration in Sand Stratum." *Applied Clay Science* 161 (September):64–69. <https://doi.org/10.1016/j.clay.2018.03.028>.

M, Kannangara K. P., W. Zhou, Z. Ding, and Z. Hong. 2022. "Investigation of Feature Contribution to Shield Tunneling-Induced Settlement Using Shapley Additive Explanations Method." *Journal of Rock Mechanics and Geotechnical Engineering* 14 (4): 1052–63. <https://www.sciencedirect.com/science/article/pii/S1674775522000294>.

Mobley, R. 2000. "8 – Lines, Fittings, and Seals," 130–49. <https://doi.org/10.1016/B978-075067174-3/50059-7>.

Mucha, K. 2023. "Application of Rock Abrasiveness and Rock Abrasivity Test methods—A Review." *Sustainability*, July. <https://doi.org/10.3390/su151411243>.

Nagrecha, Kabir, Luis Fisher, Michael Mooney, Tonatiuh Rodriguez-Nikl, Mehran Mazari, and Mohammad Pourhomayoun. 2020. "As-Encountered Prediction of Tunnel Boring Machine Performance Parameters Using Recurrent Neural Networks." *Transportation Research Record* 2674 (10): 241–49. <https://doi.org/10.1177/0361198120934796>.

Nilsen, B., and L. Ozdemir. 1993. "... Performance, PROCEEDINGS OF THE RAPID EXCAVATION AND TUNNELING CONFERENCE, SOCIETY FOR MINING, METALLOGY & EXPLORATION."

Nise, N. S. 2019. "Control Systems Engineering." <https://carleton.simplesyllabusca.com/api2/doc-pdf/fyl34cisw/Winter-2025-MAAE-3500-B-.pdf>.

Olsson, H., K. J. Åström, C. Canudas de Wit, M. Gäfvert, and P. Lischinsky. 1998. "Friction Models and Friction Compensation." *European Journal of Control* 4 (3): 176–95. [https://doi.org/10.1016/s0947-3580\(98\)70113-x](https://doi.org/10.1016/s0947-3580(98)70113-x).

Ortwig, Harald. 2005. "Experimental and Analytical Vibration Analysis in Fluid Power Systems." *International Journal of Solids and Structures* 42 (21-22): 5821–30. <https://doi.org/10.1016/j.ijsolstr.2005.03.028>.

Ozdemir, L. 1977. *Development of Theoretical Equations for Predicting Tunnel Boreability*. Golden Co.

———. 2003. "CSM Computer Model for TBM Performance Prediction." *Colorado School of Mines*.

Panciera, A., and G. Piccolo. 1997. "TBM Scudate—blocco in Rocce Spingenti."

Pan, Yucong, Quansheng Liu, Xiaoxuan Kong, Jianping Liu, Xingxin Peng, and Qi Liu. 2019. "Full-Scale Linear Cutting Test in Chongqing Sandstone and the Comparison with Field TBM Excavation Performance." *Acta Geotechnica* 14 (4): 1249–68. <https://doi.org/10.1007/s11440-018-0702-1>.

Pan, Yucong, Quansheng Liu, Xingxin Peng, Xiaoxuan Kong, Jianping Liu, and Xiaobo Zhang. 2018. "Full-Scale Rotary Cutting Test to Study the Influence of Disc Cutter Installment Radius on Rock Cutting Forces." *Rock Mechanics and Rock Engineering* 51 (7): 2223–36. <https://doi.org/10.1007/s00603-018-1460-y>.

Papacek, F. 2000. "Turnout of New Construction." *International Railway Journal*.

Park, Byungkwan, Soon-Wook Choi, Chulho Lee, T. Kang, Seungchul Do, Woon-Yong Lee, and Soo-Ho Chang. 2023. "A Geometric Model for a Shield TBM Steering Simulator." *Applied Sciences (Basel, Switzerland)*, September. <https://doi.org/10.3390/app131810087>.

Park, Byungkwan, Chulho Lee, Soon-Wook Choi, Tae-Ho Kang, and Soo-Ho Chang. 2021. "Discrete-Element Analysis of the Excavation Performance of an EPB Shield TBM under Different Operating Conditions." *Applied Sciences (Basel, Switzerland)* 11 (11): 5119. <https://doi.org/10.3390/app11115119>.

Peck, B. B. 1969. "Deep Excavation and Tunnelling in Soft Ground, State of the Art Volume." *7th ICSMFE*. <https://cir.nii.ac.jp/crid/1571135649476083328>.

Peila, D., L. Borio, and S. Pelizza. 2011. "The Behaviour of a Two-Componenet Back-Filling Grout Used in a Tunnel-Boring Machine." *ACTA Geotechnica Slovenica* 8 (1): 5–15. <https://core.ac.uk/download/pdf/234885528.pdf>.

Peng, Xingxin, Quansheng Liu, Yucong Pan, Guangfeng Lei, Lai Wei, and Ciyou Luo. 2018. "Study on the Influence of Different Control Modes on TBM Disc Cutter Performance by Rotary Cutting Tests." *Rock Mechanics and Rock Engineering* 51 (3): 961–67. <https://doi.org/10.1007/s00603-017-1368-y>.

Phadke, V., and N. Titirmare. 2017. "Construction of Tunnels, by New Austrian Tunneling Method (NATM) and by Tunnel Boring Machine (TBM)." *International Journal of Civil Engineering (IJCE)* 6 (6): 25–36. https://papers.ssrn.com/sol3/papers.cfm?abstract_id=3091573.

Poncetti, Bernardo Lopes, Dianelys Vega Ruiz, Leandro Silva de Assis, Lucas Bellini Machado, Tiago Borges da Silva, Ayokunle Adewale Akinlalu, and Marcos Massao Futai. 2025. "Tunnel Inspection Review: Normative Practices and Non-Destructive Method Advancements for Tunnels with Concrete Cover." *Applied Mechanics (Basel, Switzerland)* 6 (2): 41. <https://doi.org/10.3390/app1mech6020041>.

"Processes around a TBM." 2008. In *Geotechnical Aspects of Underground Construction in Soft Ground*, 19–30. CRC Press. <https://doi.org/10.1201/9780203879986-5>.

Pyrgidis, Christos N. 2021. *Railway Transportation Systems: Design, Construction and Operation*. Boca Raton: CRC Press. <https://doi.org/10.1201/9781003046073>.

Qi, Geng, Wei Zhengying, Meng Hao, and Chen Qiao. 2016. "Numerical and Experimental Research on the Rock-Breaking Process of Tunnel Boring Machine Normal Disc Cutters." *Journal of Mechanical Science and Technology* 30 (4): 1733–45. <https://doi.org/10.1007/s12206-016-0329-9>.

Qi, G., W. Zhengying, and M. Hao. 2016. "An Experimental Research on the Rock Cutting Process of the Gage Cutters for Rock Tunnel Boring Machine (TBM)." *Tunnelling and Underground Space Technology* 52:182–91. <https://www.sciencedirect.com/science/article/pii/S0886779815303606>.

Qi, M. X., Y. J. Wang, and H. L. Li. 2009. "Research and Application of Overall Refit of Open Type TBM." *Modern Tunnelling TechNology* 46 (4): 64–70.

Qin, Da-Tong. 2012. "Multi-Objective Optimization of Multi-Stage Planetary Gear Train Used in Shield Machine Cutter Driver." *China Mechanical Engineering* 23 (1): 12. <https://www.cmem.org.cn/EN/abstract/abstract3084.shtml>.

Ramoni, M., and G. Anagnostou. 2006. "On the Feasibility of TBM Drives in Squeezing Ground." *Tunnelling and Underground Space Technology* 21 (3–4): 262. <https://doi.org/10.1016/j.tust.2005.12.123>.

———. 2008. *TBM Drives in Squeezing Rock- Shield-Rock Interaction*. Montecarlo, Edition specifique Limonest: AFTES International Congress Monaco.

———. 2010a. "Thrust Force Requirements for TBMs in Squeezing Ground." *Tunnelling and Underground Space Technology* 25 (4): 433–55. <https://doi.org/10.1016/j.tust.2010.02.008>.

———. 2010b. "Tunnel Boring Machines under Squeezing Conditions." *Tunnelling and Underground Space Technology* 25 (2): 139–57. <https://doi.org/10.1016/j.tust.2009.10.003>.

———. 2011. "The Interaction between Shield, Ground and Tunnel Support in TBM Tunnelling through Squeezing Ground." *Rock Mechanics and Rock Engineering* 44:37–61.

Rankin, W. J. 1988. "Ground Movements Resulting from Urban Tunnelling: Predictions and Effects." *Geological Society London Engineering Geology Special Publications* 5 (1): 79–92. <https://doi.org/10.1144/gsl.eng.1988.005.01.06>.

Resnikov, J. M. 1975. *Strelochnye Elektroprivody Elektricheskoy I Gorochnoj Centralizacii [Switch Electric Drives of Electric and Mining Centralization]*. Moscow: Transport Publ.

Rezaei, A. H., Mojtaba Shirzehhagh, and M. B. Golpasand. 2019. "EPB Tunneling in Cohesionless Soils: A Study on Tabriz Metro Settlements." *Geomechanics and Engineering* 19 (2): 153. <http://www.techno-press.org/content/?page=article&journal=gae&volume=19&num=2&ordernum=5>.

Rivin, E., and L. Kops. 2010. "Handbook on Stiffness & Damping in Mechanical Design." (No Title), March. <https://doi.org/10.1115/1.4004119>.

Rojek, Jerzy, Eugenio Oñate, Carlos Labra, and Hubert Kargl. 2011. "Discrete Element Simulation of Rock Cutting." *International Journal of Rock Mechanics and Mining Sciences* (Oxford, England: 1997) 48 (6): 996–1010. <https://doi.org/10.1016/j.ijrmms.2011.06.003>.

Rostami, Jamal. 2008. "Hard Rock TBM Cutterhead Modeling for Design and Performance Prediction." *Geomechanics and Tunnelling* 1 (1): 18–28. <https://doi.org/10.1002/geot.200800002>.

———. 2016. "Performance Prediction of Hard Rock Tunnel Boring Machines (TBMs) in Difficult Ground." *Tunnelling and Underground Space Technology* 57 (August):173–82. <https://doi.org/10.1016/j.tust.2016.01.009>.

Rostami, J., and L. Ozdemir. 1993. "A New Model for Performance Prediction of Hard Rock TBMs. In: Proceedings of the Rapid Excavation and Tunneling Conference."

Rubanenko, Alexander, Mikhail Labzun, and Maksim Hryshchuk. 2017. "Definition Defects of Transformer Equipment Using Frequency Diagnostic Parameters."

Bulletin of the National Technical University «KhPI» Series New Solutions in Modern Technologies 0 (23(1245)): 41–46. <https://doi.org/10.20998/2413-4295.2017.23.07>.

Rutschmann, W. 1979. “Mechanical Tunnelling in Solid Rock.” <https://rosap.ntl.bts.gov/view/dot/30519>.

Salepciler, Volkan, John Brown, Jacek Bogdan Stypulkowski, and Sheikh Abdulrahman Al-Thani. 2023. “Launching a 148m-Long Tunnel Boring Machine from a 15m-Inner Diameter Shaft.” In *The International Conference on Civil Infrastructure and Construction*, 5–8. Qatar University Press. <https://doi.org/10.29117/cic.2023.0081>.

Samuel, A. E., and L. P. Seow. 1984. “Disc Force Measurements on a Full-Face Tunnelling Machine.” *International Journal of Rock Mechanics and Mining Sciences & Geomechanics Abstracts* 21 (2): 83–96. [https://doi.org/10.1016/0148-9062\(84\)91176-8](https://doi.org/10.1016/0148-9062(84)91176-8).

Schneider, E., and M. Spiegl. 2008. “Convergency Compatible Support Systems.” *Tunnels and Tunnelling International*, June, 40–43. <https://trid.trb.org/View/865883>.

Sebbeh-Newton, Sylvanus, Prosper E. A. Ayawah, Jessica W. A. Azure, Azupuri G. A. Kaba, Fauziah Ahmad, Zurinahni Zainol, and Hareyani Zabidi. 2021. “Towards TBM Automation: On-the-Fly Characterization and Classification of Ground Conditions ahead of a TBM Using Data-Driven Approach.” *Applied Sciences (Basel, Switzerland)* 11 (3): 1060. <https://doi.org/10.3390/app11031060>.

“Settlements above Tunnels in the United Kingdom—Their Magnitude and Prediction.” n.d. <https://trid.trb.org/View/186714>.

Sharp, W., and L. Ozdemir. 1991. “Computer Modelling for TBM Performance Prediction and Optimization.” In *Proceedings of the International Symposium on Mine Mechanization and Automation, CSM/USBM*, 1:57–66.

Shen, W., and J. Wang. 2022. “An Integral Terminal Sliding Mode Control Scheme for Speed Control System Using a Double-Variable Hydraulic Transformer.” *ISA Transactions* 124:386–94. <https://www.sciencedirect.com/science/article/pii/S0019057819304148>.

Shen, Xuesong, Ming Lu, and Wu Chen. 2011. “Computing Three-Axis Orientations of a Tunnel-Boring Machine through Surveying Observation Points.” *Journal of Computing in Civil Engineering* 25 (3): 232–41. [https://doi.org/10.1061/\(asce\)cp.1943-5487.0000087](https://doi.org/10.1061/(asce)cp.1943-5487.0000087).

Shen, X., D. Yuan, X. T. Lin, X. Chen, and Y. Peng. 2023. “Evaluation and Prediction of Earth Pressure Balance Shield Performance in Complex Rock Strata: A Case Study in Dalian, China.” *Journal of Rock Mechanics and Geotechnical Engineering* 15 (6): 1491–1505. <https://www.sciencedirect.com/science/article/pii/S1674775522001962>.

Shiau, Jim, Mathew Sams, Mohammad Reza Arvin, and Pornkasem Jongpradist. 2023. “Automating the Process for Estimating Tunnelling Induced Ground Stability and Settlement.” *Geosciences* 13 (3): 81. <https://doi.org/10.3390/geosciences13030081>.

Shi, Hu, Huayong Yang, Guofang Gong, and Lintao Wang. 2011. “Determination of the Cutterhead Torque for EPB Shield Tunnelling Machine.” *Automation in Construction* 20 (8): 1087–95. <https://doi.org/10.1016/j.autcon.2011.04.010>.

Simic, D. 2005. “Tunnel de Guadarrama : Problématique Des Tunnels Profonds : La Traversée de La Faille de La Umbria Du Tunnel de Guadarrama : Espagne.” *Tunnels et Ouvrages Souterrains*, 13–21. <https://pascal-francis.inist.fr/vibad/index.php?action=getRecordDetail&idt=17183207>.

Sloan, S. W. 2013. “Geotechnical Stability Analysis.” *Géotechnique* 63 (7): 531–71. <https://doi.org/10.1680/geot.12.rl.001>.

Soil, Norwegian, Rock Engineering Association, and Others. 1998. “Norwegian TBM Tunnelling.” *Norwegian Tunnelling Society, Oslo*, 112–13.

Souza Pinto, T. C., D. Moraes Junior, P. T. Slatter, and L. S. Leal Filho. 2014. “Modelling the Critical Velocity for Heterogeneous Flow of Mineral Slurries.” *International Journal of Multiphase Flow* 65 (October):31–37. <https://doi.org/10.1016/j.ijmultiphaseflow.2014.05.013>.

Sterpi, Donatella Valeria, and Others. 2007. “Ground Pressure and Convergence for TBM Driven Tunnels in Visco-Plastic Rocks.” In *Computational Methods in Tunnelling-EURO: TUN 2007*, 1–054. Vienna University of Technology. <https://re.public.polimi.it/handle/11311/245946>.

Sugimoto, Mitsutaka. 2006. “Causes of Shield Segment Damages during Construction.” In *International Symposium on Underground Excavation and Tunnelling*, 67–74. Bangkok. <https://scholar.google.com.au/citations?user=pPMVw5QAAAJ&hl=en&oi=sra>.

Sugimoto, Mitsutaka, and Aphichat Sramoon. 2002. “Theoretical Model of Shield Behavior during Excavation. I: Theory.” *Journal of Geotechnical and Geoenvironmental Engineering* 128 (2): 138–55. [https://doi.org/10.1061/\(asce\)1090-0241\(2002\)128:2\(138\)](https://doi.org/10.1061/(asce)1090-0241(2002)128:2(138)).

Sun, Hong, and G. T-C Chiu. 2002. “Motion Synchronization for Dual-Cylinder Electrohydraulic Lift Systems.” *IEEE/ASME Transactions on Mechatronics* 7 (2): 171–81. <https://doi.org/10.1109/tmech.2002.1011254>.

Sun, Jianzhong, Ran Liu, Yaqin Luo, and Wei Sun. 2009. “Research on Multi-Motor Synchronization Control for Cutter Head of Shield Machine Based on the Ring Coupled Control Strategy.” In *Intelligent Robotics and Applications*, 345–54. Lecture Notes in Computer Science. Berlin, Heidelberg: Springer Berlin Heidelberg. https://doi.org/10.1007/978-3-642-10817-4_34.

Sun, Wei, Xin Ding, Jing Wei, Xiaobang Wang, and Aiqiang Zhang. 2016. “Hierarchical Modeling Method and Dynamic Characteristics of Cutter Head Driving System in Tunneling Boring Machine.” *Tunnelling and Underground Space Technology* 52 (February):99–110. <https://doi.org/10.1016/j.tust.2015.11.022>.

Sun, Wei, Junzhou Huo, Jing Chen, Zhen Li, Xu Zhang, Li Guo, Haifeng Zhao, and Yu Zhao. 2011. “Disc Cutters’ Layout Design of the Full-Face Rock Tunnel Boring Machine (TBM) Using a Cooperative Coevolutionary Algorithm.” *Journal of Mechanical Science and Technology* 25 (2): 415–27.

[https://doi.org/10.1007/s12206-010-1225-3.](https://doi.org/10.1007/s12206-010-1225-3)

Sun, Wei, Jingxiu Ling, Junzhou Huo, Li Guo, Xu Zhang, and Liying Deng. 2013. "Dynamic Characteristics Study with Multidegree-of-Freedom Coupling in TBM Cutterhead System Based on Complex Factors." *Mathematical Problems in Engineering* 2013:1–17. <https://doi.org/10.1155/2013/635809>.

Sun, Wei, Maolin Shi, Chao Zhang, Junhong Zhao, and Xueguan Song. 2018. "Dynamic Load Prediction of Tunnel Boring Machine (TBM) Based on Heterogeneous in-Situ Data." *Automation in Construction* 92 (August):23–34. <https://doi.org/10.1016/j.autcon.2018.03.030>.

Sun, Wei, Xiaobang Wang, Lintao Wang, Jie Zhang, and Xueguan Song. 2016. "Multidisciplinary Design Optimization of Tunnel Boring Machine Considering Both Structure and Control Parameters under Complex Geological Conditions." *Structural and Multidisciplinary Optimization: Journal of the International Society for Structural and Multidisciplinary Optimization* 54 (4): 1073–92. <https://doi.org/10.1007/s00158-016-1455-9>.

Sun, Zhenchuan, Yandong Yang, Kui Chen, Fengyuan Li, Jianjun Zhou, Bing Zhang, and Qiao Chen. 2019. "Disc Cutter's Rock Breaking Ability and Wear Resistance in Extremely Hard Rock: A Case Study in Qinling Tunnel of Han River to Wei River Water Diversion Project." *Geotechnical and Geological Engineering* 37 (6): 4901–10. <https://doi.org/10.1007/s10706-019-00950-w>.

Sun, Zhenyu, Dingli Zhang, Qian Fang, Yanjuan Hou, and Nanqi Huangfu. 2024. "Analysis of the Interaction between Bolt-Reinforced Rock and Surface Support in Tunnels Based on Convergence-Confinement Method." *Journal of Rock Mechanics and Geotechnical Engineering* 16 (6): 1936–51. <https://doi.org/10.1016/j.jrmge.2023.09.021>.

Talmon, A. M., and A. Bezuijen. 2009. "Simulating the Consolidation of TBM Grout at Noordplaspolder." *Tunnelling and Underground Space Technology* 24 (5): 493–99. <https://doi.org/10.1016/j.tust.2008.12.004>.

Tan, Q., Z. Xu, Y. Xia, and K. Zhang. 2012. "Numerical Study on Mode of Breaking Rock by TBM Cutter in Two Cutting Orders." *Journal of Central South University*.

Theodossiades, S., and S. Natsiavas. 2000. "Non-Linear Dynamics of Gear-Pair Systems with Periodic Stiffness and Backlash." *Journal of Sound and Vibration* 229 (2): 287–310. <https://doi.org/10.1006/jsvi.1999.2490>.

Tsuiji, Y., T. Kawaguchi, and T. Tanaka. 1993. "Discrete Particle Simulation of Two-Dimensional Fluidized Bed." *Powder Technology* 77 (1): 79–87. [https://doi.org/10.1016/0032-5910\(93\)85010-7](https://doi.org/10.1016/0032-5910(93)85010-7).

Tumac, Deniz, and Cemal Balci. 2015. "Investigations into the Cutting Characteristics of CCS Type Disc Cutters and the Comparison between Experimental, Theoretical and Empirical Force Estimations." *Tunnelling and Underground Space Technology* 45 (January):84–98. <https://doi.org/10.1016/j.tust.2014.09.009>.

Tunnel Engineering Committee, Jsce. 2007. "Standard Specifications for Tunneling 2006: Shield Tunnels." *Jpn. Soc. Civil Eng.(JSCE)*.

Versteeg, H. K. 2007. "An Introduction to Computational Fluid Dynamics the Finite Volume Method, 2/E." https://www.researchgate.net/profile/Ghassan-Smaisim/post/FEM_mesh_generator/attachment/59d655b479197b80779acc78/AS%3A526908706508800%401502636233004/download/110+Versteeg+2007+an+introduction+to+computational+fluid+dynamics+the+finite+volume+method+2nd+edition.pdf.

Vlasak, Pavel, Bohus Kysela, and Zdenek Chara. 2014. "Fully Stratified Particle-Laden Flow in Horizontal Circular Pipe." *Particulate Science and Technology* 32 (2): 179–85. <https://doi.org/10.1080/02726351.2013.840705>.

Vogelhuber, M. 2007. "Der Einfluss Des Porenwasserdrucks Auf Das Mechanische Verhalten Kakiritisierter Gesteine" 230. <https://doi.org/10.3929/ETHZ-A-005399238>.

Wang, Fei, Changhao Men, Xiangwei Kong, and Lingxiang Meng. 2019. "Optimum Design and Application Research of Eddy Current Sensor for Measurement of TBM Disc Cutter Wear." *Sensors (Basel, Switzerland)* 19 (19): 4230. <https://doi.org/10.3390/s19194230>.

Wang, Lihui, Yilan Kang, Zongxi Cai, Qian Zhang, Yu Zhao, Haifeng Zhao, and Pengcheng Su. 2012. "The Energy Method to Predict Disc Cutter Wear Extent for Hard Rock TBMs." *Tunnelling and Underground Space Technology* 28 (March):183–91. <https://doi.org/10.1016/j.tust.2011.11.001>.

Wang, Lihui, Haipeng Li, Xiangjun Zhao, and Qian Zhang. 2017. "Development of a Prediction Model for the Wear Evolution of Disc Cutters on Rock TBM Cutterhead." *Tunnelling and Underground Space Technology* 67 (August):147–57. <https://doi.org/10.1016/j.tust.2017.05.003>.

Wang, Lintao, Guofang Gong, Hu Shi, and Huayong Yang. 2012. "Modeling and Analysis of Thrust Force for EPB Shield Tunneling Machine." *Automation in Construction* 27 (November):138–46. <https://doi.org/10.1016/j.autcon.2012.02.004>.

Wang, Lintao, Guofang Gong, Huayong Yang, Xu Yang, and Dianqing Hou. 2013. "The Development of a High-Speed Segment Erecting System for Shield Tunneling Machine." *IEEE/ASME Transactions on Mechatronics* 18 (6): 1713–23. <https://doi.org/10.1109/tmech.2013.2282873>.

Wang, L., W. Sun, G. Gong, and H. Yang. 2017. "Electro-Hydraulic Control of High-Speed Segment Erection Processes." *Automation in Construction* 73:67–77. <https://www.sciencedirect.com/science/article/pii/S092658016301923>.

Wang, M., J. B. Liu, X. F. Wang, X. L. Yan, L. M. Yao, and Q. B. Yue. 2022. "Automatic Determination of Coupling Time Step and Region in Unresolved DEM-CFD." *Powder Technology* 400 (117267): 117267. <https://doi.org/10.1016/j.powtec.2022.117267>.

Wang, Qi, Huayong Wei, Bei Jiang, Xuepeng Wang, Lingfeng Sun, and Manchao He. 2024. "High Pre-Tension Reinforcing Technology and Design for Ultra-Shallow Buried Large-Span Urban Tunnels." *International Journal of Rock Mechanics and Mining Sciences (Oxford, England)* 1997: 182 (105891): 105891. <https://doi.org/10.1016/j.ijrmms.2024.105891>.

Wang, Xuyang, Dajun Yuan, Dalong Jin, Hui Jin, Yi Yang, and Jin

Wu. 2022. "Determination of Thrusts for Different Cylinder Groups during Shield Tunneling." *Tunnelling and Underground Space Technology* 127 (104579): 104579. <https://doi.org/10.1016/j.tust.2022.104579>.

Wang, Zhongrong, Wenjing Guo, Wantao Ding, Keqi Liu, Wang Qin, Chengzhen Wang, and Zhicheng Wang. 2023. "Numerical Study on the Hydrodynamic Properties of Bentonite Slurries with Herschel-Bulkley-Papanastasiou Rheology Model." *Powder Technology* 419 (118375): 118375. <https://doi.org/10.1016/j.powtec.2023.118375>.

Washino, Kimiaki, Ei L. Chan, Koki Miyazaki, Takuya Tsuji, and Toshitsugu Tanaka. 2016. "Time Step Criteria in DEM Simulation of Wet Particles in Viscosity Dominant Systems." *Powder Technology* 302 (November):100–107. <https://doi.org/10.1016/j.powtec.2016.08.018>.

Watton, J. 2009. "Fundamentals of Fluid Power Control" 10. [https://books.google.com.au/books?hl=en&lr=lang_en&id=4zXiWciNKzwC&oi=fnd&pg=PR5&dq=Watton,+J.,+2009.+Fundamentals+of+fluid+power+control+\(Vol.+10\).+Cambridge+University+Press.&ots=fOzVrySFUs&sig=5wZ0wKC2nK-LC9rump0Y8jKZSZA](https://books.google.com.au/books?hl=en&lr=lang_en&id=4zXiWciNKzwC&oi=fnd&pg=PR5&dq=Watton,+J.,+2009.+Fundamentals+of+fluid+power+control+(Vol.+10).+Cambridge+University+Press.&ots=fOzVrySFUs&sig=5wZ0wKC2nK-LC9rump0Y8jKZSZA).

Wei, Jing, Qinchao Sun, Wei Sun, Jin Cai, and Jin Zeng. 2013. "Dynamic Analysis and Load-Sharing Characteristic of Multiple Pinion Drives in Tunnel Boring Machine." *Journal of Mechanical Science and Technology* 27 (5): 1385–92. <https://doi.org/10.1007/s12206-013-0319-0>.

Weirich, W., and H. Heitkamp. 1983. "Hydraulic Control Systems for and Methods of Controlling the Operation of Tunnelling Apparatus." *U.S. Patent* 4.

Wilson, Daniel W., Andrew J. Abbo, Scott W. Sloan, and Andrei V. Lyamin. 2011. "Undrained Stability of a Circular Tunnel Where the Shear Strength Increases Linearly with Depth." *Canadian Geotechnical Journal* 48 (9): 1328–42. <https://doi.org/10.1139/t11-041>.

Wittke, W., P. Wittke-Gattermann, and B. Wittke-Schmitt. 2007. "TBM-Heading in Rock, Design of the Shield Mantle." In *ECCOMAS Thematic Conference on Computational Methods in Tunnelling, EURO: TUN*.

Wu, Jian, Hang Luo, Haohao Li, Benlong Su, Youshan Wang, and Zhe Li. 2020. "The Influence of Hydrothermal Aging on the Dynamic Friction Model of Rubber Seals." *Polymers* 12 (1): 102. <https://doi.org/10.3390/polym12010102>.

Xiaohe, X., and Y. Jing. 1984. "Theory of Rock Fragmentation." *China Coal Industry Publishing House*.

Xiao, Huifang, Zedong Li, Xin Zhang, Liming Wang, Hamideh Khanbareh, and Chris Bowen. 2024. "Mathematic Modeling of Vibration Transmission Path with Discontinuous Contact Interfaces for Gear Dynamics in the Gear-Shaft-Bearing-Housing System." *Measurement: Journal of the International Measurement Confederation* 226 (114054): 114054. <https://doi.org/10.1016/j.measurement.2023.114054>.

Xia, Yi-Min, Tao Ouyang, Xin-Ming Zhang, and De-Zhi Luo. 2012. "Mechanical Model of Breaking Rock and Force Characteristic of Disc Cutter." *Journal of Central South University* 19 (7): 1846–52. <https://doi.org/10.1007/s11771-012-1218-8>.

Xie, Haibo, Xiaoming Duan, Huayong Yang, and Zhibin Liu. 2012. "Automatic Trajectory Tracking Control of Shield Tunneling Machine under Complex Stratum Working Condition." *Tunnelling and Underground Space Technology* 32 (November):87–97. <https://doi.org/10.1016/j.tust.2012.06.002>.

Yagiz, Saffet. 2008. "Utilizing Rock Mass Properties for Predicting TBM Performance in Hard Rock Condition." *Tunnelling and Underground Space Technology* 23 (3): 326–39. <https://doi.org/10.1016/j.tust.2007.04.011>.

Yang, Huayong, Hu Shi, Guofang Gong, and Guoliang Hu. 2009. "Earth Pressure Balance Control for EPB Shield." *Science in China Series E: Technological Sciences* 52 (10): 2840–48. <https://doi.org/10.1007/s11431-009-0245-7>.

Yang, J. H., X. P. Zhang, P. Q. Ji, Q. S. Liu, X. J. Lu, J. P. Wei, and Geng Y. 2019. "Analysis of Disc Cutter Damage and Consumption of TBM1 Section on Water Conveyance Tunnel at Lanzhou Water Source Construction Engineering." *Tunnelling and Underground Space Technology* 85:67–75. <https://www.sciencedirect.com/science/article/pii/S0886779818301615>.

Yang, Y., B. Zhou, X. Xie, and C. Liu. 2018. "Characteristics and Causes of Cracking and Damage of Shield Tunnel Segmented Lining in Construction Stage-a Case Study in Shanghai Soft Soil." *European Journal of Environmental and Civil Engineering* 22 (sup1): 213–27.

Yan, Tao, Shui-Long Shen, Annan Zhou, and Xiangsheng Chen. 2022. "Prediction of Geological Characteristics from Shield Operational Parameters by Integrating Grid Search and K-Fold Cross Validation into Stacking Classification Algorithm." *Journal of Rock Mechanics and Geotechnical Engineering* 14 (4): 1292–1303. <https://doi.org/10.1016/j.jrmge.2022.03.002>.

Yao, Bin, Fanping Bu, J. Reedy, and G. T-C Chiu. 2000. "Adaptive Robust Motion Control of Single-Rod Hydraulic Actuators: Theory and Experiments." *IEEE/ASME Transactions on Mechatronics* 5 (1): 79–91. <https://doi.org/10.1109/3516.828592>.

Yao, Bin, and Masayoshi Tomizuka. 1997. "Adaptive Robust Control of SISO Nonlinear Systems in a Semi-Strict Feedback Form." *Automatica: The Journal of IFAC, the International Federation of Automatic Control* 33 (5): 893–900. [https://doi.org/10.1016/s0005-1098\(96\)00222-1](https://doi.org/10.1016/s0005-1098(96)00222-1).

Yao, Jing, Xiaoming Cao, Yang Zhang, and Yao Li. 2018. "Cross-Coupled Fuzzy PID Control Combined with Full Decoupling Compensation Method for Double Cylinder Servo Control System." *Journal of Mechanical Science and Technology* 32 (5): 2261–71. <https://doi.org/10.1007/s12206-018-0437-9>.

Yin, F., S. Nie, H. Ji, and Y. Huang. 2018. "Non-Probabilistic Reliability Analysis and Design Optimization for Valve-Port Plate Pair of Seawater Hydraulic Pump for Underwater Apparatus." *Ocean Engineering* 163:337–47. <https://www.sciencedirect.com/science/article/pii/S0029801818310096>.

Yuan, Mingxing, Zheng Chen, Bin Yao, and Xingyi Liu. 2021. "Fast and Accurate Motion Tracking of a Linear Motor

System under Kinematic and Dynamic Constraints: An Integrated Planning and Control Approach." *IEEE Transactions on Control Systems Technology: A Publication of the IEEE Control Systems Society* 29 (2): 804–11. <https://doi.org/10.1109/tcst.2019.2955658>.

Yuan, Xiaoming, Xuan Zhu, Chu Wang, and Lijie Zhang. 2019. "Research on Theoretical Model of Dynamic Bulk Modulus of Gas-Containing Hydraulic Oil." *IEEE Access: Practical Innovations, Open Solutions* 7:178413–22. <https://doi.org/10.1109/access.2019.2959058>.

Yuce, Mehmet Ishak, and Aram Faraidoon Omer. 2019. "Hydraulic Transients in Pipelines due to Various Valve Closure Schemes." *SN Applied Sciences* 1 (9). <https://doi.org/10.1007/s42452-019-1146-4>.

Yu, Honggan, Jianfeng Tao, Sheng Huang, Chengjin Qin, Dengyu Xiao, and Chengliang Liu. 2021. "A Field Parameters-Based Method for Real-Time Wear Estimation of Disc Cutter on TBM Cutterhead." *Automation in Construction* 124 (103603): 103603. <https://doi.org/10.1016/j.autcon.2021.103603>.

Yu, Zhaosheng. 2012. "Research on Numerical Simulation of Rock Breaking Using TBM Disc Cutters Based on UDEC Method." *Rock and Soil Mechanics*. <https://scholar.google.com.au/citations?user=ka8WSyIAAA AJ&hl=en&oi=sra>.

Zhang, Hongliang, and C. Qu. 2023. "Research on Tunnel-Boring Machine Main Bearing Fatigue Damage and Vibration Response." *Metals*, March. <https://doi.org/10.3390/met13040650>.

Zhang, Kaizhi, Haidong Yu, Zhongpo Liu, and Xinmin Lai. 2010. "Dynamic Characteristic Analysis of TBM Tunnelling in Mixed-Face Conditions." *Simulation Modelling Practice and Theory* 18 (7): 1019–31. <https://doi.org/10.1016/j.simpat.2010.03.005>.

Zhang, K-Z, H-D Yu, X-X Zeng, and X-M Lai. 2011. "Numerical Simulation of Instability Conditions in Multiple Pinion Drives." *Proceedings of the Institution of Mechanical Engineers, Part C: Journal of Mechanical Engineering Science* 225 (6): 1319–27. <https://doi.org/10.1177/2041298310392649>.

Zhang, Ning, Jack Shuiliang Shen, Annan Zhou, and Arul Arulrajah. 2018. "Tunnelling Induced Geohazards in Mylonitic Rock Faults with Rich Groundwater: A Case Study in Guangzhou." *Tunnelling and Underground Space Technology* 74 (April):262–72. <https://doi.org/10.1016/j.tust.2017.12.021>.

Zhang, Qian, Chuanyong Qu, Yilan Kang, Ganyun Huang, Zongxi Cai, Yu Zhao, Haifeng Zhao, and Pengcheng Su. 2012. "Identification and Optimization of Energy Consumption by Shield Tunnel Machines Using a Combined Mechanical and Regression Analysis." *Tunnelling and Underground Space Technology* 28 (March):350–54. <https://doi.org/10.1016/j.tust.2011.12.003>.

Zhang, Z. X., S. Q. Kou, and P-A Lindqvist. 2003. "In-Situ Measurements of Cutter Forces on Boring Machine at Äspö Hard Rock Laboratory Part II. Characteristics of Cutter Forces and Examination of Cracks Generated." *Rock Mechanics and Rock Engineering* 36 (1): 63–83. <https://doi.org/10.1007/s00603-002-0037-x>.

Zhao, Yanru, Haiqing Yang, Zhongkui Chen, Xiangsheng Chen, Liping Huang, and Shuya Liu. 2019. "Effects of Jointed Rock Mass and Mixed Ground Conditions on the Cutting Efficiency and Cutter Wear of Tunnel Boring Machine." *Rock Mechanics and Rock Engineering* 52 (5): 1303–13. <https://doi.org/10.1007/s00603-018-1667-y>.

Zheng, Y. L., Q. B. Zhang, and J. Zhao. 2016. "Challenges and Opportunities of Using Tunnel Boring Machines in Mining." *Tunnelling and Underground Space Technology* 57 (August):287–99. <https://doi.org/10.1016/j.tust.2016.01.023>.

Zhonghai, Sun, Zheng Hengyu, and Shi Buhai. 2019. "Faults Prediction and Diagnoses of Shield Machine Based on LSTM." In *2019 Chinese Control And Decision Conference (CCDC)*, 5254–59. IEEE. <https://doi.org/10.1109/ccdc.2019.8832341>.

Zhou, J-X, G. Liu, and S-J Ma. 2011. "Vibration and Noise Analysis of Gear Transmission System." *Journal of Vibration and Shock* 30 (6): 234–38.

Zhou, Song, Yingyi Wang, and Xingchun Huang. 2009. "Experimental Study on the Effect of Injecting Slurry inside a Jacking Pipe Tunnel in Silt Stratum." *Tunnelling and Underground Space Technology* 24 (4): 466–71. <https://doi.org/10.1016/j.tust.2008.11.003>.

Zhou, Xiao-Ping, and Shu-Fang Zhai. 2018. "Estimation of the Cutterhead Torque for Earth Pressure Balance TBM under Mixed-Face Conditions." *Tunnelling and Underground Space Technology* 74 (April):217–29. <https://doi.org/10.1016/j.tust.2018.01.025>.

Zhou, Ying, Hanbin Luo, and Yiheng Yang. 2017. "Implementation of Augmented Reality for Segment Displacement Inspection during Tunneling Construction." *Automation in Construction* 82 (October):112–21. <https://doi.org/10.1016/j.autcon.2017.02.007>.

Zhou, Ying, Yu Wang, Lieyun Ding, and Peter E. D. Love. 2018. "Utilizing IFC for Shield Segment Assembly in Underground Tunnelling." *Automation in Construction* 93 (September):178–91. <https://doi.org/10.1016/j.autcon.2018.05.016>.

Zhu, Ye, Xu-Liang Wang, and Xiangyu Chen. 2020. "Evaluation of TBM Cutterhead's Comprehensive Performance under Complicated Conditions." *Journal of Beijing Institute of Technology* 29 (September):326–38. <https://doi.org/10.15918/JJBIT1004-0579.20029>.

Zou, Songchun, and Wanzhong Zhao. 2020. "Synchronization and Stability Control of Dual-Motor Intelligent Steer-by-Wire Vehicle." *Mechanical Systems and Signal Processing* 145 (106925): 106925. <https://doi.org/10.1016/j.ymssp.2020.106925>.